

**Geophysical imaging of Cuxhaven coastal
sediments: Environmental and hydrogeophysical
studies using DC, FDEM and SIP methods**

Von der Naturwissenschaftlichen Fakultät
der Gottfried Wilhelm Leibniz Universität
Hannover

zur Erlangung des Grades
Doktor der Naturwissenschaften

Dr. rer. nat.
genehmigte Dissertation

von

M.Sc. Mohamed Abdel Wahab Attwa Abdel Wahab

geboren am 22.01.1978 in Zagazig, Ägypten

Hannover 2011

Referent: *Prof. Dr. Hans-Joachim Kümpel*

Korreferentin: *Prof. Dr. Andrea Hampel*

Datum der Disputation: *17/05/2011*

ACKNOWLEDGMENTS

First, I owe a debt of thanks to prof. Dr. Hans-Joachim Kümpel who has helped and advised me over the period of this thesis. I was very pleased that he agreed to be my supervisor. Without him I would never have educated at the LIAG institute, Hannover. I deeply appreciate his valuable discussions, comments and supports during time of this work. Especially I wish to thank him for his thorough inspection of the manuscript. Thanks you!!

I wish to extend warm thanks to Dr. Thomas Günther for hours of exciting work and enriching discussions. Most of our work has been joined over the past 4 years and this thesis belongs to him as much as it does to me. No software-no calculations, no calculations-no thesis. Thanks Thomas for providing your software (DC2DInvRes, DC3DInvRes and BERT) and for revising the manuscript. You have accompanied me through 4 years with sincere opinions and immense supports.

No fieldwork- no data, no data-no thesis. Special thanks to Mr. Michael Grinat. Most of the field data presented in this thesis has been joined over the period of this thesis belongs to him. I recall with nostalgia the time we spent together during the field work. In addition, I wish to express my thanks to Ing. Wolfgang Südekum, Dieter Epping and Robert Meyer for their help and assistance during the field work.

No borehole data- no geology-, no geology-no interpretation. Sincere thanks are extended to Mr. Franz Binot for critical assessment to understand the geology of my study area. I particularly thank him for providing relevant borehole data and laboratory results. He helped me to find an accommodation during the field work!!

Without a list of names, my thanks are extended to my colleagues from S2 group of LIAG institute. You have provided a comfortable working atmosphere and valuable support. Special thanks go to Raphael Holland for providing supports during all SIP field work, processing and inversion stages. And, of course, thanks to Prof Dr. Yaramanci (Director of S2 and LIAG institute) for his helpful discussions and advices. It was an honor and pleasure to work under you.

I would particularly like to acknowledge the supports and advises of Dr. Thomas Wonik and Dr. Helga Wiederhold during time of this work. I am also thankful to Ing. Friedrich Hägedom, who watched my hardware network and fixed many problems.

I seize this opportunity to thank the Egyptian Government, which has funded my studies at LIAG institute. Thanks to Zagazig University (Egypt), which granted me for this scholarship. Special thanks to LIAG institute (Hannover) for providing equipment and technical support (geophysical instruments, computer...etc.) during time of this work.

Last, to my wife, thanks for standing by me through the difficult times and for my emotional support, you left your job and career to come with me. Thank you!! Without you I would never have made it!! Hello Mariem and Hagar, you have suffered like us too!! I also want to show my gratitude to my parents, my sister and brother, who supported and encouraged me during many years of studies.

Mohamed Attwa

*Hannover
March 2011*

CURRICULUM VITAE

Personal

Name: Mohamed Abdel Wahab Attwa

Date of Birth: 22.01.1978

Place of Birth: Zagazig City, Egypt

Nationality: Egyptian

Education and Professional Record

2007-present: Currently working on Ph.D. at Leibniz Institute of Applied Geophysics (LIAG), 30655, Hannover, Germany.

2005-2011: Lecturer assistant in faculty of science, geology department/Ph.D. student in Hannover University and Leibniz institute for applied geophysics (LIAG).

Jul. 2005: M.Sc. Geology/Applied Geophysics, Zagazig University, Egypt.

M.Sc. Thesis title (2005): Electrical and hydrogeological studies of unconsolidated aquifer, Belbeis city, Egypt.

1999-2005: Demonstrator in faculty of science, geology department, Zagazing Univ., Egypt.

2000/2001: Post graduate courses in Geology/Geophysics (Excellent).

May 1999: Bachelor of Science (B.Sc.) in Geology Special-Geophysics, Zagazig Univ., Grade: "Very good with honors 84.74%".

1984-1995: Primary, Preparatory and Secondary Schools, Nasria and Elsadat Schools, Sharkia,, Egypt.

Grant

Ph.D Fellowship to Hannover University, Germany, under supervision of Prof. Dr. Hans-Joachim Kümpel, was funded by the Egyptian Ministry of Higher Education from April, 2007-present.

DECLARATION/ERKLÄRUNG

I hereby declare that the present work was made by myself and no other than the cited sources were used.

Hierdurch erkläre ich, dass ich meine Dissertation mit dem Titel

“Geophysical imaging of Cuxhaven coastal sediments: Environmental and hydrogeophysical studies using DC, FDEM and SIP methods”

Selbständig verfasst und die benutzten Hilfsmittel und Quellen sowie gegebenenfalls die zu Hilfeleistungen herangezogenen Institutionen vollständig angegeben habe.

Die Dissertation wurde nicht schon als Masterarbeit, Diplomarbeit oder andere Prüfungsarbeit verwendet.

Muhammed Attwa

*Hannover
March 2011*

ABSTRACT

The original, natural settings of many coastal areas have been altered by anthropogenic influence. The two most widespread and serious sources of man-made coastal impact are saltwater contamination and sedimentation from extensive freshwater pumping, land-clearing and erosion. Pollution and development are changing the coastal habitats. Presently, electrical resistivity methods are applied in a wide variety of geological and environmental site investigations. From a previous airborne electromagnetic survey, a distinct conductive zone above Eemian clay was investigated at the coastal area around Cuxhaven, northern part of Germany. Geologically, the coastal tidal flat sediments formed shallow channel-like features.

We have applied three geophysical methods to image the saltwater and the shallow channel features at Lüdingworth, close to the estuary of the Elbe River, which is an open tidal coastal area in the northwestern part of Germany. The geophysical techniques comprise the following methods: Direct current resistivity (DC), frequency domain electromagnetics (FDEM) and spectral induced polarization (SIP). We aim to evaluate these methods (DC, FDEM and SIP) to show which geophysical methods can perform well under the study area conditions, i.e. to show which techniques provide the required spatial resolution and target definitions in this area. This evaluation also includes a synthetic modeling to analyze the limitations of the DC resistivity imaging technique and assess a joint inversion of data sets from DC configurations in the study area. Extensive borehole data were used to overcome the equivalence problem and to augment the validity of the 1D interpretation (DC and FDEM).

In general, our results constitute an encouraging example using these geophysical methods in characterizing the coastal aquifer. The geophysical inversion results are represented in form of 1D, 2D and 3D imaging. They show that the subsurface resistivity distribution of tidal sediments can change rapidly within a short distance. In addition, two saltwater bodies can be observed, perched saltwater and saltwater intrusion. The EM cross-sections and DC images indicate that the perched saltwater can be observed as a high conductive

layer above peat and Eemian clay layers. The saltwater intrusion is noticed in a wedge-like form. The 2D SIP inversion shows that the perched saltwater is restricted in patched forms above an impermeable layer.

The EM and DC profiles show a shallow channel-like feature within tidal deposits. In presence of extensive boreholes, the DC and FDEM soundings are quick and cost effective reconnaissance techniques for identifying a large lateral variation in the lithology of coastal areas. The integration between both methods is effective and valuable especially in presence of noise sources (e.g., current cables and metals), where the FDEM method suffers from EM wave diffusions.

Both DC sensitivity analysis and synthetic modeling are necessary to judge the model reliability. Two main limitations can be observed from the synthetic modeling: (a) A smearing in the lower boundary of the perched saltwater; (b) an amplification of the lateral effect of the high conductive layer. These limitations decrease the resolution of DC imaging for accurately defining our targets. The joint inversion of different arrays can improve the model reliability especially under no or limited prior geological information. The 2D SIP results demonstrate the suitability of this method for subsurface characterization in the coastal area with a very good resolution. The success of the SIP method supports further investigations into studying the hydraulic parameters of tidal deposits in this area. The information collected during this investigation provides an overview of the coastal aquifer and can serve as a basis for refining the conceptual model of morphological elements and sedimentary sequences of the coastal tidal flat aquifer in this part of Germany.

The integration of aquifer parameters obtained from boreholes and resistivity parameters extracted from surface resistivity measurements can be highly effective. The intention here is to assess an empirical relationship between the aquifer resistivity ρ , the transmissivity K and/or the hydraulic conductivity k_f using the DC soundings. In presence of a good correlation between the observed k_f and measured ρ , we propose a simple equation of a power-law relation between them. Its coefficients are determined using a least-squares fit between the observed and estimated k_f values. We used published data from Nigeria (gravelly to clayey sandy aquifer) and India (loose sands and highly to poorly weathered sandstone aquifer) of 1D soundings to establish this equation. In the Cuxhaven area, we used DC soundings and a 2D SIP profile to investigate the hydrogeophysical conditions of a Holocene tidal aquifer. The methodology has been correlated with k_f values obtained from observed wells and established relationships. The good agreement between aquifer hydraulic parameters obtained from sounding parameters and those obtained from pumping test and grain size analysis proves the potential of the methodology. The overall results indicate that, for an area with a particular geological setting and range of water quality, this equation has a reasonable degree of accuracy. Thus by deriving two adjustable parameters in empirical relation, it is possible to determine k_f and K in areas without boreholes.

Keywords: Resistivity; Shallow channel; Hydrogeophysics.

Kurzfassung

Die natürliche, ursprüngliche Situation vieler Küstengebiete ist durch anthropogene Beeinflussung verändert worden. Die beiden am weitesten verbreiteten und ernstesten Beeinflussungen der Küsten sind Salzwassereinträge und die Sedimentation aus Landabtragung und Erosion. Umweltverschmutzung und Entwicklung verändern die Küstenlebensräume. Derzeit werden elektrische Widerstandsmethoden zur Unterstützung einer Vielzahl von geologischen und ökologischen Untersuchungen in Küstenregionen angewendet. Aus einer früheren luftgestützten elektromagnetischen Untersuchung wurde eine deutlich leitende Zone oberhalb des Eemtons an der Küste rund um Cuxhaven im nördlichen Teil von Deutschland untersucht. Geologisch bilden die Sedimente auf den Küstenwattflächen flache kanalähnliche Formen.

Wir haben drei geophysikalische Methoden zur Abbildung der Salzwasserhältnisse und der flachen Kanalförmigkeiten bei Lüdingworth angewendet, nahe der Mündung der Elbe, die ein offener Gezeitenästuar im nord-westlichen Teil von Deutschland ist. Die geophysikalischen Techniken umfassen die Gleichstromwiderstandsmethode (DC), Elektromagnetik im Frequenzbereich (FDEM) und spektral induzierte Polarisation (SIP). Unser Ziel ist es, diese Methoden zu bewerten, um zu zeigen, welche der geophysikalischen Methoden unter Untersuchungsgebietsbedingungen gute Ergebnisse liefern, d.h., welche Techniken die erforderliche räumliche Auflösung und lithologischen Kenngrößen in dieser Küstenregion liefern können. Diese Bewertung umfasst auch eine synthetische Modellierung: (a) um die Grenzen der DC Widerstandverfahren zu analysieren und (b) um die gemeinsame Inversion von Datensätzen aus DC-Konfigurationen in der untersuchten Region zu bewerten. Umfangreiche Bohrungsdaten wurden verwendet, um das Gleichwertigkeitsproblem zu lösen und die Validität der 1D Interpretation zu erhöhen (DC und FDEM).

In der Regel sind unsere Ergebnisse ein ermutigendes Beispiel für die Verwendung dieser geophysikalischen Methoden zur Charakterisierung von Küsten aquiferen. Die geophysikalischen Inversionsergebnisse werden in Form von 1D-, 2D- und 3D-Bildern dargestellt. Sie zeigen, dass die unter der Oberfläche liegende Widerstandsverteilung der Gezeitensedimente sich schnell auf kurzer Entfernung ändern kann. Darüber hinaus können zwei Salzwasserkörper beobachtet werden: hängendes Salzwasser und lateral eingedrungenes Salzwasser. Die EM-Querschnitte und DC Bilder verdeutlichen das hängende Salzwasser als hoch leitfähige Schicht über Torf- und den Eem- Tonschichten. Das Eindringen von Salzwasser wird in einer keilförmigen

Form festgestellt. Die 2D-SIP Inversion zeigt, dass das hängende Salzwasser lateral begrenzt ist und sich über einer undurchlässigen Schicht gebildet hat.

Die EM- und DC-Profile zeigen eine flache kanalartige Form innerhalb der Gezeitenablagerungen. Mit der Hinzunahme von Bohrlochdaten bieten die DC- und FDEM-Sondierungen schnelle und kostengünstige Aufklärungstechniken zur Identifizierung einer hohen seitlichen Variation in der Lithologie der Küstengebiete. Die Integration der beiden Methoden ist effektiv und wertvoll, besonders in Gegenwart von Störquellen (z.B. Stromkabel und Metalle), wo das FDEM-Verfahren unter EM-Wellendiffusionen leidet.

Sowohl die DC-Sensitivitätsanalyse als auch die synthetische Modellierung sind notwendig, um die Zuverlässigkeit des Modells zu beurteilen. Zwei wesentliche Einschränkungen können bei der synthetischen Modellierung beobachtet werden: (a) Ein Verschmieren an der unteren Grenze des hängenden Salzwassers und (b) eine Verstärkung des seitlichen Effekts der hochleitenden Schicht. Diese Einschränkungen verringern die Auflösung des DC-Imaging für unsere Ziele. Eine Joint-Inversion der verschiedenen Datensätze kann die Zuverlässigkeit des Modells besonders unter nicht oder nur begrenzt vorhandenen vorherigen geologischen Informationen verbessern. Die 2D-SIP-Ergebnisse zeigen die Eignung dieser Methode für die unterirdische Charakterisierung der Küstenregion mit einer guten Auflösung. In dieser Studie unterstützt der Erfolg der SIP-Methode weitere Untersuchungen zum Studium der hydraulischen Parameter von Gezeitenablagerungen. Die erhaltenen Informationen bieten einen Überblick über den Küstenaquifer und können als Grundlage für die Verfeinerung der konzeptionellen Modelle der morphologischen Elemente und sedimentären Sequenzen der Wattflächen in diesem Teil von Deutschland dienen.

Die Integration von Aquiferparametern aus den Bohrungen und Widerstandsparametern, extrahiert aus Oberflächenwiderstandsmessungen, können sehr effektiv sein. In der Arbeit wird eine empirische Beziehung zwischen dem elektrischen Widerstand des Aquifers ρ und der Transmissivität K bzw. dem hydraulischen Leitfähigkeit k_f auf Grundlage der DC-Sondierungen aufgestellt. In Anbetracht der guten Korrelation zwischen den beobachteten ρ und gemessenen k_f schlagen wir eine einfache Gleichung zwischen ihnen vor. Die Koeffizienten sind dabei mit Hilfe einer Least-Squares-Anpassung zwischen den beobachteten und geschätzten k_f -Werten zu bestimmen. Wir haben zudem Daten von 1D-Sondierungen aus Nigeria (kiesig bis sandig lehmige Aquifere) und Indien (Aquifere aus Sand und Sandstein) zur Ableitung dieser Gleichung verwendet. Im Gebiet von Cuxhaven haben wir DC-Sondierungen und ein 2D-SIP-Profil auf hydrogeophysikalische Beziehungen eines holozänen Gezeitengrundwasserleiters untersucht. Diese Methodik wurde mit k_f -Werten aus den verfügbaren Brunnen und etablierten Beziehungen korreliert.

Die gute Übereinstimmung zwischen hydrogeophysikalisch erhaltenen hydraulischen Parametern und solchen aus Pumpversuchen und Korngrößenanalysen belegt das Potential der Methode. Die Gesamtergebnisse zeigen, dass für ein Gebiet mit vergleichbarem geologischen Aufbau und Wasserqualität diese Gleichung ein vertretbares Maß an Genauigkeit liefert. Durch Bestimmung zweier Parameter in dieser empirischen Beziehung ist es möglich, k_f und K auch für Bereiche ohne Bohrungen zu ermitteln.

Keywords: Widerstand; Flachwasserkanäle; Hydrogeophysik.

CONTENTS

1	INTRODUCTION	1
	1.1 Background.....	1
	1.2 Objectives.....	2
	1.3 Approach.....	4
2	STUDY AREA	6
	2.1 Location and morphology.....	6
	2.2 Geological setting.....	7
	2.2.1 Geological setting of Pleistocene sediments.....	9
	2.2.2 Geological setting of Holocene sediments.....	12
	2.3 Hydrogeological background.....	13
3	PRINCIPLES OF GEOPHYSICAL METHODS	15
	3.1 Direct current (DC) resistivity methods.....	15
	3.1.1 Basic theory.....	15
	3.1.2 Electrical properties of rocks.....	18
	3.1.3 DC resistivity soundings.....	19
	3.1.4 Electrical resistivity tomography (ERT).....	21
	3.1.4.1 2D Electrical resistivity tomography (2D ERT).....	22
	3.1.4.2 3D Electrical resistivity tomography (3D ERT).....	24
	3.2 Spectral induced polarization method.....	26
	3.2.1 Origin of induced polarization.....	27

3.2.2 Mechanism of induced polarization.....	28
3.2.3 IP measurements.....	29
3.3 Geoelectrical electrode configurations.....	31
3.4 Frequency domain electromagnetic method (FDEM).....	37
3.4.1 EM fundamentals.....	37
3.4.2 Basic physics of FDEM method.....	38
3.4.3 FDEM skin depth.....	39
3.4.4 Loop configurations.....	40
3.5 Data interpretation.....	41
3.5.1 General.....	41
3.5.2 DC interpretation.....	42
3.5.2.1 1D DC interpretation.....	43
3.5.2.2 2D/3D DC and SIP interpretation.....	44
3.5.3 FDEM data interpretation.....	47
3.6 Resistivity-hydraulic parameters relationship.....	49
3.6.1 Hydraulic parameters.....	49
3.6.2 DC ρ - K approaches.....	50
3.6.3 IP- k_f approaches.....	52
4 DATA ACQUISITION, PROCESSING AND INVERSION.....	55
4.1 DC Resistivity survey.....	55
4.2 FDEM survey.....	60
4.3 SIP survey.....	62
4.4 Data processing and inversion.....	63
4.4.1 1D resistivity soundings.....	63
4.4.2 DC and SIP tomography.....	67
4.5 Hydrogeophysical study.....	74
5 INTERPRETATION AND DISCUSSION.....	80
5.1 Resistivity spectrum.....	80
5.2 1D DC interpretation.....	81
5.1.2 Geoelectrical cross-sections.....	81
5.1.3 3D visualization.....	84
5.3 Altenbruch data interpretation.....	86
5.3.1 2D DC resistivity imaging.....	87
5.3.2 Synthetic modeling.....	90
5.3.3 3D DC resistivity imaging.....	91

5.4 Norderscheidung data interpretation.....	94
5.4.1 1D interpretation.....	94
5.4.2 2D DC resistivity imaging.....	99
5.4.2.1 Synthetic modeling.....	99
5.4.2.2 2D DC inversion results (Line 1).....	101
5.4.2.3 2D DC inversion results (Line 2).....	107
5.4.3 3D DC resistivity imaging.....	112
5.5 Süderscheidung data interpretation.....	115
5.5.1 1D interpretation.....	116
5.5.2 2D DC resistivity imaging.....	120
5.5.2.1 Synthetic modeling.....	124
5.5.2.2 2D SIP inversion results.....	127
5.6 Discussion.....	131
5.7 Hydraulic characteristics of tidal deposits.....	134
5.7.1 Qualitative interpretation.....	134
5.7.2 Quantitative interpretation.....	136
5.7.3 Discussion.....	139
6 SUMMARY AND CONCLUSIONS	141
LIST OF FIGURES	149
LIST OF TABLES	152
BIBLIOGRAPHY	153
APPENDICES	170
LIST OF SYMBOLS AND ABBREVIATIONS	180

1 INTRODUCTION

1.1 BACKGROUND

Saltwater intrusion into shallow aquifers is often an important problem along coastal areas. It is the induced flow of seawater into freshwater aquifers primarily caused by groundwater development near to the coast. Nowadays, coastal areas are often densely populated, where dense population and touristic development are coupled to scarce water resources and require intense exploitation of groundwater. Below the withdrawn freshwater in coastal aquifers, there often exists a saltwater formed by recirculating seawater (*Cameo, 2006*). Freshwater pumping produces a saltwater wedge-like feature. This wedge develops because freshwater, which floats on the top of saltwater, is less dense than saltwater. The boundary between saltwater and freshwater is not distinct; the zone of dispersion, the transition zone or saltwater interface, is brackish with saltwater and freshwater mixing. The natural movement of freshwater towards the sea prevents saltwater from entering freshwater coastal aquifers (*Barlow, 2003*).

As the majority of coastal areas are made up of unconsolidated sediments, they are also subjected to comparatively fast morphological changes. These areas are characterized by a large variety of morphological elements and depositional environments. They are regarded as a global problem (*Alley et al., 2003*) and therefore detailed knowledge about the geological setting is essential to understand the processes of coastal evolution.

In northern Germany, Cuxhaven coastal region is a tidal flat area and is considered as a densely populated area. An increasing number of people and touristic development yet have led to a stronger demand for water supply than ever before. In history, this area was influenced by tidal fluctuations, long-term climate and sea level changes and seasonal changes in evaporation and

recharge rates. Recharge rates are sometimes lowered with increased urbanization involving impervious surfaces.

Unless subsurface conditions are rather homogenous, the near surface deposits can generally not be adequately characterized by just drilling and logging a limited number of boreholes. Surface-geophysical methods provide quick, non-intrusive and relatively inexpensive alternatives for collecting continuous subsurface geologic information. They also provide information about the spatial distribution of subsurface physical properties, such as electrical conductivity (or its inverse, resistivity), dielectric permittivity, magnetic susceptibility, density and seismic velocity. Commonly employed geophysical methods include seismic, potential and geoelectric methods. In general, the geophysical methods have significant potential for environmental and hydrogeophysical applications. They have been successfully used in groundwater exploration and mapping the boundaries between freshwater and saltwater (e.g., *Sharma, 1997; Gemal et al., 2004; Corriols and Dahlin, 2008; Corriols et al., 2009*). Usually, multiple geophysical methods offer better answers than any individual exploration technique. The methods can be applied at a wide range of field scales and surveys made in arbitrary geometrical configurations (e.g., boreholes). Saltwater intrusion, buried hydrogeologic, geological features and subsurface layer characterization are ideal targets for mapping using geophysical methods.

Among geophysical techniques, geoelectrical methods are powerful tools. They have a broad range of useful applications, including mineral exploration, engineering and environmental investigations and archeological studies. They can be divided into two categories:

- a. Electrical techniques: Direct current (DC) resistivity, induced polarization (IP) and self-potential (SP).
- b. Inductive or electromagnetic techniques: Frequency domain electromagnetic (FDEM), time domain or transient electromagnetic (TEM) and magnetotelluric (MT) methods.

The area around Cuxhaven and Bremerhaven has been studied intensively geophysically and hydrogeologically (e.g., *Kessels et al., 2000; Wiederhold et al., 2005; Kirsch et al., 2006*). One purpose was to secure fresh water supply for the area from Pleistocene buried channels. Intense interdisciplinary research was performed and planned to study the groundwater dynamics in the Cuxhaven area (*Friedhoff, 2001; Siemon et al., 2001b; Fulda, 2002; Wagenschein, 2002*). High-resolution seismic reflection surveys of the offshore North Sea area have been published, for example, by *Praeg (1996)*, *Schwarz (1996)* and *Huuse and Lykke-Andersen (2000)*. Helicopter electromagnetic (HEM) methods have been successively used to map buried valleys in northern Germany (*Fluche and Sengpiel, 1997*). *Gabriel et al. (2003)* studied various buried Pleistocene subglacial valleys in northern Germany, e.g., the Ellerbeker Rinne and Bremerhaven-Cuxhaven Rinne including seismic, gravity and helicopter electromagnetic (HEM) surveys.

1.2 OBJECTIVES

The present study is focused on DC, FDEM and SIP (spectral induced polarization) investigations over a coastal area near to the Cuxhaven region. The thesis, mainly, is an

environmental geophysical study about the saltwater-freshwater problem. Despite the large amount of scientific literatures about this topic in the Cuxhaven area (e.g., *Siemon and Binot, 2003; Noell and Panteleit, 2004*), detailed studies are still required and many questions have remained open. Therefore, the first objective of this thesis is to evaluate the geoelectrical methods in imaging and characterizing the younger glaciation (Saale) freshwater Quaternary aquifer and the saltwater intrusion. From previous HEM survey, an isolated shallow distinct conductive zone is known, in addition to saltwater intrusion (*Siemon et al., 2001a; Siemon et al., 2004*). Consequently, the second objective is to identify the HEM shallow conductive zone, which was observed in the Cuxhaven region.

Heterogeneity is of extreme importance in many coastal deposits where lateral variations of facies are frequent and there exist paleochannels that act as preferential paths for incoming seawater (*Cameo, 2006*). In the research area, *Streif (2004)* expected, schematically, that the heterogeneity within the tidal deposits could produce a shallow channel-like feature, which has not been geophysically proved yet. Thereby, the third objective of this thesis is an attempt to evaluate the geoelectrical methods in imaging and characterizing this feature. Geologically, the tidal flat deposits are dominated by fine sediments, which can be considered to be a protection zone to freshwater aquifer from surface pollutants, e.g., tidal saltwater and fertilizer. The fourth specific objective of this thesis is to study the hydrogeophysical properties of the Holocene tidal deposits. Finally, we attempt to apply various geophysical approaches to understand the hydraulic properties of shallow tidal deposits. In our research, the key questions are:

- (i) How can the combined use of geoelectrical methods (DC, SIP and FDEM) resolve the subsurface layers and heterogeneities within the Quaternary deposits?
- (ii) How can we optimize the survey design and identify limitations of the resistivity technique?
- (iii) How can the detailed study of geoelectrical configurations improve the reliability of the resulting models for reconstructing the subsurface electrical resistivity distributions in two or three dimensions (2D or 3D)?
- (iv) Can EM measurements over a wide range of frequencies (FDEM method) be considered faster and more accurate than DC soundings for characterizing coastal areas?
- (v) To which extent can IP measurements of resistivity magnitude and phase angle over a wide range of frequencies (SIP method) offer a robust mean for non-invasive characterization of geological heterogeneity within tidal flat deposits?
- (vi) To which extent can DC and SIP methods provide valuable information about hydraulic conductivity of tidal deposits?

For these purposes, the steps in planning the present work were as follows (Fig. 1.1):

- 1- We collected the available topographic, geological and geophysical information about this coastal area.
- 2- 1D DC soundings were measured all over the study area to have a general overview about the subsurface layers and resistivity distributions.

3- 1D FDEM soundings were measured and a cross-section was constructed to image the saltwater and Quaternary aquifer at the central part of the investigated area. Guided by the 1D results, 2D and 3D DC resistivity imaging campaigns were conducted at three selected sites to image the saltwater occurrences and Quaternary aquifer.

4- For shallow geophysical investigation, FDEM soundings and 2D DC and SIP profilings were carried out.

5- Geoelectrical parameters and SIP empirical relations were applied to characterize the hydraulic properties of Holocene tidal sediments.

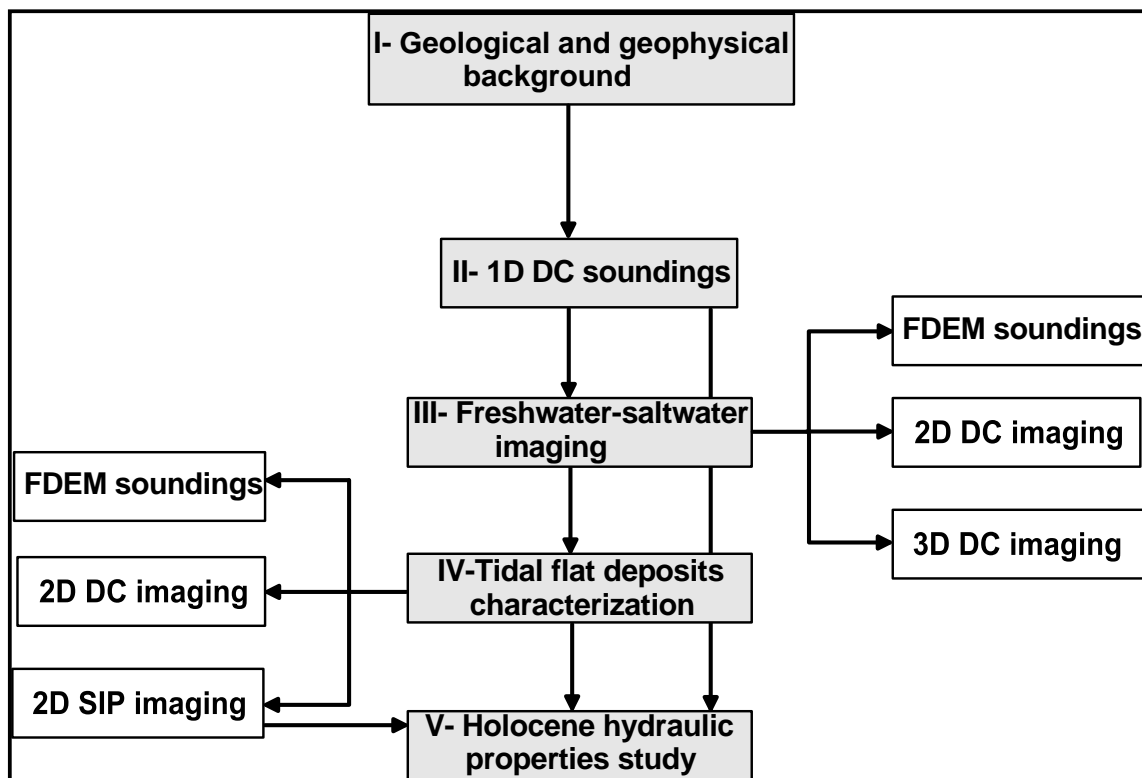


Fig. 1.1: Flowchart relevance to the steps of planning the research work.

1.3 APPROACH

This dissertation consists of seven chapters and two Appendices. After this introduction the following chapters will be presented:

Chapter 2 outlines the morphology, geological setting and hydrogeological background of the study area and provides the location map of the area.

Chapter 3 focuses on the basic theory and fundamentals of geoelectrical methods including 1D soundings (DC and FDEM), 2D imaging (DC and SIP) and 3D imaging (DC). It also gives an introduction to the inversion of DC, FDEM and SIP methods. Finally, it represents the roles of DC and SIP in hydrogeophysics. Various approaches for calculating the hydraulic conductivity and transmissivity from DC and SIP measurements will be shown.

Chapter 4 provides a detailed description on how to acquire the geophysical measurements in the study area. It explains the field parameters for each method, e.g., profile length and spacing, electrode spacing, electrode configuration and the measured frequency range. This chapter also shows a short description to the geophysical instruments which will be used in the data acquisition and outlines the data processing and inversion of our measurements in the investigated area.

Chapter 5 shows the geophysical imaging of saltwater occurrences and a Pleistocene freshwater Quaternary aquifer using DC and FDEM. Also, the limitations of DC imaging will be discussed by preparing the synthetic modeling, in addition to assess the DC combined data sets of different configurations. A shallow geophysical characterization to tidal flat deposits at the southern part of the considered area is presented. The importance of SIP measurements to image and characterize the heterogeneity within the tidal flat deposits is shown. Finally, this chapter presents DC soundings application in predicting the hydrogeological parameters of Holocene aquifers in terms of hydraulic conductivity, transmissivity, clay content, grain size distribution and potentiality of the aquifer. The transmissivity estimation using different DC empirical relations will also be discussed. SIP inversion results will be used to estimate the hydraulic conductivity using various approaches.

Chapter 6 summarizes the most important conclusions and results of this study. It also includes some recommendations for further research work.

2 STUDY AREA

2.1 LOCATION AND MORPHOLOGY

The study area is located in Lower Saxony, in the northern part of Germany. It is close to the estuary of the Elbe river and between latitudes $53^{\circ} 47' 15''$ N and $53^{\circ} 50' 12''$ N and longitudes $8^{\circ} 41' 34''$ E and $8^{\circ} 46' 40''$ E. It contains extensive drainage lines for agricultural and reclamation purposes. This flat coastal area is located between Bremerhaven and Cuxhaven (Fig. 2.1a). Before constructing the artificial coastal sea dikes next to the Elbe River, this area suffered from many phases of sea transgressions. Figure 2.1b shows locations of drilled boreholes, which will be used to construct geological cross-sections.

The southern North Sea coast of Germany was studied morphologically by several authors. The area is characterized by a large variety of morphogenetic elements and depositional environments. The climatic changes occurring during the Quaternary period have led to a series of large, rapid changes in the shallow marine and coastal lowland areas. For most of the Quaternary period, the area of the German North Sea sector including the coastal areas was well above sea-level. Sea-level oscillations of about 100 m caused shoreline displacements of 500-600 km and left behind a fragmentary sedimentary record which can be used for the reconstruction of stages of landscape development (*Streif, 2004*).

In general, the area between Cuxhaven and Bremerhaven represents a lowland of Holocene tidal deposits (Marschlands) and a highland of exposed Pleistocene deposits (Geest). Marschlands run more or less parallel to the Elbe and Weser rivers and along the shore line (Figs. 2.1a and 2.2a). The morphology of the survey is that of wet marschland just above sea level (*LGN 1999*). It is characterized by many drainage lines with spreading agricultural areas. CAT-LUD 1 is the name of scientific borehole in the Coastal Aquifer Test Field which was used to establish the hydrogeological

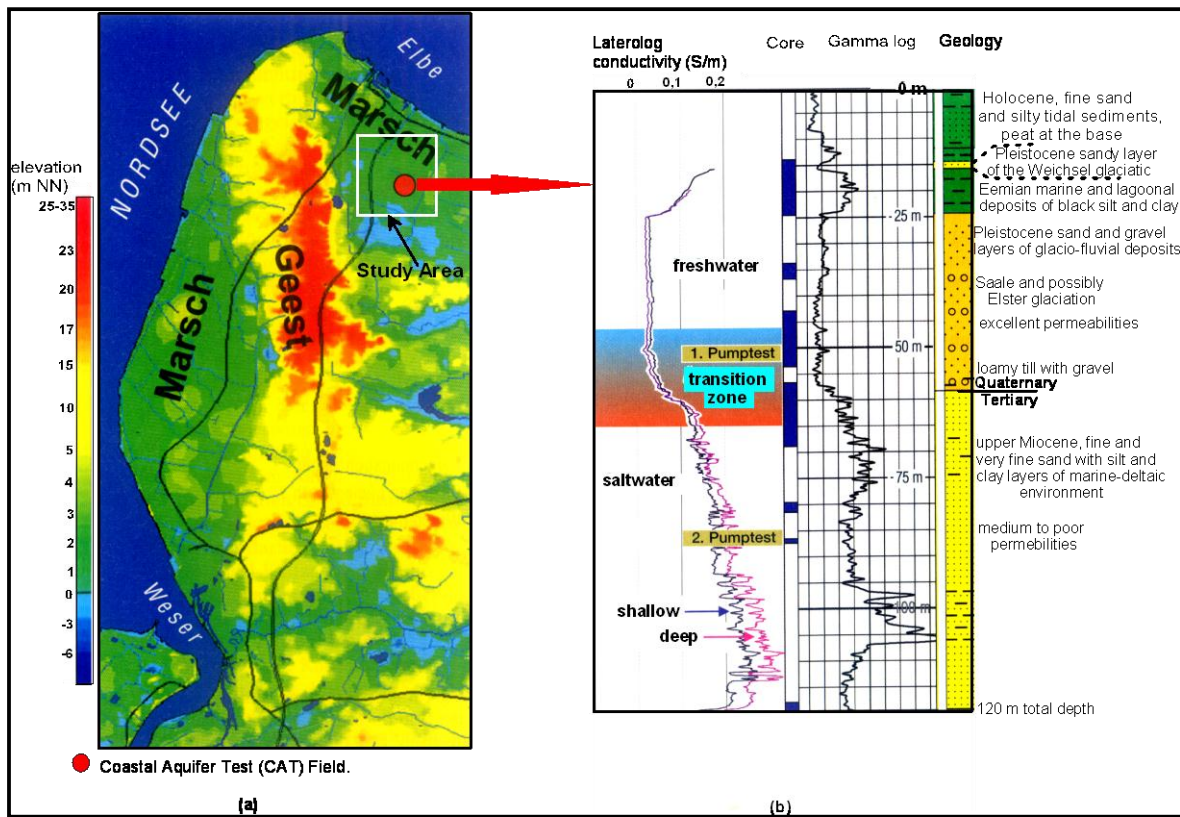
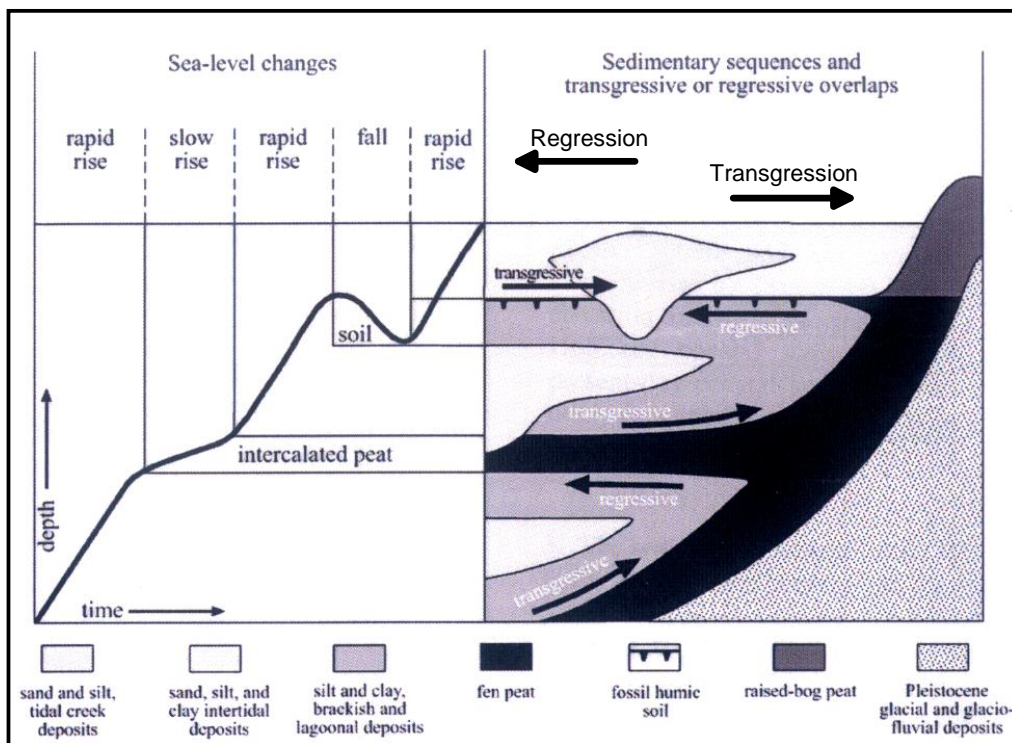


Fig. 2.2: (a) Digital elevation model of the Cuxhaven-Bremerhaven region (LGN, 1999) and (b) a borehole composite of four sections, left to right: laterolog, cored section, gamma ray log and geological profile.



2.3: Trends and dynamics of sea-level changes and their record in the sedimentary sequences of the coastal zone (Streif, 2004).

2.2.1 GEOLOGICAL SETTING OF PLEISTOCENE SEDIMENTS

The sedimentary sequence of Lower and early Middle Pleistocene reaches a total thickness of more than 800 m in the North Sea basin. Generally, during the Middle Pleistocene epoch, the survey area was periodically covered by the Scandinavian ice cap. The deposits are mainly of shallow marine to deltaic origin in the basin (Cameron *et al.*, 1987, 1993; Long *et al.*, 1988). Both seismic and borehole data provide evidence of series of marine transgression and regression which appear to have occurred during this epoch. As no exact figures are available for the amplitude of the sea-level changes, and only rough estimates are available of the duration of the phases of warm climate, the dynamics of transgressions and regressions during Lower and early Middle Pleistocene epoch are particularly unknown (Streif 2004).

The upper Pleistocene is characterized by many phases of marine regression (cold climate) and transgression (warm climate). Table 2.1 shows that three regional glaciations affected north-western Europe to different extends during the Elsterian (Anglian), Saalian (Wolstonian) and Weichselian (Devensian) glacial stages, when the Scandinavian and British ice sheets temporarily covered parts of the present-day North Sea (Streif, 2004). During the glaciation phases, very heterogeneous sediments had been deposited. Moreover, large structures, formed by subglacial erosion, cut deeply into underlying strata. They are called buried valleys, since they cannot be seen at the surface today (Kirsch *et al.*, 2006).

In the Cuxhaven area, the Elsterian glacial deposits lie on a regional unconformity which generally occurs at 80-90 m below the present sea level. The unconformity was formed as a result of the advancing ice, which left glaciofluvial deposits on a truncated fluviodeltaic sequence to shallow marine sediments (Streif, 2004). A complex system of anastomosing valleys was formed by the Elsterian ice sheet. The glacial valleys cut down deeply through the Pliocene and Miocene sediments into the Eocene clays. They reached depths of more than 350 m bsl whereas the width is only 1 or 2 km. The valleys were filled with melt water deposits, beginning with sand and gravel at the base and often grading into silt and clay deposits in their upper part. Generally, the Elsterian valleys were covered by a thick clay layer (Lauenburg clay) of tens of meters. In places the Lauenburg clay is thin or absent. The system of subglacial valleys occurs in large areas of the present-day North Sea as well as the adjacent mainland. Kuster and Mayer (1979) could reveal the average total thickness of the channel fill to be in the order of 350 m (Fig. 2.4). The Bremerhaven-Cuxhaven buried valley was well imaged by HEM and gravity methods (Gabriel *et al.*, 2003).

Holocene			
Upper Pleistocene	Weichselian cold stage	Upper Weichselian	Younger Dryas stadial Alleröd-Interstadial Older Dryas stadial Bölling-Interstadial Oldest Dryas stadial Meindorf-interval
		Middle Weichselian	Glacial Maximum Denekamp-interval Hangeic-interval Moershoofd-interval-complex Glinde-interval Ebersdorf-Stadial Oerel-interstadial Schalkholz-Stadial
		Lower Weichselian	Odderade-interstadial Rederstall-Stadial Brörup-Interstadial Hening-Stadial
Eemian interglacial stage (128,000- 117,000 Bp)			
Middle Pleistocene	Saalian complex	Warthe glacial substage	
		Drenthe glacial substage	Younger Drenthe (Lamstedt phase) Drenthe main advance (Hamein phase)
		Dömnth temperate stage	(Wacken Schönningen)
Fuhne cold stage			
Holsteinian interglacial stage (no later than 230,000- 245,000 Bp)			
Middle Pleistocene	Elsterian complex	Elsterian cold stage sensu stricto	
		Gelkenbach temperate stage	
		Bilshausen Red Clay	

Table 2.1: Stratigraphic record of Middle and Upper Pleistocene of Northern Germany with marine ingressions indicated in the right column (Streif, 2004).

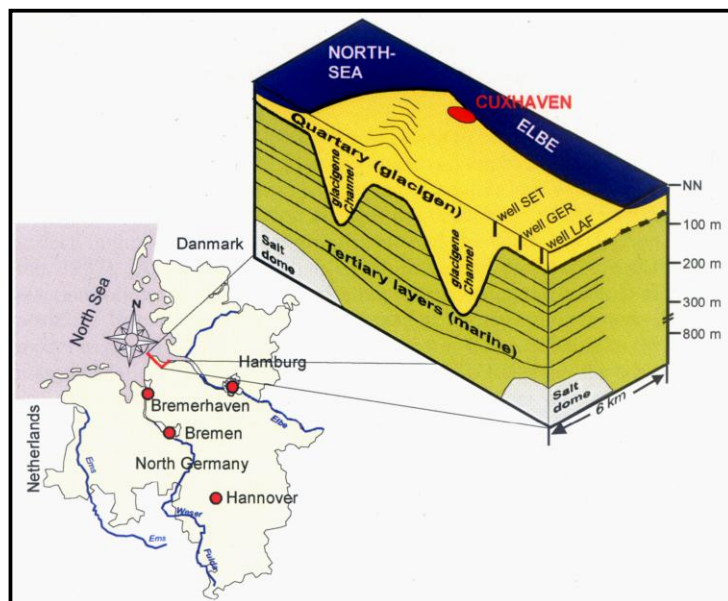


Fig. 2.4: Geological setting through the Cuxhaven area (Panteleit et al., 2001b).

The marine transgression of the Holsteinian interglacial invaded a landscape with a rough morphology shaped by the Elsterian ice sheet (*Streif, 2004*). In the Hamburg area (southeastern part of the study area, Fig. 2.1a), which is a key region for demonstrating the interaction between sea-level rise and marine sedimentation, the Holsteinian interglacial transgression started with open-water conditions and fauna, indicating a water depth of 20-30 m. Evidence of warmer, shallow water and brackish conditions are found in the middle part. Most saline and slightly deeper water conditions are observed in the uppermost part of the sequence (*Knudsen, 1993*). In northern Germany, Holsteinian interglacial marine deposits are found at 20-30 m below sea level. In the Cuxhaven area and the lower reaches of the Elbe River, the Holsteinian transgression invaded as far as 160 km inland following the partially filled meltwater runoff valleys formed during the preceding Elsterian glacial stage (*Linke, 1993; Hinze et al., 1995*). Besides the sedimentary fill of these valleys, no other morphological features were left behind by this transgression.

During the Saalian glacial stage, the Scandinavian ice sheet covered Denmark and parts of northern Germany, extending as far as about 40 km off the present-day coast of the northern Netherlands and about 110 km off the Danish coast (*Foged, 1987; Joon et al., 1990; Cameron et al., 1993; Laban, 2000*). In the Cuxhaven area, coarse grained sediments of younger glaciations (Saale) are found above the Lauenburg clay or above the Pliocene fine sands in depths of about 50 m (*Panteleit, 2004*). No data is available about the sea-level low stand during the Saalian glaciation (*Streif, 2004*).

The deposition of the Eemian clay can be attributed to a coastal transgression as deposits of marine origin (*Sindowski, 1969*). According to *Streif (2004)*, the Eemian characteristic is a simple transgression-regression hemicycle, which left behind in the coastal zone a sedimentary sequence consisting of a thin basal peat, a thick unit of tidal sediments, and a peat layer on top of it. For the post-Eemian period an average sedimentation rate of 1.2 cm/century can be calculated in the coastal zone of Lower Saxony (*Streif, 2004*). The surface of the sequence is at -9 m to -7 m. Due to extensive post-Eemian erosion, no information is available about the coastline in the present-day Weser estuary area. In contrast, considerable geological evidence is available on the paleogeography of Eemian tidal bays along the Elbe Estuary, which has been reconstructed in detail (*Höfle et al., 1985; Hinze et al., 1995*). In the Cuxhaven area, Lacustrine carbonates and marine clays of the Eemian interglacial (*Höfle et al., 1985*) are locally found at depths 7 m and 25 m b.s.l. (*Panteleit, 2004*).

In the southern North Sea area, the sea level was more than 35 m below its present-day level during the Weichselian cold stage. To date, no indication of temporary high stands of the sea level have been recorded for the phases of temperate climate which occurred during the interstadials of the lower to middle Weichselian (Table 2.1). During the Weichselian cold stage, the last glaciation is locally recorded in Cuxhaven as sandy layers above Eemian sediments (*Panteleit, 2004*). At this stage, the sea level dropped to 110-130 m below the present level.

Figure 2.5 shows a general lithological description of sedimentary layers constructed from the drilled boreholes (Fig. 2.1b). The Pleistocene geology is represented by Eemian clay, Saalian coarse sand and Lauenburg clay. These deposits were covered by Holocene tidal deposits of silt, clay, sandy silt and silty sand. The Eemian clay becomes thicker (~ 7 m thick) at well WIT01 and is absent at wells DS31, GER05 and LAF05. The Lauenburg clay was observed at about 50 m depth at wells BUL01, SET05 and HAD03. The Lauenburg clay was observed at about 50 m depth at wells BUL01, SET05 and HAD03.

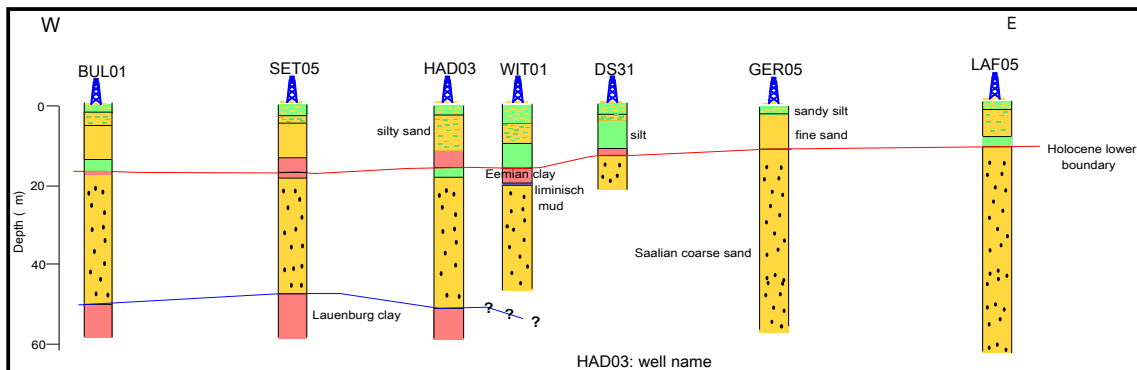


Fig. 2.5: Lithological information from boreholes used for geological description in Cuxhaven area, Lüdینگworth.

2.2.2 GEOLOGICAL SETTING OF HOLOCENE SEDIMENTS

In the Cuxhaven area, the Holocene sedimentation normally starts with a basal peat horizon, followed by brackish lagoon or tidal flat sediments (Panteleit, 2004). In offshore sections, it consists of fine-to medium-grained shell-bearing shallow marine sand. In some places these are underlain by tidal flat sediments consisting of fine grained sand as well as silty-clayey deposits. Locally, limnic mud and peat (well WIT01) occur at the base of the Holocene sequence (Streif, 2004). Onshore peat sedimentation has been preserved to a minor extent.

Three geological cross-sections were constructed from the available boreholes (Fig. 2.1a). Figure 2.6 shows the lower boundary and heterogeneity of the Holocene sedimentary sequence from northern (close to Elbe River) to southern parts. The thickness of the sequence ranges from about 11 m to 18 m. The Holocene tidal flat deposits grade from fine sand at the northern part to clay and silt deposits at the southern part. The central part is characterized by intercalations between sand and fine sediments (silt and clay).

In Lower Saxony, the coastal zone typically consists of a wedge-like body of sediments with fine-grained sand, silt and clay and intercalated layers of peat (Fig. 2.7, Streif, 2004). Such a cyclic alternation of transgressive overlaps (marine and brackish deposits overlying peat) with regressive overlaps is an indicative of repeated shoreline displacements, both landward and seaward, often of several kilometers. In general, close to the estuary of the Elbe River, the tidal flat deposits extend 80-100 km inland (Streif, 2004). The seaward part of the Holocene accumulation wedge mainly consists of pure fine-to medium-grained sand deposited on high-energy environments like the foreshore area.

Further inland, the tidal sediments consist of fine sand, silt and clay layers deposited in sheltered or open tidal flats as well as in the brackish-water environment of coastal lagoons and estuaries alternating with peat layers which were formed in coastal bogs (Streif, 2004). In the coastal zone of Lower Saxony, the post Eemian clay, which deposited over the Pleistocene aquifer, can be attributed to a coastal transgression as deposits of marine origin (Sindowski, 1969).

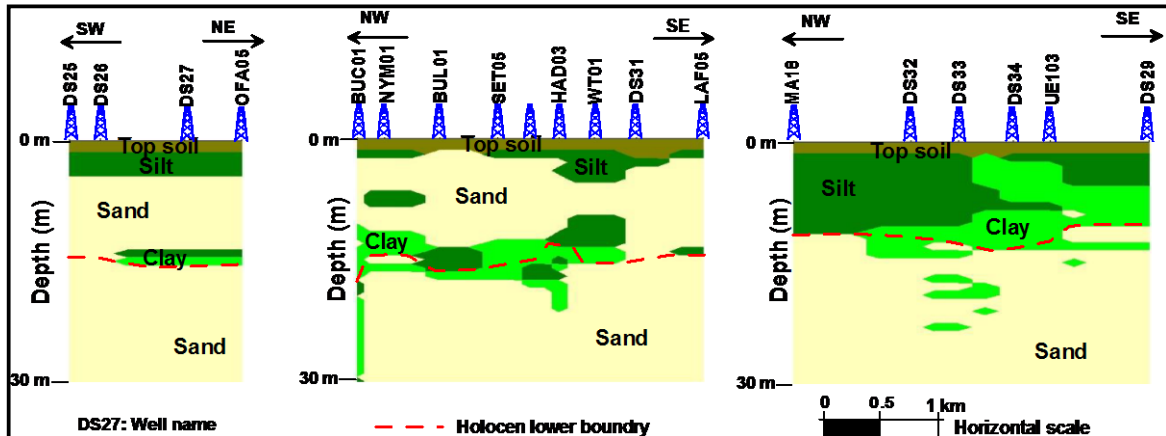


Fig. 2.6: Generalized geological cross-section through the study area from north (left) to south (right), see Fig. 2.1.

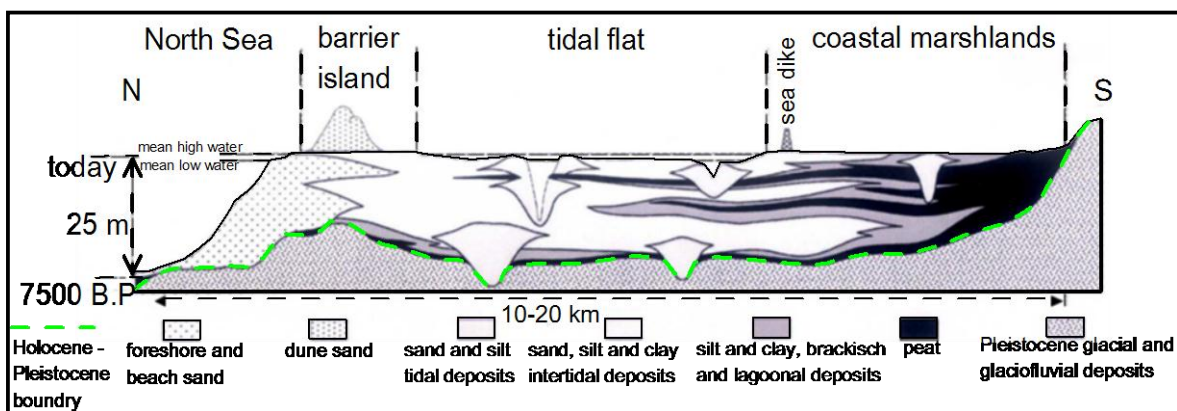


Fig. 2.7: A Schematic cross-section through the coastal Holocene showing the morphological elements and the sedimentary sequences during the last 7500 years B.P. (after Streif, 2004).

2.3 HYDROGEOLOGICAL BACKGROUND

Figure 2.8 shows a sketch of the geological setting and groundwater flow pattern in the Cuxhaven coastal area. Figure 2.8b shows that the deep glacial erosion channels cut down to the Quaternary aquifer base (Kuster and Meyer, 1979). The high hydraulic permeability of the coarse Quaternary textured sediments will lead to quicker change in the salt-fresh water distribution during a salinization or freshening scenario (Vandenbohede and Lebbe, 2002). A low permeable layer (Lauenburg clay) is intercalated into glacial sediments (Fig. 2.8b). In the flat marsh areas, Holocene

terrestrial and tidal flat sediments have a higher clay content and organic material with low permeable properties. At the well CAT-LUD1 location (marsch region), the surface cover is followed by 25 m of two interglacial (Holocene and Eemian periods) transgressive tidal flat sedimentary sequences (Fig. 2.2b), which have a poor to medium hydraulic conductivity of $k_f = 10^{-5}$ to 10^{-6} m/s (Panteleit et al., 2006). These interfinger with muds of brackish lagoonal type and with onshore peat deposits. This horizon overlays Pleistocene coarse sediments of Elster and Saale glaciations sand and gravel ($k_f = 10^{-5}$ to 10^{-2} m/s). Figure 2.2b represents two laterologs (Serra, 1984): a shallow log, reflecting the conductivity of the borehole fluid and the nearby groundwater, and a deep penetrating log, displaying the conductivity of groundwater further away from the well. These logs represent a transition zone between freshwater and saltwater, from 45 m to 65 m depth. The gamma ray log gives a good indication of increasing clay content within tidal flat deposits (Holocene and Eemian sediments) than Pleistocene deposits. Figure 2.8c shows the interaction between saltwater from the Elbe River and freshwater from the Geest area. The glaciogene-sandy deposits at the Geest ridges are important groundwater recharge areas (Panteleit et al., 2004). A natural saltwater intrusion can be observed below the marsh areas (Siemon et al., 2001b). Dispersion and advection processes create a transition zone between salt- and freshwater with intermediate salt concentrations (Panteleit et al., 2001a). There is no recharge to Holocene sediments in marsh areas due to the low permeability and to the extensive drainage for agricultural and land saving purposes, but upwelling groundwater is observed (Friedhoff, 2001).

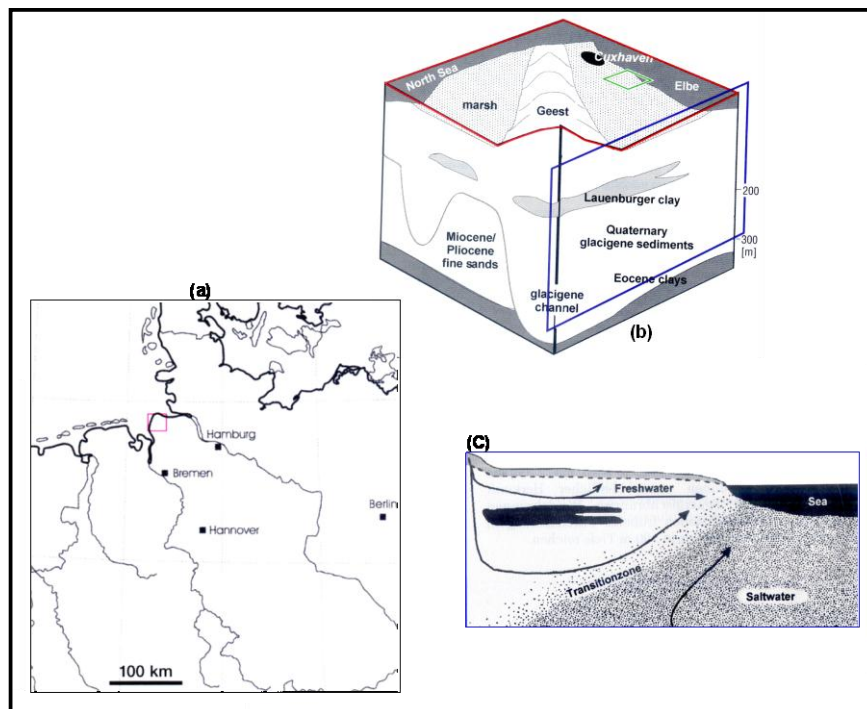


Fig. 2.8: Location map of the coastal area (a), sketch of geological units at the CAT-field (b) and the hydraulic flow pattern (c), after Cooper (1959).

3 PRINCIPLES OF GEOELECTRICAL METHODS

A geophysical survey conducted as part of a hydrological investigation to determine groundwater resources usually has an investigation depth no greater than 300 m. Geophysical investigation depths for environmental, geotechnical engineering, and archeological applications typically do not exceed 30 m (Allred *et al.*, 2008). Among geoelectrical methods, DC resistivity, IP and FDEM methods will be summarized within this chapter.

3.1 DIRECT CURRENT (DC) RESISTIVITY METHODS

3.1.1 BASIC THEORY

The direct current (DC) surveys are involving direct injection via electrodes at the ground surface. Current I is induced between paired electrodes A and B . The current used is either direct current, commutated direct current (i.e., a square-wave alternating current) or alternating current AC of low frequency (typically about 0.5 Hz to 10 Hz). Fig. 3.1 shows a square wave, which is widely used in DC method, and a background (self-potential) voltage V_{sp} . The potential difference ΔV between paired voltmeter electrodes M and N is measured. The ability to oppose the current flow by a conductive cylinder is called resistance, R . Eq. (3.1) shows Ohm's law as

$$\Delta V = RI \quad (3.1)$$

Based on Ohm's law, the resistance, R , is the voltage divided by the current, I . The situation will change if the geometry of the conductive material changes. Therefore, it is not a physical property and can be expressed as

$$V = \rho L/a \quad (3.2)$$

where ρ is the resistivity in Ωm , L is the length of the conductive cylinder in m and a is the cross-section area in m^2 .

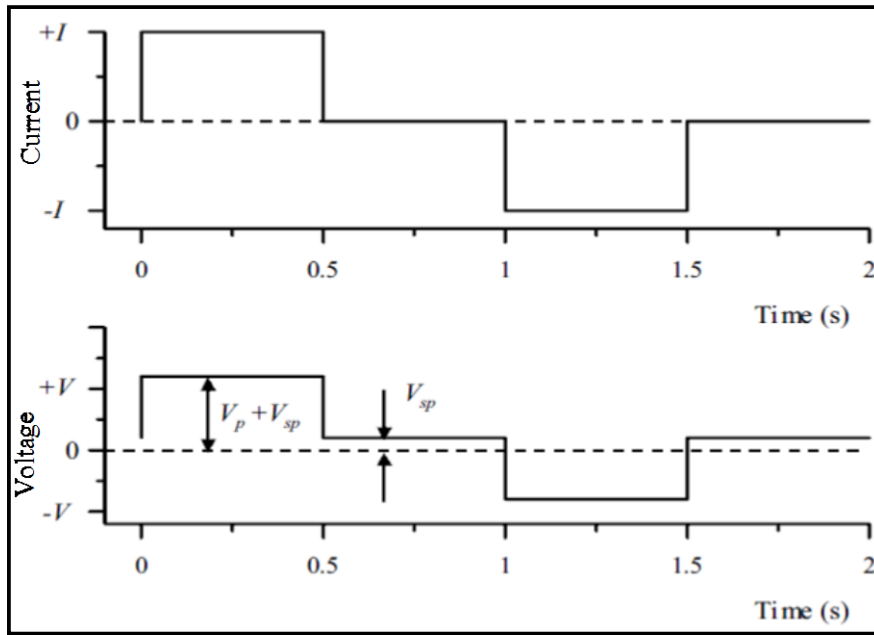


Fig. 3.1: Typical current and idealized voltage waveforms for field DC resistivity surveys. V_p is the primary voltage, V_{sp} is some self-potential voltage.

The general field layout of DC measurements is sketched in Fig. 3.2. Two pairs of electrodes are required: Current (A and B) and potential (M and N) electrodes. Stainless steel is the most widely used electrode material for field measurements. Fig. 3.2 shows the current flow lines (solid) and equipotentials (dashed) for a two layers underground. The voltage between the inner electrodes (M and N) with respecting to electrode A and electrode B respectively, can be computed as

$$V_M = \rho I / 2\pi \left\{ \frac{1}{r_1} - \frac{1}{r_2} \right\} \quad (3.3)$$

$$V_N = \rho I / 2\pi \left\{ \frac{1}{r_3} - \frac{1}{r_4} \right\} \quad (3.4)$$

where $r_1 = AM$, $r_2 = AN$, $r_3 = BM$, and $r_4 = BN$.

The voltage between the M and N electrodes can then be calculated as follows:

$$\Delta V = V_M - V_N = \rho I \left[1/2\pi \left\{ \frac{1}{r_1} - \frac{1}{r_2} - \frac{1}{r_3} + \frac{1}{r_4} \right\} \right] \quad (3.5)$$

Replacing the factor in square brackets by $1/G$, we obtain the resistivity of the homogeneous half-space as follows:

$$\rho = G \Delta V / I \quad (3.6)$$

where G is called geometric factor or configuration factor (unit: meter).

Fig. 3.2 shows the general way of the current flow in a two layers underground, where there is a distortion to current or equipotential lines at the boundary between these layers. The equipotentials are everywhere orthogonal to the current flow lines. The current distribution is uniform over hemispherical shells centered on the source for each layer. For inhomogeneous conditions, Eq. (3.6) gives the resistivity of an equivalent homogeneous half-space. For this situation the term apparent resistivity ρ_a is introduced and it will be a function of the form of the inhomogeneity. Apparent resistivity is defined as

the resistivity of an equivalent electrically homogenous and isotropic half-space that would yield the potential measured on the heterogeneous earth using the same applied current.

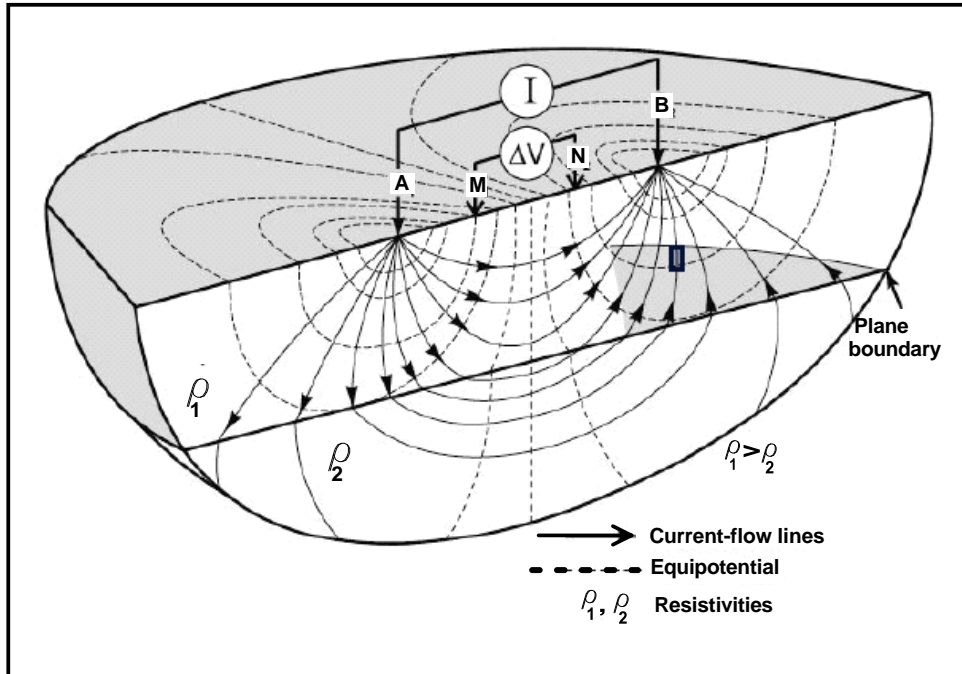


Fig. 3.2: Principle of resistivity measurement with a four-electrodes configuration (after Seidel and Lange, 2007).

Telford *et al.* (1990) and Bobachev *et al.* (1999) describe the current flow distortion in inhomogeneous ground. If we have two media of resistivities ρ_1 and ρ_2 separated by a plane boundary, the current lines will be bent in crossing the boundary. If $\rho_1 < \rho_2$, they will be bent towards the normal and they will be diverged horizontally in case of $\rho_1 > \rho_2$ (Telford *et al.*, 1990). Consequently, when the current flow is distorted in passing from a medium of one resistivity to another, the equipotential lines will be also distorted. Fig. 3.3 shows the current and potential lines distortion between two media of different resistivities using a single current electrode. Similarly, Fig. 3.4 shows the current distribution between two current electrodes for different media. The current flow lines will diverge through the low resistive layer and move horizontally, but tend to move vertically through the highly resistive layer (Telford *et al.*, 1990).

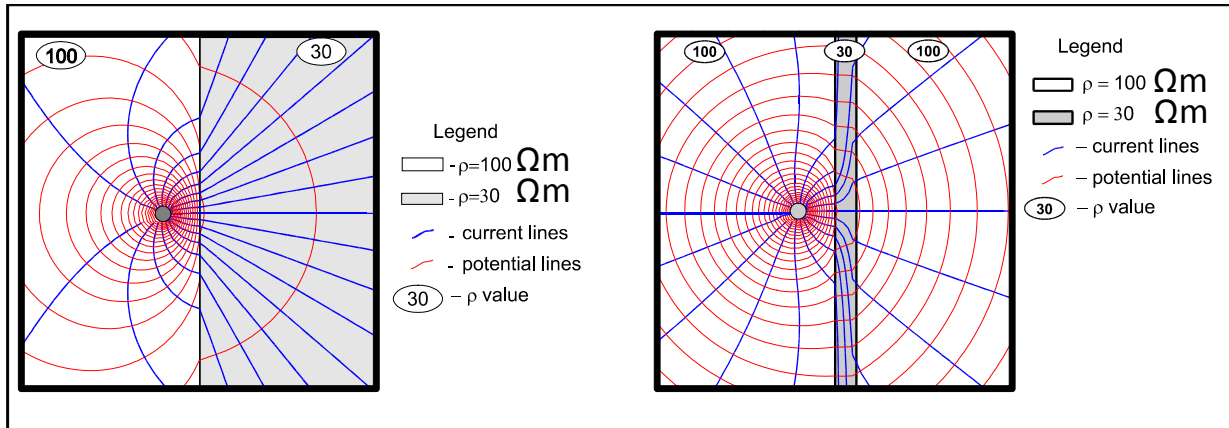


Fig. 3.3: The current flow lines form a single current electrode in near contact with a conductive medium (left) and a thin conductive layer (right) and equipotential lines at the boundary between two media (after Bobachev et al., 1999).

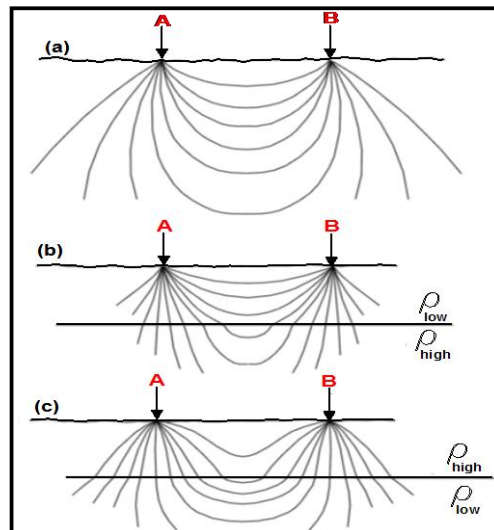


Fig. 3.4: Current flow patterns in a (a) uniform half-space; (b) two-layer ground with lower resistivity in upper layer; (c) two-layer ground with higher resistivity in upper layer (after Milsom, 2003).

3.1.2 ELECTRICAL PROPERTIES OF ROCKS

Two basic electrical properties are electrical resistivity (charge resistance) and polarization. The polarization refers to a substance that exhibits a charge separation in an electric current. The resistivity of many rocks depends upon many factors, including: Rock type, conductivity of pores and nature of the fluid and metallic content of the solid matrix. The rock resistivity is roughly equal to the resistivity of the pore fluids divided by the fraction porosity (Milsom, 2003). The resistivities of common rocks and minerals are shown as resistivity spectrum in Fig. 3.5 (Palacky, 1987). Generally, bulk resistivities of more than $10\,000 \Omega m$ or less than $1 \Omega m$ are rarely encountered in field surveys. Fig. 3.5 shows a wide variation of rock resistivities; in addition to overlappings in resistivity values of different rock types and soils. Soils and rocks are composed mostly of silicate mineral, which are essentially

insulators, meaning that they have low electrical conductivity. Therefore, conduction is largely electrolytic, and conductivity depends upon, mainly, porosity, pore fluid, clay content and concentration of dissolved electrolytes. When clay is present, the resistivity becomes frequency dependent because of a fundamental charge storage mechanism that introduces a capacitive-like element in the equivalent circuit representation of the ground. The clay minerals can absorb and release ions and water molecules on their surfaces through an ion exchange process (Parasnis, 1997). Given sufficiently wet conditions, clay minerals and organic matter contribute significantly to electric current flow in soil.

The electric current in soil is largely electrolytic, meaning that the flow of electric current is governed substantially by the movement of dissolved ions in the soil solution (Allred, 2008). Fig. 3.5 shows a large difference between the freshwater and saltwater, where, in general, the freshwater resistivity ranges between 10 Ωm and 100 Ωm and saltwater is less than 3 Ωm . This means that presence of saltwater in an aquifer can rather easily be detected by various electrical resistivity measurements either in boreholes or on the surface (Fitterman and Deszcz, 2001).

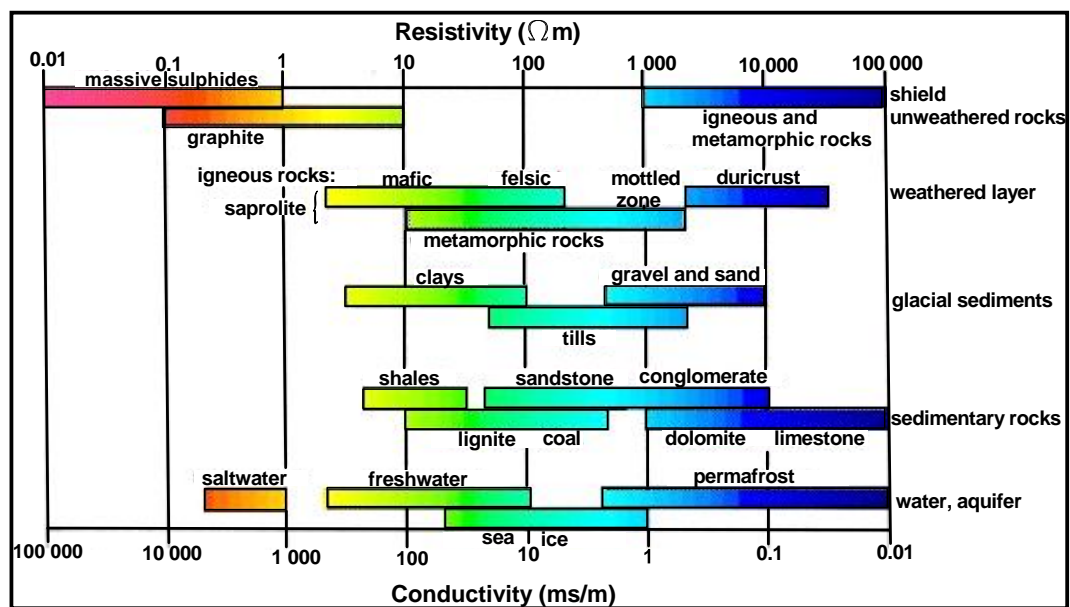


Fig. 3.5: Electrical properties of common rocks and minerals (Palacky, 1987).

3.1.3 DC RESISTIVITY SOUNDINGS

A resistivity survey can be carried out for obtaining information on resistivity variations with depth. This type of survey is known as the resistivity sounding *1D*. The basic idea of this survey type is to stepwise increase the spacing of the current-injecting electrodes AB, which leads to an increasing penetration of current lines and in this way to an increase of influence of deep-seated layers on the apparent resistivity ρ_a . The position of the measurement is taken as the midpoint of the electrode configuration. For a depth sounding, measurements of the resistance $\Delta V/I$ are made at the shortest electrode separation and then at progressively larger spacings. At each electrode separation a value of apparent resistivity ρ_a is calculated using the measured resistance in conjunction with the appropriate

geometric factor for the electrode configuration and separation being used. The measured apparent resistivity ρ_a values are plotted on a log/log scale against the half current electrode spacing $AB/2$ and interpreted to a continuous curve. This plot is called sounding curve and is the base of 1D data inversion to obtain the resistivity/depth structure of the ground (*Ernstson and Kirsch, 2006*).

Common configurations for a depth sounding are the Schlumberger and Wenner configurations (they will be discussed in detail in Section 3.3). *Beard and Morgan (1991)* compared Schlumberger and Wenner configurations by applying layered earth inversions to synthetic resistivity sounding data from 2D structures. They concluded that, in most cases, 1D layered earth solutions stitched together from Schlumberger configuration led to less ambiguous interpretation than from Wenner configurations. In a Schlumberger configuration, increasing $AB/2$ leads to rapidly reduced potential difference to be measured between electrodes M and N . This problem of insignificant low values can be resolved by occasionally increasing the distance between the potential electrodes. When the separation of the potential electrode pair is increased, the contact resistance may change, causing a discrete step up or down of the next segment of the curve. Although the value of the apparent resistivity may change from the use of one electrode pair to another, the gradient of the change of apparent resistivity as a function of current electrode half-separation should remain the same. Consequently, this shift between the segments can be interpolated by shifting measurements with both MN spacings.

Equivalence, Suppression and Anisotropy

Unfortunately, it is not generally possible to obtain a unique solution for the inverse problem. The ambiguity of sounding curve interpretation may arise from two factors: Equivalence and suppression. The principles of equivalence may be stated as the difficulty to distinguish a layer, for which the resistivity is either greater than, or less than, both the layers above and below. This means that it is impossible to distinguish between two highly resistive beds of different thickness h and resistivity ρ values if the product of $h\rho$ is the same, or between two highly conductive beds if the ratio h/ρ is the same. The solution to this problem is to get additional prior information either on the resistivity or the thickness of the layer. The suppression principle is also very significant during the interpretation. It states that if a bed is very thin compared to those above and below, such layer has practically no influence on the sounding curve as long as it does not have a large enough thickness and thus remains invisible.

Electrical anisotropy is a matter of scale and of the resolution of a vertical resistivity section (*Ernstson and Kirsch, 2006*). In 1D modeling we often have to consider a collection of many thin layers as one composite layer, which is then macro-anisotropy (*Christensen, 2000*). Resistivity anisotropy is based on the behavior of equipotential lines on a planar surface through a point current source in an electrically anisotropic material, the lines are found to form a family of concentric ellipses. These are the surface of interactions of the 'ellipsoid of anisotropy', and the ratio of major and minor axes is proportional to the ratio of the square roots of true resistivities, $(\rho_T)^{0.5}$ and $(\rho_L)^{0.5}$, in the transverse and longitudinal directions, respectively (*Sumner, 1976*).

Secondary Geoelectrical Parameters

A geoelectrical layer is described by two primary parameters: its resistivity ρ_i and its thickness h_i , where the subscript i indicates the position of the layer in the section. A sequence of homogenous, isotropic and parallel layers of different thicknesses and resistivities can be assumed as a single 'pseudo-anisotropic' layer. The total longitudinal conductance S and total transverse resistance T , the so called Dar-Zarrouk parameters by *Maillet (1947)*, for a prismatic of layers are defined as

$$S = \frac{h_1}{\rho_1} + \frac{h_2}{\rho_2} + \dots + \frac{h_n}{\rho_n} = \sum \frac{h_i}{\rho_i} \quad (3.7)$$

and

$$T = h_1\rho_1 + h_2\rho_2 + \dots + h_n\rho_n = \sum h_i\rho_i \quad (3.8)$$

From the values of S and T , the average resistivity in horizontal ρ_L and vertical ρ_T directions (*Keller and Frischknecht, 1966*), respectively, are given by the longitudinal resistivity ρ_L , in the horizontal direction,

$$\rho_L = H/S = \sum h_i / \left(\sum \frac{h_i}{\rho_i} \right) \quad (3.9)$$

and the transverse resistivity ρ_T , in vertical direction,

$$\rho_T = \frac{T}{H} = (\sum h_i\rho_i) / \sum h_i \quad (3.10)$$

Due to the limited resolution capabilities of electrical and electromagnetic methods, these model layers often consist of many thinner real layers and effective layer resistivities and thicknesses of the model layers are generally different from their campsite real layers (*Christensen, 2000*). The coefficient of anisotropy is always more than one and less than two (*Sumner, 1976*). The coefficient of pseudo-anisotropy λ is defined as

$$\lambda = \left[\frac{\rho_T}{\rho_L} \right]^{1/2} = (TS/H^2)^{1/2} \quad (3.11)$$

These parameters are derived by considering a column of unit square cross-sections cut of a group of layers of infinite extent. They could be interpreted qualitatively in terms of hydraulic conductivity, transmissivity, clay content, grain size and potentiality of the aquifer (*Khalil, 2006*).

3.1.4 ELECTRICAL RESISTIVITY TOMOGRAPHY (ERT)

Resistivity profiling or mapping in two or three dimensions (2D or 3D) can be defined as electrical resistivity tomography (ERT). A two-dimensional 2D imaging of the ground (ERT) can be seen as a combination of vertical electrical sounding and lateral profiling. In the 2D imaging, it is assumed that the resistivity of the ground varies only in the vertical and one horizontal direction. For the three-dimensional 3D imaging, a grid of electrode and/or a group of 2D profiles are used to investigate changes in the resistivity properties in all directions. This type of survey is normally very time consuming and expensive. In many practical cases the problem can be reduced to a 2D or even a 1D situation, but it must always be considered that the measurements can be influenced by objects outside the configurations (*Spitzer, 1995*).

Many different instruments have been developed for 2D and 3D measurements, usually multi-electrode systems, sometimes multi-channel ones. All systems use multi-core cables. Over the last

years, the data acquisition systems and field techniques for measuring 2D and 3D resistivity survey data have been fairly well developed, e.g., in the Continuous Vertical Electrical Sounding (CVES) system (*Van Overmeeren and Ritsema, 1988, Dahlin, 1993, Dahlin et al., 1994 and Dahlin, 1996*); or in the Pulled Array Continuous Electrical sounding (PACES) system (*Sørensen, 1996, Christensen, 2000 and Christensen and Sørensen, 2001*). The measurements are controlled by a microprocessor-driven resistivity meter or by a computer.

3.1.4.1 2D ELECTRICAL RESISTIVITY TOMOGRAPHY (2D ERT)

2D electrical resistivity tomography is often used to delineate contamination, environmental investigations and geological boundaries, e.g., *Baines et al. (2002); Friedel et al. (2006)*. 2D ERT is much more commonly used than 3D ERT. The advantage of 2D measurements are their high vertical and lateral resolution along the profile, comparatively low cost due to computer-driven data acquisition, which means only a small field crew is needed (one operator) and depending on terrain roughness and profile lengths, one or two assistants for placing electrode spacings ≥ 5 m (*Janik and Krummel, 2006*). 2D ERT is usually carried out using a large number of electrodes which are typically set up along a straight line. A constant spacing between electrodes is used. The electrodes are linked by multi-core cable and connected to a switching unit. The data needed to create a depth section can be obtained in several ways, such as through a set of electric soundings conducted at a number of regularly spaced locations along a transect. Several resistivity surveys pass over a transect with a four-electrode configuration whose length is changed each pass. The data acquired are then used as input for the forward or inverse computer modeling programs that generate the resistivity (or electrical conductivity) depth sections (*Allred et al., 2008*).

2D DC Data Acquisition and Pseudo-Section

Fig. 3.6 displays an example of an electrode arrangement in order to show the procedure of 2D ERT and to illustrate the concept of building up the pseudo-section for a 2D survey. In a 2D survey, the apparent resistivity measurements are carried out on various levels. Each survey level corresponds to different electrode spacings. The measured resistivity is plotted at the mid-point of four electrodes. Several depth levels may be entered by increasing the electrode spacing. The first step in this survey is to take all possible measurements with electrode spacing of $1a$. Therefore, the data of apparent resistivity at level no. 1 ($n=1$) can be collected. Then, the electrode spacings increase to $2a$ to collect the apparent resistivity values at the second level ($n=2$). Note that as the electrode spacings increase, the number of measurements decreases. This process is repeated further on to collect the data at level 8, where the electrode spacing will be $8a$. The number of the measured points and the investigation depth along the survey line depend on the number of the used electrodes, electrode spacings and the electrode configuration (see Section 3.3).

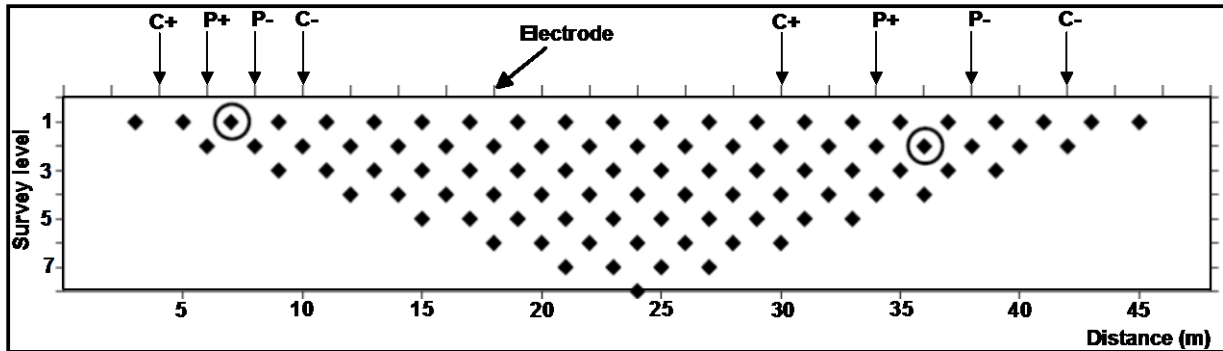


Fig. 3.6: Setup for 2D Wenner resistivity measurements: building a pseudo-section. Circles identify the location assignment for the two measurement configurations shown. Each survey level corresponds to different electrode spacings.

Fig. 3.6 illustrates the concept of building up the pseudo-section for a 2D survey. For each measurement, a survey level and lateral position (mid-point of the four electrodes) are determined, and the apparent resistivity is assigned to that position (“pseudo-depth”). Pseudo-depth and location depend on the used configuration geometry. Note, however, that the pseudo-section does not necessarily show an accurate image of the subsurface distribution of resistivity; it merely serves as a means of plotting measured data. The quality of the inversion results of the measured apparent resistivities is affected by any errors in the field measurements or data missing (Dahlin and Loke, 1998).

When a profile is longer than the electrode layout, the profile can be measured using the so called roll-along method (Dahlin, 1996). This is a rapid approach for getting information about the subsurface resistivities. Roll-along method means that several multi-core electrode cables are rolled out along a straight line and moved successively thus giving a continuous profile. Fig. 3.7 shows that the first 2D profile consists of three-core electrode cables in the form of three segments. After readings have been taken along the first layout with the segments *a*, *b* and *c*, the operator has to move the first segment *a*, after the end of the third segment *c* and take a second set of readings along the second layout using segments *b* and *c*, and so on until the end of the long profile. It is obvious from Fig. 3.7 that the maximum depth reached for the first layout is equal to the second layout and so on. The roll-along method can also be applied for 3D measurements.

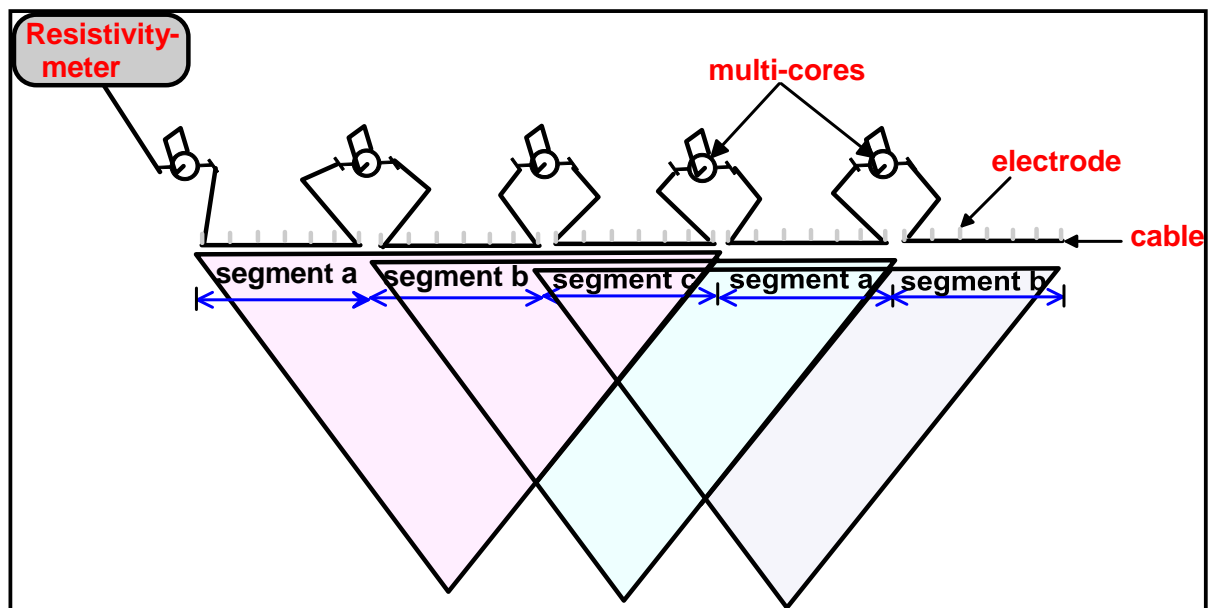


Fig. 3.7: The use of the roll-along method to extend the area covered by a 2D survey.

3.1.4.2 3D ELECTRICAL RESISTIVITY TOMOGRAPHY (3D ERT)

Three dimensional (3D) resistivity imaging technique has been applied to several field data sets for site investigations. It could not be obtained a reliable image of the subsurface using conventional 2D surveys and, consequently, 3D imaging technique was preferred in the investigation of these sites. Over the past decade, significant progress has been made in the development of field equipment and inversion programs for conducting and processing 3D ERT surveys (e.g., *Loke and Barker, 1996a, b; Zhang et al., 1995; Li and Oldenburg, 1992; Sasaki, 1994*). As far as concerning the 3D interpretation of resistivity data, there are many authors who programmed a 3D inverse code for the DC resistivity method, the main difference being the forward modeling algorithm (e.g., *Sasaki, 1994; Loke and Barker, 1996a; Günther et al., 2006; Rücker et al., 2006*). Recently, some papers reported successful application of 3D resistivity imaging technique (e.g., *Drahor, et al., 2007; Chang, et al., 2011*).

3D Survey Design and Layout Strategies

Survey designs and layout strategies have been studied by several authors (e.g., *Dahlin and Loke, 1998; Maurer et al., 2000; Stummer et al., 2004*). For convenience the electrodes are usually arranged in a square grid with the same unit electrode spacing in the x- and y-directions (*Loke and Barker, 1996a*). Fig. 3.8 shows one possible arrangement of the electrodes for a 3D survey using a 25-electrode system.

Loke and Barker (1996b) presented two techniques for 3D grid surveys: Complete data set and cross-diagonal techniques. In the complete set techniques (Fig. 3.9a), the potential measurements will be measured at all other electrodes with high index number. Fig. 3.9a shows a 3D grid of 25 electrodes and an example of the potential measurements at electrode no. 8. The current electrode is

positioned at electrode no. 8 and the potentials will be measured at all electrodes, which have high index number. It can be very time-consuming to make such a large number of measurements with typical single channel resistivity meters commonly used for 2D surveys. Generally, the measurement speed is based on the grid spacing and the magnitude resistance (Griffiths *et al.*, 1985 and 1990; Griffiths and Barker, 1993).

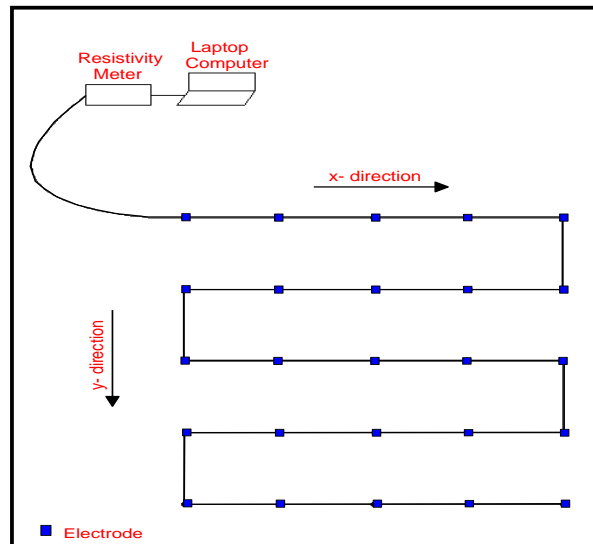


Fig. 3.8: Arrangement of electrodes along a multicore cable for 3D resistivity survey.

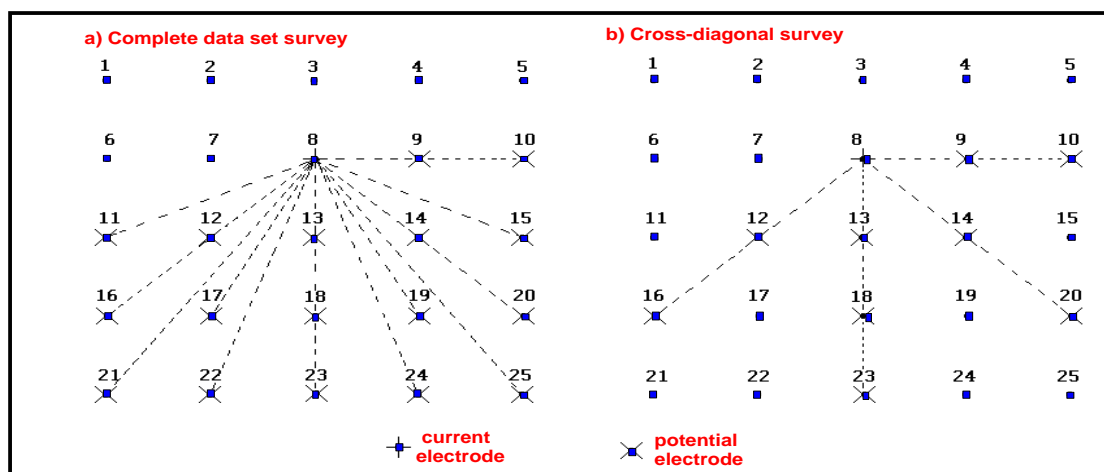


Fig. 3.9: The 3D survey techniques corresponding to a single current electrode: a) Complete data set survey and b) cross-diagonal survey (after Loke and Barker, 1996b).

The cross-diagonal technique can be used to reduce the number of measurements required without seriously degrading the quality of the model obtained. In this survey type, the potential measurements are only made at the electrodes along the horizontal, vertical and 45° diagonal lines passing through the current electrode (Loke and Barker, 1996b). Fig. 3.9b shows an example of 3D measurements, using a pole-pole configuration, which current electrode no. 8 using the cross-diagonal survey.

If large areas are investigated, an electrode grid cannot be applied due to limitations in electrode number. In most cases profile configurations are measured allowing for independent 2D inversion (Günther, 2004). 3D ERT using sets of orthogonal 2D survey lines provide an efficient and cost effective tool for site characterization in environmental and engineering investigations (Gharibi and Bentley, 2005). A 3D survey design using sparse sets of lines reduce the survey time at the expense of the resolution. Ideally there should be a set of survey lines with measurements in the x-direction, followed by another series of lines in the y-direction. The use of measurements in two perpendicular directions helps to reduce any directional bias in the data. However, in some cases, only the data from a series of survey lines in one direction is available (Loke, 2004). Bentley and Gharibi (2004) demonstrated distortions in 2D images and described a 3D ERT survey design in which orthogonal sets of 2D resistivity survey lines are combined to create a 3D dataset. The 2D lines are jointly inverted to produce a 3D image. They concluded that appropriately designed 3D configurations can be used efficiently for site characterization. Gharibi and Bentley (2005) studied the effect of line spacing on the resolution of 3D electrical resistivity images using numerical modeling with synthetic and field data for two standard configurations, dipole-dipole and Wenner configurations.

3.2 SPECTRAL INDUCED POLARIZATION METHOD (SIP)

The fundamentals of material physical properties can be explained in the frequency domain by Maxwell's second equation, which may be written as

$$J_t(\omega) = \sigma^*(\omega) E(\omega) \quad (3.12)$$

and,

$$\nabla \times H = J_t(\omega) \quad (3.13)$$

where $J_t(\omega)$ is the total current density in the frequency domain, σ^* is the electrical conductivity and ρ^* its reciprocal value (electrical resistivity), H is the magnetic field strength and $E(\omega)$ is the electrical field. The electrical conductivity ($\sigma^*(\omega)$), or its reciprocal ($\rho^*(\omega)$) are always considered to be complex and can be written as

$$\sigma^*(\omega) = \sigma'(\omega) + i\sigma''(\omega) \quad (3.14)$$

where $\sigma'(\omega)$ is real conductivity and $\sigma''(\omega)$ is imaginary conductivity, $i = \sqrt{-1}$ and ω is the angular frequency ($=2\pi f$).

Following Eq. (3.14), the estimated geoelectrical properties of the earth materials may be equally represented by a complex electrical conductivity σ^* and/or a complex resistivity ρ^* . Each of these parameters contains a total energy storage term (polarization) and a total energy loss term (conduction). The imaginary parts in Eq. (3.14) shall account for any polarization effect occurring within rocks at the lower frequency scale (<10 kHz). At this scale the observed delay of the response to an impressed excitation is caused by polarization effects which involve the movement of charge carriers over some distance up to the order of centimeters (Pelton *et al.*, 1983).

3.2.1 ORIGIN OF INDUCED POLARIZATION

The passage of current through a rock as a result of an externally imposed voltage is accomplished mainly by electrolytic flow in the pore fluid. This normal mode of conduction may be described by electrolytic conduction (charge transport) σ_{el} as a contribution to the bulk conductivity of the whole formation σ . Beside electrolytic conduction, a second component (IP effect) contributing to overall conductivity is given by the interface conductivity σ_{int} mainly controlled by surface properties. The two components electrolytic and interfacial conductivity can be described as a parallel conductor system with a total conductivity $\sigma = \sigma_{el} + \sigma_{int}$ (Waxman and Smits, 1968). However, whereas σ_{el} may be regarded as a real quantity, interfacial electrical properties are directly accessible via the measurement of the imaginary component of σ . The origin of interfacial conductivity lies in the electrical double layer.

Electrical Double Layer (EDL)

The flow of alternating current across the interface between an electrode and an electrolyte is called electrode impedance and includes solution resistance, capacitances in the EDL and the Warburg impedance¹. The EDL is divided into three regions that interact only electrostatically, i.e. the matrix, the *fixed layer* (or *Stern layer*) and the *diffuse layer* (Fig. 3.10). The thickness of the EDL can also be defined as Debye length². The existence of the EDL is responsible for the so-called membrane polarization (see the next subsection 3.2.4).

All minerals that are in contact with water develop a net surface charge on their surface because of the chemical reactivity and adsorption forces. This charge is counterbalanced by charges that are more or less weakly adsorbed onto the mineral surface in a monolayer called the *Stern layer*. It also contains a net electrical charge and it is within this layer that charge transfer reaction between the solution and the electrode is assumed to take place. This layer is situated between the o-plane and the d-plane in Fig. 3.10. The o-plane corresponds to the true mineral surface while the d-plane corresponds to the inner surface of the electrical diffuse layer. The existence of this Stern layer is consistent with molecular dynamic simulations of the electrical double layer (Tournassat *et al.*, 2009).

The *diffuse layer* is adjacent to the fixed layer on the solution side and is considered to be similar to the rest of the solution, except that any net change in the *fixed layer* creates an electrical field which unbalances the positive and negative concentrations in the zone (Fig. 3.10). The cations of the *diffuse layer* are loosely held to the surface and, therefore, can be easily exchanged for other cations and implicitly add to the normal ion concentration within the electrolyte. This phenomenon constitutes an additional mode of ohmic conduction, consequently referred to as ohmic interface conductivity. The potential drop across the *diffuse layer* is known as the *zeta potential*, the effects of which cannot be directly observed (Sumner, 1976).

¹ The Warburg impedance is the rate limiting effect and is proportional to $\omega^{-1/2}$ for a single electrode. It can be difficult to recognize because it is always associated with charge-transfer resistance.

² The Debye length is the distance over which significant charge separation can occur.

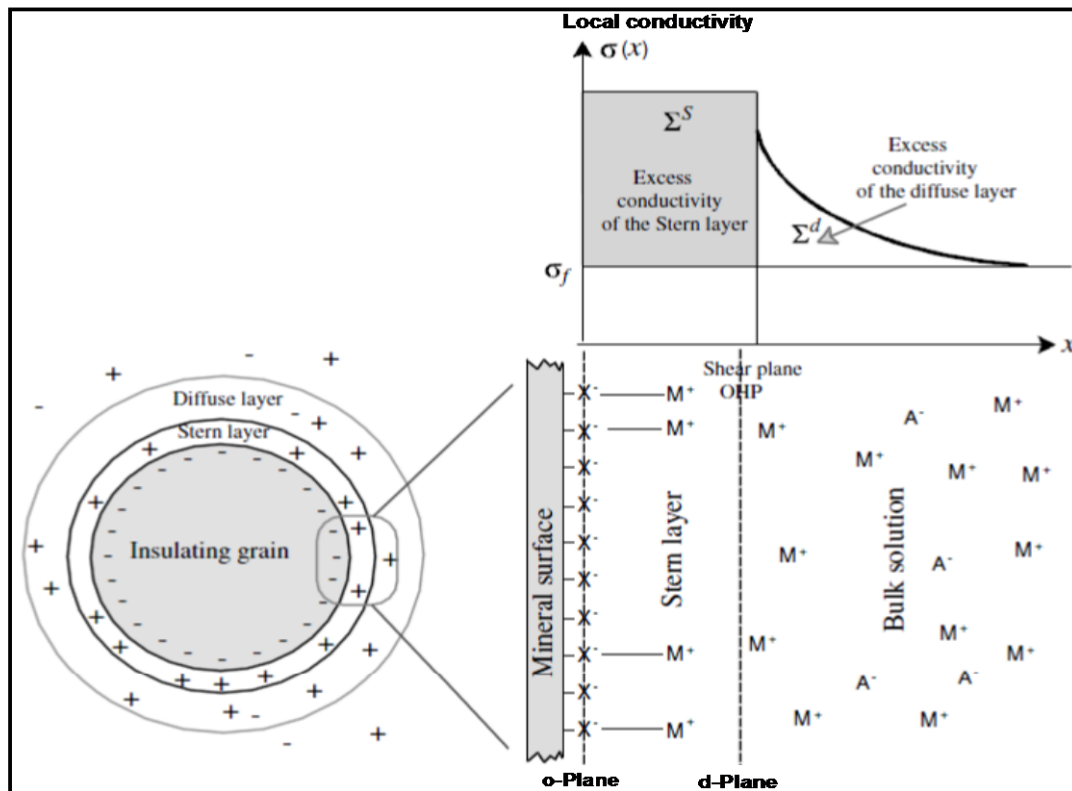


Fig. 3.10: Sketch of the distribution of the ionic species in the electrical double layer. The Stern layer is responsible for the excess surface conductivity Σ^s (in S) with respect to the conductivity of the pore water σ_f , while the diffuse layer is responsible for the excess surface conductivity Σ^d . The Stern layer is comprised between the o-plane (mineral surface) and the d-plane, which is the inner plane of the electrical diffuse layer. The diffuse layer extends from the d-plane into the pores (after Revil and Florsch, 2010).

3.2.2 MECHANISM OF INDUCED POLARIZATION

The IP mechanism can be explained by understanding the mechanism of the electric current movement across the metallic minerals, which produces an electrode polarization, and its movement within the pore channel in the vicinity of the EDL, which produces a membrane polarization. Presently, many approaches have been discussed to understand the mechanism of the SIP method (e.g., Leroy *et al.*, 2008; Leroy and Revil, 2009; Jougnot *et al.*, 2010).

Electrode polarization occurs at the faces of the metallic minerals, where the electric current transmission changes from electrolytic to electronic. The piled up charges create a voltage that tends to oppose the flow of electric current across the interface and the particle is said to be polarized. When the current is interrupted, a residual voltage continues to exist across the particle, due to the bound ionic charges, but it decreases continuously as the ions slowly diffuse back into the pore electrolytes, which gives the induced polarization effect (Parasnis, 1973). The induced polarization effect opposes the buildup and collapse of the primary potential difference, and is referred to as the overvoltage.

Membrane polarization is based on the different mobility of cations and anions within the pore solution in the vicinity of a double layer (Ward and Fraser, 1967). There are two causes of membrane or electrolytic polarization: (1) a presence of clay particles or filament of fibrous minerals and (2) by constriction within a pore channel (Reynolds, 1997). In presence of an electric field, the cations can readily pass through the diffuse layer via the process of cation exchange capacity (CEC)³ and the anions are blocked by the corresponding cationic cloud and, consequently, accumulate within the pore passages. It may be emphasized that the occurrence of membrane polarization is not only restricted to porous rocks containing clay minerals, but inherent to any rock exhibiting minerals with charged surfaces (e.g., silicate minerals) (Kemna, 2000). A representation of the concepts of membrane polarization is given in Dukhin and Shilov (1974) and it is depicted schematically in Fig. 3.11.

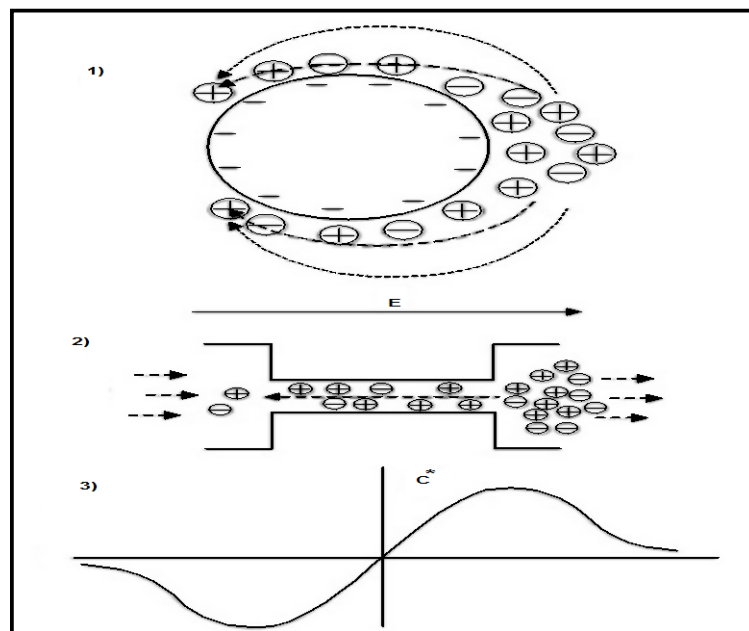


Fig. 3.11: Schematic of ion-conductive zones in porous rocks after Titov et al. (2004). (1) Excess and deficiency in ion concentration around a polarized spherical negatively charged particle. The solid arrow shows the direction of the electrical field, the dotted shows the diffusion flow of both, anions and cations and the dashed arrow shows the local diffusion flow near the surface mostly by cations. (2) Excess and deficiency along a polarized pore throat. (3) Schematic distribution of the ion concentration around a polarized spherical particle or along a polarized pore throat. C^* denotes the excess concentration produced by the polarized field.

3.2.3 IP MEASUREMENTS

When discussing IP measurements, it is usually assumed that resistivity and IP measurements have been made simultaneously. In the field, these parameters are described as apparent resistivity and

³ CEC is the total number of positive charges from exchangeable cations that neutralize the negative charges on the soil particles.

apparent polarization. Actual resistivity or IP values are determined in the interpretation process with the aid of computer modeling and inversion.

In time-domain IP, a direct current is applied into the ground, and what is recorded is the decay of voltage between two potential electrodes after the current is switched off. The most commonly measured parameter is the chargeability m (Seigel, 1959), defined as

$$m = \frac{V_s}{V_p} \quad \text{and} \quad M = \frac{1}{V_p} \int_{t_1}^{t_2} V_{s(t)} dt = \frac{A}{V_p} \quad (3.15)$$

where V_s is the secondary voltage, V_p is the primary voltage, M is the integral chargeability and $V_{s(t)}$ is the off-time measured MN voltage at time t .

Frequency-domain IP involves the measurement of apparent resistivity at two or more AC frequencies. In the frequency-domain method, the IP effect is commonly described by the so-called frequency effect FE , which is the normalized difference between the asymptotic resistivity magnitudes at zero and infinite frequency. It can be expressed as

$$FE = \frac{\rho_0 - \rho_\infty}{\rho_\infty} \quad (3.16)$$

where the apparent resistivity at low frequency ρ_0 is greater than the apparent resistivity at a higher frequency ρ_∞ because the resistivities of rocks decrease as the frequency of an alternating current is increased. Both m and FE are easily interrelated via the initial- and final-value theorems of the Laplace transform⁴ (Wait, 1959),

$$m = \frac{FE}{1+FE} = \frac{\rho_0 - \rho_\infty}{\rho_0} \quad (3.17)$$

SIP Measurements (Parameters and Related Quantities)

The SIP method, which is also called complex resistivity (CR) method, is a multifrequency version of the IP method. The same field arrangement is used in time- and traditional variable-frequency surveys but the equipment is considerably more sophisticated. In environmental and hydrogeological applications, the SIP method has showed encouraging results (e.g., Kemna *et al.*, 1999; Klitzsch, 2003; Hördt *et al.*, 2007). The SIP commonly measured quantities are both magnitude $|\rho|$ and phase φ at a number of frequencies; these parameters are related to the real ρ' and imaginary ρ'' components of resistivity. If the input current is a square wave, the phase measurement is defined as the phase angle between the fundamental harmonic of the transmitted and received signals. Fig. 3.12 shows the resistivity magnitude and phase shift of a sample recorded relative to a reference resistor upon stimulus with an alternating current.

⁴ The Laplace transform is formally equivalent to the Fourier transform extended to complex-valued arguments.

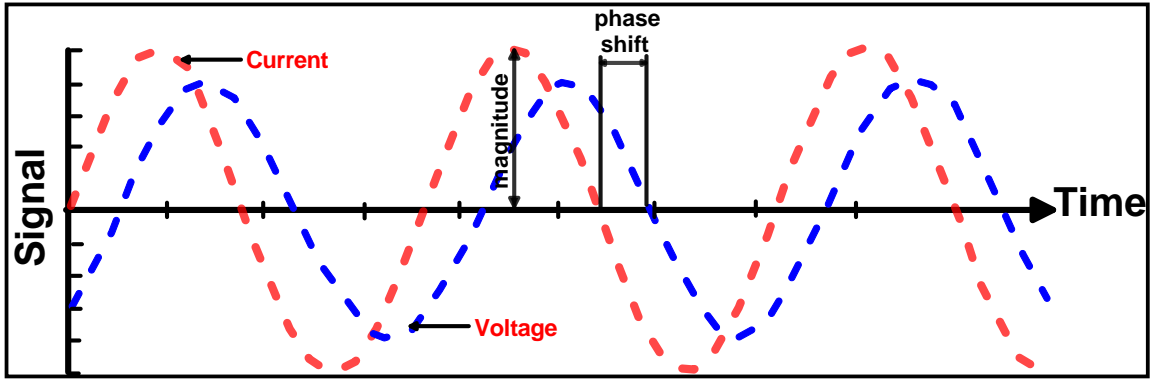


Fig. 3.12: Complex resistivity signal for a distinct frequency. The applied voltage (V) causes a subsequent current (A) signal, which is shifted in time. The amplitude ratio of the two signals is the resistivity magnitude and their time shift is related to the phase angle ϕ (mrad or deg) (after Kruschwitz, 2007).

The inphase (real, energy loss) and the out-of-phase (imaginary/quadrature, energy storage) components are more easily measured with modern electronic systems than the phase angle alone and the two components provide additional useful information about IP phenomena. The inphase represents the ohmic conduction, whereas the out-of-phase represents the much smaller polarization term. The complex resistivity ρ^* can be expressed as

$$\rho^* = |\rho|e^{i\phi} = \rho' + i\rho'' = 1/\sigma^* \quad (3.13)$$

$$|\rho| = \sqrt{\rho'^2 + \rho''^2}, \quad (3.14)$$

The phase angle is defined as the angle, whose tangent is the ratio between the imaginary and real components of the received voltage, $V(\omega)$, or resistivity, $\rho(\omega)$, and expresses as

$$\phi = \arctan \left[\frac{V''}{V'} \right] = \arctan \left[\frac{\rho''}{\rho'} \right] \quad (3.15)$$

Electromagnetic coupling (EM) is a complex problem and it is more bothersome to frequency-domain than time-domain systems. The term 'coupling' refers to the electrical linkage relationship between an IP transmitter and a receiver. The IP transmitter and receiver circuits behave like the primary and secondary windings of an ordinary electrical transformer. The electrical induction effect is more pronounced at higher frequencies (Sumner, 1976). This electromagnetic induction or EM coupling causes spurious IP-like effects that are not due to natural causes. It must be stressed that EM coupling is not "noise" and must be avoided to give interpretable data.

For geophysical configurations, inductive coupling is a function of a^2f/ρ , where 'a' is the dipole length, 'f' is the signal frequency and 'ρ' is the resistivity. This means that the inductive or EM coupling increases for larger configurations, lower resistivities and higher frequencies. It also increases with complicated geological layering, structure and inhomogeneities (Zonge et al., 2005).

3.3 GEOELECTRICAL ELECTRODE CONFIGURATIONS

Since the 1950s, many different electrode configurations have been used in electrical exploration techniques, such as pole-pole (PP), pole-dipole (PD), half-Wenner (HW), Wenner- α (WN),

Wenner-Schlumberger (SC), dipole-dipole (DD), Wenner- β (WB) and Wenner- γ (GM) (Dahlin and Zhou, 2004). Szalai and Szarka (2008) collected approximately one hundred different electrode configurations from published geophysical literature. In practice, a few configurations are commonly used and they are compiled in Fig. 3.13. The current and potential electrode position and the geometric factor (G) for each electrode type are also listed.

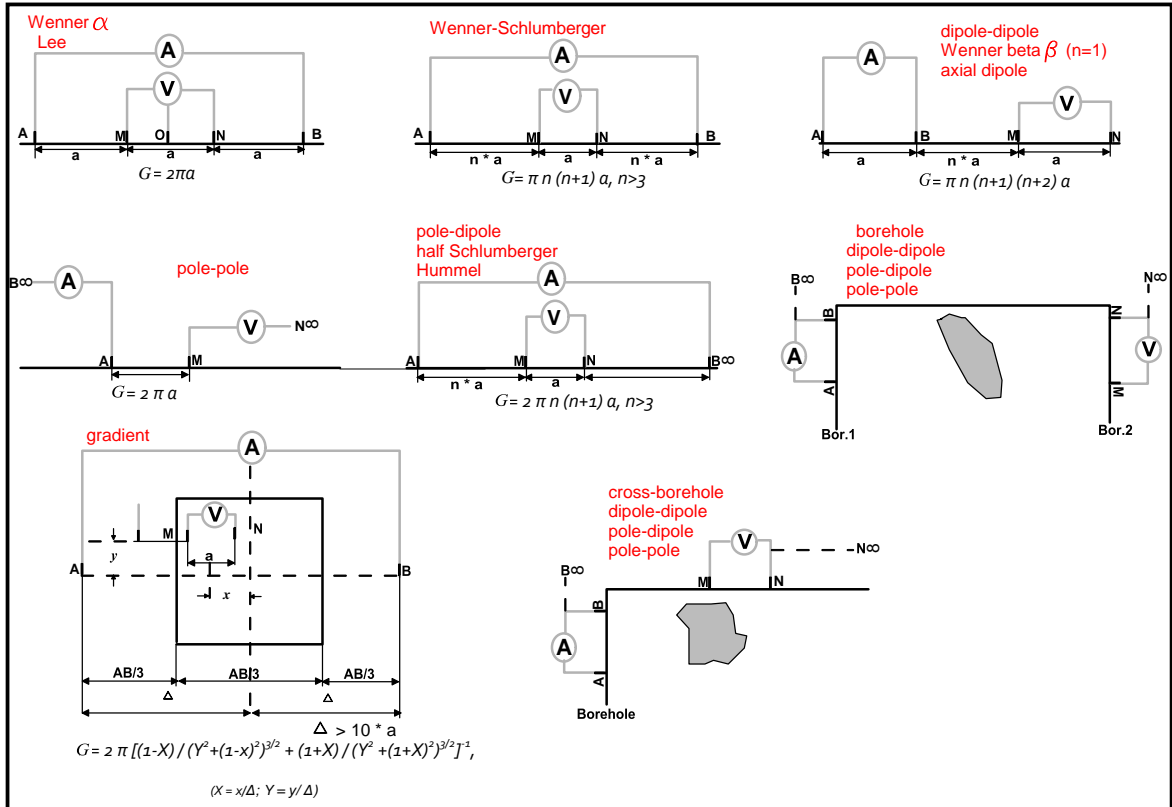


Fig. 3.13: Some common electrode configurations and their geometric factors used in ERT (after Seidel and Lange, 2007).

Sensitivity Analysis

The sensitivity patterns play an important role in the capability of an configuration to resolve the subsurface structure (Dahlin and Zhou, 2004). Sensitivity is defined as the change of forward response, $f_i(m)$, with respect to the change of the model parameter, m_j . Mathematically sensitivity $S_{ij}(m)$ can be defined as

$$S_{ij}(m) = \partial f_i(m) / \partial m_j \quad (3.16)$$

The sum of the absolute sensitivities of all the measurements yields a cumulative sensitivity or coverage cov_j given by Günther (2004),

$$cov_i = \sum_{i=1}^n |s_{ij}| \quad (3.17)$$

The sensitivity function⁵ helps to derive a numerical value for the depth of investigation. It can be easily shown, that for a pole-pole measurement with the distance $\overline{AM} = a$ the layer sensitivity in a homogenous half-space is (Roy and Apparao, 1971 and Günther, 2004)

$$\frac{\partial \rho_a}{\partial \rho} = \int_{z_2}^{z_1} \frac{4az}{\sqrt{a^2 + 4z^2}^3} dz = - \left. \frac{4az}{\sqrt{a^2 + 4z^2}} \right|_{z_1}^{z_2} = \frac{a}{\sqrt{a^2 + 4z_1^2}} - \frac{a}{\sqrt{a^2 + 4z_2^2}} \quad (3.18)$$

where z_1 and z_2 are the upper and lower layer boundaries, respectively.

When $z_1 = 0$, the cumulative sensitivity can be expressed as

$$S_{cum} = 1 - \frac{a}{\sqrt{a^2 + 4z^2}} \quad (3.19)$$

The sensitivity for a four electrode configuration by superposition is

$$\frac{\partial \rho_a}{\partial \rho} = \frac{G}{2\pi} \left[\frac{1}{\sqrt{AM^2 + 4z_1^2}} - \frac{1}{\sqrt{AM^2 + 4z_2^2}} - \frac{1}{\sqrt{AN^2 + 4z_1^2}} + \frac{1}{\sqrt{AN^2 + 4z_2^2}} - \frac{1}{\sqrt{BM^2 + 4z_1^2}} + \frac{1}{\sqrt{BM^2 + 4z_2^2}} - \frac{1}{\sqrt{BN^2 + 4z_1^2}} + \frac{1}{\sqrt{BN^2 + 4z_2^2}} \right] \quad (3.20)$$

When $z_1 = 0$, the cumulative sensitivity can be expressed as

$$S_{cum} = 1 - \frac{G}{2\pi} \left[\frac{1}{\sqrt{AM^2 + 4z^2}} - \frac{1}{\sqrt{AN^2 + 4z^2}} - \frac{1}{\sqrt{BM^2 + 4z^2}} + \frac{1}{\sqrt{BN^2 + 4z^2}} \right] \quad (3.21)$$

By integration from z_1 to z_2 , Eq. 3.18 can be written as

$$S = \frac{4Kz}{2\pi} \left[\frac{1}{\sqrt{AM^2 + 4z^2}^3} - \frac{1}{\sqrt{AN^2 + 4z^2}^3} - \frac{1}{\sqrt{BM^2 + 4z^2}^3} + \frac{1}{\sqrt{BN^2 + 4z^2}^3} \right] \quad (3.22)$$

In case of a four electrode configuration, e.g., WN, the sensitivity can be derived as

$$\frac{\partial Z}{\partial \rho} = \frac{1}{G} \frac{\partial \rho_a}{\partial \rho} = \frac{1}{2\pi} \left[\frac{1}{\sqrt{a^2 + 4z_1^2}} - \frac{1}{\sqrt{a^2 + 4z_2^2}} \right] \quad (3.23)$$

where Z is the impedance ($Z = \rho_a / G = Z_{AM} - Z_{AN} - Z_{BM} + Z_{BN}$) and G is a geometric factor ($G = 2\pi a$).

In two-dimensional inversion the model cells have infinite length in y-direction (Günther, 2004). Friedel (2000) showed that the sensitivity function of a pole-pole configuration can be written as

$$S(x, z) = \frac{1}{4\pi^2} \{T_1[(x - x_A)(x - x_M) + z^2] + T_2\} \quad (3.24)$$

where x_A and x_M are the positions of the current and potential electrode. T_1 and T_2 read

$$T_1 = \frac{2}{ab^2(a^2 - b^2)^2} [(a^2 + b^2)E(\eta) - 2b^2K(\eta)] \quad \text{and,}$$

$$T_2 = \frac{2}{ab^2(a^2 - b^2)^2} [(a^2 + b^2)K(\eta) - 2a^2E(\eta)].$$

where a^2 and b^2 are the maximum and minimum values of $(x - x_A)^2 + z^2$ and $(x - x_M)^2 + z^2$, respectively, $K(\eta)/E(\eta)$ are elliptic integrals of first/second order and $\eta = 1 - b^2/a^2$.

Fig. 3.14 represents the sensitivities for commonly applied electrode configurations: The left side shows the sensitivity for small electrode spacings, whereas the right side shows the sensitivity for larger electrode spacings. Shown are areas of positive and negative sensitivity values. Generally, the spatial sensitivity decreases with increasing distance from the electrodes (Friedel, 2000). A positive

⁵ The sensitivity function basically tells us the degree to which a change in the resistivity of a section of the subsurface will influence the potential measured by the configuration.

sensitivity can be observed always in between the two current electrodes and the two potential electrodes, whereas negative sensitivity occurs in the space between a current and a potential electrode.

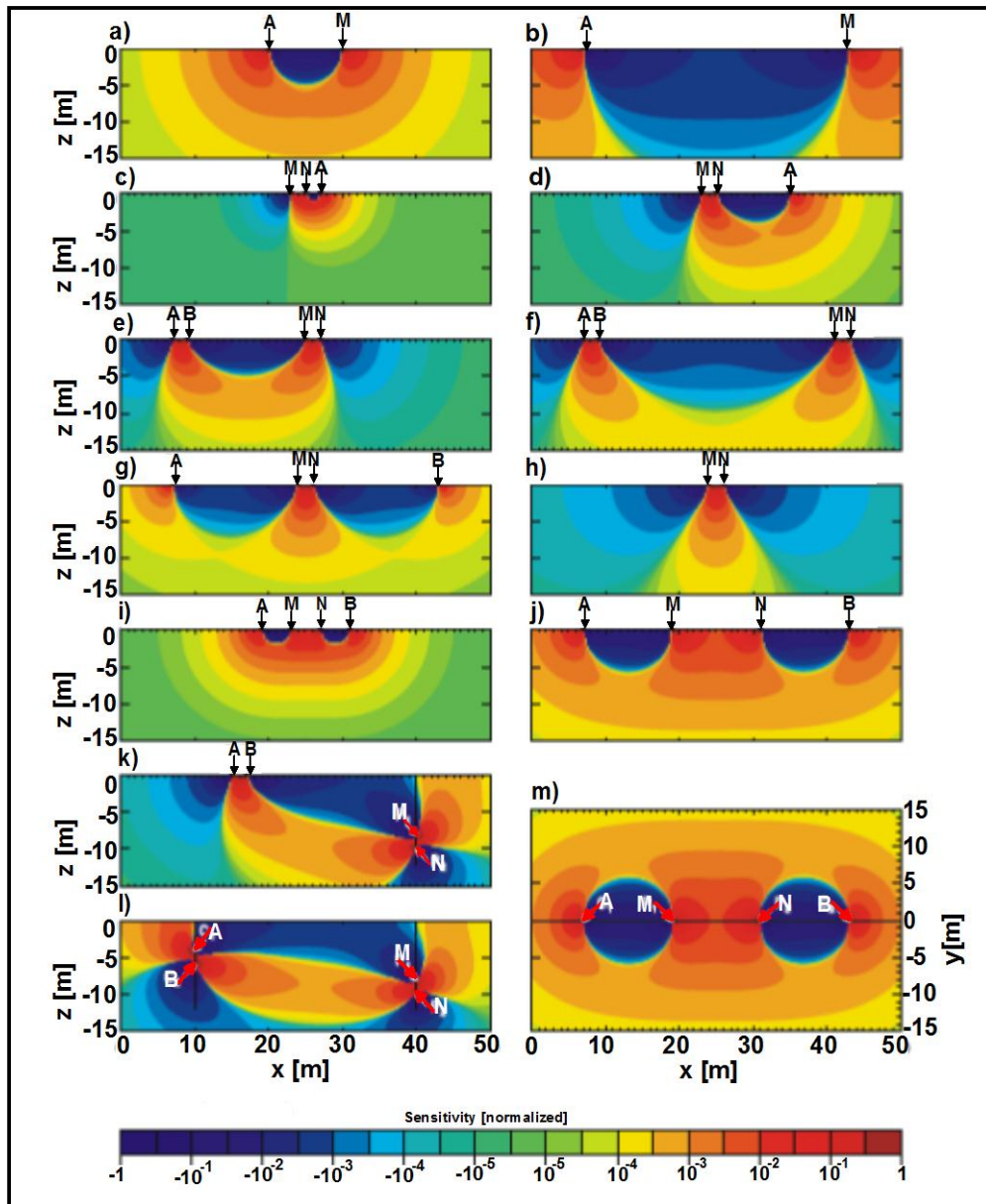


Fig. 3.14: 2D sensitivity section for the common electrode configurations; (a,b) pole-pole, (c,d) pole-dipole, (e,f) dipole-dipole, (g,h) Wenner-Schlumberger configuration, (i,j) Wenner configuration, (k,l) dipole-dipole with electrodes in boreholes, (m) Wenner configuration but x-y-plane of the sensitivity. All plots are normalized with respect to the maximum of each matrix (after Friedel, 2000).

Depending on the configuration characteristics and the objective, the appropriate configuration has to be selected for each survey. In the present work, we applied only five electrode configurations for ERT: WN, SC, DD, WB and PP. The principles, advantage and limitations of these configurations are summarized, in brief.

WN and SC

The WN is a symmetrical configuration, with the current electrodes on the outside and the potential electrodes on the inside of the configuration (Fig. 3.13). The spacing between all adjacent electrode pairs is the same within the WN ($\overline{AM} = \overline{MN} = \overline{NB} = a$). The geometric factor for the WN is “ $2\pi a$ ”. This is smaller than the geometric factor for other configurations. The equation of ρ_a is

$$\rho_a = (2\pi a)V/I$$

The WN configuration is used mainly for resistivity profiling or for rapidly covering large areas with small spacings. It is not used for vertical sounding and very seldom used for induced polarization (IP) because of increased wire-to-wire EM coupling. The effects of EM coupling provide a negative apparent IP response. The signal contribution indicates that for horizontally layered media, the WN has a high vertical resolution (Reynolds, 1997). The sensitivity section (Fig. 3.14 I and J) shows large negative values near the surface between A and M electrodes, as well as between the B and N electrodes. This means that if a small body with a higher resistivity than the background medium is placed in these negative zones, the measured apparent resistivity value will decrease. This phenomenon is also known as an “anomaly inversion” (Loke, 2004). Based on the sensitivity section, the WN configuration is good in resolving vertical changes, but relatively poor in detecting horizontal changes.

It is favored alone for electrical depth sounding work. Schlumberger electrical soundings (SC) are usually designed to discriminate between electrical resistivity associated with lithologic and/or hydrologic characteristics (Hodlur et al., 2006). It can be used for imaging by several lateral movements of potential electrodes without increasing the current electrode spacings (Fig. 3.13). The “ n ” factor⁶ for an SC configuration is the ratio of the distance between the A-M (or N-B) electrodes to the spacing between the M-N potential pair. The number of the data level can be expressed by the values of “ n ”. The geometric factor for the SC configuration is “ $\pi n(n+1)a$ ”. The equation of apparent resistivity is

$$\rho_a = (\pi n(n+1)a)V/I$$

The area of highest positive sensitivity below the center of the SC configuration becomes more concentrated beneath the central M-N electrodes as the “ n ” factor is increased (Fig. 3.14 g and h). The sensitivity contours have a slight vertical curvature below the center of the configuration. The high positive sensitivity lobe beneath the M-N electrodes becomes more separated from the high positive sensitivity values near the A and B electrodes. This means that this configuration is moderately sensitive to both horizontal (for low “ n ” values) and vertical structures (for high “ n ” values). It is also characterized by poor lateral resolution and excellent vertical resolution to the signal/noise limit. Because of extensive wire-to-wire coupling, IP data usually are not acquired.

The WN configuration has less noise contamination and better signal-to-noise ratios than the SC configuration (Dahlin and Zhou, 2004). The WN is an attractive choice for a survey carried out in a noisy area and also if good vertical resolution is required. The SC configuration has a slightly better

⁶ Note that the WN is a special case of this configuration where the “ n ” factor is equal to 1 (Loke, 2004).

horizontal coverage compared with the WN configuration. The SC is a reasonable all-round alternative if both good and vertical resolutions are needed, particularly if good signal strength is required. While the depth of investigation of the WN and SC are similar, the section of the subsurface mapped by the two configurations will be slightly different due to the different sensitivity patterns. Consequently, the two measurements will give slightly different information about the subsurface (Loke, 2004).

DD and WB

The DD configuration is employed both for mapping lateral changes in ρ_a and for assessing the variation of resistivity with depth. It is popular in IP work because of the complete separation of current and voltage circuits, which reduces the vulnerability to inductive noise. On other side, it is an unusual configuration for depth sounding except IP sounding. The spacing between the current electrodes pair, B-A, is given as “ a ” which is the same as the distance between the potential electrodes pair M-N (Fig. 3.13). The “ n ” factor is the ratio of the distance between the A and M electrodes to the B-A dipole length “ a ”. For surveys with this configuration, the “ a ” spacing is initially kept fixed at the smallest unit electrode spacing and the “ n ” factor is increased from 1 up to ≈ 6 in order to increase the depth of investigation (Loke, 2004). The highest factor “ n ” used in the modeling was 6 and it is often not advisable to go beyond that value in real situations, due to the resulting very low signal-to-noise ratios (Dahlin and Zhou, 2004). Generally, the DD configuration has a shallow investigation depth compared to the WN configuration but it has better horizontal data coverage than WN (Turberg and Barker, 1996). The geometric factor for the DD configuration is “ $\pi n(n+1)(n+2)a$ ”. The equation of ρ_a is

$$\rho_a = (\pi n(n+1)(n+2)a)V/I$$

Fig. 3.14 (e and f) indicates that the largest sensitivity values are generally located between the B-A dipole pair, as well as between the M-N pair. This means that this configuration is most sensitive to resistivity changes below the electrodes in each dipole pair. As the “ n ” factor is increased, the high sensitivity values become increasingly more concentrated beneath the A-B and M-N dipoles, while the sensitivity beneath the center of the configuration between the B-M electrodes decreases.

The WB configuration is a special case of the DD configuration where the spacings between the electrodes are the same. It has a higher signal-to-noise ratio than the DD configuration, but has, in some cases, much lower spatial resolution than DD (Dahlin and Zhou, 2004). Because of lower signal-to-noise ratios of the DD, compared with WB, the WB configuration has higher vertical resolution than the DD configuration. The WB configuration has poor sensitivity to vertical structures in comparison with the DD configuration, which can be attributed to the concentration of DD sensitivity values beneath A-B and M-N with increasing distance between dipole pairs (Fig. 3.14f). Both DD and WB are more sensitive to spacing errors and 3D geological bodies than other configurations (Zhou and Dahlin, 2003).

PP

This configuration is not as commonly used as the WN, DD and SC configurations (Loke, 2004). The current and potential electrodes are inline and the distance between them is “ a ” (Fig. 3.13).

The other current (B) and potential (N) are at “infinity” (greater than 10 a-spacings away). The geometric factor for the pp configuration is “ $2\pi a$ ”. It is more popular for 3D surveys than 2D resistivity profiling. It is characterized by a good horizontal coverage. *Bazinet (2000)* indicated that the PP configuration is characterized by better penetration depth and faster field procedures than other configurations. In surveys where the inter-electrode spacing along the survey line is more than a few meters, there might be practical problems in finding suitable locations for the B and N electrodes to satisfy this requirement. Another disadvantage of this configuration is that because of the large distance between the M and N electrodes, it can pick up a large amount of telluric noise that can severely degrade the quality of the measurements. Fig. 13.4 (a and b) shows that the PP sensitivity is decreased between the current A and potential electrode M with increasing distance between them. Consequently, the PP imaging resolution ranks low among WN, SC, WB and DD configurations.

3.4 FREQUENCY-DOMAIN ELECTROMAGNETIC METHOD (FDEM)

3.4.1 EM FUNDAMENTALS

Electromagnetic (EM) induction, which is a source of noise in resistivity and IP surveys, is the basis of a number of geophysical methods. The EM method is widely utilized for locating conductive and metallic objects in the subsurface. It performs well in conductive soils or high radar reflectivity zones where GPR often encounters difficulties. It also performs well in highly resistive terrains where establishing good electrode contact with the ground, as required for most DC methods, often is problematic (*Everett and Meju, 2005*).

The EM theory was first comprehended by Maxwell who recognized that Ohm’s law, Ampere’s law and Faraday’s law⁷ are the fundamental laws for all EM theory. They can be expressed in the form of Maxwell’s equations,

$$\nabla E = -\partial B / \partial t \quad (3.25)$$

$$\nabla H = J + \partial D / \partial t \quad (3.26)$$

$$\nabla B = 0 \quad \text{and} \quad \nabla D = \rho_d \quad (3.27)$$

where E is the electric field intensity (V/m), H is the magnetic field intensity (A/m), B is the magnetic induction (W/m^2), D is the displacement current (C/m^2), J is the current density (A/m^2), ρ_d is the free charge density and t is time.

To relate Maxwell’s equations to properties of the subsurface, the constitutive equations must be used as

$$D = \epsilon E \quad (3.28)$$

$$B = \mu H \quad (3.29)$$

⁷ Ampere’s and Faraday’s laws are the two fundamental laws for all EM theory. Ampere’s law shows the relationship between the magnetic field (B) and a current (I) passing through a wire ($B = \frac{1}{2\pi r}$, where r is the radius from the wire). Faraday’s law showed the principles of induction by moving a magnet through a loop.

$$J = \sigma E \quad (3.30)$$

In most materials, μ (magnetic permeability) and ϵ (dielectric permittivity) do not differ appreciably from the values of μ_0 and ϵ_0 in free space.

The EM techniques can be classified as both frequency-domain and time-domain systems. In frequency-domain electromagnetics (FDEM), the change in the inducing primary magnetic field is produced by flow of a sinusoidal alternating current in a wire or coil. Alternatively, transient electromagnetic (TEM) methods may be used, in which the changes are produced by abrupt termination of current flow.

The Frequency domain helicopter-borne electromagnetic is a modern method for mapping subsurface resistivity where ground access is difficult. Saltwater intrusion is an ideal target for mapping with this technique because of the high electrical conductivity of saline water and its contrast with that of freshwater. The coils are mounted, e.g. in a cigar shaped enclosure called bird and it is slung about 30 m below a helicopter. The use of the HEM method has become very widespread in the fields in engineering and environmental geophysics (e.g., *Sengpiel, 1983; Sengpiel, 1990; Sengpiel and Siemon, 1998; Siemon and Binot, 2003; Siemon, 2006*).

3.4.2 BASIC PHYSICS OF FDEM METHOD

In FDEM surveys, two small coils, so called loop-loop systems, are used. An EM transmitter outputs a time-varying electric current into a transmitter coil. The current in the transmitter coil generates a magnetic field of the same frequency and phase, which is called a primary field. For geophysical applications, frequencies of the primary alternating field are usually less than a few thousand Hertz. The force lines of this primary field penetrate the earth and may penetrate a conductive body. According to Faradays' law, an electromagnetic force or voltage (EMF_{\circ}) will be produced within the conductor.

The EMF in the conductor will produce an induced current, so called eddy current, which flows in the conductor in planes perpendicular to lines of the magnetic field of force from the transmitter, unless restricted by conductor's geometry. The magnitude of the eddy current is a function of the transmitter frequency, power, and geometry and the distribution of all electrical properties in the subsurface, i.e., not just an isolated conductor. The field caused by the eddy currents induced in the subsurface terrain and any buried object in the subsurface is called the secondary field. The direction (sign) of the secondary field induced by the conductive object in the subsurface is opposite to the primary field (Fig. 3.15a).

If the transmitter and receiver are located above the surface of the ground, then the field measured at the receiver is a combination of the field that propagates directly from the transmitter (the primary field) and the induced secondary field from the object of a contrasting conductivity located in the subsurface.

The resulting total field has the same frequency as the primary field but differs in intensity, direction and phase. The total field is described by a complex-valued function consisting of both real and imaginary parts. The real part, which has the same phase as the primary field, is called inphase. The imaginary part, which shows a 90-degree phase difference from the transmitted signal, is called out-of-phase or quadrature (Fig. 3.15b). A secondary field that is 90° out-of-phase with the primary field has its maximum amplitude (or zero crossing) shifted one-quarter cycle in time with respect to the primary field. A phase shift of 180° means the secondary field is the mirror image of the primary field (Fig. 3.15c).

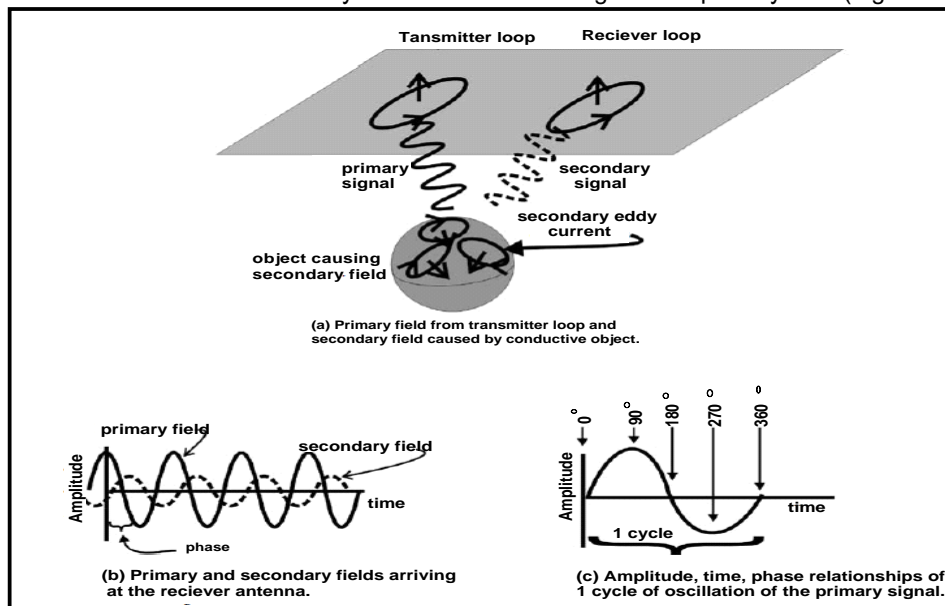


Fig. 3.15: The primary and secondary electromagnetic field: (a) the received signal referenced to the primary field, and (b) the amplitude and phase of the received signal related to several descriptions of the field. A single cycle (c) representing a continuously oscillating frequency domain wave for a single point on the spreading primary field and the induced secondary field is shown (Daniels et al., 2008).

In an FDEM survey, the electromagnetic response of a body is proportional to its mutual inductances with the transmitter and receiver coils and inversely proportional to its self-inductance, L , which limits the eddy current flow. The depth and size of the conductor primarily affect the amplitude of the secondary field. The quality of the conductor mainly affects the ratio of inphase to out-of-phase amplitude, a good conductor (high quality) having a higher ratio and a poor conductor having a lower ratio. Anomalies also depend on a response parameter ($\alpha = 2\pi fL/R$) which involves frequency, f , self-inductance, L , and resistance, R . Based on the model response parameter, the quadrature field is very small at high frequencies, where the distinction between good and merely moderate conductors tends to disappear (Klein and Lajoie, 1980).

3.4.3 FDEM SKIN DEPTH

The depth of penetration varies with the separation of the transmitter and the receiver coils (Geonics Limited [Date Unknown]—Technical Note TN-31). At the usual frequencies (< 5 kHz) used in EM survey

attenuation effects are virtually negligible, but signal losses occur by diffusion. The depth at which the amplitude of a plane wave has been attenuated to 37% ($1/e$) of its original value is called the skin depth δ , also called effective depth (Sheriff, 1991). The mathematical definition of skin depth is given by the following equation:

$$\delta [m] = \sqrt{\frac{2}{\sigma\mu\omega}} \approx 503 \sqrt{\frac{1}{\sigma [Sm^{-1}] f [Hz]}} \approx 503 \sqrt{\frac{\rho [\Omega m]}{f [Hz]}} \quad (3.31)$$

This relationship is only valid for plane waves⁸ from large distances to the source (far-field conditions). For FDEM systems, the penetration depth is less than that derived from Eq. (3.31) due to the difference in the wave-front geometries. Generally, the penetration depth increases with increasing loop separation and decreasing frequency. Although Reynolds (1997) states that “a realistic estimate of the depth, to which a conductor would give rise to a detectable EM anomaly is $\approx \delta/5$ ”, the use of general rules for depth estimation is not recommended (Lange and Seidel, 2007).

The ratio of the inter-coil spacing (S) divided by the skin depth (δ) is known as the induction number ($B = S/\delta$). Where the induction number is much less than one, the ratio of the secondary to the primary magnetic fields at the receiver is directly proportional to apparent conductivity (σ_a). Under this condition (known as “low induction numbers”), virtually all response from the ground is in the quadrature phase component of the received signal. With these constraints, the secondary magnetic field can be represented as

$$\frac{H_s}{H_p} = \frac{i\omega\mu_0\sigma S^2}{4} \quad (3.32)$$

where H_s is the secondary magnetic field (90° out-of-phase with the primary field) at the receiver coil, H_p is the primary magnetic field at the receiver coil, ω is the angular frequency and μ_0 is the permeability of free space.

3.4.4 LOOP CONFIGURATIONS

The EM penetration depth, resolution and sensitivity mainly depend on the loop configuration. Anomaly shapes depend on system geometry as well as on the nature of the conductor (Milsom, 2003). Coils are described as horizontal or vertical according to the plane in which the windings lie. ‘Horizontal’ coils have vertical axes and they are alternatively described as vertical dipoles. In many geophysical applications, EM signals are transmitted and received by straight wires (commonly called lines) or by loops (or coils) of wire. Most lines have electrodes in the ground at each end of the line. The term magnetic dipole is used to describe the orientation of the transmitter and receiver coils to each other and the ground. In the practice, mainly horizontal coplanar, vertical coplanar and vertical coaxial are commonly used configurations in EM surveys (Fig. 3.16).

⁸ The Plane wave is a constant-frequency wave whose wave fronts (surface of constant phase) are infinite parallel planes of constant amplitude normal to the phase velocity vector (the rate at which the phase of the wave propagates in space).

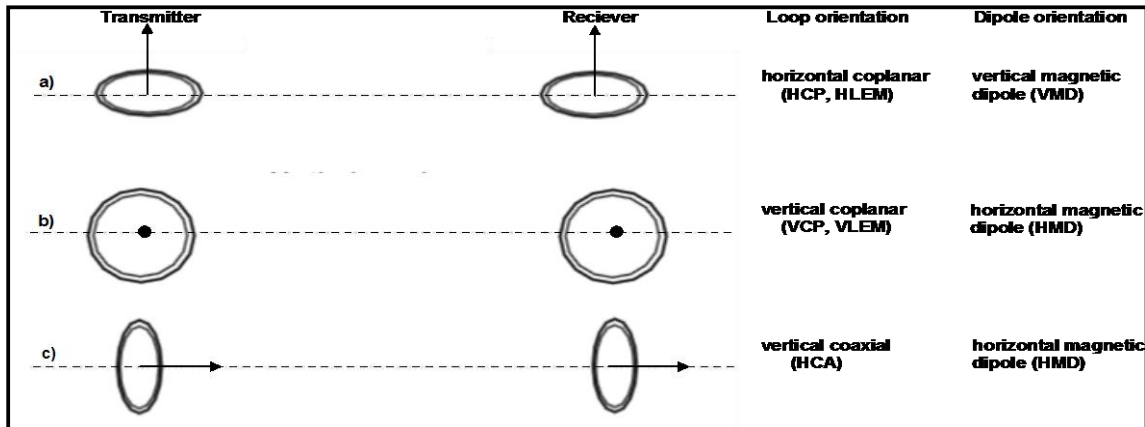


Fig. 3.16: Common loop configurations of small loop dipole-dipole systems

Most ground EM systems use horizontal coplanar coils ('horizontal loop'), usually with a shielded cable carrying a phase-reference signal from transmitter to receiver. The Swedish term Slingram is often applied to horizontal loop systems but without any general agreement as to whether it is the fact that there are two mobile coils, or that they are horizontal and coplanar, or that they are linked by a reference cable that makes the term applicable. In general, an FDEM system in which two small coils, one transmitter and one receiver, separated by a constant distance between 4 m and 100 m, are moved along a survey transect. The primary field is nulled so that the inphase and quadrature components of the secondary field can be measured.

3.5 DATA INTERPRETATION

3.5.1 GENERAL

In the interpretation process, we try to derive a distribution of electrical properties of the subsurface from a set of measurements conducted on the boundary of the object, or at least outside the region of interest. The outcome is called a model that gives a response that is similar to the actual measured values. The model has a set of model parameters that are the physical quantities we want to estimate from the observed data. The model response is the synthetic data that can be calculated from the mathematical relationships defining the model for a given set of model parameters using a linear filter. The simulation of synthetic data for a given model parameterization is known as "forward calculation" or "forward problem". A least squares fit of the model to the input data is then made until a selected fitting error is reached using the Newton algorithm to solve the "inverse problem". Fig. 3.17 shows the main steps of the data interpretation in the form of forward and inverse problems.

The overall goal of the inversion is to minimize the deviation between the measured and calculated data. The minimization process is based on the quality of the observation as well as the input model. To determine how well the model fits the measured data, the weighted least-squares criterion (i.e., χ^2 misfit) (Jackson, 1972) is used:

$$x^2 = \sum_{i=1}^N \left[\frac{d_i - f(m)}{\sigma_{si}} \right]^2 \quad (3.33)$$

where N is the number of the measured data points, σ_{si} is a relative standard deviation or error, d denotes the measured values, m the free model parameters and f is the response function.

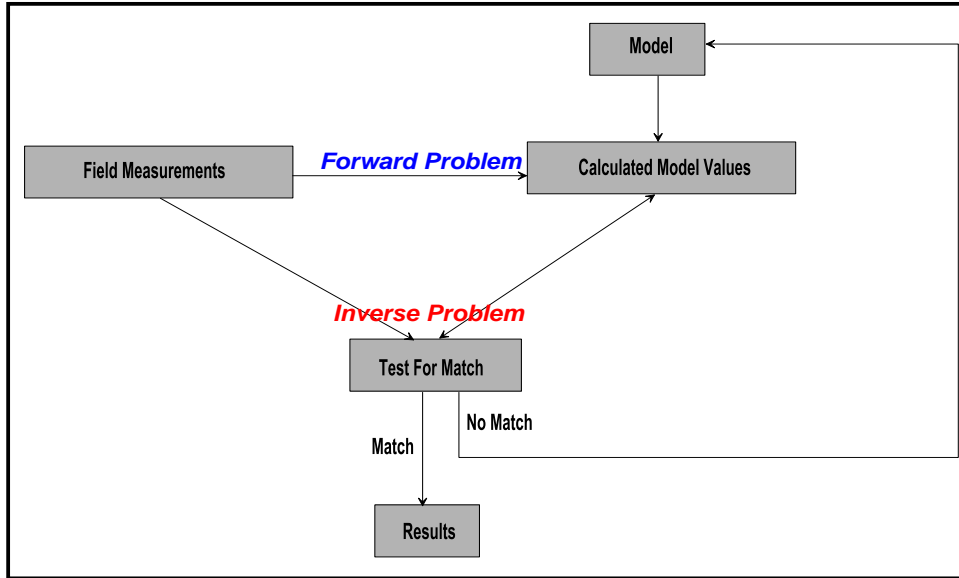


Fig. 3.17: Schematic diagram showing the resistivity data interpretation process.

3.5.2 DC INTERPRETATION

Resistivity and IP data are usually plotted in the form of curves (1D sounding) and pseudosections (2D/3D imaging). The synthetic model is governed by a physical law, the Poisson equation, which can be expressed as

$$\nabla(\rho \nabla V) = \nabla \rho \nabla V + \rho \nabla^2 V = -I \delta(r) \quad (3.34)$$

where $\rho(r)$ is the electrical resistivity distribution, $V(r)$ is the electric potential at a point r due to a single current electrode, idealized as a point source at the origin with strength I , and δ is the Dirac delta function.

For a 2D problem, the Poisson Eq. (3.34) can be written as (e.g., Hohmann, 1988):

$$\frac{\partial}{\partial x} \left(\rho \frac{\partial \tilde{V}}{\partial x} \right) + \frac{\partial}{\partial z} \left(\rho \frac{\partial \tilde{V}}{\partial z} \right) - k^2 \rho \tilde{V} = -\frac{1}{2} \delta(x) \delta(z) \quad (3.35)$$

with k being the wave number. Once this differential equation is solved for the transformed potential $\tilde{V}(x, k, z)$, an inverse Fourier transform must be applied to obtain $V(r)$ (e.g., LaBrecque et al., 1996; Kemna, 2000).

The linear filter technique is based on the determination of the potential V at a distance X from the current source, over a 1D horizontal layered sequence from the resistivity transform of the field data. Assuming for instance an SC configuration, the apparent resistivity is given by the so-called Stefanescu integral (e.g., Koefoed, 1979):

$$V = \frac{I \rho_l}{2\pi} \int_0^\infty K(\lambda) J_0(\lambda x) d\lambda \quad (3.36)$$

where, $K(\lambda)$ is the Kernel function and is controlled by resistivities and thicknesses of subsurface layers. $J_0(\lambda x)$ is the Bessel function of zero order.

The computation of the successive layer effects can be made using the relationship between the Kernel function and the resistivity transform function $T_i(\lambda)$ which is defined by *Koefoed (1979)*:

$$T_i(\lambda) = \rho_i K(\lambda) \quad (3.37)$$

For 1D resistivity distributions, the integral in Eq. (3.36) can be readily calculated, for instance using fast filtering techniques (e.g., *Christensen, 1990*). On the other hand, for arbitrary 2D or 3D resistivity distributions, computationally more expensive numerical approaches are required to solve Eqs. (3.34) or (3.35) e.g. by using finite difference and finite element methods (see subsection 3.4.2.2). In general, the inversion process is carried out in a number of iterations using a Newton algorithm. To solve the inversion problem, the Gauss-Newton and the quasi-Newton inversion methods are widely used (see subsection 3.4.2.2).

3.5.2.1 1D DC INTERPRETATION

The measured apparent resistivity can be interpreted qualitatively or quantitatively. The maximum angle of slope that the rising portion of a resistivity graph may have on a log/log graph is 45°. If the field curve rises more steeply, then this suggests an error in the measured data (*Reynolds, 1997*). The qualitative interpretation includes recognizing the curve type and preparing apparent resistivity maps and cross sections to show the lateral and vertical variations of subsurface resistivities. In general, the minimum number of horizontal layers and the relative magnitudes of the respective layer resistivities can be estimated from the curve shape alone.

The quantitative interpretation of sounding data (inversion) is to use the curve of apparent resistivity versus electrode spacing to obtain the layer resistivities and thicknesses. The theoretical background of DC sounding quantitative interpretation is discussed in detail by *Mundry and Dennert (1980)*. Today, the old graphical procedures using master curves (e.g., *Cagniard, 1952*) are rarely used. In recent years, purely automatic inversion programs without any assumptions of layering exist as well as programs that require the handling of the interpreter. The 1D DC handle inversion involves the following four steps:

1. The person responsible for data interpretation constructs a one-dimensional resistivity depth model based on the available information regarding subsurface conditions.
2. Computer software is used to generate a synthetic vertical electric sounding curve corresponding to the initial one-dimensional model of soil resistivity variation with depth.
3. The computer-generated synthetic sounding curve is then compared to the sounding curve measured in the field.
4. The interpreter then adjusts the initial one-dimensional resistivity model, followed by the generation of a new synthetic sounding curve.

The starting model can be derived from known geological parameters, available borehole data or the results of other geophysical methods, which control the inversion process. The synthetic data was calculated using a linear filter technique (Eq. 3.36). The inversion process is repeated until there is a good fit between the measured resistivity data and the synthetic sounding curve. The inversion program will stop the iteration at the best fit between the starting model and the observed apparent resistivities. The best fit may be defined by calculating a root mean square error (RMS), and/or preferentially by the interpreter. We have

$$RMS = \frac{\sqrt{\sum_{i=1}^N \left(\frac{\rho_{oi} - \rho_{ci}}{\rho_{oi}} \right)^2}}{\sqrt{N}} * 100 \quad (3.38)$$

where, ρ_{oi} is the observed apparent resistivity for the i^{th} layer, ρ_{ci} is the calculated apparent resistivity for the i^{th} layer and N is the number of digitized apparent resistivity points.

3.5.2.2 2D/3D DC AND SIP DATA INTERPRETATION

The 2D and 3D smooth-model inversion of resistivity and IP data produces image-like, electrical property sections which improve the data's interpretability. Recent software improvements enable routine smooth-model inversion of resistivity and IP data (Zonge *et al.*, 2005).

Forward Problem

The mathematical link between the model parameters and the model response for the 2D and 3D resistivity models is provided by finite-difference (Dey and Morrison 1979a, 1979b) or finite-element methods (Silvester and Ferrari, 1990). The algorithms of these methods are used to calculate the direct current response of the current model section and the sensitivity of calculated values to correct the model parameters. In both methods, the conductivity distribution is approximated by a mesh of individual elements or cells, each with constant conductivity. The potential is then calculated at discrete points (nodes of the mesh) by solving a linear system of equations derived from discretized differential equation and boundary conditions (Binley and Kemna, 2005). Details on the use of finite difference and finite element methods to solve the DC electrical problem are well documented in the literatures (e.g., Lowry *et al.*, 1989; Spitzer, 1995; Bing and Greenhalgh, 2001; Auken and Christiansen, 2004; Günther, 2004; Günther *et al.*, 2006; Rücker *et al.*, 2006).

The basis of the finite difference technique is the construction of a discrete model in form of a hexahedral grid with nodes at the cell corners (Günther, 2004). The existing partial derivatives are replaced by finite differences. Oldenburg and Li (1994) shows that the finite difference modeling requires a rectangular mesh that cannot be used to match irregular terrain, limiting the accuracy for topographic modeling.

The finite element methods have been used early to calculate electromagnetic and electrical fields (Coggon, 1971; Pridmore *et al.*, 1980). The main advantage of the finite element method is the incorporation of topography (Fox *et al.*, 1980), which cannot be accomplished using hexahedrons.

Tetrahedrons allow for the simulations of arbitrary geometry. *Bing and Greenhalg (2001)* presented a finite element simulation based on regularly arranged tetrahedron elements. In general, finite element methods are preferred if greater flexibility with respect to mesh geometry is desired. Only few approaches using an unstructured tetrahedral grid have been published (*Sugimoto, 1999; Rücker et al, 2006; Günther et al, 2006*).

To model IP data, presences of polarization dipoles effectively reduce the overall current density. For time-domain measurements, the model response of a polarizable medium with conductivity σ_{dc} and intrinsic chargeability m can be interpreted as the response of a non-polarizable medium with decreased conductivity $\sigma_{ip} = (1-m)\sigma_{dc}$ (*Seigel, 1959*). Consequently, the apparent chargeability (m_a) can be modeled by carrying out DC resistivity forward models for σ_{dc} and σ_{ip} (e.g., *Oldenburg and Li, 1994*):

$$m_a = \frac{f[(1-m)\sigma_{dc}] - f[\sigma_{dc}]}{f[(1-m)\sigma_{dc}]} \quad (3.39)$$

where f represents the forward modeling operator.

For frequency-domain measurements, the model response bases on the combined description of conduction and polarization properties by means of a complex conductivity, σ^* . In the quasi-static frequency limit (typically <10Hz), a complex-valued Poisson equation,

$$\nabla(\sigma^* \nabla V^*) = \nabla \sigma^* \nabla V^* + \sigma \nabla^2 V^* = -I \delta(r) \quad (3.40)$$

may be solved for a complex potential, V^* , analogous to the DC case. *Weller et al. (1996)* followed this approach using a finite difference framework.

Inverse Problem

In the Inversion process, apparent resistivities are completely inverted first, followed by a separate inversion of IP data. At each iteration, the difference between the observed and the calculated data are determined; then improved model parameters are estimated for the next iteration. In general, the mathematical basis of 3D inversion is similar to the 2D inversion. Extension of the inversion methodology to 3D resistivity and IP data is limited by two factors: (a) The computation techniques are still relatively slow due to large number of measurements; (b) the data acquisition systems are still limited compared to 2D surveys (*Nabighian and Asten, 2001*).

The smoothness-constrained least-squares method has been widely used in the inversion of geoelectrical data using 2D and 3D subsurface models (e.g., *Sasaki, 1989, 1994; deGroot-Hedlin and Constable, 1990*). This smoothness constrained least-squares method (l_2 -norm optimization method) aims to minimize the sum of the squared differences, or roughness, between the apparent and modeled resistivities. The l_2 -norm method is preferable for most data sets (*Loke, 2001*). This approach is acceptable if the actual subsurface resistivity varies in a smooth and gradual manner (*Loke, 2004*).

The smoothness-constrained inversion method is based on an analytical calculation of the sensitivity matrix (Jacobian matrix) for a homogenous halfspace. The sensitivity matrix is re-calculated

using the finite difference or the finite element methods at each step of iteration. The optimization equation (Ellis and Oldenburg, 1994a) can be represented as

$$(J_i^T J_i + \lambda_i C^T C) p_i = J_i^T g_i - \lambda_i C^T C r_{i-1} \quad (3.41)$$

where i is the iteration number, J_i is the sensitivity matrix of partial derivatives, g_i is the discrepancy vector which contains the differences between the logarithms of the measured and calculated apparent resistivity values, λ_i is the damping factor and p_i is the perturbation factor to the model parameters for the i^{th} iteration. The flatness filter C is used to constrain the smoothness of the corrected model parameters to some constant value. The amplitude values of the flatness filter matrix are increased for deeper blocks (Sasaki, 1989 and 1992). The second term on the right hand side of Eq. (3.41) applies the smoothness constraint directly on the model resistivity vector, r_{i-1} . This guarantees that the model will be smooth subject to the damping factor used (Ellis and Oldenburg, 1994a).

Both the Gauss-Newton and quasi-Newton methods are smoothness constrained least squares inversion methods, where by default the vertical and horizontal smoothness constraints are the same (deGroot-Hedlin and Constable, 1990). In the Gauss-Newton or quasi-Newton methods, the spatial variations in the model parameters (i.e. the model resistivity values change in a smooth or gradual manner) are minimized. Both methods are similar, but the quasi-Newton method is used to reduce the numerical calculation, by means of a fast approximation update of the sensitivity matrix. The main problem in using the Gauss-Newton method is the time and memory space required to calculate the elements of the Jacobian matrix (J_i) (e.g., Sasaki, 1989). However, since the Gauss-Newton method uses the exact partial derivatives, it should produce more accurate results (Loke and Dahlin, 1997). The quasi-Newton inversion is based on an analytical calculation of the sensitivity matrix for the homogenous half-space. The sensitivity matrix is used for updating the model resistivity at each step of iteration, and it will change with the change of the resistivity distribution within the model. This approach can be expected to work well for small resistivity contrasts but not necessarily for larger contrasts (Dahlin and Loke, 1998). The quasi-Newton method (Broyden, 1965) uses the following updating equation:

$$B_{i+1} = B_i + u_i p_i^T \quad (3.42)$$

where $u_i = (\Delta y_i + B_i p_i) / p_i^T p_i$ and $\Delta y_i = y_{i+1} - y_i$.

B_i and y_i are the Jacobian matrix J_i and model response for the i^{th} iteration, respectively. The approximation of the Jacobian matrix B_{i+1} for the $(i+1)^{\text{th}}$ iteration is calculated using the Jacobian matrix approximation B_i , the parameter perturbation vector p_i and the change in the model response Δy_i for the i^{th} iteration. The updating matrix $u_i p_i^T$ is a rank-one matrix and Broyden's method is a rank-one quasi-Newton method (Scales, 1985).

In some cases, the subsurface geology consists of a number of regions that are internally almost homogeneous but with sharp boundaries between different regions. For such cases, the Gauss-Newton robust model constrained (l_1 -norm) is preferable to be used, or more commonly known as a blocky inversion method. The l_1 -norm method aims to minimize the sum of the absolute values of the differences between the apparent and modeled resistivities (Claerbout and Muir 1973). One simple

method to implement an l_1 -norm based optimization method using the standard least-squares formulation is the iteratively reweighted least-squares method (Wolke and Schwetlick, 1988).

Finally, in the least-squares optimization methods the initial model is modified such that the sum of squares error of the difference between the model response and the observed data values is minimized. Both the l_1 and the l_2 methods proceed by iterative alteration of the model resistivity until the Root Mean Square (RMS) error reaches to the best fit between the model response and the observed data. In general, the l_1 method leads to a higher RMS error than the l_2 method (Loke, 2001).

3.5.3 FDEM DATA INTERPRETATION

Determination of conductivity from EM measurements is much more complicated than from DC resistivity data (Das, 1995). The simplest analysis consists of visual inspection (qualitative) of the data, and the most complex interpretations involve inverse modeling. The qualitative interpretation is based on inspection of inphase and out-of-phase curves behavior. It includes a location determination of anomalies and their types; e.g., a long linear feature will indicate presence of an elongated conductive body. Depending upon the spatial sampling interval relative to the position of the target, the anomaly peaks and lows may be slightly broader or narrower than one dipole length by the sampling being skewed relative to the target (Reynolds, 1997). However, if more detail is required from the data, then it is necessary to model the data, using a numerical simulation of the EM response of a buried object to an external EM field.

Forward Problem

In case of geophysical measurements that follow the laws of Newton and Maxwell, the forward models are related to, in the form of, or can be derived from the wave equation (Daniels et al., 2008). The closed-form expressions for the FDEM field components are Hankel transforms or integrals over Bessel functions. A 1D forward modeling code based on a fast, reliable Hankel transform subroutine should be an essential part of the EM induction geophysicist's computational toolbox, since it permits rapid, quantitative layered-earth interpretations of measured FDEM responses (Everett and Meju, 2005).

In case of a horizontal loop transmitter of radius a carrying current I and situated on the surface of a uniform half-space of electrical conductivity σ , the vertical magnetic field $B_z(r)$ on the surface at distance r from the transmitter is given by the formula (Ward and Hohmann, 1987):

$$B_z(r) = \mu_0 I a \int_0^\infty \frac{\lambda^2}{\lambda + i\gamma} J_1(\lambda a) J_0(\lambda r) d\lambda \quad (3.43)$$

where $\gamma^2 = i\mu_0\sigma\omega - \lambda^2$ and J_0, J_1 are Bessel functions. Similar analytic solutions are available for layered earths excited by other Tx/Rx configurations.

Finding the FDEM response to 3D subsurface conductivity distributions requires the application of numerical methods for solving the governing Maxwell partial differential equations. A good introduction to integral equation, finite element, and finite difference techniques is provided by Hohmann (1988).

Inverse Problem

The determination of the electrical conductivity, or its reciprocal, resistivity of the subsurface structure is the main goal in FDEM inversion. The inverse problem is thus the search for a model m whose responses best replicate the field observations in the least-squares sense, but within bounds defined by the data errors (Everett and Meju, 2005). The minimization process between the measured and calculated data can be expressed by introducing a model objective function $\Phi(m)$ of the form,

$$\Phi(m) = e^T e = (d - f(m))^T (d - f(m)) \quad (3.44)$$

$$f(m) \approx f(m_0) + J\Delta m \quad \text{with} \quad \Delta m \approx m_0 - m$$

where e is the $N \times 1$ column vector containing N data, superscript T denotes the transposition, d is the measured data, f is the non-linear response function, J is the Jacobian matrix, m is the model, m_0 is the starting model and Δm is the model update (or perturbation).

If we define the vector $y = d - f(m_0)$ as the discrepancy vector, then Eq. (3.44) can be written as,

$$\Phi(m) = e^T e = (y - J\Delta m)^T (y - J\Delta m) \quad (3.45)$$

$$\Delta m = (J^T J)^{-1} J^T y$$

This is the classical Gauss-Newton solution to improve the m_0 until an optimal Δm is obtained.

With the Marquardt-Levenberg optimization algorithm the least-squares solution of the 1D EM inverse problem is regularized to minimize the model update (Jupp and Vozoff, 1975; Lines and Treitel, 1984). It is also referred to as ridge regression optimization (Inman, 1975). It modifies the layer resistivities and thicknesses in the starting model iteratively to best fit the data. The objective function can be written as

$$\begin{aligned} \Phi(m) &= \|e\|^2 + \varepsilon^2 (\|\Delta m\|^2 - \Delta m_0^2) \\ \Phi(m) &= e^T e + \varepsilon^2 (\Delta m^T \Delta m - \Delta m_0^2) \end{aligned} \quad (3.46)$$

where $\|\cdot\|$ denotes the usual L_2 (Euclidean) norm, Δm_0 is a finite quantity and ε is the Marquardt-Levenberg damping factor (Levenberg, 1944; Marquardt, 1963).

The minimization of the objective function leads to so-called damped least-squares solution,

$$\Delta m = (J^T J + \varepsilon^2 I)^{-1} J^T y$$

where I is the $M \times M$ identity matrix.

With the Occam optimization algorithm the least-squares solution of the EM inverse problem is regularized to minimize the change of a model update or roughness (converse of smoothness) (Constable et al., 1987). The scheme is a standard implementation of the 1D smoothed-earth inversion. The philosophy of this scheme is to find the smoothest resistivity model which matches the measured data to some required level. The Occam inversion is an important step in the 1D interpretation strategy, as it can formulate a good starting model for the further full nonlinear layered earth inversion. The inverse problem in mathematical terms can be stated as (e.g., Meju, 1994): minimize the objective function as

$$\begin{aligned} \Phi(m) &= \|Dm\|^2 + \mu^{-1} (\chi(m)^2 - \chi^*(m)^2) \\ &= \|Dm\|^2 + \mu^{-1} (\|Wd - Wf(m)\|^2 - \chi^*(m)^2) \end{aligned} \quad (3.47)$$

where $\|Dm\|^2$ is the model roughness ($\|Dm\|^2 = \int \left(\frac{\partial m}{\partial z}\right)^2 dz$), μ^{-1} is the Lagrange multiplier which controls both the model roughness and data misfit. The μ^{-1} is usually chosen so that $\chi(m) = \chi^*(m)$, where $\chi^*(m)$ is the desired data misfit.

3.6 RESISTIVITY-HYDRAULICAL PARAMETERS RELATIONSHIP

The relationship between electrical parameters and hydraulic parameters of an aquifer, in general, is empirical and semi-empirical and often tuned to individual locations. Hydrogeophysics can be defined as the use of geophysical measurements for mapping subsurface features, estimating properties and monitoring processes that are important to hydrological studies (Rubin and Hubbard, 2005). It should be born in mind that the resistivity readings are not absolute but relative, and therefore only relative conclusions about the area's hydraulic parameters could be made. Currently, the hydrogeological parameters are determined from pumping tests and/or tracer tests or grain size analysis and require boreholes, which are relative expensive, with sparse results and low resolution of the resulting maps. The use of DC resistivity methods alone may be feasible in particular situations where a lot of prior information is available, but in general, a unique relationship between DC resistivity and hydraulic conductivity does not exist (e.g., Mazac et al., 1985 and 1988; Purvance and Andricevic, 2000). The surface geophysical techniques are comparatively simpler, more cost effective and faster than drilling. Several hydrogeophysical approaches have been suggested (e.g., Niwas and Singhal, 1981 and 1985; Börner et al., 1996) to predict relationships between the hydraulic parameters and both DC and SIP parameters.

3.6.1 HYDRAULIC PARAMETERS

The most important hydraulic parameters are the porosity Φ , the permeability P , the hydraulic conductivity k_f and transmissivity K . Φ is defined as the ratio between the volume of pores V_p and that of the rock V_t , note that $\Phi = V_p/V_t$. The hydraulic permeability (which, as defined in the usual hydrogeological language, is actually the hydraulic conductivity, k_f) is the ability of material to let a fluid current flow through it when a hydraulic pressure $P = k_f \mathcal{L} / g \mathcal{b}$ is applied, where \mathcal{L} is fluid dynamic viscosity, g is gravitational acceleration and \mathcal{b} is fluid density. The K of an aquifer layer is the ability of the layer to transmit fluids through its entire thickness h . It can be expressed as the product of k_f of the aquifer by its thickness, $K = \int k_f dz$.

Much of the early work for predicting P within porous media is based on capillary tube models, the fundamental basis being the Kozeny-Carman equivalent channel equation (Kozeny, 1927; Carman, 1939). This model represents flow through a network of capillaries. Based on this equation, the permeability will be

$$k_f = \frac{\Phi}{a S_{por}^2 T} \quad \text{and} \quad S_{por} = 1/r = S_s \rho_s (1 - \Phi) / \Phi \quad (3.48)$$

where, S_{por} is the surface area per unit pore volume, a is a shape factor (Scheidegger, 1974), T is tortuosity, r is the hydraulic radius, S_s is the specific surface area and ρ_s is the mineral density.

Grain-based hydraulic conductivity models predict k_f to be dependent on the square of an effective grain size. The Hazen model (1911) is applicable to predict k_f based on grain size analysis of sediments. In the Hazen model, $k_f = C d_{10}^2$, where the effective grain size d_{10} (in mm) corresponds to the grain size for which only 10 % of the grains are finer and the coefficient C depends upon grain sorting.

k_f can be estimated by using the Kozeny-Carman-Bear equation, given by *Domenico and Schwartz (1990)* as

$$k_f = (6g/\epsilon)(d^2/180)[\phi^3 / (1 - \phi)^2] \quad (3.49)$$

where d is the grain size and ϵ is the fluid density (1000 kg/m³ for water at normal condition).

3.6.2 DC ρ - K APPROACHES

Archie's Laws and Formation Factor

Archie's first law (*Archie, 1942*) relates the bulk resistivity ρ_0 of a fully saturated granular medium to its porosity and the resistivity ρ_w of the fluid ρ_w within the pores

$$\rho_0 = a\rho_w\Phi^{-m} \quad (3.50)$$

where m is known as the cementation factor, although it is also interpreted as grain-shape or pore-shape factor, and the coefficient a is associated with the medium. Its value in many cases departs from the commonly assumed value of one.

For a clay-free medium, ρ_0/ρ_w ratio is known as the intrinsic formation factor, F_i . Thus, Eq. (3.50) could be easily reformulated into

$$\Phi = e^{\frac{1}{m}\ln(a) + \frac{1}{m}\ln(1/F_i)} \quad (3.51)$$

The values of the coefficients a and m , ideally, should be determined for each site under investigation. They have been reported to vary widely for different formations, e.g., The coefficient a often has the value of one while m is allowed to vary from 1.3 to 2.5 as suggested by *Jackson et al. (1978)*, *de Lima and Sharma (1990)*, *Schön (2004)* and *de Lima et al. (2005)*.

When the medium is not fully saturated, water saturation plays an important role, where the degree of saturation changes the effective porosity (accessible pore space). Accordingly, Archie's second law is

$$F_i = \frac{\rho_0}{\rho_w} = a\Phi^{-m}S_w^{-n} \quad (3.52)$$

where n is the saturation index (often value is 2).

For clay/silty sand material, additional corrective parameters for clay conductivity are required. A large number of empirical models are currently in use to calculate the intrinsic formation factoring case of dirty sand (e.g., *Waxman and Smits, 1968*; *Clavier et al., 1984*; *Sen et al., 1988*). According to *Worthington (1993)*,

$$F_a = F_i(1 + BQ_v\rho_w)^{-1} \quad (3.53)$$

where, Q_v is the cation-exchange capacity (CEC) per unit pore volume of the rock in units of equiv 1/liter, an electrical measure of shaliness, and B is the equivalent conductance of (sodium) clay-exchange cations expressed as a function of ρ_w (Waxman and Thomas, 1974). The term BQ_v is related to the effects of surface conduction, mainly due to clay particles. If surface conduction effects are non-existent, the apparent formation factor becomes equal to the intrinsic one. Re-arranging the terms of Eq. (3.53), we obtain a linear relationship between $1/F_a$ and ρ_w ,

$$1/F_a = 1/F_i + \left(\frac{BQ_v}{F_i}\right)\rho_w$$

where $1/F_i$ is the intercept of the straight line and BQ_v/F_i represents the gradient (Huntley, 1986; Worthington, 1993).

The DC geoelectrical parameters are widely used to predict the hydraulic conductivity of the aquifer. The relationship between k_f and σ' using DC measurements depend on the physical and chemical properties of the minerals and pore fluids at a site ignoring whether σ_{el} or σ'_{int} dominates the measured σ' . In several publications, the so called Dar-Zarrouk parameters (Maillet, 1947) were used to predict the transmissivity and hydraulic conductivity of an aquifer (e.g., Kosinski and Kelly, 1981; Niwas and Singhal, 1981; Yadav, 1995; Chandra et al., 2008).

Kosinski and Kelly (1981) have attempted to establish a direct equivalence between 'normalized transverse resistance' ($T, \Omega m^2$) and aquifer transmissivity ($K, m^2/day$).

$$K = T^- = T \frac{\rho_w^-}{\rho_w} \quad (3.54)$$

where ρ_w^- is the average aquifer water resistivity and ρ_w is the water resistivity close to the sounding point.

Niwas and Singhal (1981) determined analytically the relationship between transmissivity and transverse resistance of an aquifer and the transmissivity and longitudinal conductance. This empirical relation was based on Darcy's law of fluid flow and on Ohm's law of current flow (see Appendix A).

$$K = (k_f \sigma)T \text{ and } K = (k_f \rho)S \quad (3.55)$$

where the ratios of $k_f \sigma$ or $k_f \rho$ remain constant in a particular area. Note that k_f values are derived from pumping tests or grain size analyses. In addition, σ and ρ are the interpreted values close to the observed wells. Consequently, when $k_f \sigma$ or $k_f \rho$ are constant over a particular area, this approach can be applied using the average of these products.

In 1985, Niwas and Singhal modified these relationships by using a 'modified aquifer resistivity' which is known as 'normalized aquifer resistivity' by Kosinski and Kelly (1981). The

$$K = (k_f \sigma^-)T^- \quad (3.56)$$

where $\sigma^- = 1/\rho^- = \rho_w/\rho\rho_w^-$. Similar to Eq. (3.57), $k_f \sigma^-$ remains constant for a particular area.

Yadav (1995) established an empirical relationship between 'normalized aquifer resistivity' ρ^- and transmissivity K . He has observed very good correlation between these two parameters, using

$$K = (k_f S^-)\rho^- \text{ , } S^- = \sum h_i/\rho_i \quad (3.57)$$

where S^- is normalized longitudinal conductance and $k_f S^-$ remains constant for a particular area.

Chandra *et al.* (2008) presented a methodology to estimate the hydraulic conductivity and transmissivity of a hard rock granite aquifer from geoelectrical parameters. They showed a negative correlation between k_f and ρ (or ρ^{-}) and a positive correlation between K and S (or S^{-}). Based on their approach, the transmissivity can be calculated using the following equation:

$$K = AS \quad (3.58)$$

where A is equal to $k_f \rho$ and/or $k_f \rho^{-}$, which will be constant where the groundwater quality remains equal.

Purvanca and Andricevic (2000) have studied the log-log relationships (positive or negative) between k_f and σ' using a modification of a microscale network model for fluid and electrical charge transport. They show that the $\sigma'-k_f$ relationship is positive when interconnected pore volumes dominate electrical current flow and negative when interconnected pore surface areas dominate electrical current flow. They derived the expected linear log-log empirical relation between σ' and k_f ,

$$k_f = a(\sigma')^b \quad (3.59)$$

The constants a and b would be necessary based on comparison of geoelectrical measurements with k_f values (e.g., from pumping test or slug tests). The constant b will be positive in the case of $\sigma' \approx \sigma_{el}$, but will be negative in the case of $\sigma' \approx \sigma_{int}$.

3.6.3 IP- k_f APPROACHES

Several authors have suggested semi-empirical relationships between IP parameters and k_f . The IP method can overcome some limitations of the DC method whereby both $|\sigma|$ and a measure of the charge storage associated with interfacial polarization are recorded. The imaginary part of conductivity is only a function of the interfacial properties ($\sigma'' \approx \sigma''_{int}$), i.e., the properties of the interconnected pore surface area S_{por} alone, which is very important in estimating k_f . In many articles a power-law dependence of σ'' and S_{por} has been shown (e.g., Börner and Schön, 1991; Slater and Lesmes, 2002a; Slater *et al.*, 2006). It is important to emphasize that S_{por} in the Kozeny-Carman type equation (see Eq. 3.48), is a commonly used measure of r ($S_{por} = r^{-1}$), being the ration of pore volume to surface area and historically judged to be the only natural length scale of a porous medium (Thompson *et al.*, 1987).

The Kozeny-type equation has been widely used to estimate k_f using the sensitivity of IP data to estimate S_{por} . Fig. 3.18 summarizes the steps of using IP measurements to calculate k_f using the Kozeny-Carman equation. Pape *et al.* (1987) reformulated the Kozeny-type equation for sedimentary rocks into the so called PARIS equation,

$$k_f = \frac{a}{F(S_{por})^c} \quad (3.60)$$

where k_f is in m/s and S_{por} in μm^{-1} , F is the electrical formation factor and a and c are adjustable parameters.

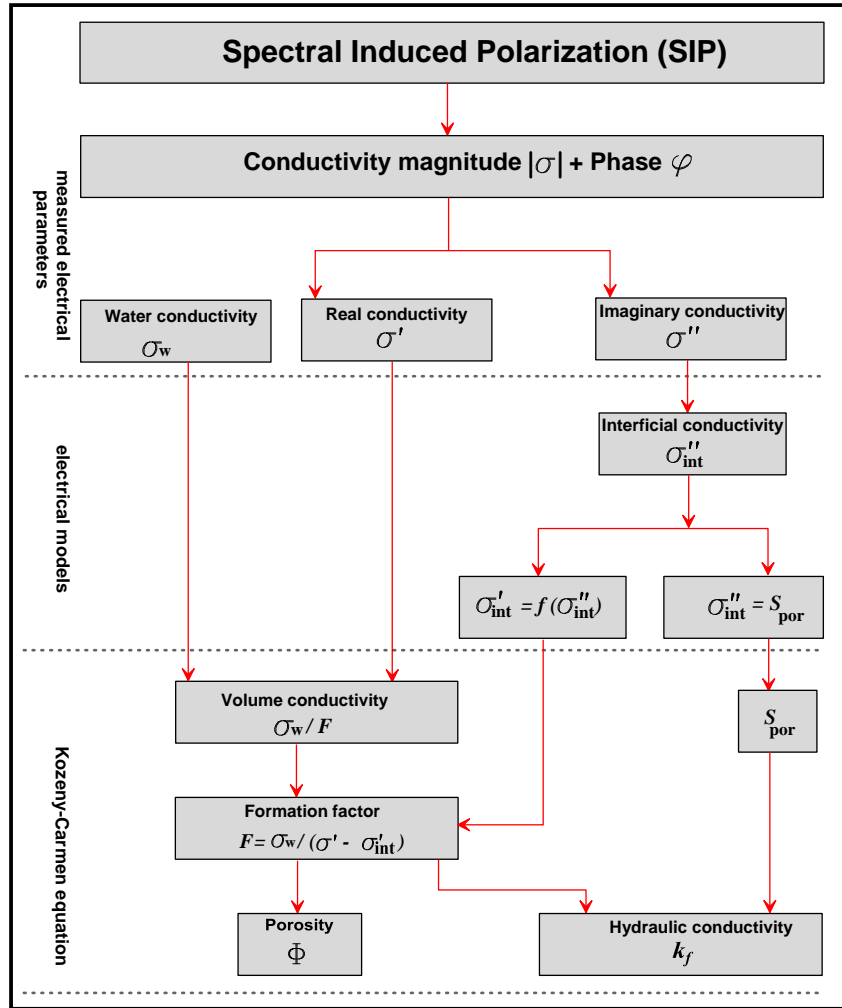


Fig. 3.18: Simplified overview of IP based estimation of k_f using a Kozeny-Carman approach (modified after Slater, 2007).

Börner et al. (1996) estimate hydraulic conductivity from the formation factor and inner surface area, using a Kozeny-Carman type equation. Their model, hereinafter called “Börner model” for convenience, requires the complex electrical conductivity distribution only at a single frequency over the “constant-phase-angle” (CPA) model⁹ (preferably around 1 Hz). The method is based on the PARIS equation Eq. (3.60). The main idea of Börner model is to estimate the formation factor, F , and the specific surface area, S_{por} . First, the formation factor, F , is calculated:

$$F = \frac{\sigma_w}{\sigma' - \sigma''/l} \quad (3.61)$$

where the factor l is the ratio between imaginary and real part of the surface conductivity. For unconsolidated sediments, it was suggested (Börner et al., 1996) to use $l = 0.1$. Second, the S_{por} is calculated:

$$S_{por} = (8.6 \cdot 10^4) \sigma'' \quad (3.62)$$

⁹ CPA model is a relaxation model which exhibits a steady decrease of resistivity magnitude with increasing frequency and a constant phase angle over the whole frequency range (Börner and Schön, 1991; Börner et al., 1993).

where σ'' is given in S/m and S_{por} in μm^{-1} . Eq. (3.62) was empirically derived from laboratory measurements.

Pape et al. (1987) suggested $a = 0.00475$ for consolidated sediments. *Börner et al. (1996)* formulated a proportionality for unconsolidated sediments using $a = 1$. *Slater and Glaser (2003)* and *Lesmes and Friedman (2005)* provided $a = 10^{-5}$, which also gives different results. The power law exponent c is another adjustable parameter often found to be $c = 3.1$ by *Pape et al. (1987)*, as a result of their theory. *Börner et al. (1999)* and *Sturrock et al. (1998)* obtained c in the range between 2.8 and 4.6, depending on the method of permeability measurement. *Slater and Lesmes (2002a)* reported another range for exponent c for unconsolidated sediments; namely from 0.9 to 1.6.

Weller et al. (2010) showed a single linear relationship between σ'' and S_{por} across a range of single frequency IP datasets comprised of sandstones and unconsolidated sediments. They applied a recent approach, defined as Debye decomposition (*Nordsiek and Weller, 2008*) (see appendix B), to determine a new parameter defining the global polarization magnitude from available SIP datasets. S_{por} is calculated after *Weller et al. (2010)*

(a) for a power law relation between σ'' and S_{por}

$$S_{por} = \frac{(\sigma'')^{1/b_p}}{a_p} \quad (3.63)$$

(b) for a linear relation between σ'' and S_{por}

$$S_{por} = \frac{(\sigma'')}{C_p} \quad (3.64)$$

where S_{por} is in μm^{-1} , σ'' is in mS/m, and a_p , b_p and C_p are constants. The authors observed that a_p , b_p and C_p are 0.0113, 1.023 and 0.0115, respectively, for sand-clay mixture, while for sand samples are 0.0101, 0.916 and 0.00931, respectively.

Slater and Lesmes (2002a) found that, for a wide range of unconsolidated soils, only S_{por} , and not Φ , was strongly correlated with k_f . They attributed the lack of significant Φ - k_f relation to a relatively narrow range of Φ in such soils. *Slater and Lesmes (2002a)* suggested a second approach to predict the hydraulic conductivity from SIP measurements based on an effective grain-size (*Hazen, 1911*) approach that used a measure of σ'' only. Their model, hereinafter called "*Slater and Lesmes model*" for convenience. They used natural and artificial sediments during the laboratory studies to extract an electrical-hydraulic relationship for unconsolidated sediments. They observed that k_f can correlate with σ'' and S_{por} but not with F or Φ . An empirical relationship between k_f and σ'' at 1 Hz was suggested, without using the real part and/or the formation factor

$$k_f = m/(\sigma'')^n \quad (3.65)$$

where σ'' is given in μSm^{-1} . m and n are adjustable parameters with $m = (2.0 \pm 0.3) \cdot 10^{-4}$; $n = 1.1 \pm 0.2$, and k_f is in m/s. In the *Slater and Lesmes* model these exponents have a smaller range than in the *Börner (1996)* model.

4 DATA ACQUISITION, PROCESSING AND INVERSION

The field surveys comprised of DC resistivity, FDEM and SIP measurements. The location of the geophysical measurements is shown in Fig. 4.1. According to the objectives of the present work (see section 1.2), the field surveys were carried out through gradual stages. First, 1D DC resistivity and FDEM soundings were executed. Then, DC resistivity profiling in the form of 2D and 3D imaging was carried out. In addition 2D SIP profiles were also measured based on the 2D DC resistivity results. At the last, DC resistivity soundings and the 2D SIP profile were used to identify the hydraulic characteristics of tidal deposits. Note that the locations of the detailed study, i.e., 2D and 3D imaging, were selected according to 1D DC resistivity and FDEM soundings results, previous HEM results and the geological background.

4.1 DC RESISTIVITY SURVEY

We started the DC resistivity survey by measuring 30 soundings to cover the whole area (Fig. 4.1). The locations of the measurements were marked using GPS positioning. The DC resistivity measurements were carried out along the available roads and reclaimed lands using a RESECS 8-channel multi-electrode instrument (Fig. 4.2). Most of these locations are characterized by a high resistive surface layer. The DC resistivity sounding data were acquired using a Schlumberger configuration, which is widely used in electrical prospecting for groundwater and environmental characterization (e.g., *Gemil et al., 2004* and *Eleraki et al., 2010*). A symmetrical, collinear configuration of current A and B and potential electrodes M and N about a central point was employed. The maximum half electrode spacing $AB/2$ ranged from 200 m to 500 m. The selection of maximum $AB/2$ spacing was based on the depth of saltwater in the study area, which was observed from available boreholes, geological background and/or previous HEM results. The $AB/2$ spacings were 1.5,

2, 2.5, 3, 4, 5, 6, 8, 10, 12, 15, 20, 25, 30, 40, 50, 60, 75, 60, 75, 100, 125, 150, 175, 200, 250, 300, 400 and 500 m. When with increasing spacing between the current electrodes AB, the potential difference value ΔV between potential electrodes was unreadable; the current was increased at gradual steps; in addition the spacing between the potential electrodes MN was occasionally increased. The minimum and maximum MN/2 spacings were 0.5 m and 5 m, respectively. To overcome the non-uniqueness or equivalence problems (see subsection 3.1.3), 15 soundings were measured close to available boreholes in the survey area (Fig. 4.1).

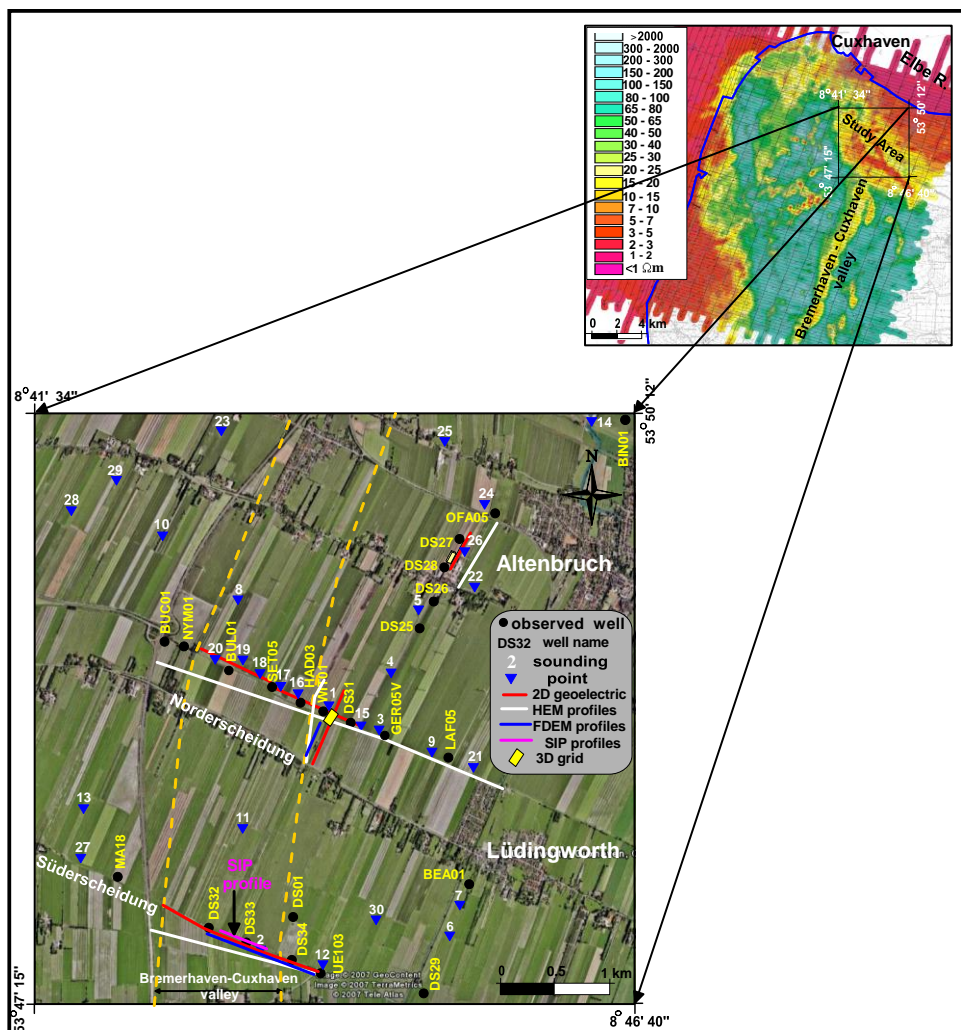


Fig. 4.1: (bottom) Location map of the study area showing the geophysical measurements (inset map © Google Earth) and (top) HEM apparent resistivity map, after Siemon et al., 2001a.



Fig. 4.2: RESECS multi-channel (8-channels) resistivitymeter for DC resistivity measurements.

The resistivity imaging was carried out using different electrode configurations. The choice of these configurations was based on their advantages and disadvantages (see section 3.3). In an attempt to confirm the interpretation process, for each selected location of resistivity imaging, more than one configuration was applied. At Altenbruch site (Fig. 4.1), the geoelectrical measurements were carried out during the summer season, which was characterized by frequent rain and a shallow groundwater level (~ 2 m depth). Based on the field observations and HEM results, the saltwater intrusion at this site is shallower than the central and southern part of the study area. Consequently, we aim to characterize the horizontal variations within the tidal deposits and also image the saltwater intrusion at this site. A 2D profile was measured using two types of configurations, WN and WB. In practice, WN is commonly used in 2D imaging for different environmental problems (e.g., *Kilner et al., 2005* and *Corriols et al., 2009*). Both WN and WB are characterized by a high signal to noise ratio. Because WB is a special case of DD, the detection of horizontal structures within the tidal deposits is expected. In addition, WN provides a good vertical resolution, which means that the depth of saltwater intrusion can be well detected. Based on these advantages, the WN and WB were applied at this site. The 2D profile length was 380 m long. The minimum electrode spacing was 2 m using 192 electrodes. The maximum electrode spacing, a , was 66 m and 48 m, respectively, for WN and WB, i.e., the maximum data level n was 33 and 24, respectively.

The 3D survey was carried out close to the borehole DS28 and the 2D profile (Fig. 4.1). Note that the study area is an agriculture land and we used the available and free location to carry out the 3D measurements. A 3D survey design using sets of 2D profiles was executed to characterize the tidal flat deposits and freshwater aquifer, in three dimensions. Because both WB and DD are good in resolving the horizontal changes (i.e., horizontal structures), the 3D survey was carried out using WB and DD configurations. The 3D survey was executed using a system of 288 electrodes, which were arranged in a 32×9 grid. A series of 9 ERT lines separated by 2 m spacing were constructed. Each line consisted of 32 electrodes with 2 m electrode spacing. The orthogonal 2D sets were measured in one direction (y), i.e., from ESE to WNW direction. For each 2D profile, the maximum current electrode

spacing for WB and DD was 20 m and 2 m, respectively. The number of data points for the 3D grid was 1385 and 3385, respectively, for WB and DD configurations.

At the central part of the study area (Lüdingworth, Norderscheidung) (Fig. 4.1, bottom), DC resistivity measurements in the form of a couple of 2D DC perpendicular profiles and a 3D grid were carried out. The 3D survey was executed at the intersect point between the 2D resistivity profiles. These measurements were carried out during a dry autumn season. The HEM apparent resistivity map presents an isolated shallow low resistivity layer over this site (Fig. 4.1, top). *Loke (2004)* stated that the SC configuration can provide a better horizontal and vertical resolution than an individual WN with good signal strength. Because WN showed some limitations in imaging the saltwater intrusion at Altenbruch site, it was replaced by a SC configuration at the central part of the study area. Consequently, for the 2D survey at this site, WB and SC configurations were applied to image the saltwater and quaternary aquifer.

The first profile runs from SSW to NNE direction (Fig. 4.1, line 1). The profile length was 715 m. It was measured along an agricultural area passing through well WIT01. At 480 m distance, the profile runs perpendicular to a narrow drainage lake. The maximum depth and width of the lake were ~ 4 m and ~ 2 m, respectively. The depth of the groundwater level and conductivity were ~1.5 m and 888 $\mu\text{S}/\text{cm}$, respectively. The 2D profile was executed using a system of 144 electrodes with an electrode spacing of 5 m. For WB, the maximum electrode spacing was 235 m ($n= 47$). For SC, we started with the “ a ” spacing (which is the distance between the P1-P2 potential dipole) 5 m and we repeated the measurements with “ n ” values of 1, 2, 3, 4, 5, 6, 7 and 8. Then, the “ a ” spacing was increased to 10 m, and measurements with “ n ” equal to 1, 2, 3, 4, 5, 6, 7 and 8 were carried out. This process was repeated until “ a ” equals 40 m. The number of data points produced by such a survey was more than twice that obtained with a normal WN survey. Thus the price of better horizontal data coverage and resolution is an increase in the field survey time (*Loke, 2004*).

The second 2D resistivity profile at Norderscheidung runs from WNW to ESE direction (Fig. 4.1, line2). It was parallel to the narrow drainage lake and 7 drilled boreholes. The DC measurements were carried out during the autumn season. Similar to the first 2D profile (line1), the survey was executed using a system of 144 electrodes with an electrode spacing of 5 m. The profile length was 1615 m. The roll along-method (see Fig. 3.7), in which a part of the original layout (16 electrodes, i.e., 75 m) is shifted in the desired direction, was used for the data collection along this profile. The same WB and SC parameters (“ a ” and “ n ”) as of the first profile (line 1) were used for this long profile (line2), but the maximum “ a ” distance was 45 m for SC. At this site, the conditions of measurements were more difficult due to high resistance contact and inhomogeneities of the surface cover. This place is a reclaimed road and consists of sand mixed with gravel, which is characterized by a relatively high resistivity value. To overcome the high contact resistance, we added saltwater, in a hole, around a poor contact electrode.

The 3D DC resistivity survey at Norderscheidung (Fig. 4.1, bottom) was executed using orthogonal sets of 2D DC resistivity profiles and a complete data set survey technique (see subsection 3.1.4.2). This location was chosen according to the results of the 2D DC resistivity inversion and the previous HEM measurements. The 3D DC resistivity survey was carried out to image the shallow (perched) saltwater in three dimensions. The field survey was carried out using a system of 128 electrodes, which were arranged in a 16 * 8 grid. The electrode and line spacings were 5 m. Similar to the 3D DC resistivity survey at Altenbruch, eight orthogonal 2D parallel profiles were measured in one direction (y) using WB configuration. The maximum current electrode spacing was 25 m. The number of data points was 280.

In general, the simple electrode configuration makes it easy to automate the data acquisition and to check data quality with measuring the reciprocity¹⁰ and stacking error in the field. DD and PP configurations were used to execute the potential measurements in three dimensions using the complete data set survey technique. They are widely used for 3D survey (Loke, 2004). For DD, the maximum spacing a between electrode pairs (potential and current pairs) was 15 m. For PP, the maximum spacing a between the current A and potential M electrodes was 75 m (see Fig. 3.15). The maximum current electrode spacing was 15 m and 75 m, respectively, for DD and PP. The number of measured potentials was 20809 and 16384 for DD and PP, respectively; about 8 hours were consumed for such survey. Both 3D DD and PP surveys exhibit a strong acquisition in the field to measure a good quality data with a low level of systematic errors. 3D DD DC resistivity survey required more acquisition effort with reciprocity measurements and is more sensitive to noise than 3D WB and PP survey. Despite of reciprocity measurements, the 3D DD data set represents a lot of noise and bad data points, e.g., 150 and 1652 points of zero and negative values, respectively.

Similar to the Altenbruch site, resistivity imaging (2D) was carried out using WN and WB configurations at the southern part of the study area, the Süderscheidung site (Fig. 4.1). It was observed that SC configuration, which was applied at the central part, requires a lot of time (~2 days) to acquire the data in the field. In addition, it is not recommended for a very long profile. Regarding to the borehole information, the saltwater intrusion depth at the Süderscheidung site is deeper than the northern and central parts of the study area. Consequently, the limitations of WN, which were observed at Altenbruch, were reduced at the Süderscheidung site. Based on these reasons, WN and WB were applied at the southern part. These measurements were executed during the autumn season. The 2D profile runs from WNW to ESE direction. It was measured along a narrow road between agriculture lands and it was bounded by two drainage lakes. The 2D profile was measured using a system of 192 electrodes with an electrode spacing of 5 m. The profile length was 1675 m. Similar to the 2D data acquisition at Norderscheidung, the roll along-method was applied to collect the 2D data. The

¹⁰ Reciprocity can be obtained by exchange of the positions of source and receiver and can be expressed in the form of $V(r_s, r_p)$ and $V(r_p, r_s)$, where r_s and r_p represent the position of the current source and potential electrode.

maximum current electrode spacing was 705 m and 235 m for WN and WB, respectively. The number of data points for WN and WB was 11823 and 11895, respectively.

4.2 FDEM SURVEY

The study area is characterized by many sources of noise, e.g., old pipes, metal buildings, tanks, metal, wind-wheels, etc., which may degrade the quality of EM data and reduce the reliability of any quantitative analysis. Consequently, we attempted to carry out the EM measurements away from these sources of noise. A metal detector instrument was used to detect suitable locations for FDEM measurements. At the central part, Norderscheidung, FDEM soundings (36 points) were measured to evaluate this method for imaging the saltwater-freshwater boundary by constructing a 2D cross-section. The EM measurements were carried out close to the short 2D profile (line 1) and the borehole WIT01. The sounding points were measured along a 360 m long profile from SSW to NNE direction (Fig. 4.1, bottom). They were measured using an APEX MaxMin I+10 EM system (Fig. 4.3). The measurements were executed during the rather dry autumn season. The FDEM survey was operated in vertical-dipole mode (horizontal co-planar coils) with a broad frequency range (10 frequencies, from 110 Hz to 56320 Hz). The transmitter-receiver separation was 100 m and the station interval was 10 m. These field parameters were tested over a buried conductor beneath quaternary sediments in north-eastern Ontario, Canada by *Palacky (1991)*. We failed to measure another FDEM profile parallel to a long DC resistivity profile (Fig. 4.1, line 2) at this site because there are power lines and metal pipes which are sources of noise.



ig. 4.3: MaxMinI+10 EM instrument for FDEM measurements.

Another suitable location for EM measurements was detected at the southern part, Süderscheidung (Fig. 4.1 bottom). The FDEM measurements were done to evaluate this method, by constructing a 2D cross-section, for characterizing the perched saltwater and the heterogeneity within the tidal flat deposits. The measurements were carried out during the spring season. Prior to the FDEM field measurements, a few soundings in the form of a short profile (EM test profile) were tested in order to obtain the optimal field parameters (coil separation and station intervals) which can be applied for this survey (Fig. 4.4). This test was carried out using 10 m, 20 m and 50 m coil spacings and 2 m, 4 m and 10 m station intervals, respectively. Moreover, the stray coupling effect¹¹ between the transmitter Tx and receiver Rx was also examined at the same location. It was carried out by reversing the receiver-transmitter position and then the measurements were repeated (MAXMIN I+10 EM system manual, APEX, 1998) using the optimized field parameters. Finally, a total of 115 FDEM soundings, 1135 m profile length, were measured using the optimal field parameters. To overcome the non-uniqueness or equivalence problems and to robust the inversion process, the sounding points were measured close to four boreholes (Fig. 4.1, bottom) and the 2D DC resistivity profile. The FDEM profile was located between 475 m and 1611 m distance, related to the 2D DC resistivity profile length. Similar to FDEM measurements at Norderscheidung site, the FDEM survey was operated in vertical-dipole mode (horizontal coplanar coils) with a broad frequency range (10 frequencies, from 110 Hz to 56320 Hz).

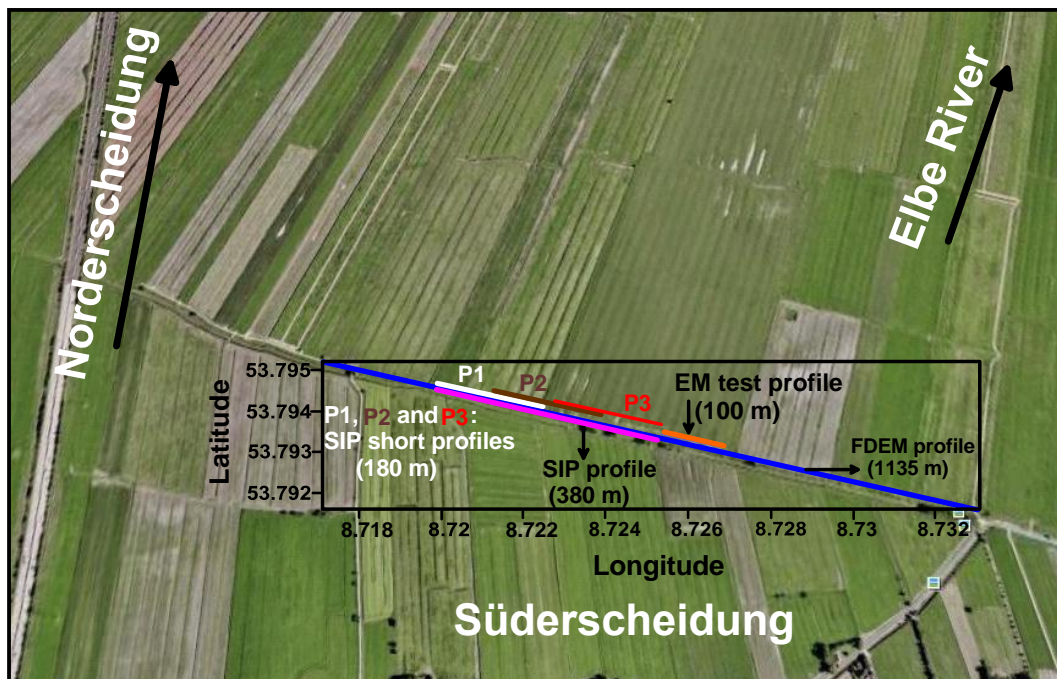


Fig. 4.4: Location map of EM and SIP measurements (inset map © Google Earth).

¹¹ The stray coupling effect is a change in reading as the electrical coupling changes between the coils and the ground. It leads to spurious readings at large coil spacings and high frequencies. They are at the worst under wet condition and high frequency (APEX, 1998).

4.3 SIP SURVEY

At Süderscheidung site (Fig. 4.1, bottom), a long spectral induced polarization (SIP) profile was executed using the DD configuration with 5 m electrode spacing. The multichannel equipment SIP256C, by Radic Research (*Radic et al., 1998; Radic, 2004*), was used for SIP data acquisition (Fig. 4.5). The SIP measurements were carried out during the summer season under a slightly wet condition. The SIP survey was carried out using 36 remote units and a wide frequency range from 0.625 Hz to 1 kHz (12 frequencies). The remote units registered the voltage and current signals. They digitized the data and transferred them to the controlling PC through a fiber optics cable to avoid interference of current supply cables with the voltage dipoles. Acquisition of very low frequency data is limited by the data acquisition time. It was observed that the measured data $|\rho_a|$ and φ_a at higher frequencies were acquired faster with higher systematic errors than the lower frequency data, which can be attributed to EM coupling effect. It was noted that above 125 Hz, a lot of negative measured data points and ambiguous apparent phase values (e.g., $\varphi_a > 500$ mrad) were recorded. The SIP 2D profile was 380 m long and it was located over the FDEM profile (between 675 m and 1025 m, related to the 2D DC resistivity profile length), and in vicinity of the borehole DS33 (Fig. 4.1). The data of the long 2D SIP profile was obtained in the form of a combined data set from the three overlapping profiles (P1, P2 and P3); each profile was 180 m long with an overlap of 80 m (Fig. 4.4). To value one profile, it needs several hours (~ 2 hours), even though the system efficiently measures voltages at all receiver channels simultaneously.

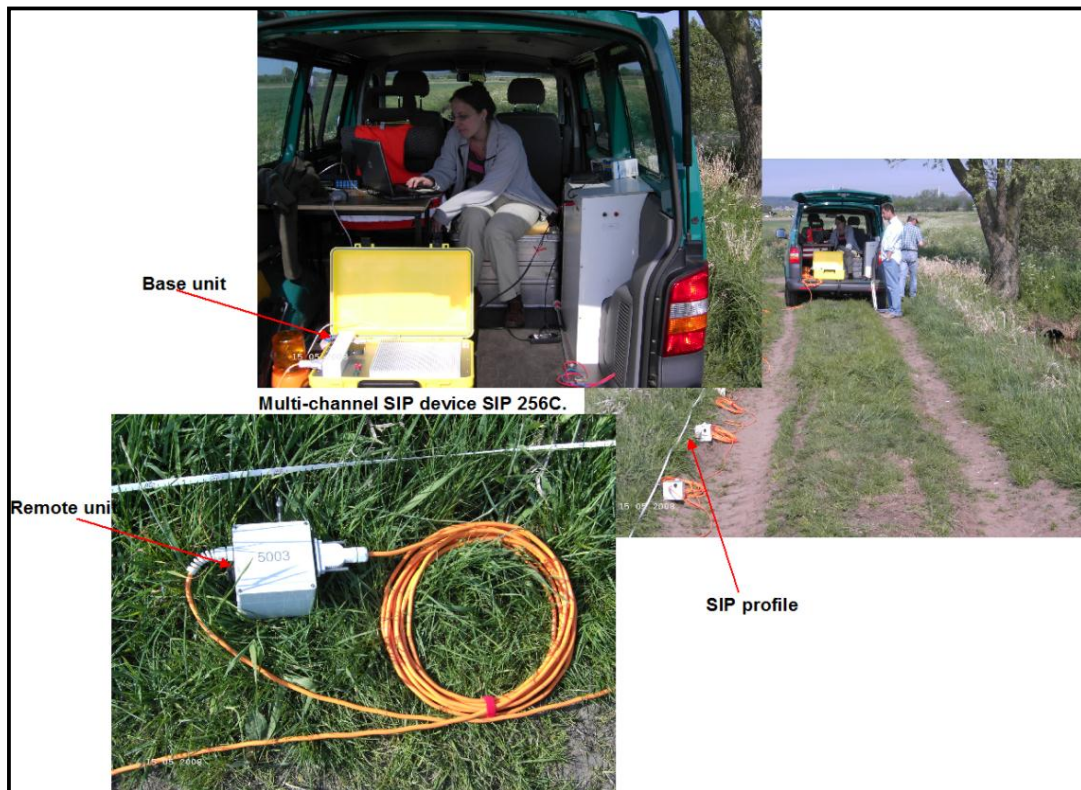


Fig. 4.5: SIP256C instrument for IP measurements.

4.4 DATA PROCESSING AND INVERSION

The processing and inversion procedures were done using five inversion programs (IPI2Win, IX1Dv3, DC2DInvRes, DC3DInvRes and BERT). The main purpose of the interpretation process is to recognize the subsurface electric stratigraphy in the form of successive geoelectrical layers having specific resistivities, depths and thicknesses. The goal and basics of FDEM, DC and SIP techniques (Fig.3.17) were denoted in chapter no. 3 (see section 3.5).

4.4.1 1D RESISTIVITY SOUNDINGS

1D DC Soundings

The 1D DC resistivity soundings were processed and inverted using IPI2Win (Bobachev, 2002 and Bobachev et al., 2003). In general, the processing of soundings includes rejecting bad-data-points, which show abrupt resistivity changes over surrounding points ($> 45^\circ$). In the present work, the sounding curves show two types of distortions. The first one is represented in the form cusps on Schlumberger sounding curves. Zohdy (1968 and 1989) concluded that the formation of a cusp generally is caused by a lateral heterogeneity, by current leakage from poorly insulated cables, by electrode spacing errors, or by errors in calculation. This distortion can be avoided partly by a weighting average smoothing technique during the 1D forward modeling. The second type is a segmentation of curves the observed sounding curves when the spacing \overline{MN} is enlarged while \overline{AB} remains constant (see subsection 3.1.3). This distortion can be corrected easily by shifting the distorted segment of the curve vertically to where it should be. The segmented curves are desegmented automatically by parallel shifting all the segments to the level of the rightmost segment. Away from the first and last segments which are normally affected by noise sources, the best smoothed segment will be moved down and up to fit other segments of the measured DC sounding points.

Several computer programs are available for the forward and inversion process allowing data processing such as shifting of overlapping segments to produce continuous sounding curves. IPI2Win program is based on a linear filtering as 1D forward modeling and a Newton algorithm of the least number of layers to solve the inverse problem (see subsection 3.5.2.1). It works in an iterative mode and at the end of each step the model parameters (layer thickness and resistivity) and the misfit function between observed and calculated data will be shown. The starting model was derived from the observed boreholes in the study area. The borehole information regularizes the process of minimizing the fitting error. Note that the error indicates the degree of misfit between the observed and calculated curves. The inverse problem is solved separately for each sounding curve. The results show that an acceptable fit can be obtained considering six and four-layer models for the measured soundings with 9 % maximum errors. The results of the 1D modeling are illustrated in columns with the same scale, geoelectric horizons, and are correlated with the obtained data from boreholes as exemplified in Fig. 4.6. The bad misfit between the apparent resistivity field data and the calculated model data was observed near to the very low resistivity layer (i.e., saltwater). This can be attributed to the divergence

of electrical current within the low resistivity layer, which decreases the potential gradient and produces distortions of the current flow at a plane interface. The inversion results of sounding points were used to construct resistivity maps and cross-sections. The sounding inversion results are shown in Appendix C.

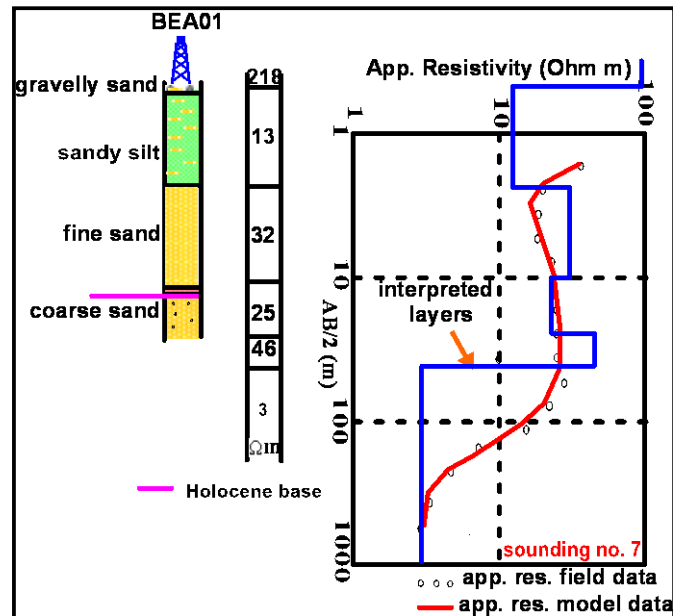


Fig. 4.6: Correlation between the interpreted resistivity layers and the observed borehole data at sounding no. 7.

1D FDEM Soundings

The 1D FDEM resistivity soundings were processed and inverted using the IX1Dv3 (2006) program. The measured inphase and quadrature raw data were inverted to obtain the true resistivities and thicknesses of the subsurface layers. The forward modeling is run using linear filters in a manner similar to that described by *Davis et al. (1980)* and *Anderson (1989)*. To overcome the equivalence problem, the initial model was derived from a-priori information. The number of layers of the initial model was derived from the nearest borehole data or inversion results of DC resistivity soundings. Then the layer parameters, resistivity and thickness, were changed to best fit the measured data points and the input model, in a manner similar to the 1D DC resistivity sounding interpretation. The inversion is carried out using the Ridge regression in a manner similar to that described by *Inman (1975)*, which is more adequate to incorporate a-priori information. In the IX1Dv3 program, a part of the smooth model estimation uses single or multiple iterations (*INTERPEX, 2006*). For each iteration, a model correction is calculated using the best damping factor for that iteration (see subsection 3.5.3). The iterative process estimates depths and resistivity values for each EM sounding from the initial model in a least-squares sense (*Inman, 1975*). The data are expressed in percent of the primary field and this unit is used also for the RMS error (Eq. 3.38).

Fig. 4.7 shows an example of FDEM sounding data and the inversion results in correlation with the borehole DS33. The number of layers of the initial model was derived from the number of

layers of DS33. In this example, the input layer parameters were changed (Fig. 4.7, middle) until the best between the computed model and the measured data was achieved (Fig. 4.7, left). In general, the RMS error percentages, i.e., fitting errors, of DC resistivity soundings are better than that of the FDEM soundings. This can be attributed to two reasons. First, the FDEM method is more sensitive to surface noise sources than the DC resistivity method (see Section 4.2), which affects the data quality. Second, in the FDEM method the number of measured components, which have to be fitted to the computed models, is higher than for DC resistivity soundings. Moreover, the response of the FDEM components from conductive layers at different frequencies is different. For low values of the response parameter¹² (<1), the low quadrature component anomaly will be produced; at moderate values of the response parameter (10-100), the response will be a moderate-amplitude inphase and quadrature anomaly, whereas for high values of the response parameter ($>1,000$), the response will usually be in the inphase component (Klein and Lajoie, 1980). The 1D inversion results of FDEM soundings were stitched to construct resistivity cross-sections using the IX1Dv3 program (INTERPEX, 2006).

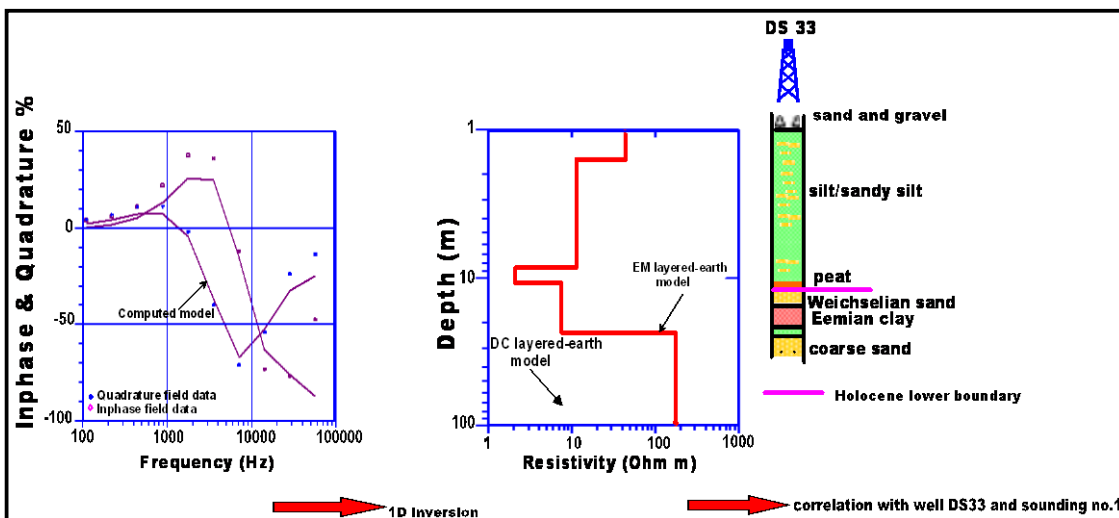


Fig. 4.7: An example of FDEM sounding data (inphase and quadrature) for different frequencies (left) and 1D inverse model (middle) results in correlation with borehole no. DS33.

The EM test profile (Fig. 4.4), between 1060 m and 1160 m distance, was related to the 2D DC profile (Fig. 4.1). Fig. 4.8 represents the inversion results in the form of three stitched resistivity sections of 10 m, 20 m and 50 m coil spacings and 2 m, 4 m and 10 m station intervals, respectively. The resistivity sections of 10 m and 20 m coil spacings show two main layers: A high resistivity surface layer and a medium resistivity layer with a thin embedded, high conductivity layer. The total thickness of the medium resistivity layer cannot be detected from these two sections. It was observed that the best coil spacing and station interval was 50 m and 10 m, respectively (Fig. 4.8, bottom). The

¹² The response parameter of a conductor is defined as the product of conductivity-thickness (σh), permeability (μ), angular frequency (ω) and the square of the mean dimension of the target (a^2).

maximum thickness of the medium resistivity layer resting on a high resistivity layer can be well identified using these parameters. The maximum penetration depth was about 40 m.

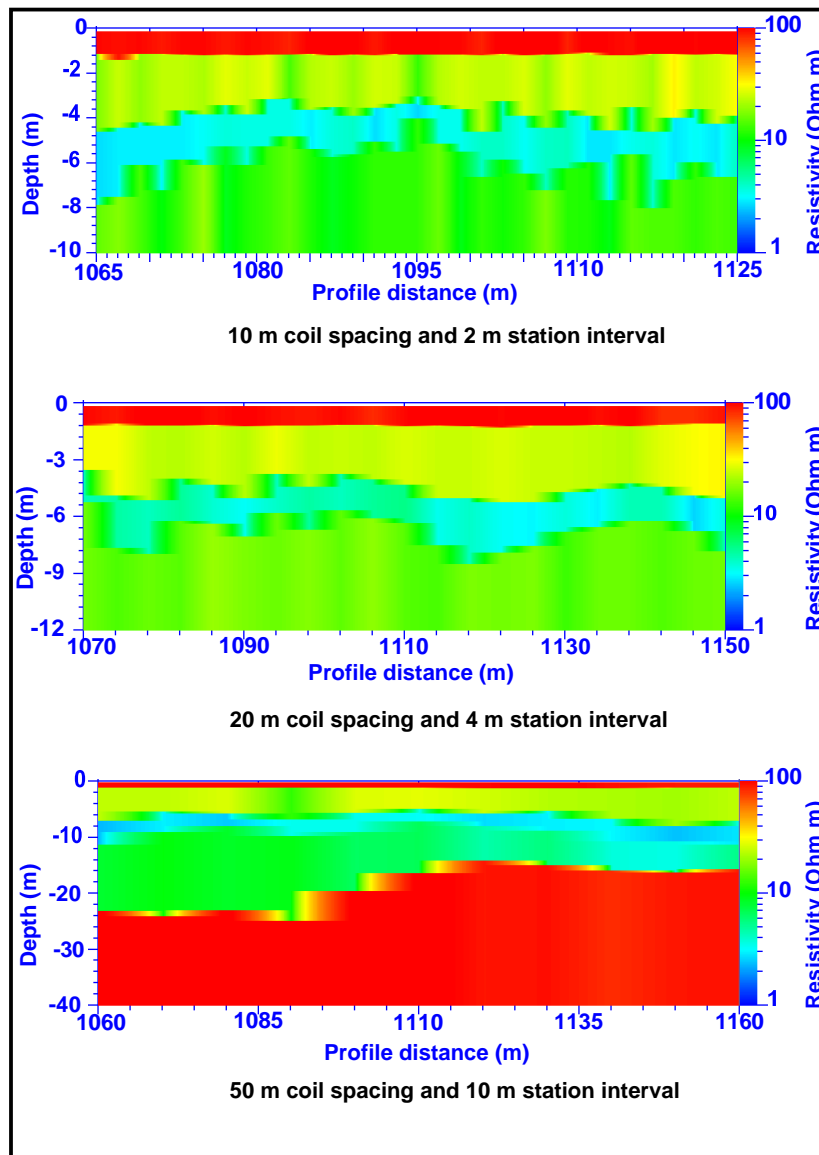


Fig. 4.8: Stitched resistivity sections from 1D FDEM inversion at different coil spacings and station intervals for the short test profile (see Fig.4.4). The profile distance is related to the 2D profile length (Fig. 4.1).

Because of using small coil spacings at this site, the stray coupling effect was studied using 50 m coil spacings, 2 m station intervals and 10 frequencies (see section 4.2). Good repeated results were observed with just few differences in readings at the three higher frequencies (14080 Hz to 56320 Hz). This indicates that unacceptable/inaccurate readings as a result of coupling effects can be expected. An example of repeated inphase measurements is shown in Fig. 4.9.

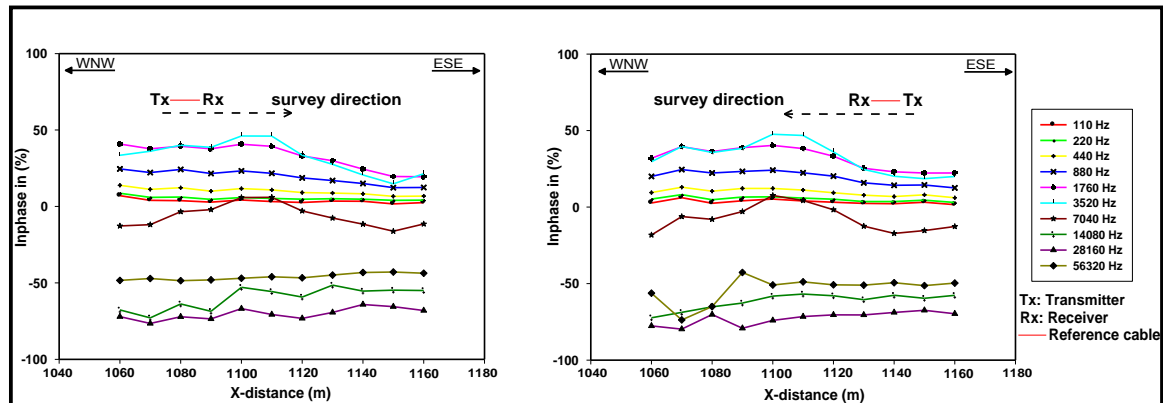


Fig. 4.9: Inphase component for different frequencies to demonstrate the stray coupling effects by repeating measurements with reversing coil orientation (Tx and Rx).

4.4.2 DC AND SIP TOMOGRAPHY

The 2D and 3D DC and SIP data were processed and inverted using the DC2DInvRes/DC3DInvRes (Günther, 2004) and BERT (Günther et al., 2006 and Rücker et al., 2006) resistivity inversion programs. They are based on numerical modeling techniques using finite-difference, FD, (e.g., Dey and Morrison, 1979a) and finite-element, FE, (e.g., Sasaki, 1994 and Rücker et al., 2006) methods, respectively (see subsection 3.4.2).

The DC apparent resistivity data are plotted in the form of resistivity pseudo sections. In theory combined inversion of data sets, coming from surveys with different electrode configurations obtained over the same site, would allow us to combine the relative advantages of every configuration and thus to produce superior results (Athanasiou et al., 2007). Consequently, combined data sets of different configurations were applied during the inversion process in our study. The aim of combined configuration technique was to assess the reliability of this techniques to map the saltwater and shallow sedimentary structures. The selection of the configurations depended on our targets and the geological situations.

In our study, we combined 2D WN and WB data sets at the northern (Altenbruch) and southern parts (Süderscheidung). On the other hand, 2D WB and SC data sets were combined at the central part (Norderscheidung). Fig. 4.10 shows an example of the 2D DC apparent resistivity section, for combined WN and WB configurations, in addition to the forward calculated model and misfit error percentages. The inversion results will be shown in the next chapter (see subsection 5.2.1).

The 3D data set was plotted in the form of 2D apparent resistivity sections (in x-and y-directions). Figs. 4.11 and 4.12, respectively, show the detailed pseudosections of the recorded 3D data sets using spares of WB 2D parallel profiles and complete data set technique of PP. The 2D data along a series of parallel 2D survey lines (in y-direction) were combined in a data file with the respective field locations (x and y distances) in an attempt to gleam new information out of 2D data

sets. DC3DInvRes reads this data set in the form of 3D grid and consequently the data can be inverted and interpreted three-dimensionally.

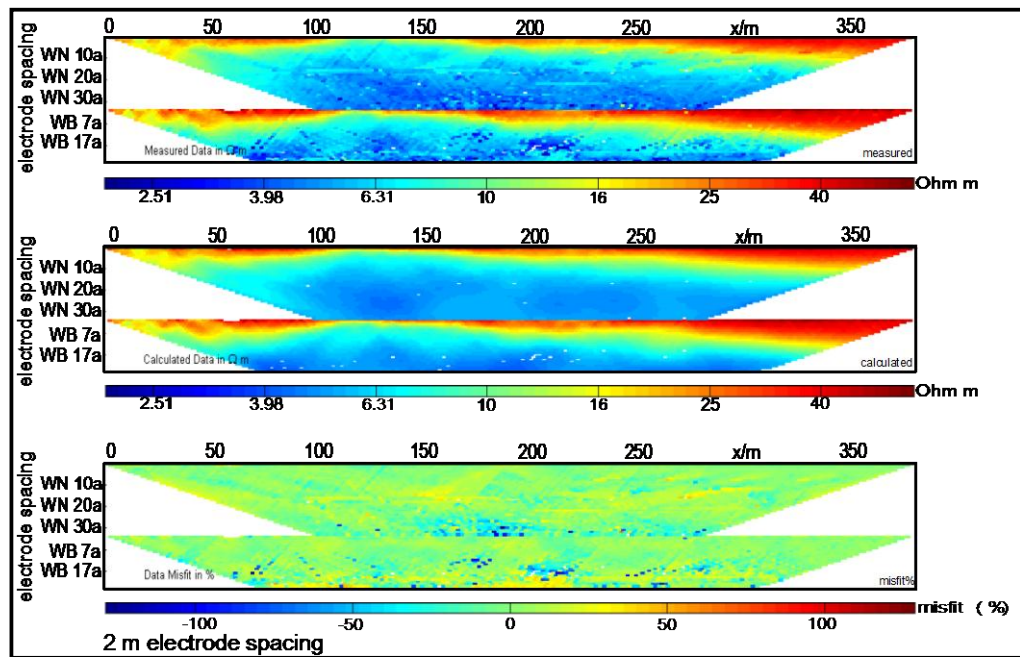


Fig. 4.10: Pseudosections of the measured apparent resistivity (top panel), calculated resistivity (middle panel) and relative difference between measured and calculated apparent resistivity (bottom panel) of combined 2D DC WN and WB profiles.

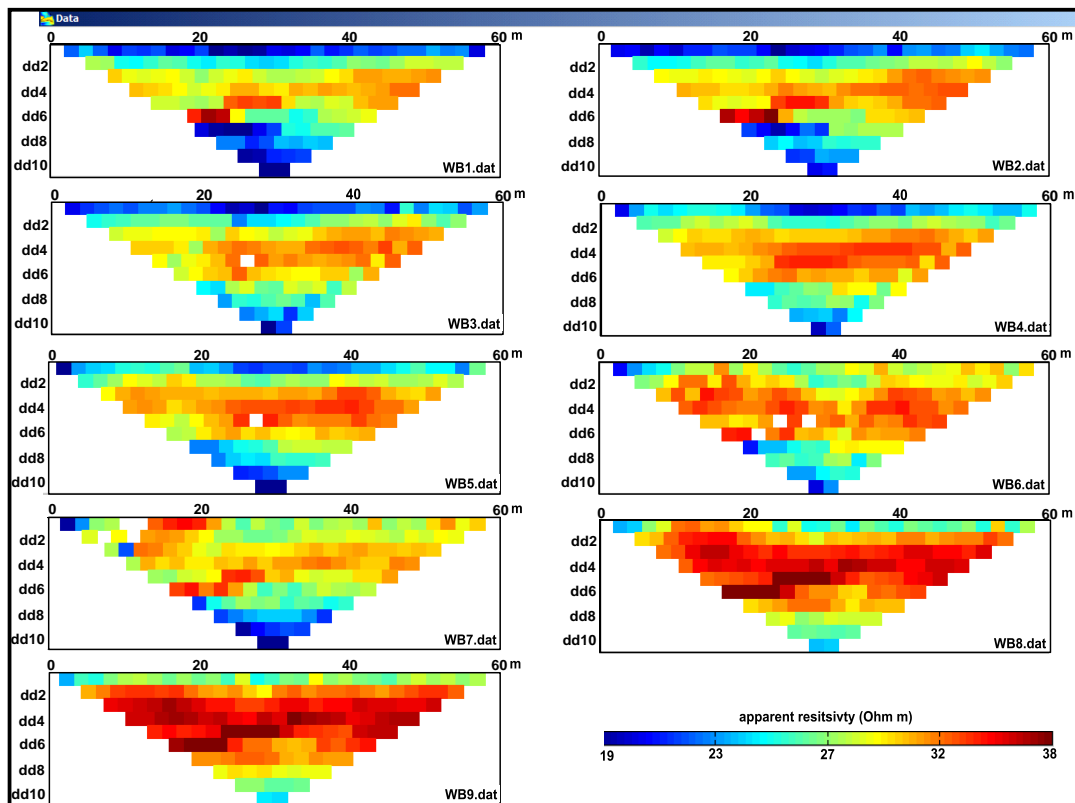


Fig. 4.11: 3D data set, derived from orthogonal 2D WB profiles, in form of 2D pseudo-sections at Altenbruch site.

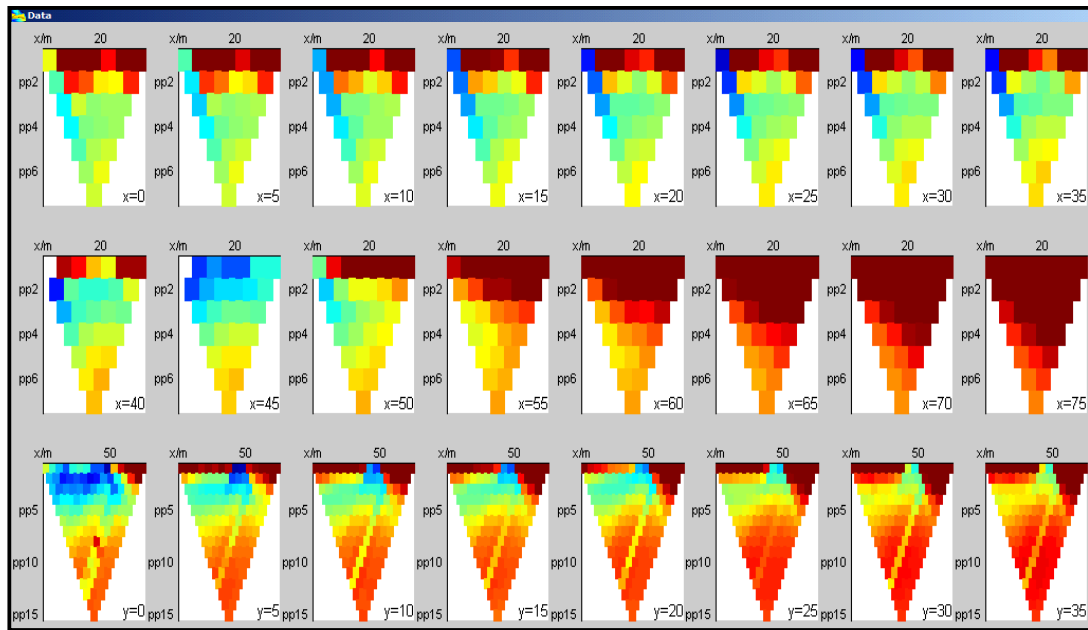


Fig. 4.12: 3D PP data set, derived from complete data set technique, in form of 2D pseudo-sections at Norderscheidung site.

For the SIP data, inspection of the $|\rho_a|$ and the φ_a spectra is required to select the best frequencies for the 2D inversion process. To detect the EM coupling effect, the measured data were plotted vs. frequencies at different dipole lengths. Fig. 4.13 shows a sample of an SIP measured data set, displayed as $|\rho_a|$ (top) and φ_a (bottom) vs. frequencies using 5 m dipole length with different dipole distances. The $|\rho_a|$ behavior shows relatively constant values with increasing frequencies up to 125 Hz. The φ_a values are almost constant over a limited range of frequencies up to 10 Hz and show inductive or capacitive coupling at higher frequencies (> 20 Hz), which is caused by the electromagnetic effect. In general, the coupling effect can also be noticed at lower frequencies (< 20 Hz) but it is not high as compared to the data above 20 Hz. Attempts have been made to remove the inductive and capacitive coupling from the data (e.g., *Xiang et al., 2002* and *Radic, 2004*), but here we used data in the range below 20 Hz where the data were not significantly affected. Similarly to the 2D DC resistivity profile, the SIP parameters $|\rho_a|$ and φ_a were plotted in the form of pseudo-resistivity and-phase sections. The inversion results of particular frequencies (up to 20 Hz) for the large-scale SIP profile will be discussed in detail in the next chapter.

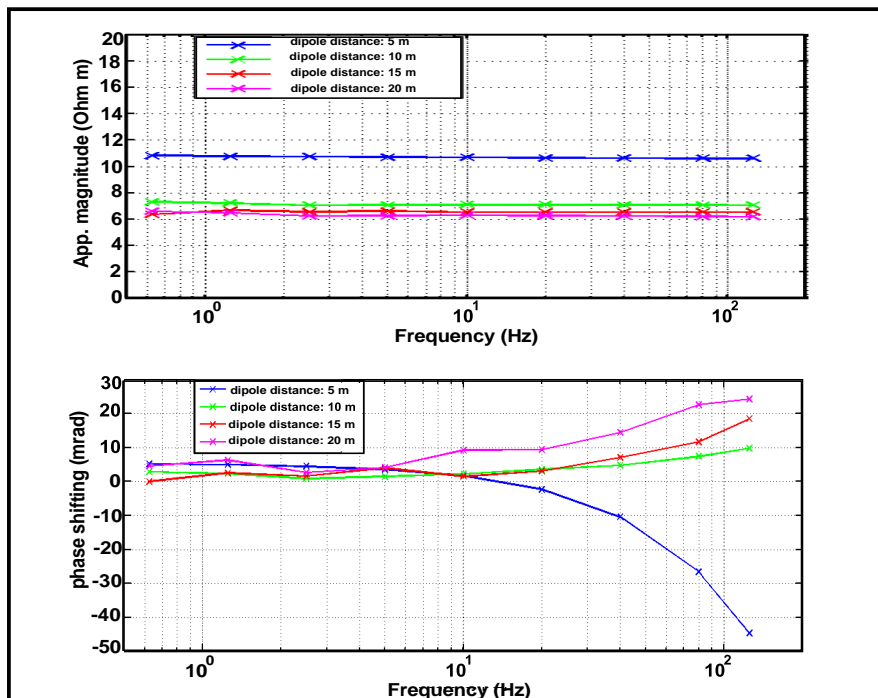


Fig. 4.13: A complex apparent resistivity data set of dipole-dipole configuration, 5 m in length, with different dipole distances from Süderscheidung site. Top panel: apparent resistivity magnitude vs. frequency. Bottom panel: Phase spectra vs. frequency.

The 2D and 3D processing included the filtering process to the measured data by rejecting bad quality data-points, i.e., for which the stacking error was more than 1 % and/or the anomalous measured apparent resistivity reading, e.g., zero values, than surrounding data. *LaBrecque et al.* (1996) found that the stacking errors may be poor estimates of the noise because they don't include systematic errors, e.g., from poor electrode coupling and used reciprocal measurements to quantify noise. Consequently, the reciprocal measurements from the 3D survey were used to check the data quality. The data with very big misfits between forward and reverse measurements (i.e., reciprocity) were deleted prior to the inversion process. Fig. 4.14 shows an example of the processed 3D DD data set. The number of rejected data was 2793, which includes zero, negative and data points of greater than $60 \Omega\text{m}$. In addition, the data of big reciprocity misfits and the data with geometric factor G greater than 10^4 and less than $-8 \cdot 10^4$ was deleted. This large number of noise data reflects the fact that DD bears a risk of noise contamination which can be attributed to the lower signal-to-noise ratios of DD than other configurations (*Dahlin and Zhou, 2004*). The number of rejected data from the measured PP data set was only 12. PP configuration shows better reciprocity data and smaller stacking errors than DD.

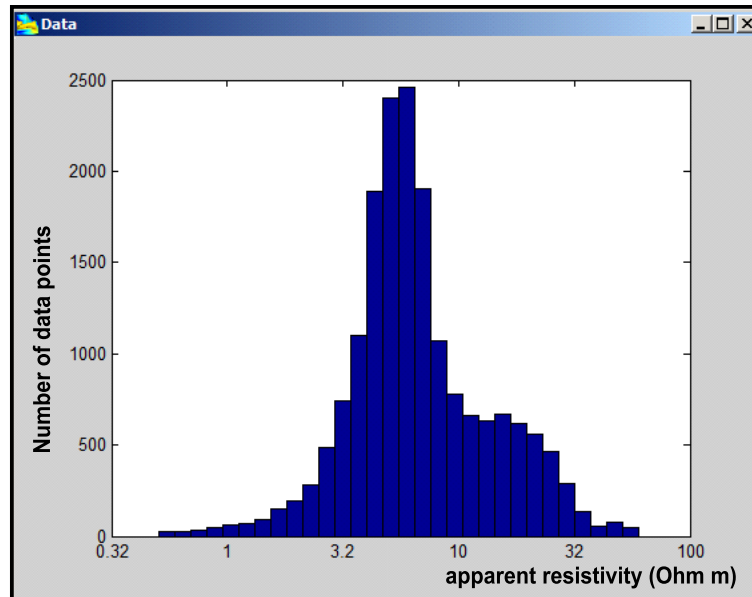


Fig. 4.14: Histogram of apparent resistivity 3D DD data set after rejecting the bad data points.

The rejected data were about 1% and 3% of the measured DC and SIP resistivity data, respectively. For 2D DC resistivity data, the reciprocal data were not measured and consequently a 3% estimated error was added to the staking error. For 3D DD and PP data sets, reciprocity data were measured to assess the measured data accuracy and 3% estimated error was also added during the inversion process as a result of systematic errors. Fig. 4.15 represents an example of the reciprocity crossplot between normal and reverse 3D PP data set after deleting the bad data points. It is observed that the misfits between the normal and reverse data are not very big and, consequently, we used these data in the inversion process.

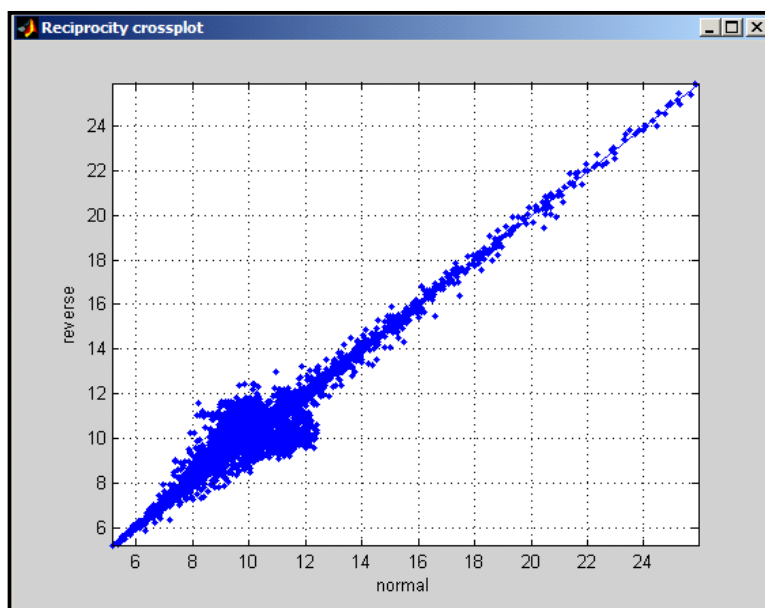


Fig. 4.15: Reciprocity crossplot of normal and reverse 3D PP data set.

Because of the EM coupling effect, the 2D SIP data required more processing than the 2D DC resistivity data. Above 125 Hz, more than 70% of the measured data were rejected and, consequently, have not been used in the inversion process. The measured complex apparent resistivity data up to 20 Hz showed a general increase of systematic errors with increasing frequencies. In addition, a gradual decrease of apparent $|\rho|$ values and a strong increase of φ values were observed above 125 Hz. The maximum $|\rho|$ and φ values at 0.625 Hz are 25 Ωm and 10 mrad and 15 Ωm and 30 mrad at 20 Hz, respectively. Fig. 4.16 shows an example of a processed complex resistivity data set (2947 points) in the form of apparent sections and histograms; note that the measured data were derived from the three overlapping profiles at 1.25 Hz. In this data set, it was observed that for larger dipole distances ($n > 8$) the measured phase values were higher than the surrounding points, which can be attributed to the EM coupling. These noisy data points (139) were rejected during the data processing. It is clear that the pseudosections do not exhibit a clear layering but show variations in $|\rho|$ and φ values. In general, the inversion process is able to simulate the measured data. In addition, because of using an asymmetrical dipole configuration, i.e., unequal dipole length, the values of dipole length a can not be written on the z-axis of either $|\rho|$ and φ pseudo sections (Fig. 4.16, top and bottom, respectively).

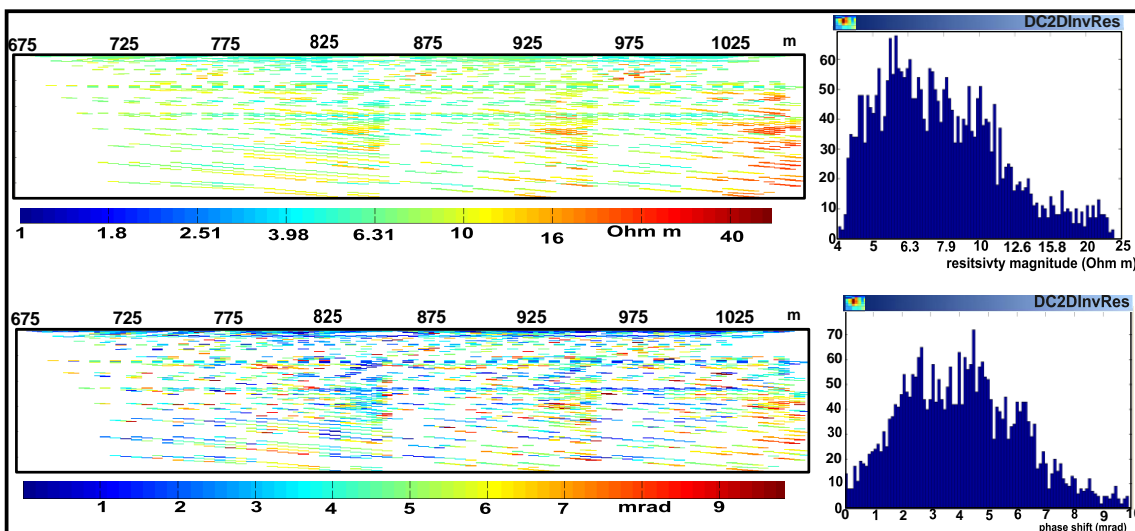


Fig. 4.16: Top: (left) measured apparent resistivity section and (right) histogram at 1.25 Hz. Bottom: (left) phase pseudosection and (right) histogram at 1.25 Hz.

DC2DInvRes/DC3DInvRes programs (Günther, 2004) aim to obtain the apparent resistivity values of rectangular blocks and to minimize the difference between the calculated and measured values during the inversion process. In recent years, more and more FE approaches appeared (e.g., Rücker et al., 2006). The BERT program aims to obtain the apparent resistivity values by the use of triangles (2D) and tetrahedrons (3D). It presents also a triple-grid inversion technique that is based on unstructured tetrahedral meshes and FE forward calculation. The theory and technology of BERT is described in Günther et al. (2006) and the basics of the finite element modeling technique are given in

Rücker *et al.* (2006). The inverted models show that with the same maximum electrode separation in profiling surveys, all electrode configurations give similar penetration depths.

For preparing a synthetic modeling, a finite difference scheme was used with the forward calculation. The synthetic model, forward calculation, model response, resistivity pseudosection and 2D quasi-Newton inversion were carried out using the DC2DInvRes program. In order to test the sensitivity of the interpretation routines, Gaussian-distributed random noise was added to the calculated responses for the synthetic models. In general, noise with 3% standard deviation was added. The number of layers for each synthetic model was 11. The resistivity of these meshes is adjusted in an iterative manner to reduce the difference between the measured pseudo section and the calculated model.

The used DC2DInvRes/DC3DInvRes and BERT programs for 2D and 3D inversion procedures are based on both the quasi-Newton robust model constraining L1 and the quasi-Newton smoothness constraining the least-squares L2 algorithms (see subsection 3.4.2). The L2 method is preferable for most data sets (Loke, 2001) and hence it was used for all data presented in this thesis. The 2D/3D inversion algorithm was implemented for a global regularization scheme using a first-order smoothness constraint (Günther, 2004). The regularization parameter λ , which is also referred to as damping factor, is a weight to the model smoothness constraints against the data misfit. It is a trade-off between data fit and model roughness and has, therefore, to be chosen appropriately. Rough-textured models with a good data fit can be obtained by using small values of λ ; whereas large values correspond to smooth models with weak data fit (Tikhonov and Arsenin, 1977). In the FD programs (DC2DInvRes and DC3DInvRes) the vertical constraint is a weight for the smoothness in vertical direction (z-axis direction) and it is known as w_z , which is equal to 1 for isotropic medium. A small value of λ (or w_z) will produce a highly structured model with huge parameter contrasts, explaining data well, whereas a big value will not be able to fit the data but provide a smooth model. In the FE program (BERT), the vertical constraint is known as *z-power*, which is equal to zero for an isotropic medium. To enhance the layer (sediments) structures, the *z-power* value should be increased (0.1 to 0.5). Consequently, the values of the regularization parameter depend on our expectation to the geological situation in the study area; i.e., more detailed structures need low values of regularization parameters and *vice versa*. In order to determine the optimal λ and w_z and/or *z-power* values, the data misfit functional and model smoothness functional for a wide-ranging λ and w_z and/or *z-power* are plotted, which is called the L-curve (Hansen and O'Leary, 1993). The data misfit is obtained by monitoring the RMS error as

$$RMS = \sqrt{\frac{1}{N} \sum_{i=1}^N \left(\frac{d_i - f_i}{d_i} \right)^2}$$

where d_i and f_i , respectively, are the measured and the calculated apparent resistivity or phase values for i^{th} data point and N is the total number of data points.

The models obtained from the 3D inversion are controlled by available geological and hydrogeological data and 1D soundings. The inversion model is visualized three-dimensionally in the form of slices (e.g., Fig. 4.17). Generally, the maximum depth for the obtained model was controlled according to the sensitivity analysis for each configuration.

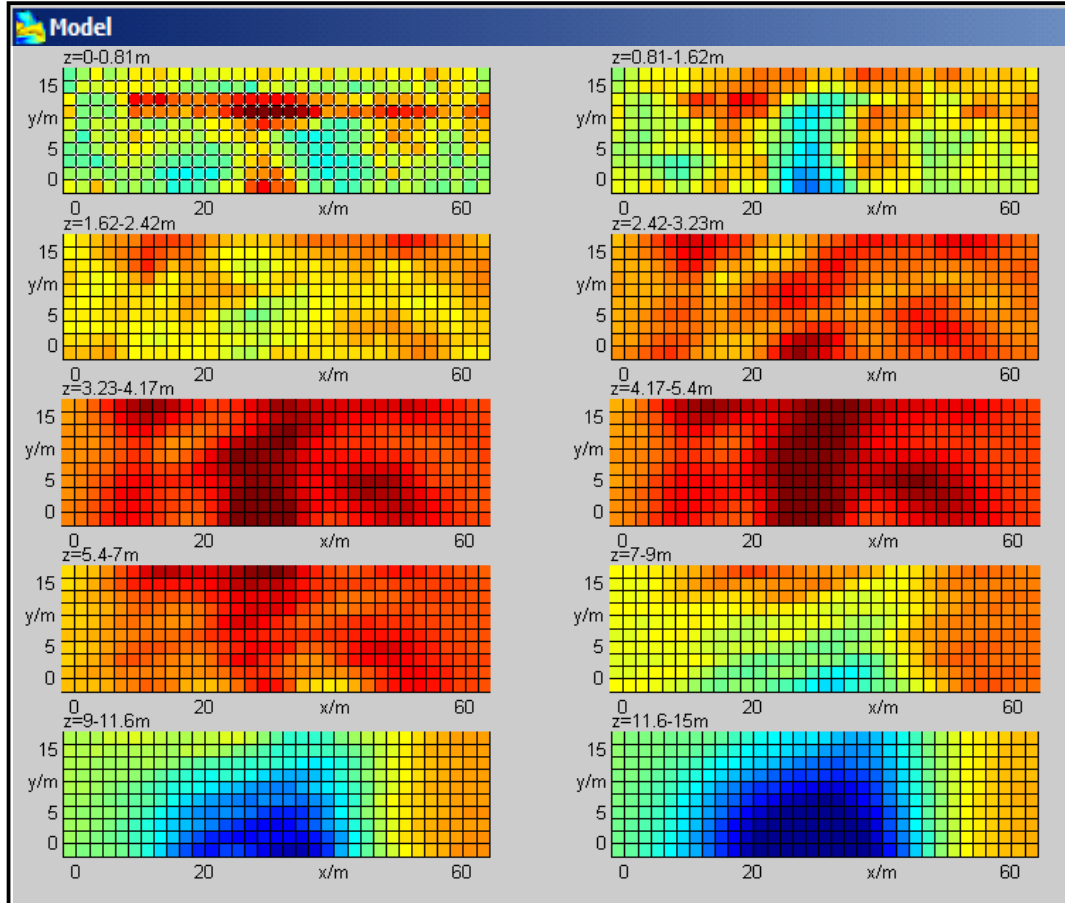


Fig. 4.17: Horizontal slices of the model obtained from the 3D inversion of orthogonal sets of nine 2D WB profiles at Altenbruch site.

4.5 HYDROGEOPHYSICAL STUDY

Theoretical Development

The correlation of hydraulic conductivity k_f with electrical resistivity is often directly proportional on a regional scale (higher resistivity corresponds to higher hydraulic conductivity), but sometimes on a local scale the correlation is inversely proportional (Mazac *et al.*, 1990). In Mazac *et al.* (1990), the influence of groundwater salinity and clay content on soil resistivity is not taken into account. Such effects of salinity and clay content can distort the correlation between soil resistivity and hydraulic conductivity (Shevvin *et al.*, 2006). Our intention here is to assess an empirical relationship between the aquifer resistivity ρ and K/k_f using DC soundings. We have only four known k_f values in the study area and consequently other published data was used to assess this relation.

In general, the electrical path is similar to the hydraulic path at the pore level and resistivity values must reflect this. Darcy's and Ohm's laws (see Appendix A) show that the water and current flow depend on the presence of a gradient between two points. Consequently, for isotropic homogeneous medium the divergence of specific discharges and current density becomes zero, where there is no hydraulic and potential gradient $\Delta h/L$ and $\Delta V/L$, respectively, between two points in the conductive medium. According to the fundamentals and the analogy of Darcy's and Ohm's laws, they can be combined together in one equation, as also suggested by *Niwas and Singhal (1981)* and *Chandra et al. (2008)*, as

$$k_f = (q/\Delta h)(\Delta V/J) \sigma \quad (4.1)$$

where $q/\Delta h$ and $\Delta V/J$ are ratios.

Eq. (4.1) was used by *Niwas and Singhal (1981)* and *Chandra et al. (2008)* to derive a linear relationship between transmissivity and the aquifer resistivity (see subsection 3.6.2). They assumed that the two ratios $q/\Delta h$ and $\Delta V/J$ are constant over a survey area.

Based on above discussions and observations, a direct relation between ρ and k_f can be deduced. Then, this relation was tested using different data sets and we observed a log-log relationship between the aquifer ρ and the k_f values (will be shown below). In presence of a good correlation coefficient between the observed $\log-k_f$ and the measured $\log-\rho$, this relation can be written as

$$k_f = A\rho^B \quad \text{and} \quad K = A\rho^B h \quad (4.2)$$

where, h is the aquifer thickness and the constants A and B are adjustable parameters that can be calculated using a least-squares fit between the $\log-\rho$ and estimated $\log-k_f$ values. To study the correlations among k_f and ρ , we looked for the value of free parameters that minimized the mean-squared logarithmic error of fit,

$$\varepsilon^2 = 1/N \sum_{i=1}^N [\ln(k_f)_o - \ln(k_f)_e]^2, \quad \delta = e^\varepsilon \quad (4.3)$$

where N is the number of data points, $(k_f)_o$ and $(k_f)_e$ are the observed and estimated hydraulic conductivity values, respectively, and δ is the error factor. The constants A and B in Eq. (4.2) are chosen to minimize ε^2 .

The Methodology Testing

Published data have been utilized to assess the methodology discussed above.

1- Poor to moderate weathered sandstone of the Jayant aquifer, India (*Yadav, 1995*)

Fig. (4.18a) shows that the product $k_f S$ remains nearly constant throughout the area. According to this condition, Eq. (3.57) was applied using $k_f S = 18.14$ (see subsection 3.6.2). Fig. (4.18b) shows a least squares regression between the aquifer resistivity and hydraulic conductivity. This positive relationship has a goodness fit with correlation coefficient 0.86. Consequently, Eq. (4.2) can be applied and adjustable parameters A and B can be calculated. Table (4.1) shows a comparison

between estimated k_f values using Eqs. (3.59) and (4.2) with those obtained from pumping tests. A strong correlation between the estimated and observed k_f was achieved.

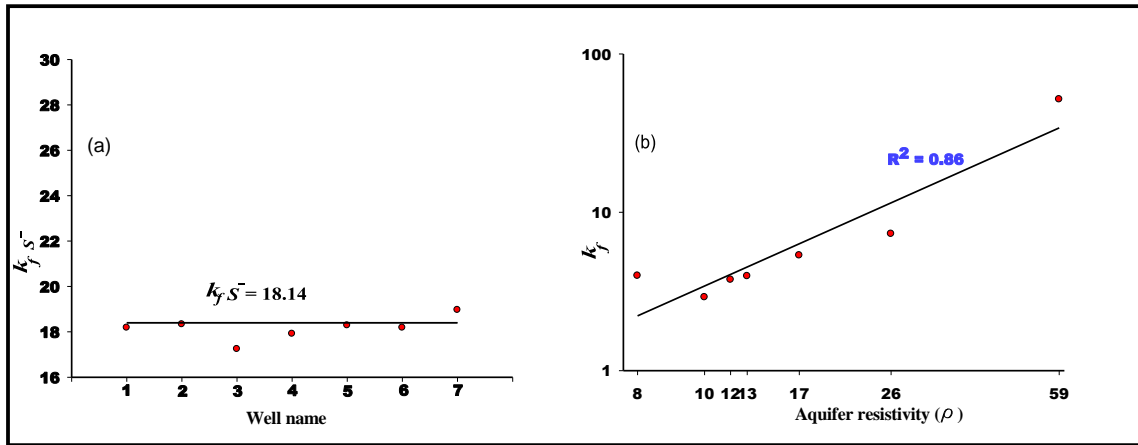


Fig.4.18: $k_f S^-$ for various wells and (b) relationship between aquifer resistivity and k_f .

Sounding no. & well no.	Aquifer thickness (h) m	Aquifer resistivity (ρ) Ωm	Normalized aquifer resistivity (ρ') Ωm	k_f -values (pumping test) m/day	$k_f S^-$	$k_f = ((k_f S^-) \rho') / h$ m/day	$k_f = A \rho^B$ m/day
1	41	7.5	8.95	3.97	18.18	3.96	1.8
2	62.7	11.8	12.85	3.7	18.33	3.7	3.6
3	77.7	12.8	17.8	3.9	17.24	4.2	4.1
4	53.9	10.4	8.76	2.9	17.91	2.9	2.9
5	44	16.5	12.85	5.3	18.28	5.3	5.9
6	48	25.8	19.27	7.3	18.18	7.3	11.9
7	30	58.5	81.72	51.7	18.96	49.4	42.1
where $k_f S^- = 18.14$, $A = 0.08$ and $B = 1.54$						$\delta = 1$	$\delta = 1.2$

Table (4.1): Aquifer parameters of DC soundings (Yadav, 1995) and estimated k_f using Eqs. (3.59) and (4.2) in correlation with known values from pumping test.

2- Sand mixed with gravel aquifer at south-eastern Nigeria, zone A (Ekwe et al., 2006)

Ekwe et al. (2006) applied Eq. (3.57) to calculate the k_f for a gravelly sand aquifer. Fig. (4.19a) shows a plot of $k_f \sigma$ for four well locations. The deviation of the $k_f \sigma$ at each well from the mean value (0.0076) is not serious, which reflects that this region has rather homogeneous hydrogeological condition and a similar water quality (Niwas and Singhal 1981). In addition, Fig. (4.19b) shows a positive linear relationship between the aquifer resistivities and the observed k_f values (derived from pumping tests). A strong correlation ($R^2 = 0.86$) was achieved, which was encouraging to apply Eq. (4.3). The adjustable parameters A and B in Eq. (4.2) can be calculated by fitting the k_f and ρ of the aquifer using the least squares method. Accordingly, the coefficients A and B are 1.4 and 0.0004, respectively. Table (4.2) shows the aquifer parameters of sounding measurements and k_f estimation using Eqs. (3.57) and (4.2).

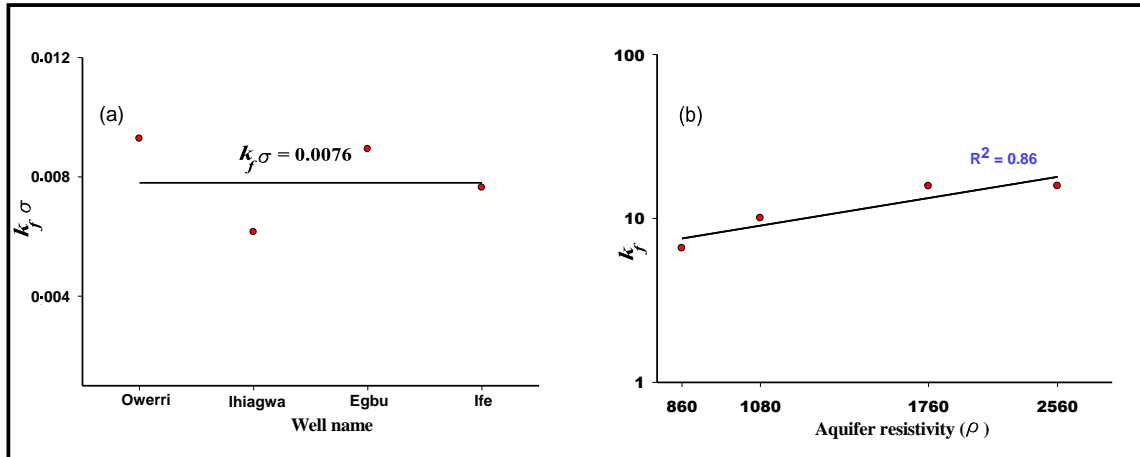


Fig.4.19: $k_f \sigma$ for various wells and (b) relationship between aquifer resistivity and k_f .

Sounding no.	Well name	Aquifer thickness (h) m	Aquifer resistivity (ρ) Ωm	k_f -values (pumping test) m/day	$k_f = ((k_f \sigma) T) / h$ m/day	$k_f = A \rho^B$ m/day
1	Owerri	62.7	1080	10.02	8.3	7.1
2	Ihiagwa	34.2	2560	15.7	19.4	23.6
3	Egbu	26.2	1760	15.72	13.6	14
4	Ife	8.3	860	6.57	6.6	5.1
where $k_f \sigma = 0.0076$, $A = 0.0004$ and $B = 1.4$					$\delta = 1$	$\delta = 1.1$

Table 4.2: Aquifer parameters of sounding locations across zone A (Ekwe et al., 2006) and estimated k_f using Eqs. (3.57) and (4.2) in correlation with known values from pumping tests.

In absence of borehole data, the k_f values were calculated using Eqs. (3.57) and (4.2). Table (4.3) shows the estimated k_f values using the same adjustable parameters as in Table (4.1).

Sounding no.	Aquifer thickness (h) m	Aquifer resistivity (ρ) Ωm	$k_f = ((k_f \sigma) T) / h$ m/day	$k_f = A \rho^B$ m/day
5	50.9	3120	24.02	31.18
6	51.9	3430	26.41	35.6
7	62.8	1054	8.12	6.8

Table 4.3: Aquifer parameters of sounding locations across zone A (Ekwe et al., 2006) and estimated k_f using Eqs. (3.57) and (4.2).

3- Hard rock granite aquifer, Hyderabad, India (Chandra et al., 2008)

A published data set by Chandra et al. (2008), belonging to the Hyderabad hard rock granite aquifer, India, has been used to test the power law empirical relation (Eq. 4.2). Chandra et al. (2008) used the normalized aquifer resistivity $\rho^- = \rho \rho_w^- / \rho_w$ and longitudinal conductance $S^- = h / \rho^-$ in

estimating the k_f and K using their empirical relation (Eq. 3.60). Fig. (4.20a) shows a weak correlation ($R^2 = 0.056$) between aquifer resistivity and the observed k_f values from pumping tests. Consequently, a weak correlation between the ρ and the estimated k_f , using Eq. (4.2) will also be achieved. Table (4.4) shows a correlation between estimated k_f values, using Eqs. (3.60) and (4.2), and those calculated from pumping tests. Table (4.4) shows to some extent a good correlation ($\delta = 1.6$) between the estimated k_f using Eq. (3.60) and those calculated from pumping tests. On the other hand, a high error factor ($\delta = 2.2$) is observed in using a power law relation.

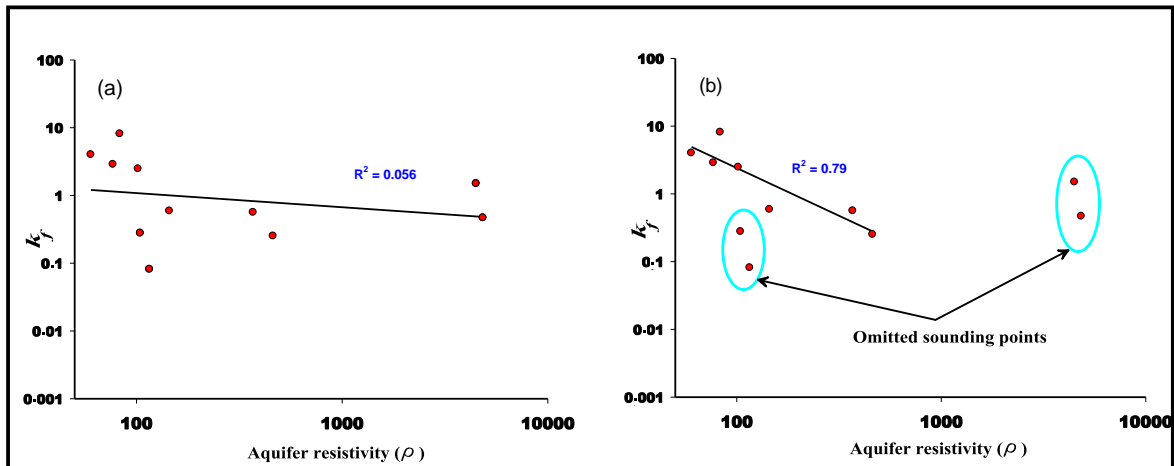


Fig.4.20: Relationship of aquifer resistivity vs. k_f with regression line for (a) 11 DC soundings and (b) 7 DC soundings. The two circles (b) show the omitted sounding points.

Fig. 4.20a indicates that the weak correlation coefficient (R^2) can be attributed to 4 ambiguous data points in comparison with other sounding points. These data points can be easily detected from Table 4.4 (red numbers) using the power law relation (Eq. 4.2). For these ambiguous data, the estimated k_f values using Eq. (4.2) provide exceptionally large differences in comparison with the observed k_f and hence they were omitted (Fig. 4.20b). After deleting these ambiguous data, the correlation coefficient becomes 0.79 (Fig. 4.20b). Accordingly, a strong relationship between aquifer resistivity and hydraulic conductivity can be achieved. A good fit between estimated k_f values and those observed from pumping tests is shown in Fig. (4.21).

Sounding no. & well name	Aquifer thickness (h) m	Aquifer resistivity (ρ) Ω m	Normalized aquifer resistivity (ρ') Ω m	k_f -values (pumping test) m/day	$k_f = ((k_f \rho') S) / h$ m/day	$k_f = A \rho^B$ m/day
1	20.8	115.9	217.3913	0.08	0.87	1.4
2	41.6	369.5	400	0.6	0.46	0.6
3	32	461.9	500	0.25	0.38	0.5
4	50	104.5	196.1	0.28	0.96	1.5
5	39	4850	200	0.47	0.92	0.07
6	25	144.8	149.3	0.59	1.24	1.17
7	36	4490.7	185.2	1.49	1	0.075
8	7	101.96	140.8	2.47	1.36	1.56
9	20.2	76.98	71.4	2.87	2.6	1.95
10	14.1	60.1	58.8	3.98	3.1	2.38
11	19.2	83.04	62.5	8.1	2.96	1.84
where $k_f \rho' = 188$ (Chandra et al., 2008), $A = 63$ and $B = -0.8$					$\delta = 1.6$	$\delta = 2.2$

Table 4.4: Aquifer parameters of DC soundings (Chandra et al., 2008) and estimated k_f using Eqs. (3.60) and (4.2) in correlation with known values from pumping tests. The red numbers denote the omitted sounding points which show ambiguous readings.

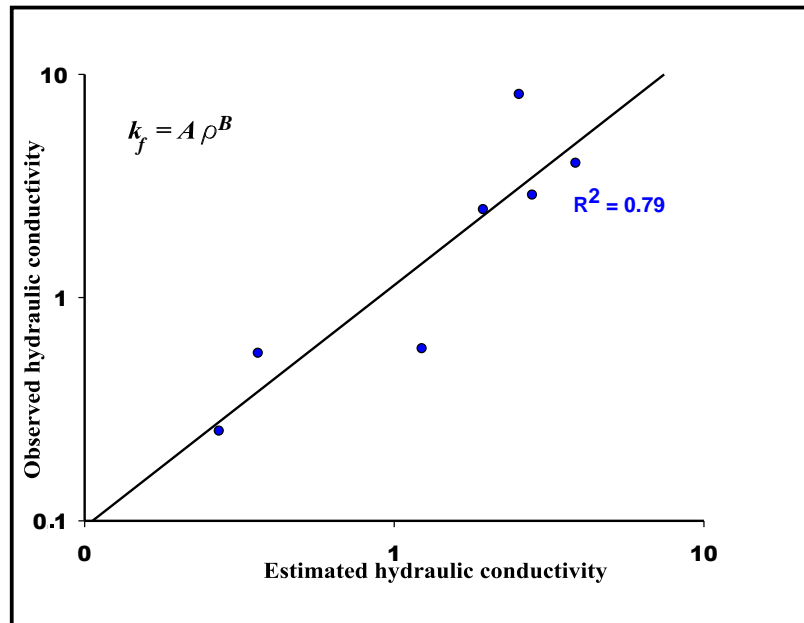


Fig.4.21: Correlation of the estimated hydraulic conductivity using the power law relation ($k_f = A \rho^B$) with those observed from pumping tests (data taken from Chandra et al., 2008), after deleting the ambiguous data points (see Fig. 4.20b).

5 INTERPRETATION AND DISCUSSION

5.1 RESISTIVITY SPECTRUM

It is important to remember that the electric resistivity of rocks from the sounding data depends on many factors such as lithology, porosity, water quantity and quality. Correspondingly, there are no generally applicable guidelines for interpreting the lithology of the contrasting resistivity layers, i.e., each area has its own conditions. 15 DC resistivity soundings adjacent to available boreholes were used to construct a resistivity spectrum and lithology for subsurface layer distributions.

Models of soundings obtained from 1D inversion exhibit different geoelectrical layers (see Appendix C). The inspection of the sounding results corresponding to borehole horizons showed a good agreement with the borehole lithological data. Based on the calibration between the borehole data and geoelectrical results, a resistivity spectrum can be deduced (Fig. 5.1) which can be used to construct the resistivity cross-sections with different directions to cover the surveyed area.

In general, the upper surface layer is characterized by a wide resistivity range with 2.5 m maximum thickness, which corresponds to recent unconsolidated deposits (silt, gravel, gravelly sand, sandy silt and gravelly silt). The saltwater saturated sand can be well recognized by very low resistivity values ($< 3 \Omega\text{m}$). In resistivity values of different layers also can be observed an overlap, which can be attributed to the variation of quality and amount of water and porosities of these sediments. The Holocene tidal deposits (clay, silt and fine to medium sand) represent a wide resistivity range, $5 \Omega\text{m}$ to $33 \Omega\text{m}$. The Pleistocene sandy aquifer represents high resistivity values ($> 33 \Omega\text{m}$).

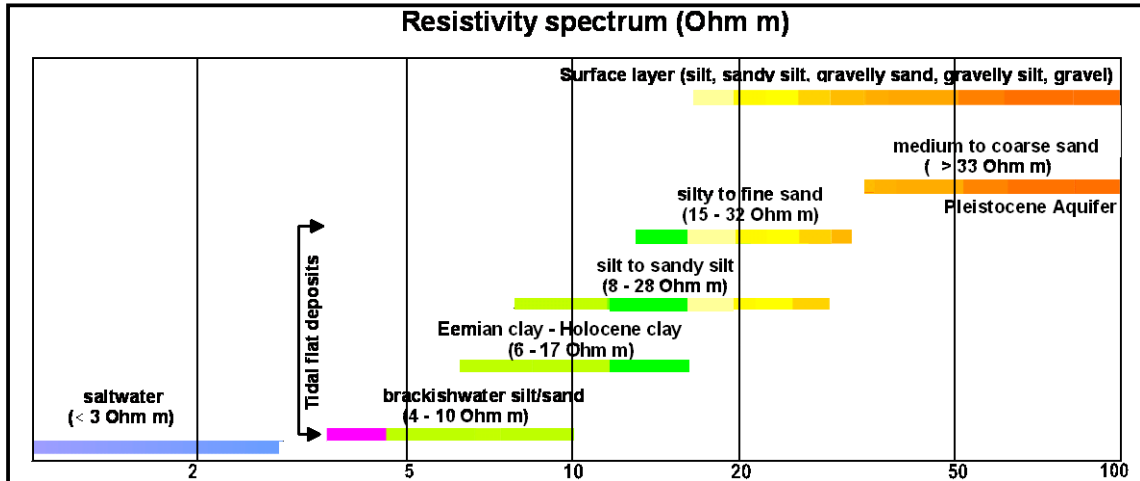


Fig. 5.1: A resistivity spectrum showing the true resistivities based on the boreholes and soundings calibration.

5.2 1D DC INTERPRETATION

DC soundings are often used to estimate the layer thickness and resistivity of successive strata below different sites. The interpreted DC resistivity soundings are presented in the form of resistivity cross-sections and horizontal/vertical slices, as will be shown below.

5.2.1 GEOELECTRICAL CROSS-SECTIONS

Four geoelectrical cross-sections (Fig. 5.2) were constructed at different locations and directions to cover the surveyed area (Fig. 4.1). The constructed sections (named C1, C2, C3 and C4) are useful in defining the subsurface layer distributions. Three profiles (C1, C2 and C3) run from the western to the eastern part (WNW-ESE) and one profile (C4) runs from south to north direction (SSW-NNE). Fig. 5.2 shows an apparent resistivity section and the stitched geoelectrical cross-section for each profile. The apparent resistivity sections present the apparent resistivity distribution along each profile. Such sections are generally constructed by plotting the apparent resistivity values (ρ_a) for a given electrode spacing ($AB/2$). The DC resistivity sounding data are qualitatively interpreted to illustrate the lateral and vertical variations of electrical properties, as well as to show the geological and hydrogeological conditions prevailing in the measured area. The obtained resistivity spectrum (Fig. 5.1) was used to construct and interpret the geoelectrical cross-sections. The inverted soundings were stitched, in the form of geoelectrical columns, to construct the geoelectrical cross-sections. Such sections are generally constructed by plotting the true resistivity values for a given depth. The geoelectrical column has a width equal to the half distances between the next and the former soundings.

The apparent resistivity section C1 (Fig. 5.2) including soundings 13, 11, 30 and 6, for location see Fig. 4.1. The maximum $AB/2$ spacing is 300 m, at sounding no. 13. Along this section, the surface cover is represented by medium apparent resistivity values. The surface cover is represented by high resistivity values at the eastern part (sounding no. 6). By increasing the penetration depth (i.e.,

increasing AB/2), the apparent resistivity regime begins with low values and then increases to high values. At the central part of the profile and at 3 m AB/2, the low resistivity layer represents a thicker layer than layers at the eastern and western parts of the profile, which may be attributed to the presence of a high thickness of silt and Eemian clay. At 100 m AB/2, the western part of the profile presents higher resistivity values than the eastern part.

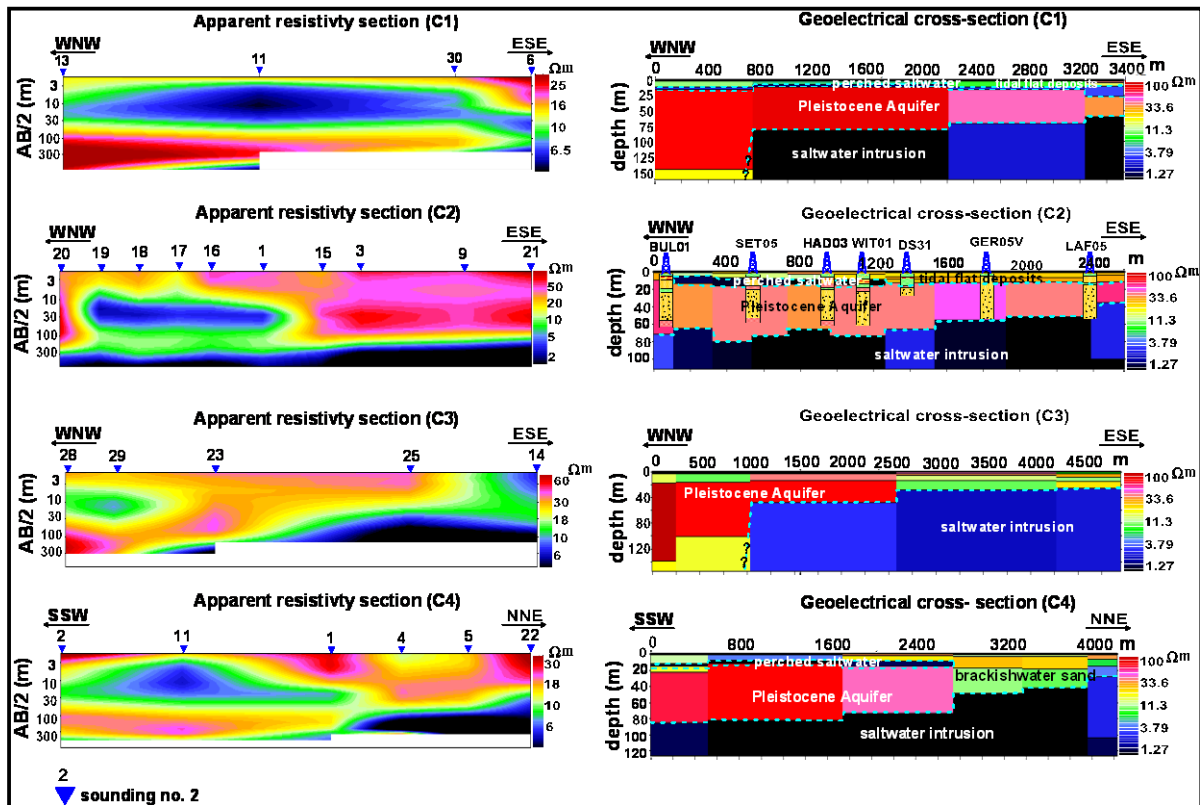


Fig. 5.2: (left) Apparent resistivity and (right) stitched resistivity sections, named C1, C2, C3 and C4, along Cuxhaven Coastal area; for location see Fig. 4.1.

Cross-section C1 (~ 3450 m long) gives evidence for distinct vertical and horizontal variations of resistivities (Fig. 5.2). It presents a shallow thin low resistivity layer ($< 3 \Omega\text{m}$), which corresponds to the perched saltwater, between an upper layer corresponding to the tidal flat aquifer ($< 33 \Omega\text{m}$) and lower high resistivity layer ($> 38 \Omega\text{m}$). The tidal flat deposits are represented by a resistivity range from $5 \Omega\text{m}$, which corresponds to brackishwater silt to sandy silt (sounding no. 11), to $32 \Omega\text{m}$ at sounding no. 6, which corresponds to fine sand deposits. The perched saltwater depth ranges from ~ 7 m to ~ 11.7 m. The maximum thickness is ~ 12 m at the central part, sounding no. 6. This layer is followed by a high resistivity layer corresponding to the freshwater Pleistocene aquifer. The thickness of the aquifer ranges from ~ 24 m to more than 100 m at soundings 6 and 13, respectively. A second low resistivity layer ($< 3 \Omega\text{m}$) may correspond to saltwater intrusion from the Elbe River. Its depth ranges from ~ 55 m to more than 82 m at the western part. It is not recorded at

sounding no. 13, due to the increase of the Pleistocene aquifer thickness towards the western part of the survey area.

The apparent resistivity section C2 (Fig. 5.2) passes through the soundings 20, 19, 18, 17, 16, 1, 15, 3, 9 and 21 in a WNW-ESE direction. It runs parallel to boreholes Bul01, SET05, HAD03, WIT01, DS31, GER05V and LAF05 (Fig. 4.1). The apparent resistivity values show a general decrease towards the western part. A shallow low resistivity zone can be observed between sounding no. 1 and sounding no. 20, which appears between 10 m and 30 m AB/2. The eastern part (soundings 15, 3, 9 and 21) is dominated by high resistivity values (up to AB/2=100 m). A low resistivity layer can be observed at the eastern part (~ 100 m AB/2). It becomes deeper towards the western part, ~ > 300 m AB/2.

The stitched resistivity cross-section C2 (~ 2600 m long) presents three main geoelectrical layers (Fig. 5.2). The near surface layer is represented by medium resistivity values corresponding to tidal flat deposits as indicated by borehole data. The resistivity of this layer ranges from 38 Ωm at the eastern part of the profile, which corresponds to medium sand, to 15 Ωm at the western part corresponding to clay, silt, sandy silt and silty sand. The shallow low resistivity layer (< 3 Ωm) within the tidal deposits can be attributed to perched saltwater. The maximum thickness and depth of this layer are 9 m (sounding no. 18) and 8 m (sounding no. 1), respectively. The second geoelectrical layer shows high resistivity values (> 38 Ωm), which corresponds to the Pleistocene coarse sand aquifer as indicated from the available boreholes. The thickness of this layer ranges from 23 m at the eastern part (sounding no. 21) to 63 m at the western part (sounding no. 18). The third geoelectrical horizon has very low resistivity values, < 4 Ωm , corresponding to saltwater intrusion. Its depth ranges from ~ 45 m close to the Elbe River (sounding no. 21) to ~ 80 m, towards the western direction. Regarding to the borehole information, the Lauenburg clay, ~ 50 m depth, cannot be recognized in the geoelectrical section. This can be attributed to two reasons; (a) its resistivity is close to the saltwater resistivity value and/or (b) its thickness is small compared to the total depth.

The apparent resistivity section C3 (~ 4800 m long) includes soundings 28, 29, 23, 25 and 14; for location see Fig. 4.1. Generally, with increase of the penetration depth, the apparent resistivity regime begins with rather medium resistivity values and then decreases to very low resistivity values. The low resistivity layer is shallower and it can be better recognized at the eastern part than at the western part. The main difference between cross-section C3 and sections C1 and C2 is the absence of the perched saltwater layer. Similar to cross-section C1, the second low resistivity layer corresponding to the saltwater intrusion is deeper (> 80 m) towards soundings 29 and 28 and when compared to soundings 14 and 25 (~ 24 m). The maximum thickness of the near surface medium resistivity layer, which corresponds to tidal deposits, is 16.7 m (sounding 28). Its resistivity ranges from 10 Ωm (sounding no. 14) to 35 Ωm (sounding no. 23). A high resistivity layer (> 38 Ωm) corresponding to the Pleistocene aquifer can be well recognized at soundings 18 and 29. Its average depth and maximum

thickness are ~ 20 m and 120 m, respectively. Towards sounding 23, the freshwater Pleistocene aquifer thickness becomes ~ 30 m, where the saltwater intrusion becomes shallow.

The apparent resistivity section C4 (~ 4200 m) runs from south to north direction and includes soundings 2, 11, 1, 4, 5 and 22. It shows, in general, similar features seen in the apparent resistivity section C2. The study of resistivity distribution along the stitched resistivity cross-section C4 (Fig. 5.2) indicates the same subsurface layers seen in section C2. The near surface medium resistivity layer, which corresponds to the tidal flat deposits, displays a wide range of resistivity. It ranges from 5 Ωm (sounding no. 11), which can be attributed to brackishwater sand, to 34 Ωm (sounding no. 22) corresponding to medium sand. Its thickness ranges from ~ 6 m (sounding no. 1) to ~ 17 m (sounding no. 5). A shallow low resistivity layer corresponding to the perched saltwater can be recognized at the western part of the profile, between sounding no. 1 and sounding no. 2. Its thickness ranges from 3 m to 6.2 m at soundings 2 and 11, respectively. A second low resistivity layer corresponding to saltwater intrusion can be observed at ~ 28 m depth (sounding no. 22). It becomes deeper, ~ 80 m depth, towards sounding no. 2. A high resistivity layer (> 40 Ωm) corresponding to the Pleistocene aquifer can be observed at sounding no. 11 with ~ 71 m maximum thickness. This aquifer can not be observed towards the northern part of the study area, i.e., soundings 4, 5 and 22. The freshwater aquifer is replaced by a brackishwater to saltwater aquifer towards the northern part (Elbe River).

5.2.2 3D VISUALIZATION

According to the obtained results of Schlumberger soundings, 3D visualization models (horizontal slices) were constructed. The 3D visualization model (Fig. 5.3) shows a clear picture about the vertical and horizontal resistivity variations in the whole area, the resistivity distributions and depths were constructed in the form of horizontal slices at different depths. The output 3D visualization resistivity model was created using the inverse distance-anisotropic modeling method of the rockworks software package (*Rockware, 2009*), where the interpreted true resistivities were sampled through -60 m depth from the ground surface. The sampling process started with small rate at shallow depths and increased with depth to detect the rapid changes in the soil material and the subsoil layers. During the 3D gridding process, the input gridding space (X, Y and Z) were applied to produce a relatively fine mesh grid (1 m, 1 m and 2 m, respectively).

Fig. 5.3 shows that the surface layer has a wide resistivity range (> ~ 15 Ωm), which reflects a high heterogeneity in the soil sediments. This surface cover is followed by a medium to low resistivity layer (< 38 Ωm) to about 16 m depth corresponding to tidal flat deposits in comparison with the available borehole data (see Appendix C). Hydrogeologically, this layer can be considered the upper groundwater aquifer in this area (*Panteleit et al., 2006* and *Panteleit et al., 2010*). At depth greater than ~18 m depth, a high resistivity layer (> 38 Ωm) at the western part can be recognized (Fig. 5.3). This layer corresponds to a Pleistocene sandy aquifer as indicated from available boreholes. Geologically, the upper boundary of the high resistivity coarse sandy layer is considered a base of tidal flat deposits.

This aquifer is the main freshwater aquifer in this area. The thickness of the Pleistocene freshwater aquifer shows an increase towards the western part (> 60 m), e.g., soundings 10, 13 and 28 (Fig. 5.4a). It should be noticed that the northeastern part are characterized by low resistivity ($< 10 \Omega\text{m}$) values corresponding to brackishwater to saltwater intrusion from Elbe River and North Sea. The brackishwater to saltwater intrusion depth ranges from ~ 12 m at the northwestern part to > 60 m at the western part.

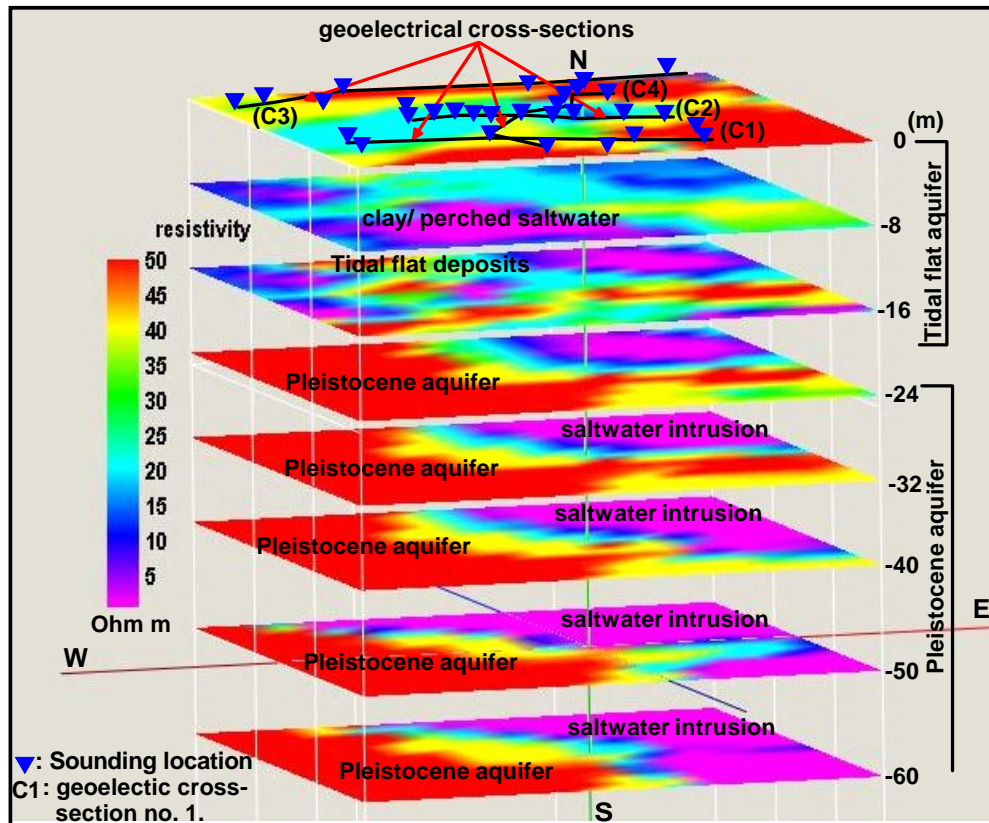


Fig. 5.3: 3D visualization resistivity model shows the distribution of resistivity with different depths (horizontal slices) and the geoelectrical cross-sections locations. The geoelectrical cross-sections are shown in Fig. 5.2.

The resistivity distributions within the tidal deposits are shown in Fig. 5.4b. At shallow depth (< 6 m), the tidal flat deposits represent a medium resistivity layer ($15 \Omega\text{m}$ - $38 \Omega\text{m}$) at northern and central parts, which corresponds to sandy silt, fine to medium sand, while it represents low resistivity values ($< 10 \Omega\text{m}$) at the south western part corresponding to clay to silty sediments and/or brackishwater fine sediments (Fig. 5.4b). At depth greater than 6 m, a very low resistivity value ($< 3 \Omega\text{m}$) can be observed at central and southwestern parts corresponding to perched saltwater layer. The maximum depth of this layer is 16 m. The thickness of tidal deposits increases at the southern part up to 22 m, while it decreases at the western part. The southern part received a great amount of floods from a series of tidal effects from Elbe River (Streif, 2004), which produced a great thickness of fine tidal sediments.

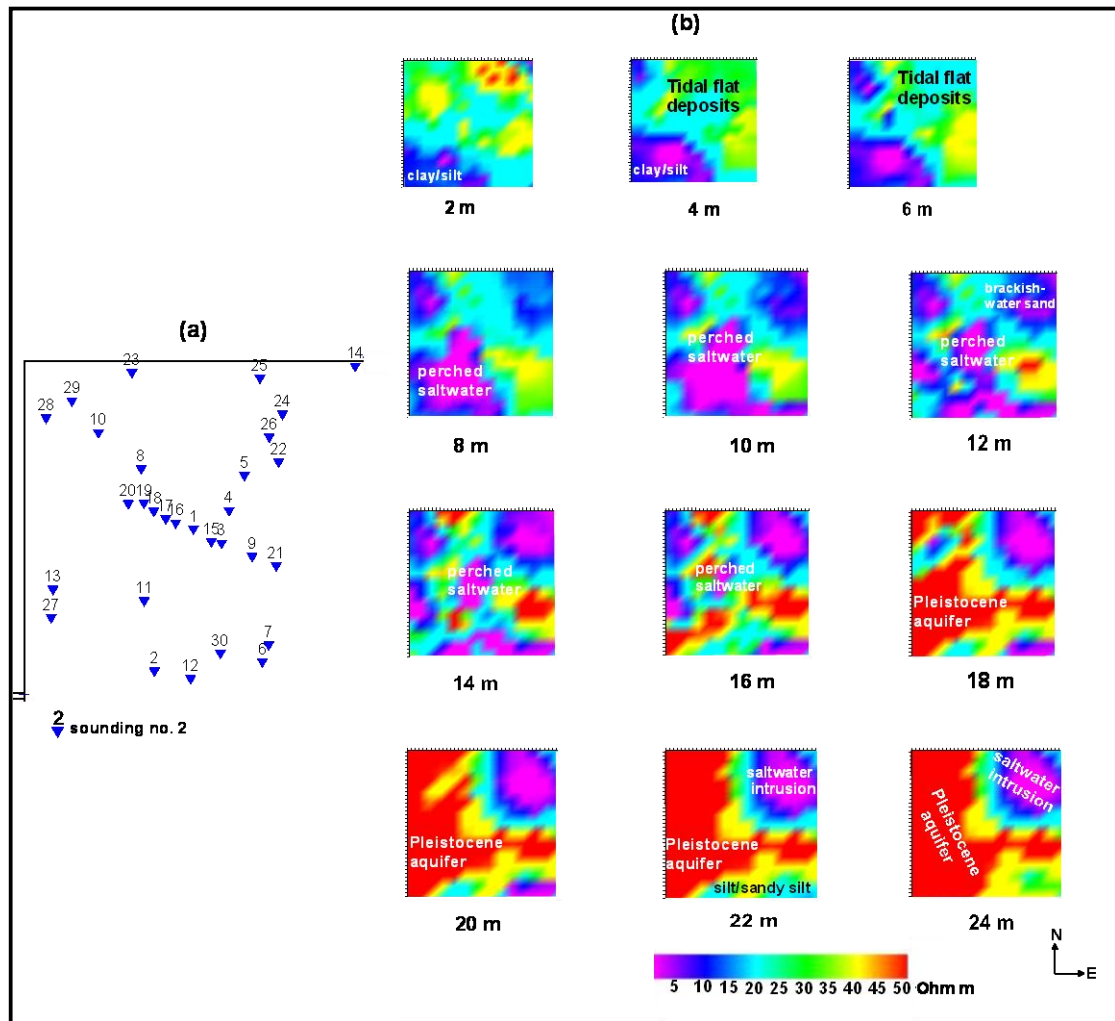


Fig. 5.4: (a) location and numbers of DC sounding points and (b) the resistivity distribution of tidal flat deposits with different depths in the form of horizontal resistivity slices through 3D interpolation model.

5.3 ALTENBRUCH DATA INTERPRETATION

Altenbruch site (named A) locates at the northeastern part (Fig. 4.1) and it is the nearest site to the Elbe River, which is characterized by saltwater. From the former Schlumberger soundings and the field observations, this site is characterized by a shallow saltwater intrusion. Fig. 5.5 shows drilled boreholes and geophysical measurements at this site. They include three boreholes, DS27, DS28 and OFA05, five DC resistivity soundings, 2D DC profile and 3D grid. Three soundings (sounding nos. 14, 22, 24 and 26) were measured close to three boreholes. A resistivity cross-section from HEM inversion results (Siemon *et al.*, 2004) was used for comparison with the geoelectrical results. The soundings inverted models and their calibration with boreholes are shown in Appendix C. Fig. 5.6 shows an example of 1D model of sounding no. 26 with the borehole data (DS27). It represents 5 geoelectrical layers in a good comparison with borehole DS27. The brackishwater can be observed at 8 m depth (<

10 Ωm). In addition, the freshwater aquifer is incorporated within tidal flat deposits of fine sand (28 Ωm). The 1D DC interpretations were discussed in detail above (section 5.2).

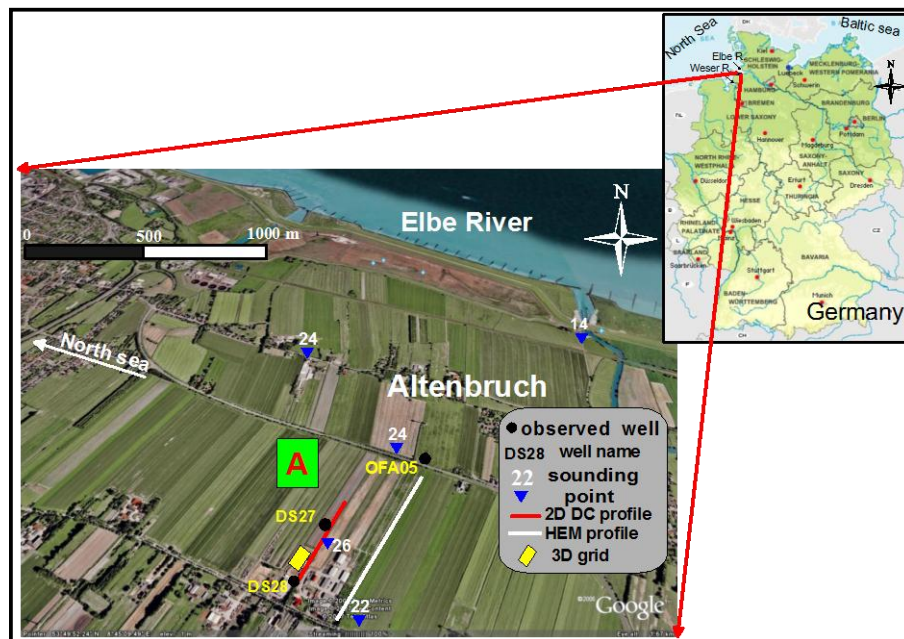


Fig. 5.5: Location map of Altenbruch site (named A), northern Cuxhaven area, showing the boreholes and geophysical measurements (inset map © Google Earth).

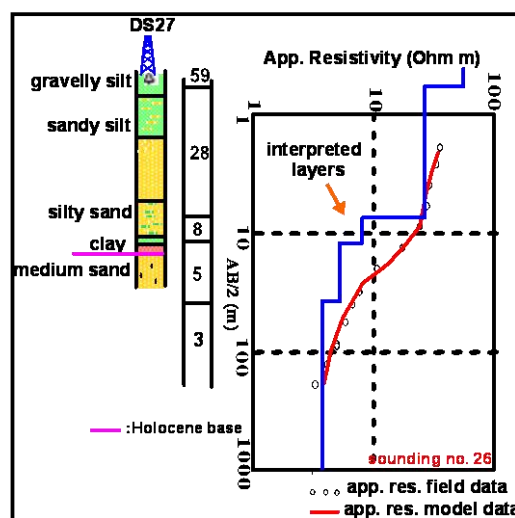


Fig. 5.6: Comparison of borehole lithology with the measured apparent resistivity and interpreted resistivity values at borehole location, i.e., along DS27.

5.3.1 2D DC RESISTIVITY IMAGING

The 2D DC profile runs over sounding no. 26 and close to two boreholes (DS 27 and DS28) and HEM profile (Fig. 5.5). The number of measured 2D data was 4653 and 3708 for WN and WB, respectively. The rejected data were 36 and 30 points for WN and WB, respectively. The apparent resistivity data and misfit error was presented in the previous chapter (Fig. 4.9). The inversion results

of individual WN and WB configurations are presented in Fig. 5.7a and b using DC2DInvRes software. The maximum depth for each model was chosen based on the sensitivity analysis and the median depth of investigation (*Edwards, 1977*) of each configuration. Additionally, the regularization parameters (λ and w_z) were chosen to obtain the best data fit in correlation with the borehole information. The detail explanation of the regularization parameters were presented in the previous chapter (subsection 4.4.2).

It is seen that the geoelectrical model obtained by the inversion of the WN data set using $\lambda=500$ and $w_z=0.1$ clearly delineates three geoelectrical layers. The maximum depth of this model is 37 m. Similarly, the WB model using $\lambda=333$ and $w_z=0.1$ shows the same number of layers but the maximum depth is 30 m. Both models show a medium resistivity layer from the land surface to ~10 m maximum depth. The maximum thickness can be observed at the eastern part of the profile, while it becomes thin (< 2 m) between 100 m and 160 m profile distance. The resistivity of this layer ranges from ~ 17 Ωm , at western part, to 38 Ωm , at the eastern part. A relatively low resistivity layer (8 Ωm -13 Ωm) follows the medium resistivity layer and it represents a variation in the thickness. The maximum thickness of this layer can be observed between 100 m and 150 m profile distance in WN model, while it is between 150 m and 200 m profile distance and at ~ 250 m distance in WB model. At about 17 m average depth, a very low resistivity layer (< 3 Ωm) corresponding to saltwater intrusion can be observed. From these results, it can be seen that in spite of the relatively greater depth of WN than WB, WB gives high horizontal and vertical resolution for the third geoelectrical layer. It is also notable that the depth of this layer is poorly mapped by WN configuration.

The joint inversion of WN and WB data sets ($\lambda=330$ and $w_z=0.1$) improved the reliability of the resulting model (Fig. 5.7c). It shows higher lateral resolution and coverage than individual WN and better penetration depth than WB. The deduced inverted model particularly combines the characteristics of both individual WN and WB models. The upper surface of the very low resistivity layer shows a weak undulation. Accordingly, the combination of individual WA and WB configurations is effective under these geological conditions.

The 2D inversion results were correlated with the known lithology from available borehole data, 1D DC resistivity sounding (no. 26) and HEM results (Fig. 5.7d). Both HEM section and 2D DC model represent the three main geoelectrical layers. The lithological comparison indicates that the first geoelectrical layer represents sandy silt to silty sand, towards the western part, and fine to medium sand, towards the eastern part. This layer can be considered as the freshwater tidal aquifer. The HEM section shows this layer in yellowish color. The second geoelectrical layer corresponds to brackishwater fine tidal flat deposits of silt, clay and silty sand which are followed by saltwater intrusion from the North Sea and the Elbe River, < 3 Ωm (third geoelectrical layer).

The HEM section represents the second and third geoelectrical layers in yellow to orange and pink, respectively. The increase of the second layer thickness between 100 m and 150 m profile

distance in the WN model and between 150 m and 200 m in the WB model can be attributed to increase of tidal deposits thickness and/or the 3D effect of the near surface layer, which decreases the configuration resolution. A variation in depth for the third layer, saltwater intrusion, can be observed in both the 2D DC profile and the HEM section. On the right of the 2D DC profile and close to well DS27, the saltwater intrusion is shallower than at the central and left part of the profile (Fig. 5.7c).

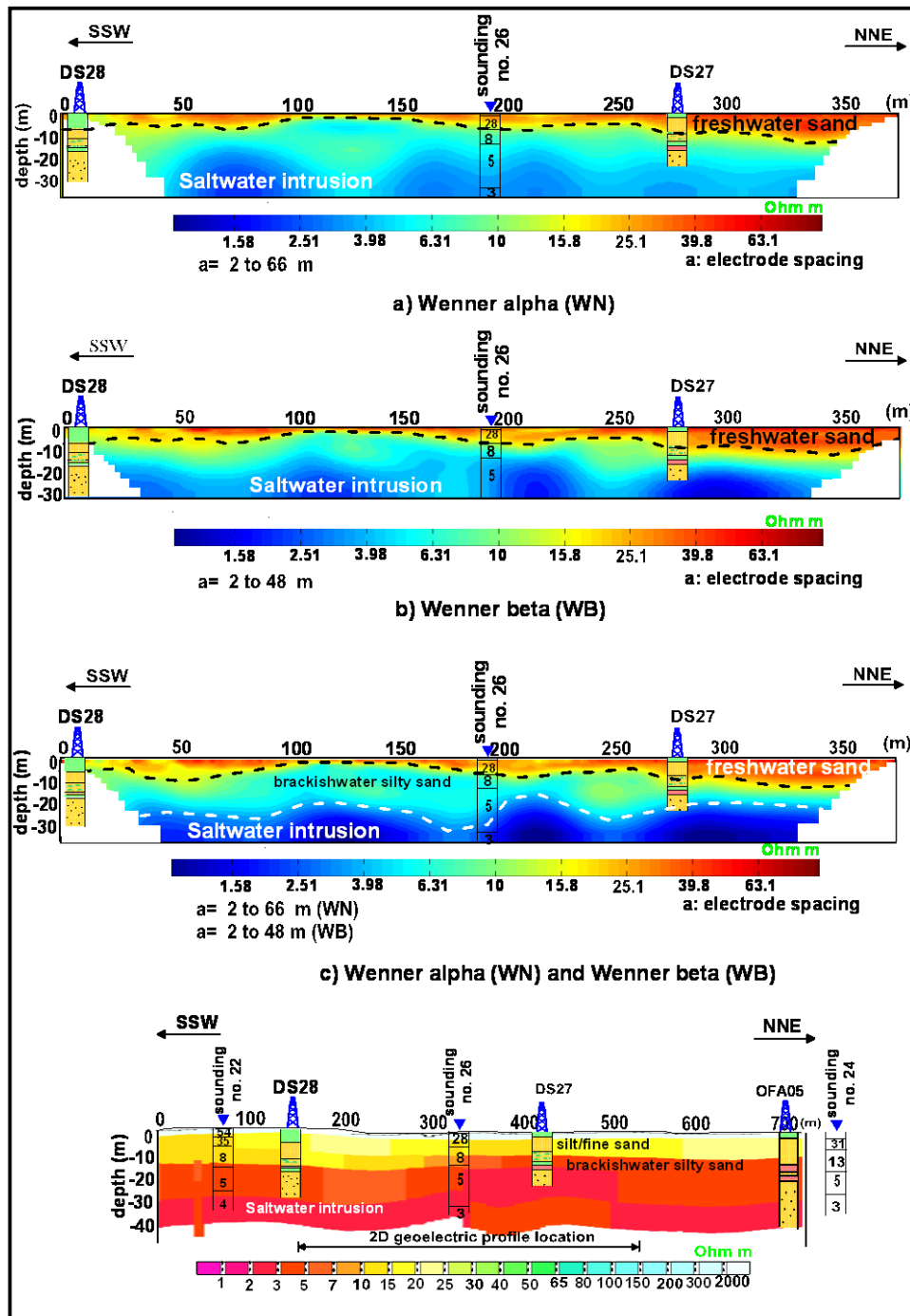


Fig. 5.7: The 2D interpretation sections obtained from inversion of (a) WN, (b) WB, (c) combined WA and WB data sets and (d) HEM data (Siemon et al., 2004). For location see Fig. 5.5. Note the reverse colour coding of resistivity values in the HEM data.

5.3.2 SYNTHETIC MODELING

Numerical modeling of 2D resistivity imaging was done in order to gain a better understanding of the resolution of the WA and WB configurations under our geological and hydrogeological situation. In addition to know to which extent can the joint inversion of WN and WB data sets improve the inversion results. The synthetic model (Fig. 5.8A) was prepared using 2 m electrode spacing. The profile length was 200 m. The synthetic data were contaminated by potential dependent random noise of 3% plus 100 nV at 300 mA. It consists of three main geoelectrical layers. The near surface layer represents variations in resistivity values and thicknesses. Its resistivity ranges from 18 Ωm , which corresponds to silt, to 28 Ωm , which corresponds to fine to medium sand. Its thickness ranges from 1.7 m to 9 m. The second geoelectrical layer shows a relatively low resistivity value of 8 Ωm , which corresponds to brackishwater fine sand to silty sand. The maximum thickness (20 m) of this layer can be observed at the central part of this model. This layer rests on a low resistivity layer of 1 Ωm corresponding to saltwater intrusion. The heterogeneity within the second geoelectrical layer can be presented in the form of intercalations of a low resistivity value (3 Ωm) corresponding to perched saltwater and a medium resistivity value (15 Ωm) corresponding to clayey to sandy silt.

Fig. 5.8B shows the inverted models for WN, WB and combined WN and WB data sets using the DC2DInvRes program. According to the sensitivity analysis of each configuration (see section 3.3), the maximum depth was calculated of WN and WB models and it was 37 m and 30 m, respectively. It can be seen that both configurations success to image the near surface layer (Fig. 5.8B). They demonstrate varying spatial resolution for imaging the saltwater layers. WB represents a higher horizontal coverage and its vertical and horizontal resolution is more than WN. The vertical weight parameter, w_z , was equal to 0.1 for both WN and WB configurations. The regularization parameter (λ) was 500 and 333 for both WN and WB, respectively. Fig. 5.8C shows the coverage plot for each model, derived from sensitivity values using Eq. (3.17), to determine the significance of model parameters and the depth range for which data are sensitive to the resistivity values. In addition to demonstrate the depth range for which the data are sensitive to the resistivity values. The higher coverage model is a more reliable resistivity model (Günther, 2004). The saltwater intrusion can be well identified only at the central part of WN model. The WB model shows a better resolution to saltwater intrusion than the WN model. A smearing to the upper surface of saltwater layer can be observed in WB model. Obviously, this smearing increases with increasing the thickness of the second geoelectrical layer (8 Ωm). In both WN and WB models, the heterogeneity within the second geoelectrical layers cannot be correctly resolved and consequently the resistivity of the second geoelectrical layer will be lower than in reality.

The combined inverse geoelectric model obtained by both WN and WB data sets ($\lambda=330$ and $w_z=0.1$) is presented in Fig. 5.8B. In this model the contact between the second and third layers is clearly identified with less smearing to the upper surface of saltwater layer than individual WN and

WB. Due to the high coverage of WB configuration, the combined WA and WB data set model is quite similar to the results of WB configuration, which dominates the combined inversion image, but it shows a higher depth with better horizontal resolution than individual WB.

Finally, the inversion results of synthetic data show that the combination of WN and WB will present satisfactory results, which can be attributed to its higher sensitivity values than individual WN and WB configuration (Fig. 5.8C). In addition, the heterogeneity can be better resolved by combined WN and WB data sets than individual configurations. The undulation of the upper surface of the saltwater layer in the combined WA and WB inverse model will be less than with individual configurations.

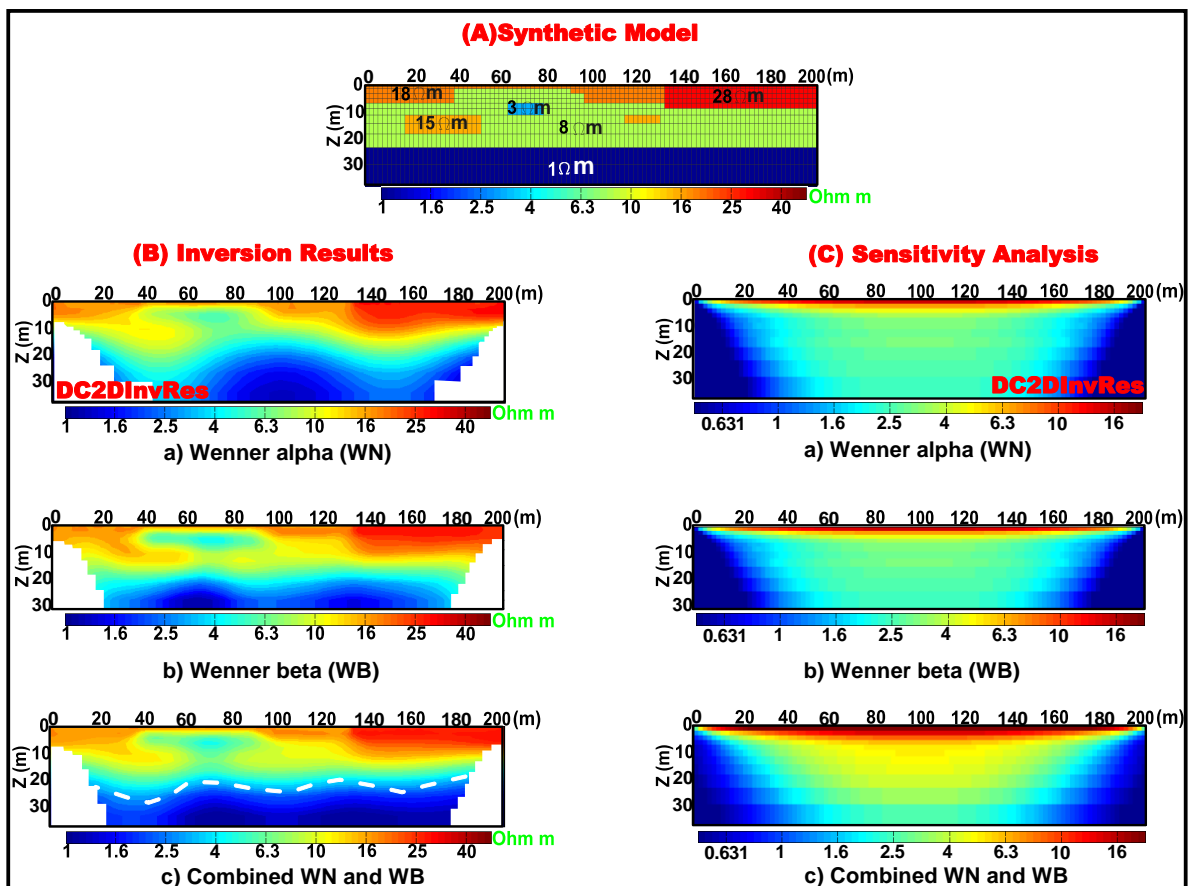


Fig. 5.8: (A) Input resistivity model, (B) inverted resistivity models and sensitivity coverage plots of (a) WN, (b) WB and (c) combined WN and WB data sets using DC2DInvRes program.

5.3.3 3D DC RESISTIVITY IMAGING

The 3D grid location at Altenbruch site is shown in Fig. 5.5. The aim of 3D imaging is to map the subsurface conditions and heterogeneity within the selected site and to assess the combination of WB and DD data sets in the 3D resistivity imaging. A 3D finite element method scheme was used as the platform for the forward resistivity calculation using the BERT program. In the form of horizontal slices in y-direction, the results of the 3D inversion of individual WB and DD data sets are

shown in Fig. 5.9a and b, using fixed regularization parameters of $\lambda = 100$ and $z\text{-power} = 1$ (see Subsection 4.4.2).

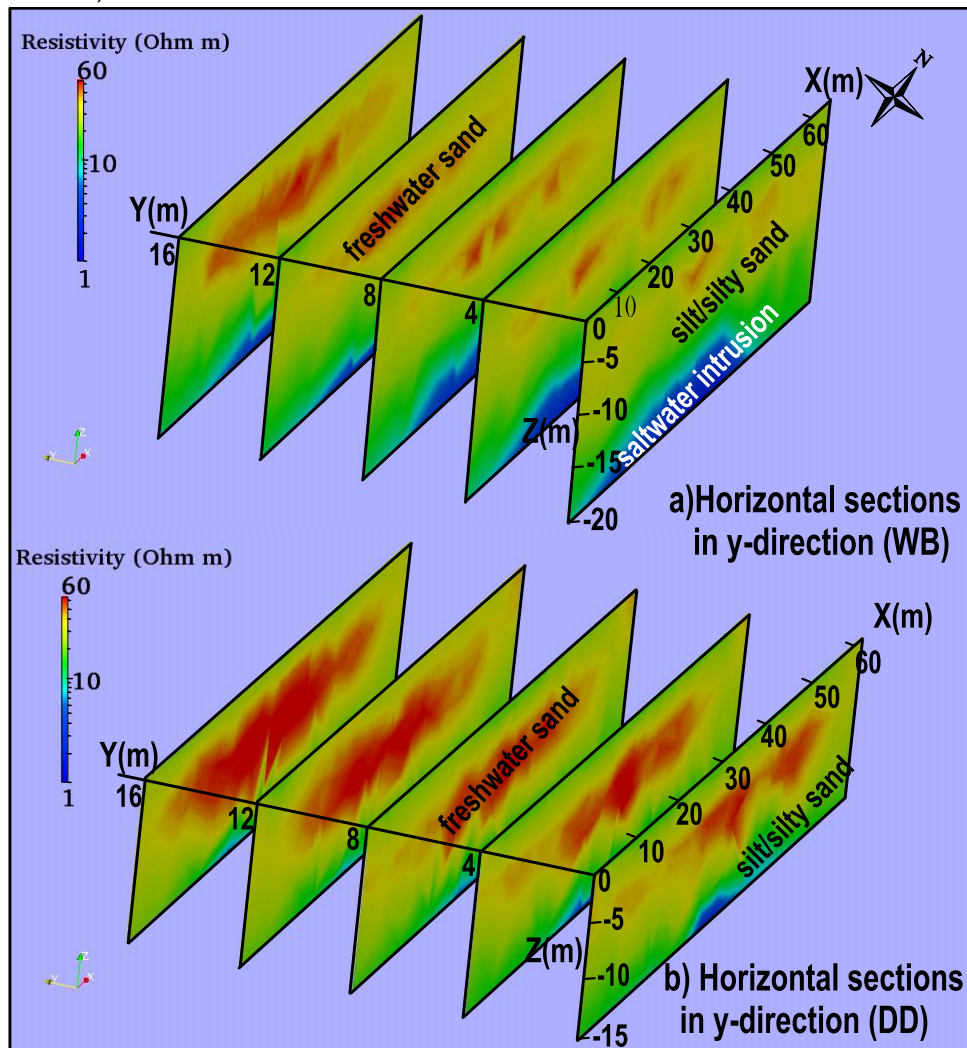


Fig. 5.9: 3D obtained model from the inversion of (a) WB and (b) DD survey in the form of horizontal sections.

The geoelectrical model obtained by the inversion of WB data set (Fig. 5.9a) clearly depicts the boundary between the low resistivity layer ($< 3 \Omega\text{m}$), which corresponds to saltwater intrusion (at a depth of $\sim 15 \text{ m}$), and the upper medium resistivity layer ($17 \Omega\text{m}$ to $38 \Omega\text{m}$) corresponding to freshwater aquifer. The maximum depth of the WB and DD models are 20 m and 15 m , respectively. Consequently, the saltwater intrusion is not clearly identified in the DD inverted model. Because the DD configuration is sensitive to horizontal resistivity changes, the resolution of the freshwater aquifer from the DD model is better than that of the WB model (Fig. 5.9a). The aquifer can be easier identified from the DD model than from the WB model. At $\sim 10 \text{ m}$ depth, a medium resistivity layer ($\sim 10 \Omega\text{m}$ - $15 \Omega\text{m}$) corresponding to silt and/or brackishwater sand can be observed below the high resistivity layer ($\sim > 40 \Omega\text{m}$), which corresponds to a freshwater medium or to coarse sand.

In the form of horizontal slices in x- and y- directions, the geoelectrical models obtained by the combined inversion of both WB and DD data sets are presented in Fig. 5.10a and b. It is observed that the joint inversion ($\lambda = 100$ and $z\text{-power} = 1$) combines the characteristics of both WB and DD models. The models show a good vertical and horizontal resolution and a good agreement with the borehole data (DS28). The heterogeneity and the saltwater intrusion can be easier identified than in the individual WB and DD data sets. The wet ground surface is seen of relatively low resistivity ($\sim 12 \Omega\text{m}$) as green color corresponding to silt and clay. It is followed by a medium resistivity layer which corresponds to silt and sandy silt. It extends to $\sim 5 \text{ m}$ depth. It is underlain by sandy freshwater aquifer which shows a variation in resistivity from medium to high values corresponding to medium to coarse sand, respectively. A relatively low resistivity layer can be well identified under the freshwater sandy aquifer, which corresponds to silt and silty sand. A very low resistivity value ($< 3 \Omega\text{m}$) can be well and easily recognized at about 15 m depth which corresponds to saltwater intrusion.

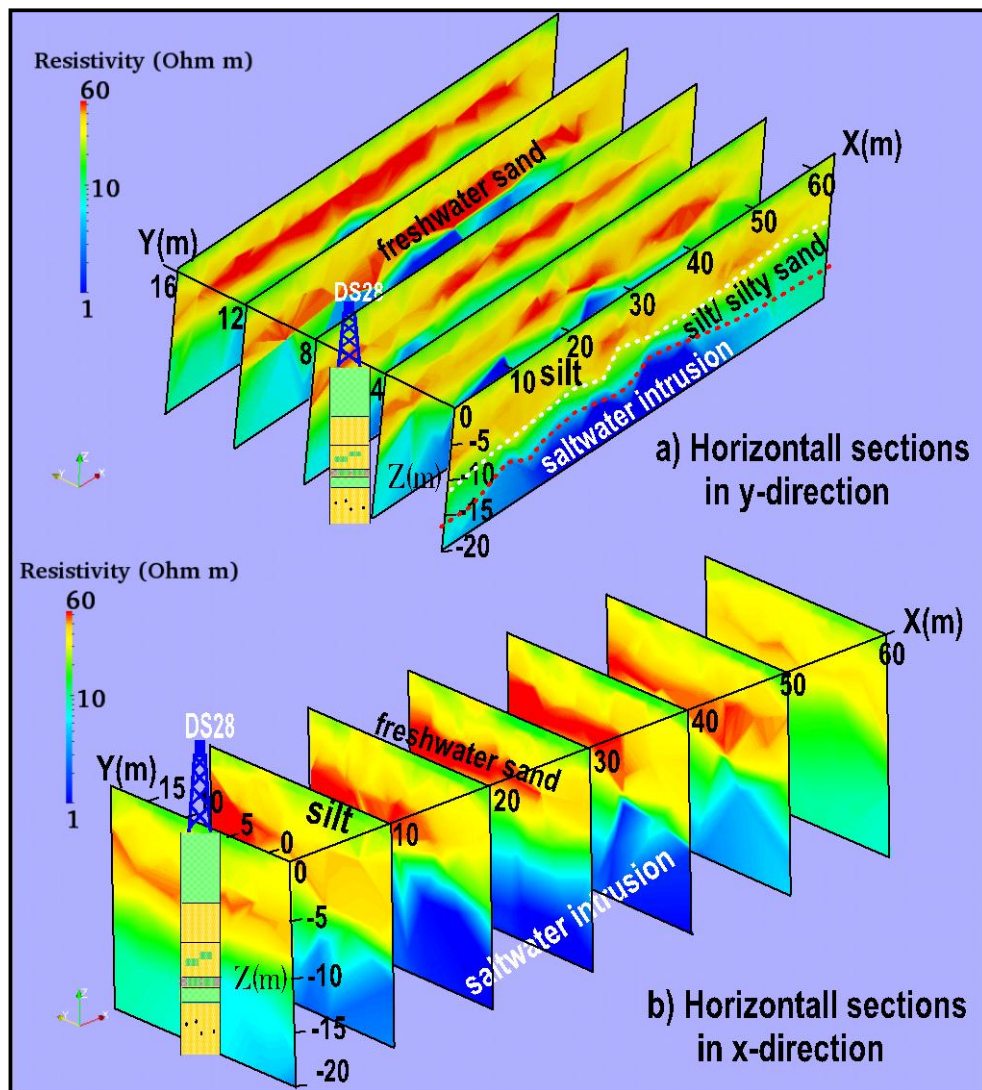


Fig. 5.10: 3D joint inversion results of combined WB and DD data sets in the form of horizontal sections in (a) x- and (b) y-directions.

Inverted DC resistivity sections (2D and 3D) were plotted in the form of 3D visualization to compare the DC inversion results and the borehole data. The 3D model of joint inversion of WB and DD data sets and its location as corresponding to the 2D profile (combined WN and WB data sets) are shown in Fig. 5.11. Generally, two major electrical layers were observed of freshwater tidal aquifer and saltwater intrusion. An excellent fitting between the borehole data and the DC inversion results can be noted. Consequently, the joint inversion of WB and DD and/or WN and WB can improve the interpretation of DC inversion results.

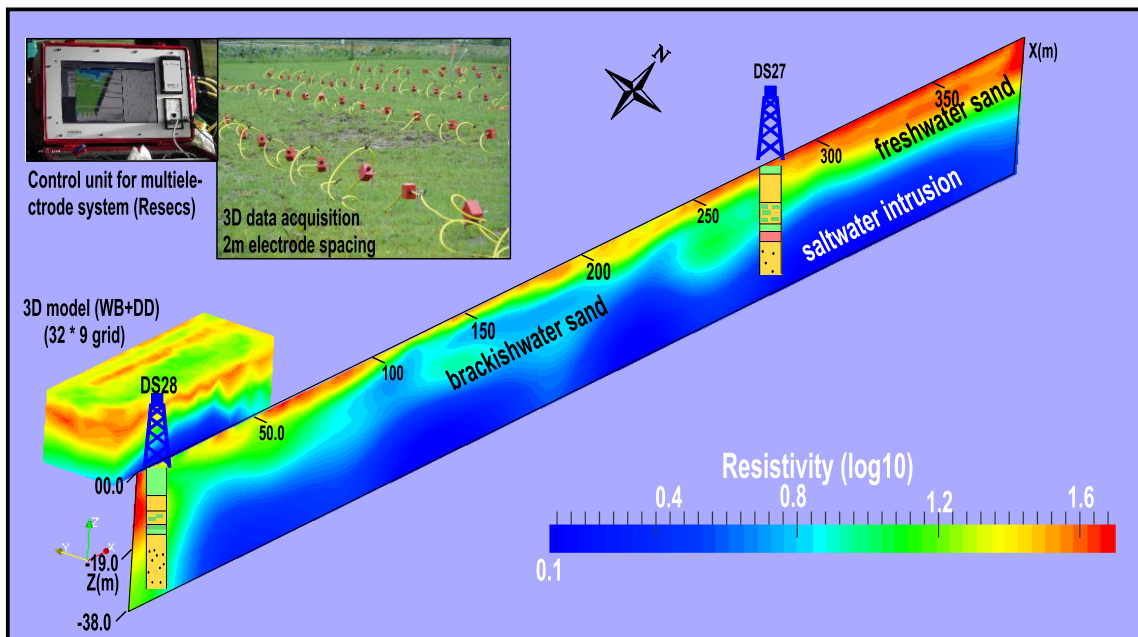


Fig. 5.11: (top) DC Resecs instrument and the 3D grid using 2 m electrode spacing to acquire the DC data at Altenbruch site. (bottom) 3D visualization model of 2D DC profile (of combined WN and WB data sets) and 3D model (of combined WB and DD data sets).

5.4 NORDERSCHIEDUNG DATA INTERPRETATION

The selected site locates at Lüdingworth area and is named “B” (Fig. 5.12). It is an open tidal flat area. The interpreted geoelectrical layers were correlated with the borehole information in order to improve the characterization of the lithological resistivity values.

5.4.1 1D INTERPRETATION

The results of the 1D DC interpretation (see Appendix C) and geoelectrical layers were discussed and presented in subsection 5.2.1 (geoelectrical cross-section no. C2). Consequently, the results of the 1D FDEM interpretation will only be discussed in this Subsection.

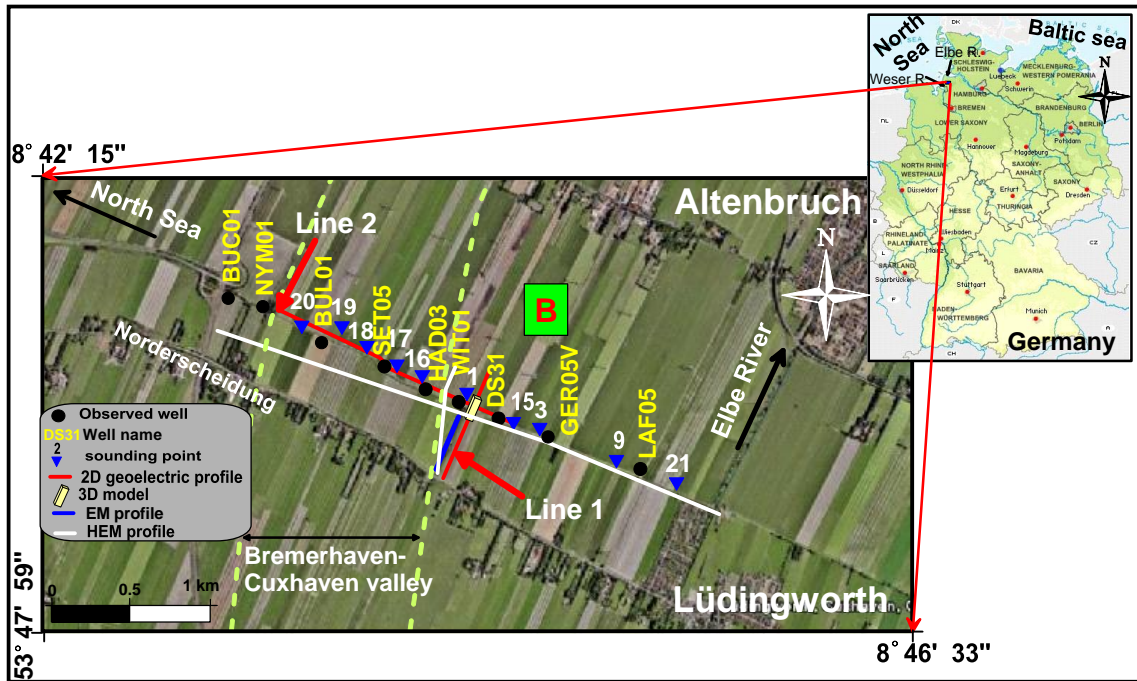


Fig. 5.12: Map of the Norderscheidung (named B) survey site showing the geophysical measurements (inset map © Google Earth).

The FDEM raw data, in- and quadrature-phase, is shown in Fig. 5.13. At the beginning of the profile, a buried current cable was detected perpendicular to the measured profile direction. Close to this cable, the raw data shows anomalous readings at the highest frequencies (> 3520 Hz). Similarly, from profile meter 90 to 180, anomalous data can be observed for the five highest frequencies, which represent abrupt changes in inphase and quadrature readings. This can be attributed to a presence of anthropogenic features, e.g. small metal buildings, close to the FDEM measurements, west to the profile. The quadrature components are more affected by these noise sources than the inphase components, where they show higher amplitudes than inphase readings. In general, the inphase and quadrature raw data show only significant lateral variations (see Fig. 5.13). For the three lowest frequencies, the raw data shows monotonous changes along the whole profile except soundings 1 to 3, which were affected by the buried current cable.

In the forward modeling process, the nearest borehole (WIT01) and DC sounding (no. 1) data was used to derive the starting model. Fig. 5.14 shows the smoothed-earth model for FDEM sounding no. 36 using the Ridge regression inversion (see subsection 3.5.3). A four-layer model shows an acceptable fit between EM raw data and the calculated model. The EM inversion results at sounding no. 36 show satisfactory results in comparison with the known borehole and 1D DC inversion results. In Fig. 4.14 (middle), the third high resistivity layer ($61 \Omega\text{m}$) can be observed between two very low resistivity layers ($\sim 2 \Omega\text{m}$). Regarding the borehole data, this can be attributed to a freshwater sandy Pleistocene aquifer (~ 26 m thick) between two saltwater layers. The upper low resistivity layer (at ~ 7 m depth) can be interpreted as perched saltwater above silt and Eemian clay. The thin silt and

Eemian clay can not be discriminated and consequently the low resistivity layer corresponding to the perched saltwater is presented thicker (~ 10 m thick) than in reality. The perched saltwater layer is covered by a medium resistivity layer (34 Ωm and 7.5 m thick) corresponding to a Holocene fine to medium sandy tidal aquifer. The second low resistivity layer at 43.4 m depth can be interpreted as saltwater intrusion.

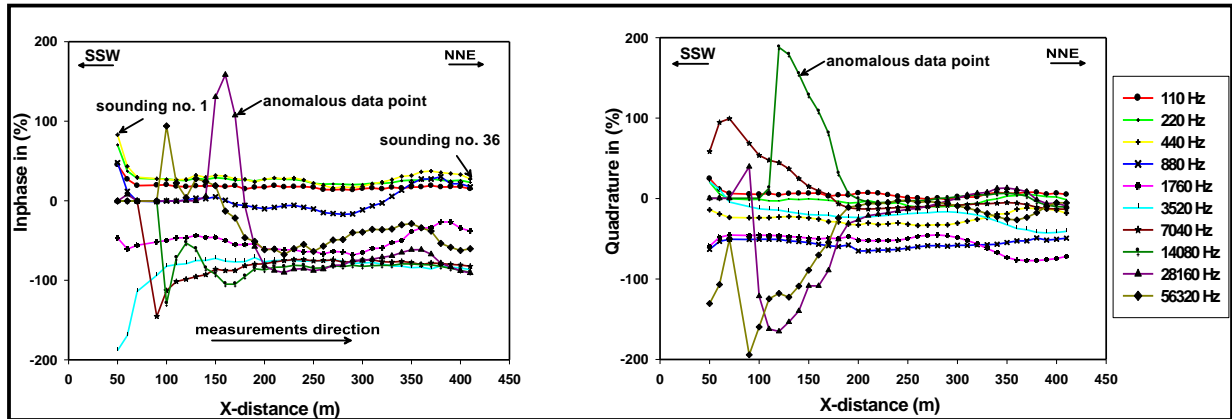


Fig. 5.13: FDEM raw data at Norderscheidung site: Inphase and quadrature components for different frequencies.

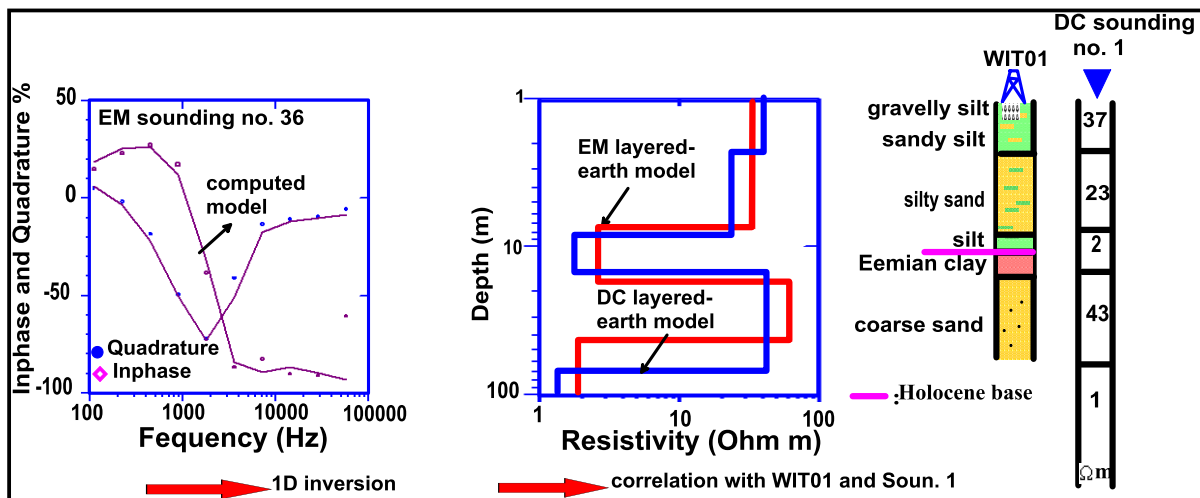


Fig. 5.14: FDEM sounding data (no. 36) for different frequencies (left) and 1D inverse model (middle) results in comparison with borehole data (WIT01) and DC sounding no. 1 (right).

The obtained model at EM sounding no. 36 was used as a reference model for other EM soundings. In general, the inversion results (Fig. 5.15) are satisfactorily correlated with the known borehole geology and DC sounding no. 1, except at the western part of the profile. The results at EM soundings 1 to 4 (i.e., the first 30 m profile distance) neither agree with neighboring-sounding results nor correlate with the known borehole geology. Fig. 5.15 shows four geoelectrical layers, as deduced from borehole calibration above (Fig. 5.14). The first geoelectrical layer shows medium resistivity

values ($11 \Omega\text{m}$ to $35 \Omega\text{m}$), which correspond to the Holocene tidal aquifer. It is interpreted as sand to silty sand at the central and eastern parts to silt at the western part. Its maximum thickness is 12 m at sounding no. 7 (60 m profile distance). The second geoelectrical layer shows very low resistivity values, which correspond to perched saltwater. It shows variations in depth and thickness. Its maximum depth and thickness is 9 m and 13 m, respectively, at sounding no. 20 (180 m profile distance). From profile meter 80 to 360, the third geoelectrical layer shows medium to high resistivity values ($35 \Omega\text{m}$ to $> 100 \Omega\text{m}$). It corresponds to the Pleistocene aquifer, which represents medium to coarse sand sediments. Interesting is the fact that the third geoelectrical layer is more conductive at the western part than at the eastern part, from profile meter 0 to 80. It could be interpreted as Eemian clay. The last very low resistivity layer corresponding to saltwater intrusion shows variations in depth. Its depth ranges from 43 m at the eastern part to more than > 60 m at the western part, in wedge-like form.

From profile meter 0 to 50 (Fig. 5.15), it can be noted that the maximum depth at the western part is ~ 40 m. This can be attributed to the presence of many conductive layers, perched saltwater and Eemian clay, which generates diffusion to electromagnetic waves. Consequently, the penetration depth will also be decreased. To image the saltwater intrusion at the western part, the chosen coil separation has to be increased more than 100 m. Therefore, the FDEM method cannot be considered as alternative to DC sounding in order to combine information from greater depth as obtained with DC soundings. It shows many limitations in this coastal area.

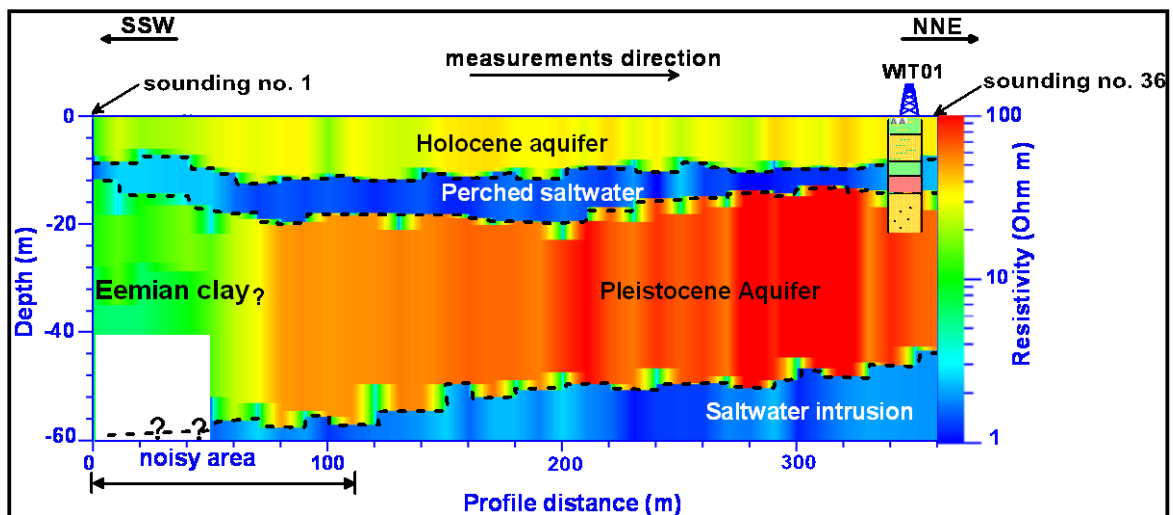


Fig. 5.15: Stitched resistivity section from 1D FDEM inversion of 36 sounding points.

Fig. 5.16 displays examples of the EM 1D inverse models for 3 EM sounding points to show the effect of noise sources on the inversion results and to delineate the interpretation reliability. Sounding nos. 3 and 7 were close to the noisy area and sounding no. 20 was in the noise free area. The sources and detection of noise were discussed in the previous chapter (see Subsection 4.4.1). For sounding nos. 3 and 7, it was observed that at the highest frequencies (> 3520 Hz) the computed

model cannot fit the measured data (Fig. 5.16). On the other hand, a good fit can be achieved for low frequency data. Upon inspection of this behavior over the noisy area, it becomes clear that the shallow layer parameters are poorly resolved. In addition the high RMS error percentage between the computed model and measured raw data is expected. Fig. 5.17 shows RMS percentages over the noisy and noise free areas. For EM sounding no. 20, the inversion result shows an acceptable fit considering a four-layer model. At low frequencies, a good fit between the measured field data and the computed model of both inphase and quadrature components can be observed. On the other hand, at higher frequencies, a better fit of the measured data and the computed model with the inphase component than with the quadrature component can be observed. This can be attributed to the linear response of the inphase component with high frequencies (Klein and Lajoie, 1980).

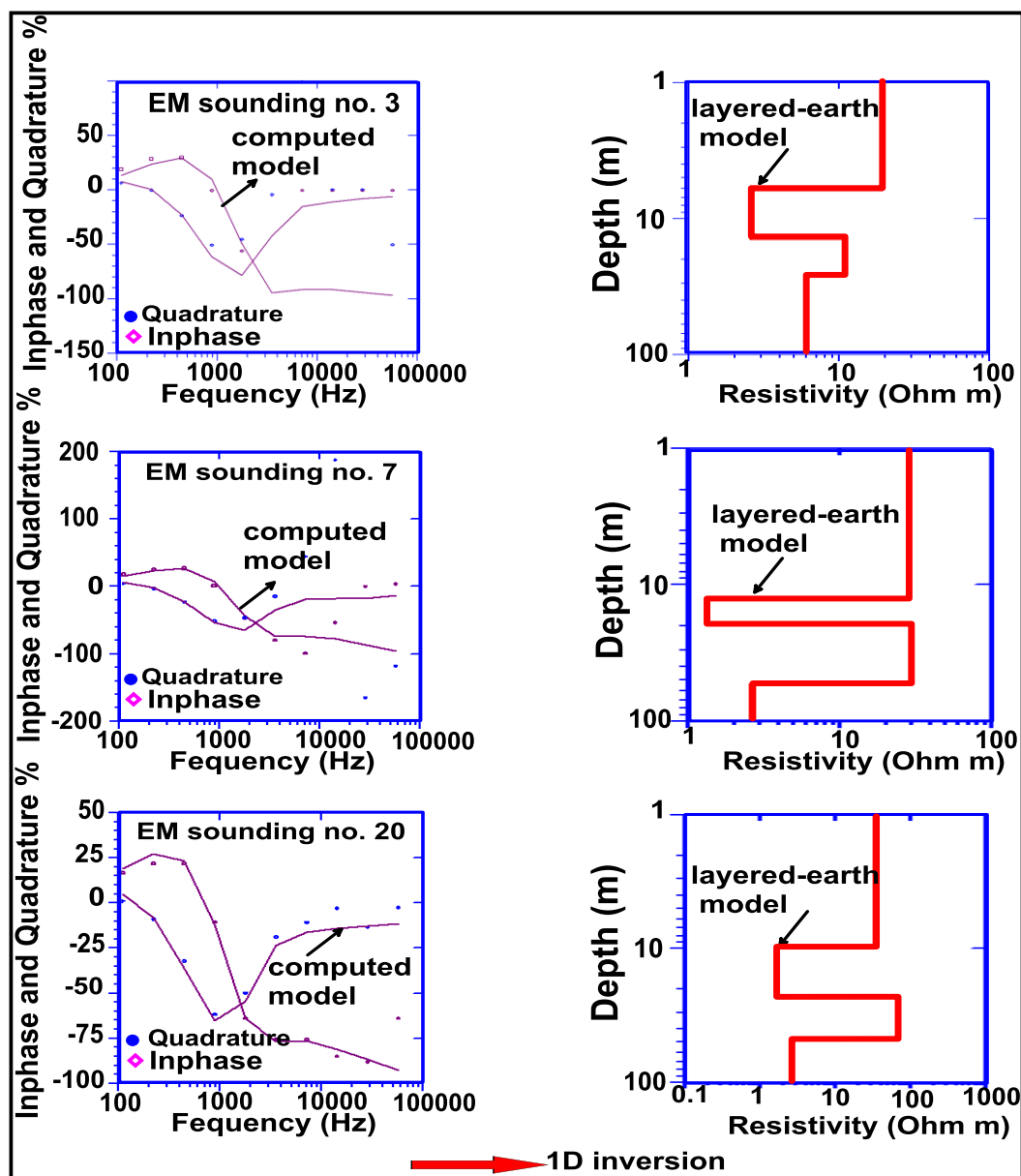


Fig. 5.16: The observed data, computed model (right) and 1D Ridge Regression inversion results (right) for EM sounding nos., from top to bottom, 3, 7 and 20, respectively.

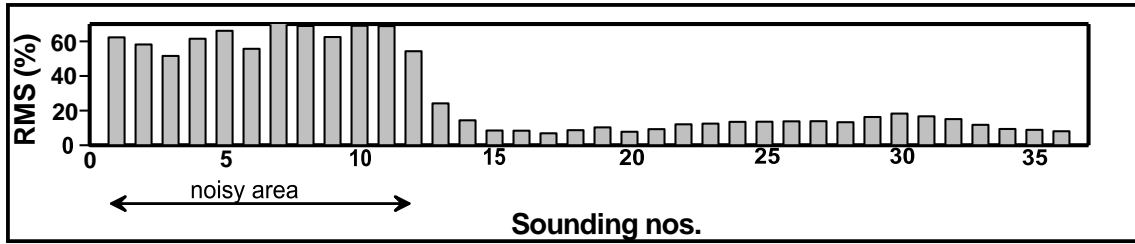


Fig. 5.17: The RMS misfit values of all FDEM soundings at Norderscheidung site.

5.4.2 2D DC RESISTIVITY IMAGING

EM results are not usually diagnostic and, consequently, other geophysical techniques, including DC methods, should be used to support the interpretation results. From the previous discussion, FDEM measurements have been measured over a noisy area and, consequently, the inversion results showed high misfit percentages. Prior to the 2D DC resistivity measurements, the imaging capabilities of WB and SC electrode configurations were investigated by designing a synthetic modeling, which represents the general geological or environmental situation in this site.

5.4.2.1 SYNTHETIC MODELING

The synthetic model simulates the geological information of borehole WIT01 and the inversion results of FDEM soundings (Fig. 5.15). The electrode numbers and spacing were 50 m and 5 m, respectively. The near surface layer has a resistivity of 20 Ωm corresponding to a silty layer. Its thickness ranges from 6 m to 10 m, towards the right end of the model. From 0 m to 160 m profile distances, this layer rests on a low resistivity layer of 2 Ωm , which corresponds to the perched saltwater. Its thickness ranges from 3 m to 5 m. From 0 m to 75 m profile distances, the perched saltwater rests on a 15 Ωm resistivity layer corresponding to clay. From 75 m to 160 m profile distances, it rests on a high resistivity layer (80 Ωm to 100 Ωm), which can be linked to the Pleistocene aquifer. From 160 m to 250 m profile distances, the silty surface layer rests on this aquifer. At 30 m depth, a low resistivity layer (2 Ωm) can be observed, which corresponds to saltwater intrusion. WB and SC configurations were used to image this model.

The calculation of the apparent resistivity data was carried out using the DC2DInvRes forward modeling program, which includes an FD approach to calculate the potential distribution due to the point current source. The synthetic data were contaminated by potentializ dependent random noise of 3% plus 100 nV at 300 mA. These data sets were used as input for the 2D inversion process using the BERT program. The inversion process was carried out using a nonlinear smoothness constrain least-squares optimization technique. The regularization parameters (λ and $z\text{-power}$) for all the inversions of WB, SC and combined WB and SC data sets were $\lambda=20$ and $z\text{-power}=0.1$ (Fig. 5.18). The regularization parameters were chosen to give the best fit between the input model and the inversion results. Because of presence of vertical and horizontal resistivity variations in the synthetic data, it is observed that a small value of λ and a high value of $z\text{-power}$ were used to increase the model roughness (see Subsection 4.4.2).

It is notable that the WB model (5.18b) gives a poor resolution to the boundary between the Pleistocene aquifer and the saltwater intrusion. In addition, the lateral and vertical effects of the perched saltwater are amplified. The model represents the perched saltwater with greater thickness than in reality as a result of smearing to its lower boundary. The smearing reaches up to ~ 4 m. The clay layer thickness is not perfectly mapped and its resistivity assigned lower values than in the input model. While the perched saltwater and a high resistivity layer are present, the saltwater intrusion can well not be resolved at the central part. On the other hand, it can be well detected but deeper, ~ 6 m, than in reality at the western part, i.e., between 0 m and 75 m profile distances. Away from the perched saltwater and towards the eastern part, the saltwater intrusion can be slightly identified.

The SC model assigns incorrect Pleistocene aquifer resistivity below the perched saltwater. On the other hand a true Pleistocene resistivity can be observed at the eastern part of the profile. The amplification of the horizontal and vertical effects of the perched saltwater in the SC model is less than in the WB model. The SC model shows a worse horizontal coverage than the WB model and, consequently, the saltwater intrusion can well be resolved only at the central part.

A joint inversion to the WB and SC data sets (5.18d) yields good resolution and horizontal coverage in comparison with the individual WB and SC models. The saltwater intrusion depth can be well identified (i.e., be assigned with the correct resistivity value). The upper boundary between Pleistocene sand and the saltwater intrusion is sharply detected on the left side of the profile, where clay and perched saltwater are present, and assigns a correct depth. On the other hand, a smearing to the upper boundary of the saltwater intrusion over ~ 6 m can be observed at the central part. This can be attributed to the presence of the perched saltwater and high resistivity layer. Consequently, a misinterpretation to saltwater intrusion depth will be assigned. The model also represents a high resolution to the boundary between saltwater intrusion and freshwater at the eastern part of the profile and assigns an increase of the depth, ~ 6 m.

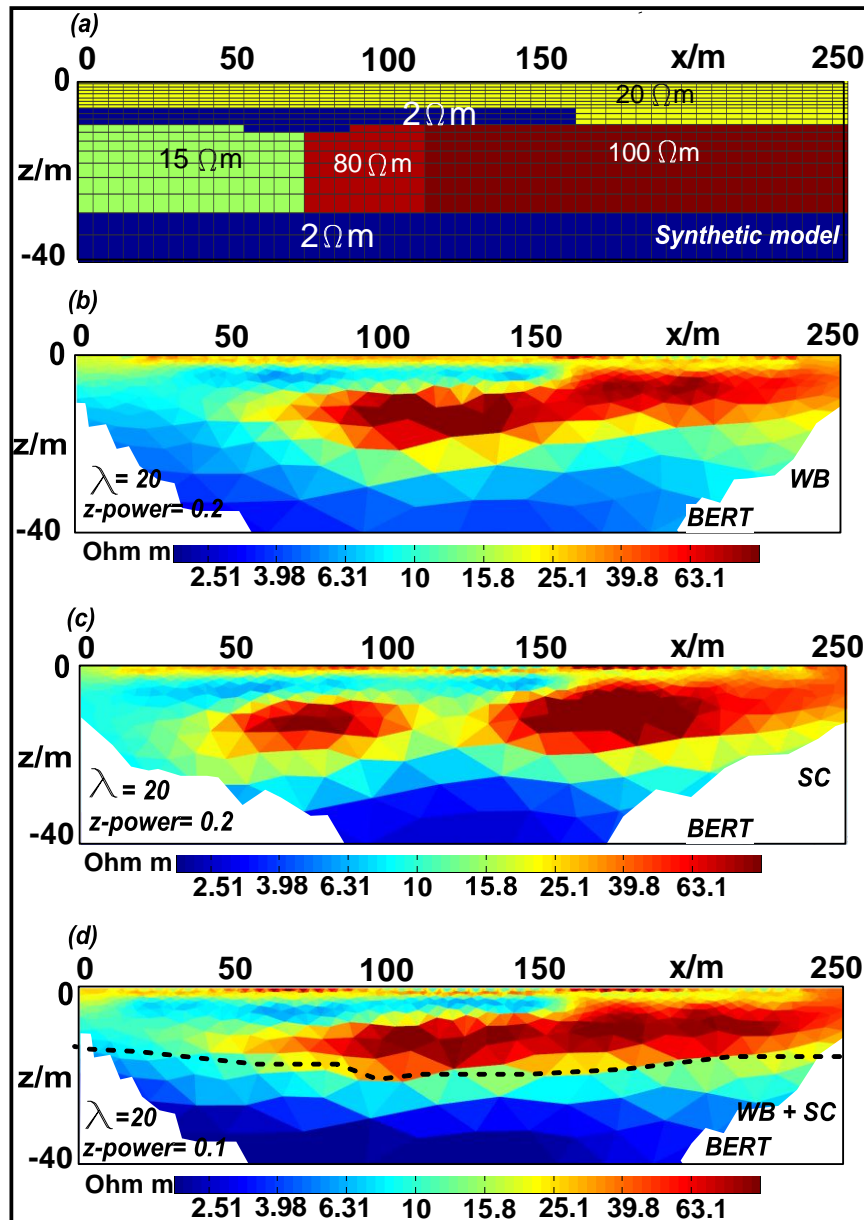


Fig. 5.18: (a) A synthetic model for numerical imaging experiment. Inverted models using smoothness constrained inversion for (b) WB, (c) SC and (d) combined WB and SC data sets.

5.4.2.2 2D DC INVERSION RESULTS (LINE 1)

Fig. 5.12 shows the 2D DC profile location (line 1), which runs in parallel to FDEM soundings. Figs. 5.19 and 5.20 show the pseudo-sections of apparent resistivity data, together with calculated data and misfit errors for the WB and SC configurations, respectively. A good fitting between measured and calculated data can be observed for both configurations. The SC model shows different levels of data points, which are related to the increase of potential electrode spacings (a). The inspection of WB and SC data indicates that the apparent resistivity values decrease towards the west

direction. In addition, a shallow low resistivity layer can be observed between 0 m and ~500 m profile distance.

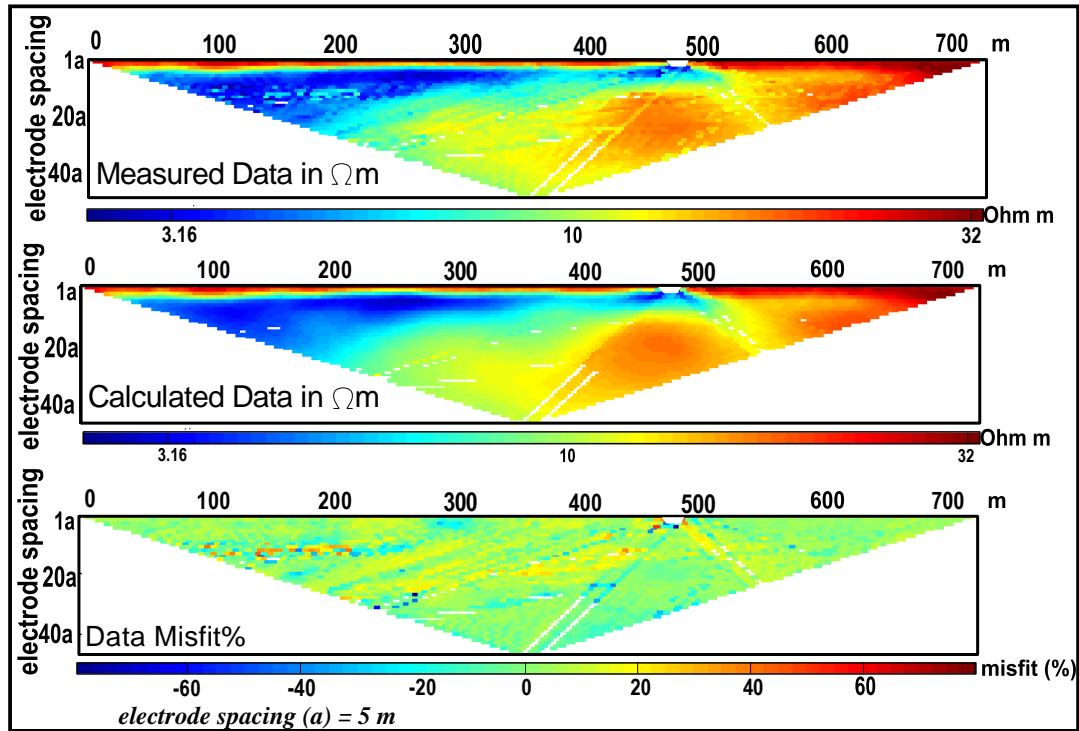


Fig. 5.19: WB 2D DC pseudo-section (line 1, see Fig. 5.12) of the measured apparent resistivity (top panel), calculated resistivity (middle panel) and relative difference between them (bottom panel).

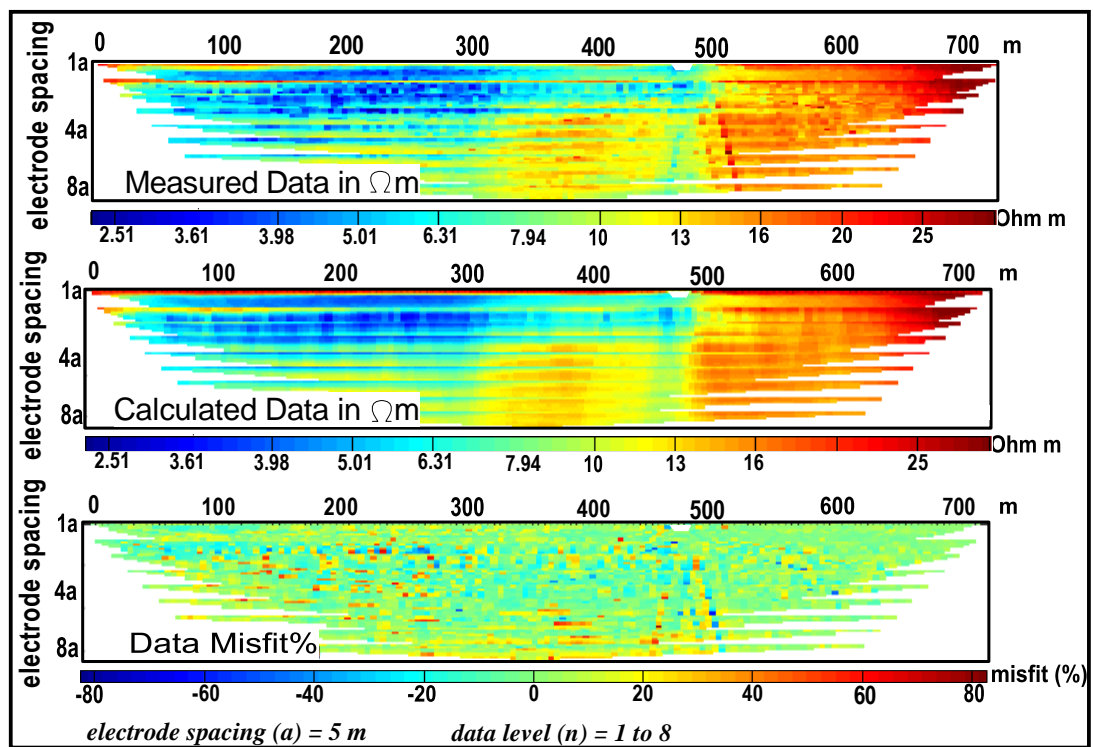


Fig. 5.20: SC 2D DC pseudo-section (line 1, see Fig. 5.12) of the measured apparent resistivity (top panel), calculated resistivity (middle panel) and relative difference between them (bottom panel).

In Fig. 5.21, the geoelectrical models of both WB and SC configurations are presented using the BERT software. The inverted sections show a top medium resistivity layer (15 Ωm to 20 Ωm), which can be associated to Holocene silt and silty sand materials. The maximum thickness of this layer is ~ 11 m, at the eastern part of the profile. The upper low resistivity layer (< 3 Ωm) is observed at about 9 m depth. In comparison with the 1D interpretation, it corresponds to the perched saltwater layer. The upper boundary of the perched saltwater can be well detected from all models. On the other hand, a smearing to its lower boundary can be observed with different ratios. At ~ 470 m profile distance, the perched saltwater is replaced by a medium resistivity layer (10 Ωm to 15 Ωm) corresponding to fine sediments of silt to silty sand and clay.

It is clearly seen that the geoelectrical model obtained by the inversion of the WB data set ($\lambda = 200$ and $z\text{-power} = 0.3$) delineates a high resistivity layer (> 40 Ωm) at the central part (Fig. 5.21 top). In comparison with borehole WIT01, it can be related to the Pleistocene coarse sandy aquifer. The average depth and thickness of the Pleistocene aquifer are 26 m and 50 m, respectively. From 500 m to the end of the profile, the Pleistocene aquifer resistivity ranges from 20 Ωm to 30 Ωm corresponding to medium to fine sand. From 0 m to 180 m profile distances, the absence of the Pleistocene aquifer is associated with the dominance of a medium resistivity layer (~ 8 Ωm). Regarding to the previous synthetic modeling (Fig. 5.18), it is probably associated with the presence of clay enriched materials. This layer can be also observed at borehole WIT01 for the Eemian clay but it is thinner than the western part. The second very low resistivity layer can be seen at about 70 m depth corresponding to saltwater intrusion. It is well-defined at the central part of the profile and it has ~ 2 Ωm resistivity. A smearing to the upper and lower surfaces of the Pleistocene aquifer can be observed.

Compared with the WB model, the SC model ($\lambda = 1$ and $z\text{-power} = 0.1$) exhibits some differences (Fig. 5.21 middle). Despite of differences, the results in general, but not in full, are in agreement with the information deduced by the WB model. The perched saltwater and the medium resistivity feature, at the western part, are well defined. The SC model clearly demonstrates how it can resolve a narrow horizontal structure, between 90 m and 200 m distances, that could not be easily detected from the WB model. Regarding to the synthetic modeling results (Fig. 5.18), it has been noted that the WB inversion model amplifies the vertical effect of the perched saltwater, up to ~ 4 m, more than SC model. The SC model represents the Pleistocene aquifer with warm color and high resolution in comparison with the available borehole, WIT01. The high resolution of the perched saltwater and Pleistocene aquifer can be attributed to the high data density of the SC configuration. Despite of advantages, generation of the SC model is time consuming and it represents a bad horizontal coverage. Also, the saltwater intrusion can be only defined at the central part of the model (Fig. 5.21 middle).

The combined inversion of both the WB and SC data sets ($\lambda = 50$ and $z\text{-power} = 0.1$) shows the Pleistocene aquifer and saltwater in a balanced way. As it is seen (Fig. 5.21 bottom), this model is quite similar to the WB model (Fig. 5.21 top), which “dominates” the inversion image. This can be

attributed to the higher coverage of the WB over the SC configuration. In comparison with borehole WIT01, the combined inversion model represents a better horizontal coverage than the SC model and a slightly better horizontal resolution than the WB model. The medium resistivity feature, which is observed at the western part and under the perched saltwater, can be well-defined in the form of a funnel-shaped bay. This feature may be associated with the Saalian ice age erosion which left behind isolated ice block. During the Eemian interglacial stage, the melting ice block could be stored in a small lake and deposited fine sediments of clay and silt.

Regarding to the previous synthetic modeling (Fig. 5.18), the depth of the saltwater intrusion can be corrected to be ~ 64 m, where the smearing to the upper boundary of the saltwater intrusion can reach up to 6 m. It can also be noted that this smearing increases between 200 m and 500 m profile distances of the SC and joint inversion models, where the perched saltwater and high resistivity values are present. Similarly, the depth to the upper boundary of the Pleistocene aquifer can be corrected to ~ 22 m, i.e., ~ 4 m smearing. This can be proved by the comparison with the borehole WIT01, which assigns the aquifer at 22 m depth, and the previous synthetic model results. The deduced geoelectrical model produced by the joint inversion combined the characteristics of both the WB and SC geoelectrical models and exhibits a more effective model. Despite of the anthropogenic features (e.g., metal pipes etc.) at this site, the inversion results exhibit acceptable RMS errors.

Figure 5.22 shows the HEM inversion results in the form of a 2D resistivity section near to the 2D DC profile (line 1, Fig. 5.12). It is quite evident that this section is almost identical to the 2D DC inversion results (5.21). From the 2D DC imaging than from the HEM resistivity section, a higher resolution of the saltwater layers and the Pleistocene aquifer can be observed. The deep low resistivity ($< 3 \Omega\text{m}$) layer of the saltwater intrusion can be observed at about 60 m depth on the right of the section. It can not be detected on the left of the profile, which can be attributed to the diffusion of EM waves due to the presence of the perched saltwater.

The HEM resistivity section represents the saltwater intrusion shallower than the 2D DC inversion results. This can be attributed to the smearing effect which can be observed in 2D imaging, as we discussed above. Similar to the 2D DC inversion results, a low resistivity feature can also be observed on the left of HEM section, which was interpreted as Eemian clay layer. Outside the area of Eemian clay and towards the eastern part, there is a good fit between the very high resistivity layer of green color ($> 40 \Omega\text{m}$; borehole WIT01) and the coarse sandy Pleistocene aquifer. Further to the east of the profile, this aquifer represents medium resistivity values ($15 \Omega\text{m} - 25 \Omega\text{m}$) corresponding to medium to fine sand, yellowish color.

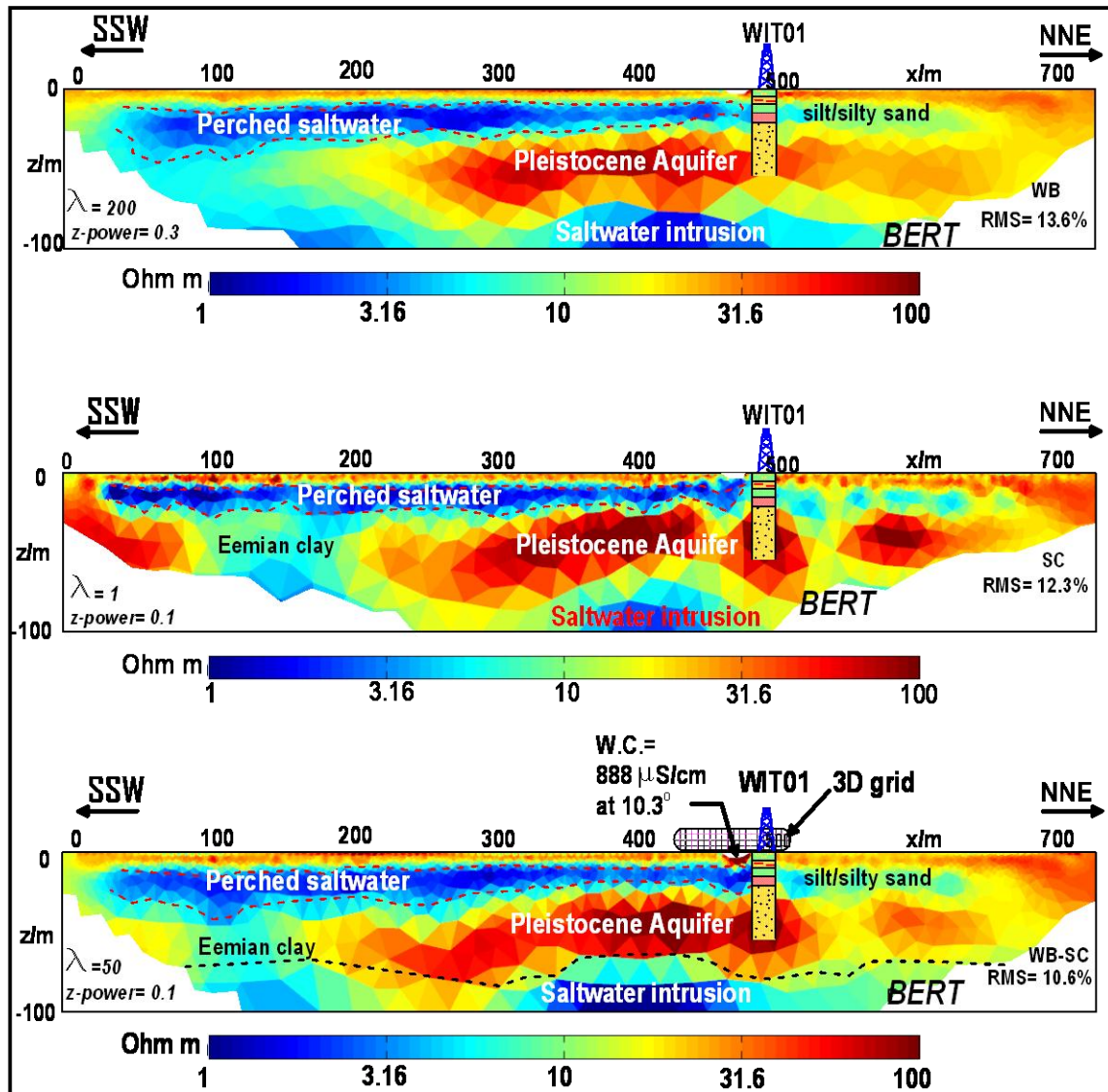


Fig. 5.21: Inversion results: (top and middle) Inverse model resistivity sections obtained by WB and SC data sets, respectively. (bottom) Combined inverse model obtained by WB and SC data sets, λ and $z\text{-power}$ are the used regularization parameters.

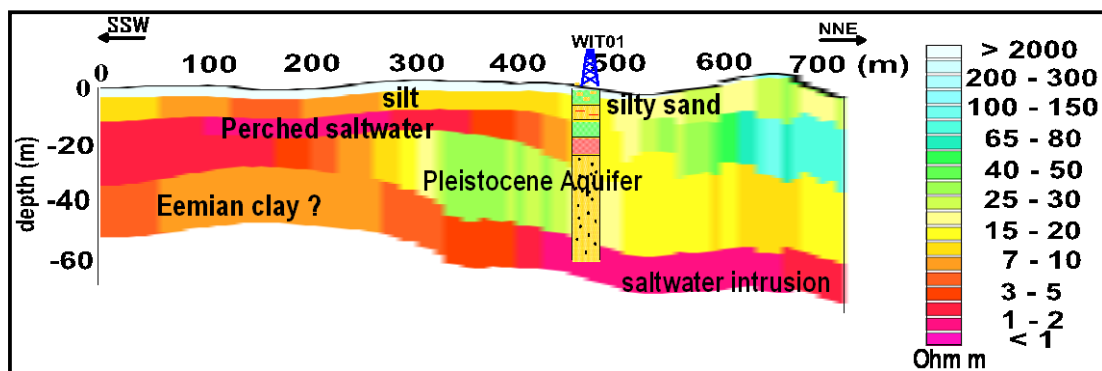


Fig. 5.22: HEM resistivity section (Siemon et al., 2004) showing saltwater intrusion, the freshwater aquifer and the perched saltwater. Note inversion of colours in resistivity with respect to convention in this thesis.

Model Reliability and Regularization Parameters

Given that usually the interpreter, due to limited prior information, is unable to judge which inversion result is best, a sensitivity analysis has been carried out. The coverage plots demonstrate the zones for which the data are sensitive to the changes in resistivity values, see section (3.3). The zones of higher coverage values indicate that the reliable resistivity model can be derived from inverted data (Günther, 2004). The penetration depth of each configuration was taken as the maximum depth of the sensitive area of the data and beyond this depth the data has no capability to resolve the heterogeneity between sedimentary layers. Fig. 5.23a represents the coverage plots for combined WB and SC data sets model. The individual WB and SC coverage plots are shown in Appendix D. The WB, SC and combined WB and SC sensitivity models show that the depth of investigation is 100 m, which is sufficient to cover the freshwater Pleistocene aquifer.

The coverage model of the combined WB and SC data sets represents a better horizontal and vertical coverage than that of the individual WB and SC configurations. The sensitivity analysis demonstrates that the combination of WB and SC will provide more reliable results than the individual configurations. The SC sensitivity model shows higher coverage values (~ 5) than the WB model at shallow part, until about 40 m depth, but with increasing depth this high sensitivity will concentrate at the central part of the SC model, which does in line with the bad horizontal coverage (Fig. 5.23a). On the contrary, the WB model shows a better horizontal coverage than the SC model with increasing depth.

The regularization parameters (λ and *z-power*) were changed until the best data fit, i.e., low RMS, and good correlation with the borehole data and previous HEM results were obtained. According to the geological situation in our study area, we started the inversion process for WB, SC and combined WB and SC data sets using $\lambda=200$ and *z-power*= 0.01 (default parameters). Then, the regularization parameter λ was decreased to be 10 for getting rough-textured models (see subsection 4.4.2). It is noted that with decreasing λ the SC model shows a new layer at about 80 m depth, which can be correlated to the saltwater intrusion. Consequently, the improvement of the SC model can be expected with decreasing the regularization parameters. On the other hand, both WB and combined WB and SC data set show a data misfit, i.e., RMS, with decreasing λ value. According to these attempts, the optimum regularization parameters (λ and *z-power*) were selected by performing a numerical experiment using for each data set.

Figs. 5.23b shows the effect of regularization parameters on the combined WB and SC data sets model. Compared with HEM and geological data, it is clear that all models of combined WB and SC data sets using different regularization parameters retain the shallow conductive features of the perched saltwater and the Eemian clay structure. As shown in Fig. 5.21, the best inverted models with the best RMS values using the optimum regularization parameters were selected for data interpretation.

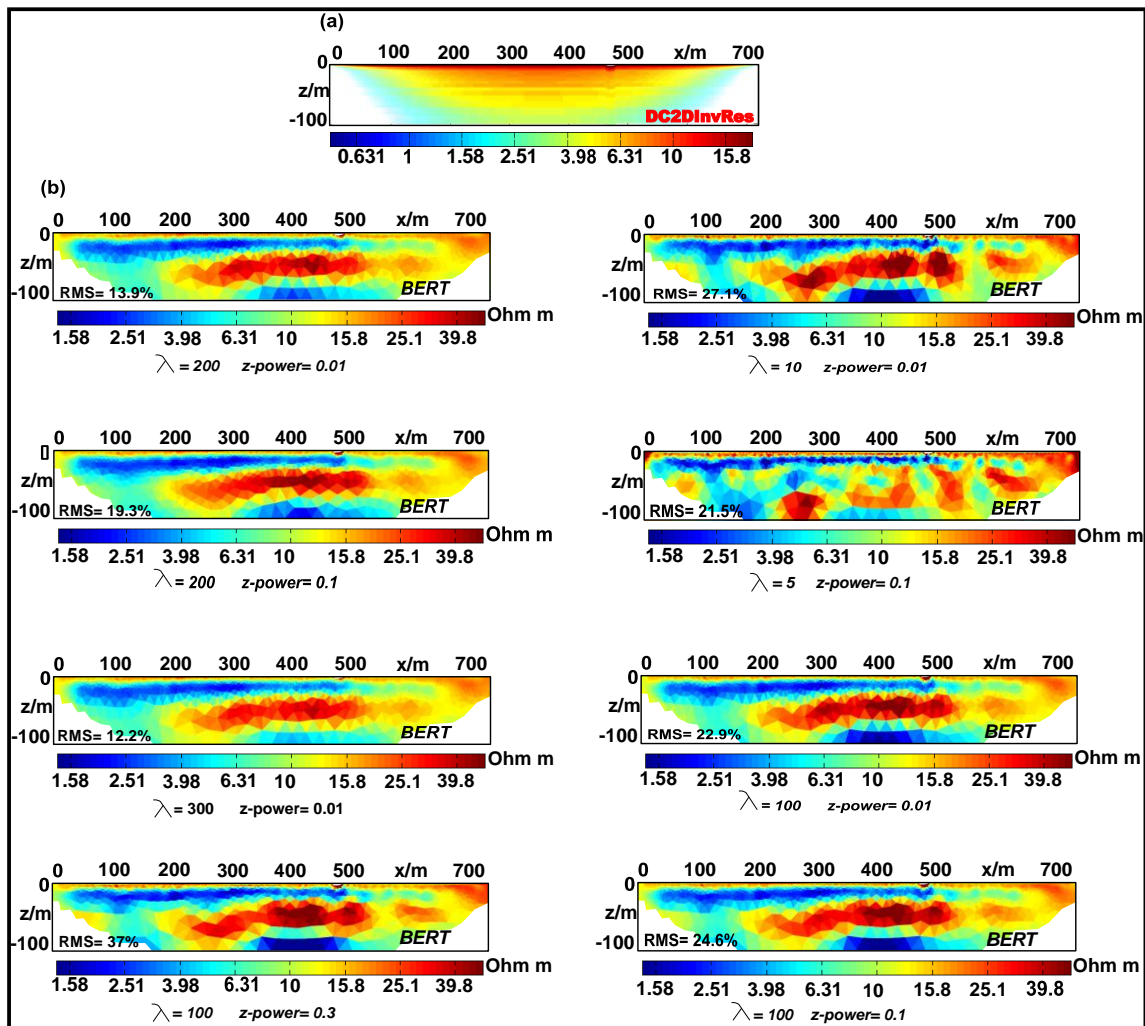


Fig. 5.23: (a) Coverage plot and (b) inversion results for 8 selected regularization parameters, λ and z-power, for combined WB and SC data sets.

5.4.2.3 2D DC INVERSION RESULTS (LINE 2)

The above described joint inversion of WB and SC data sets was applied also over “line 2” situated perpendicular to “line 1” (Fig. 5.12). Because of presence of a buried electrical power line and a drainage lake, high levels of noise and an apparent 3D effect were expected. At well SET05, a brackishwater was detected at ~2 m depth (1600 $\mu\text{S}/\text{cm}$) and saltwater at ~5 m depth (11000 $\mu\text{S}/\text{cm}$). Here, we aimed to follow the extension of the perched saltwater, which was observed over “line 1”, and to image the Pleistocene freshwater-saltwater boundary. Because of using the roll along method, the WB raw data represents 12 times of overlapping data process (see subsection 3.1.4.1).

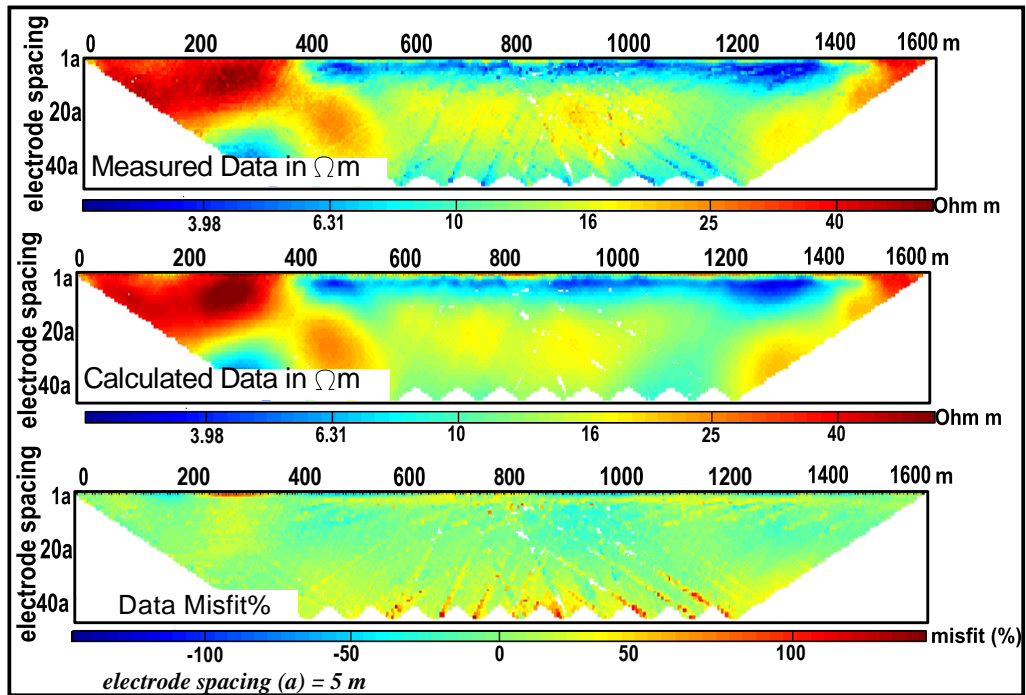


Fig. 5.24: WB 2D DC pseudo-section (line 2, see Fig. 5.12) of the measured apparent resistivity (top panel), calculated resistivity (middle panel) and relative difference between them (bottom panel).

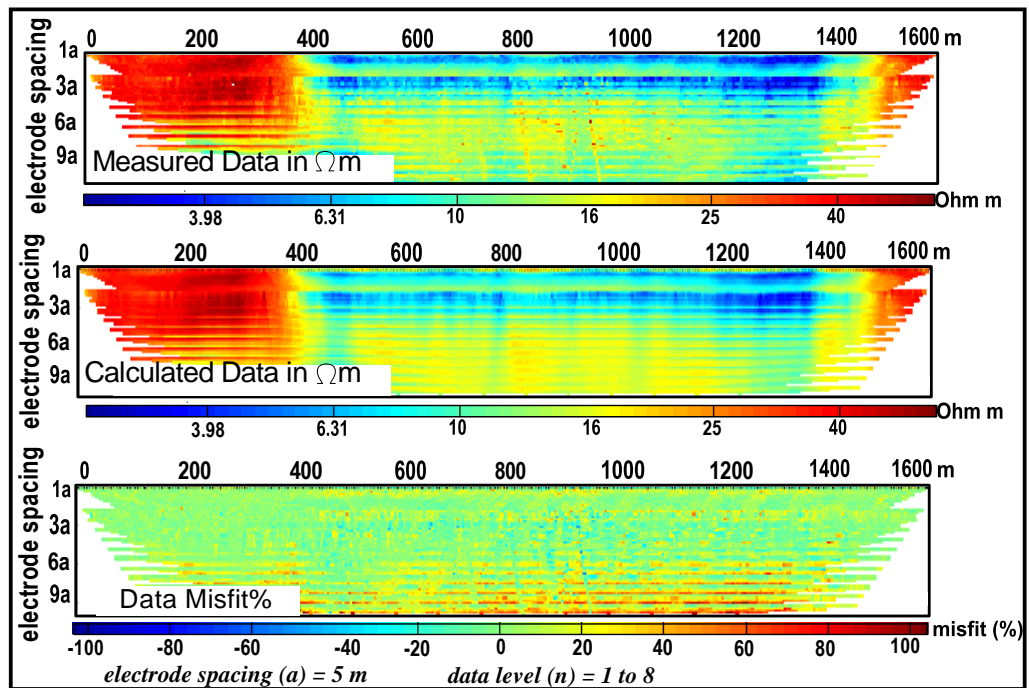


Fig. 5.25: SC 2D DC pseudo-section (line 2, see Fig. 5.12) of the measured apparent resistivity (top panel), calculated resistivity (middle panel) and relative difference between them (bottom panel).

The measured apparent resistivity data for WB and SC (Fig. 5.24 top and 5.25 top) represents in general the same features which were observed over "line 1" (Figs. 5.19 top and 5.20 top). The upper low resistivity layer can be observed from $\sim 400\text{ m}$ and $\sim 1400\text{ m}$ profile distances. In

addition, a high apparent resistivity values can be observed between 0 m and ~400 m profile distances. Clearly, the noise level increases with increasing electrode separation. This can be attributed to longer cable layouts and smaller measured potentials which decrease the signal-to-noise ratio. It has been noted that the misfit error with increasing electrode separation of SC configuration is greater than WB.

In addition to the medium resistivity surface layer corresponding to silt and sandy silt (~4 m thickness), the inverted sections of the WB and SC configurations (Fig. 5.26 top and middle) show three main geoelectrical layers. Based on the borehole data and the hydrogeological background, they can be associated with three hydrogeophysical units. First, the upper very low resistivity unit ($< 3 \Omega\text{m}$) can be associated with the perched saltwater. Its depth ranges between 4 m to 9 m. Its maximum thickness is 16 m (at well WIT01). It is easier to follow the perched saltwater from the SC inverted model than from the WB model, which can be attributed to its higher sensitivity at shallower parts (see subsection 5.4.2.2). The perched saltwater is observed between 400 m and 1500 m profile distances. In comparison with the borehole data, it is observed that there is a strong relation between the presence of perched saltwater and Eemian clay, i.e., the perched saltwater is concentrated above the Eemian clay. The perched saltwater covered by a $\sim 12 \Omega\text{m}$ resistivity layer corresponding to Holocene tidal sediments of silt and sandy silt. On the left of the profile and in comparison with borehole BUL01, the absence of the perched saltwater is replaced by a medium resistivity layer ($25 \Omega\text{m}$ to $30 \Omega\text{m}$). It is probably associated with the dominance of fine sand to silty sand sediments. In general, the results are in agreement with the available borehole information. Second, the high resistivity unit ($> 38 \Omega\text{m}$) can be associated with the freshwater Pleistocene aquifer. Its thickness ranges from ~45 m (at the western part) to ~55 m (at the eastern part). Third, the lower hydrogeophysical unit is characterized by low resistivity values which can be associated with the saltwater intrusion. Its depth ranges from ~62 m up to ~76 m. The WB configuration shows, quite well, the saltwater intrusion depths with a good resolution and horizontal coverage. The SC configuration neither shows the depth variations of the saltwater intrusion nor its true resistivity.

The joint inversion model of WB and SC data sets (Fig. 5.26 bottom) depicts the perched saltwater, Pleistocene aquifer and saltwater intrusion satisfactorily. The perched saltwater and saltwater intrusions are well detected, without amplifying effect, better than by the individual WB configuration. A better horizontal coverage than for the SC configuration can be observed. In spite of using the same optimum regularization parameters of the SC configuration, this model is quite similar to the results of the WB configuration, which dominates the inversion result. Although different, it is difficult to say which of the WB and combined WB and SC data sets reconstructs the better model. In fact, the RMS errors of the combined data sets is slightly larger than for the individual WB and SC data which can be attributed to a high data density and the attempt of the program algorithm to combine information of different configuration types.

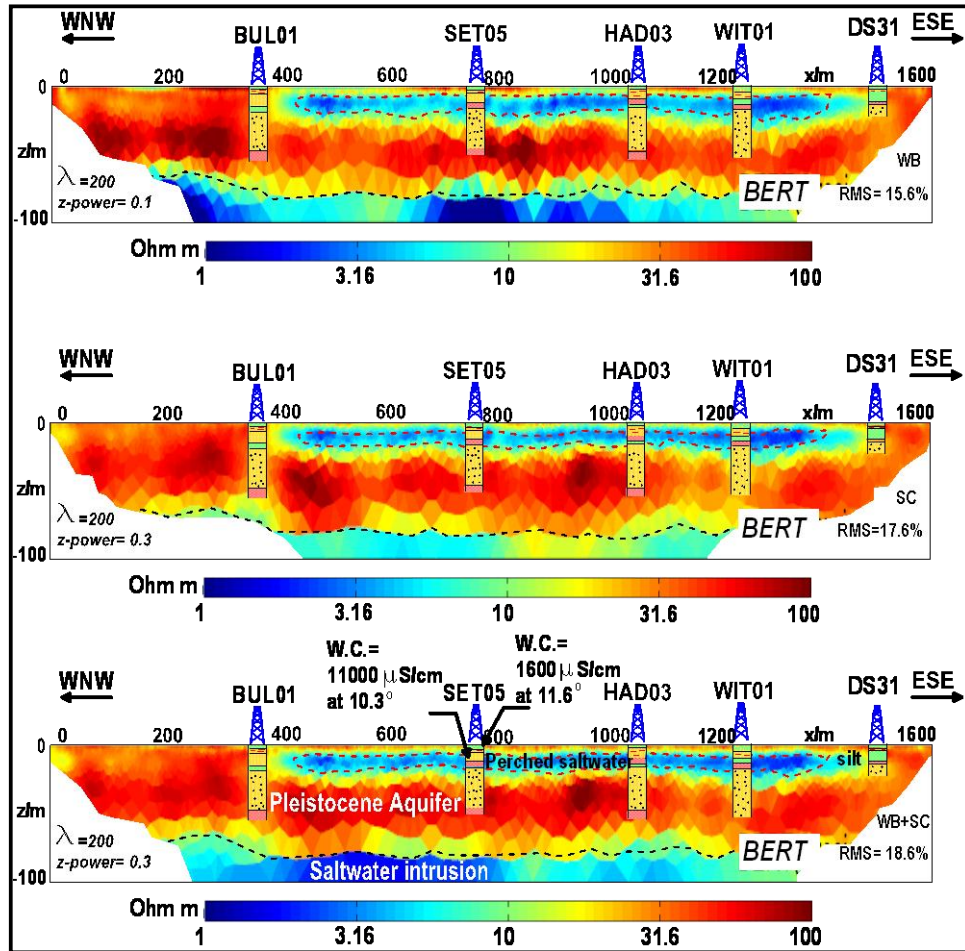


Fig. 5.26: Inversion results: (top and middle) Inverse model resistivity sections obtained by WB and SC data sets, respectively. (bottom) Combined inverse model obtained by WB and SC data sets with optimum regularization parameters (λ and z -power).

3D Visualization and HEM Inversion results

Fig. 5.27 shows the 2D DC resistivity imaging over the Norderscheidung site, line 1 and line 2, in the form of a fence diagram. It represents the extension of the perched saltwater and the depth of saltwater intrusion. It is clear that the perched saltwater is absent towards WNW and NNE directions. The average depth and thickness of the Pleistocene aquifer, respectively, is about 20 m and 55 m and the average depth of the saltwater intrusion is 70 m. The freshwater aquifer thickness and the water quality increases towards the WNW direction.

Fig. 5.28 shows a long HEM resistivity section (3300 m) which runs from NNW to ESE directions (Fig. 5.12). It runs parallel to the DC sounding points at this site (see geoelectrical cross-section C2, Fig. 5.4). Fig. 5.28 shows the location of the 2D DC profile, line 2, in comparison with the HEM section. Similar to the DC inversion results, the HEM section represents the upper shallow very low resistivity layer ($< 3 \Omega\text{m}$), which is interpreted as the perched saltwater. The upper surface layer represents a wide range of resistivity values corresponding to silt ($10 \Omega\text{m}$ to $15 \Omega\text{m}$) and fine to

medium sand ($15 \Omega\text{m}$ to $40 \Omega\text{m}$). The silty surface layer can be observed on the left of the section, which covers the perched saltwater, while the sandy surface layer can be observed on the right side. The high resistivities, colored green to blue ($> 40 \Omega\text{m}$), indicate Pleistocene coarse sandy material. The yellowish to orange colored areas of medium resistivity ($10 \Omega\text{m}$ to $20 \Omega\text{m}$) correlate with Lauenburg clay and/or brackishwater sand, which was observed from the available boreholes. The deeper low resistivity layer ($3 \Omega\text{m}$) can be interpreted as saltwater intrusion from the Elbe River. The average depth of the saltwater intrusion is 60 m. Similar to the discussed short HEM section (Fig. 5.22), regarding the appearance of the perched saltwater, the saltwater intrusion can not be observed. In general, the HEM results are in agreement with the DC inversion results. The detection of the saltwater intrusion depth and the thickness of the freshwater aquifer can be easily detected from the DC inversion results.

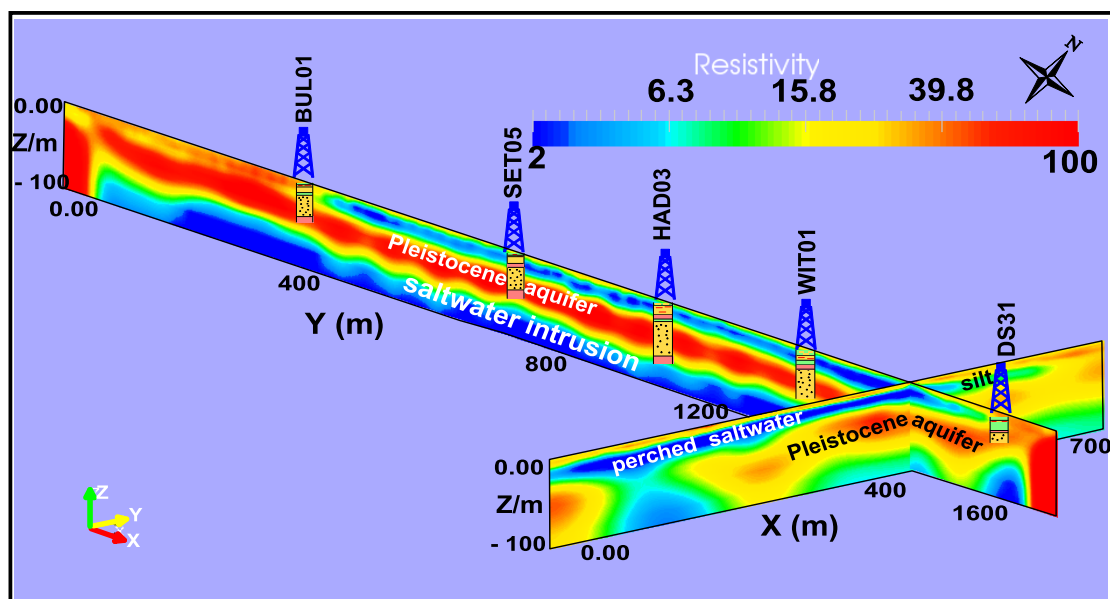


Fig. 5.27: Fence diagram showing the relation between Norderscheidung 2D resistivity sections (Line 1 and Line 2, see Fig. 5.12).

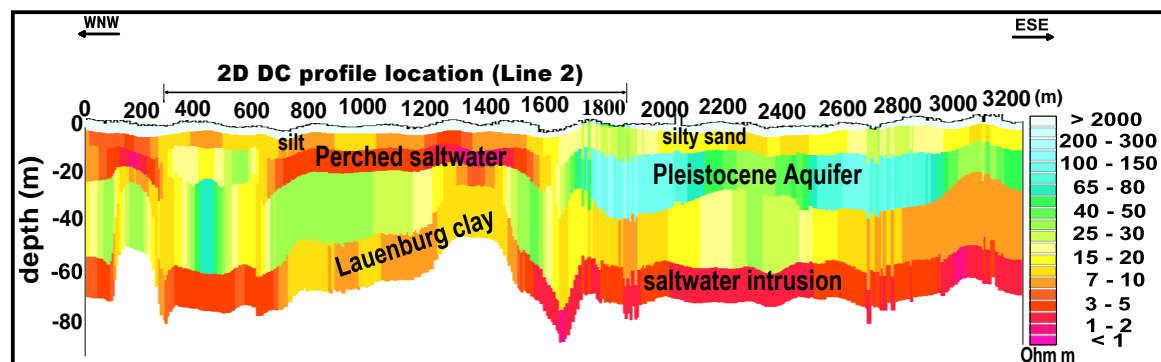


Fig. 5.28: HEM resistivity section (Siemon et al., 2004) showing the location of 2D DC profile (Line 2, Fig. 5.12), perched saltwater, Pleistocene aquifer and saltwater intrusion. Note the reverse colour coding for resistivity data.

5.4.3 3D DC RESISTIVITY IMAGING

The 3D visualization of the 2D DC profiles (line 1 and line 2) show that the perched saltwater are replaced by silt and fine sediments towards NNE and ESE directions (Fig. 3.29). At the transition zone between the perched saltwater and the dominance of fine sediments, 3D WB, PP and DD surveys were carried out. Fig. 5.29 shows the position of the 3D model with respect to the 2D profiles and the fitting between the 2D and 3D inversion results. The 3D WB and PP data sets were inverted using the BERT software. Because the DD data bear a high noise level and a strong processing is required (see 4.4.2), DC3DInvRes software was used to invert the 3D DD data set. The forward modeling process using the FD method is faster and less sensitive to noise than the FE method. Because of the huge number of DD data points, the FD method was used for forward calculations to introduce a smooth reliable model.

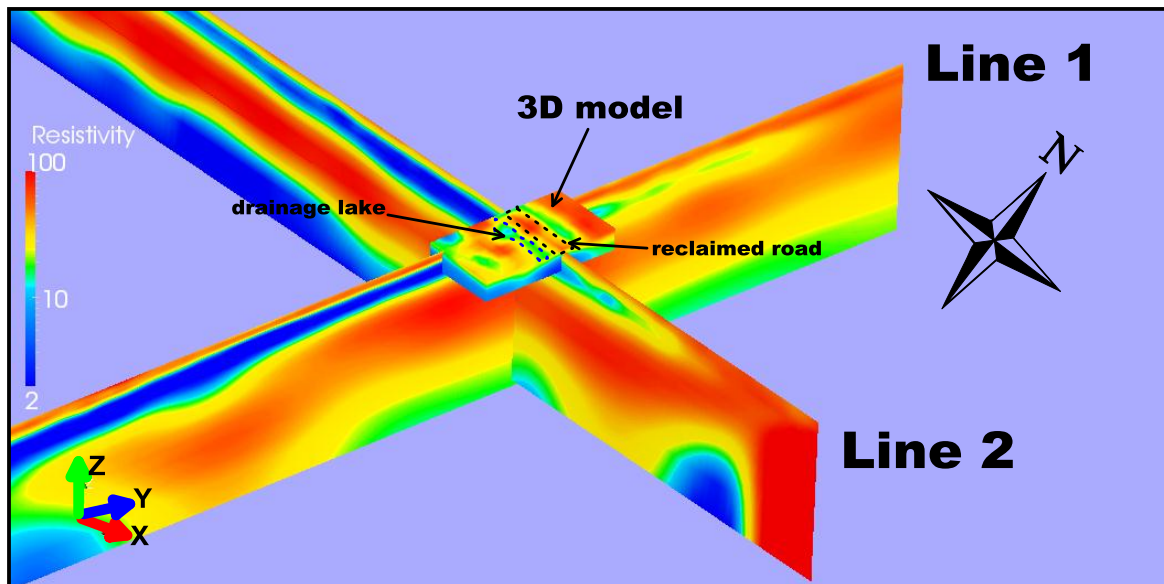


Fig. 5.29: A fence diagram showing the 3D WB model in comparison with the 2D DC resistivity profiles (Line 1 and Line 2, see Fig. 5.12) at Norderscheidung (using DC2DInvRes and DC3DInvRes programs).

Fig. 5.30 depicts the 3D WB inversion results in the form of horizontal sections in y- and x-directions. The maximum depth of the model is 15 m. The analysis of the 3D sections shows two well-defined geoelectrical layers. A near surface layer presents medium resistivity values ($\sim 20 \Omega\text{m}$) associated with sandy silt to sandy silt materials. Underlying this layer a very low resistivity layer ($< 3 \Omega\text{m}$) can be observed, which is associated with the perched saltwater. The horizontal sections in y-direction (Fig. 5.30 top) indicate that the perched saltwater moves in a wedge-like feature, it becomes deeper towards the SSW than towards the NNE direction. It is clear that the perched saltwater can not be observed at NNE direction where the silt and sand silt materials are dominating. Regarding to the HEM and 2D DC resistivity results, these materials act as barrier to the perched saltwater extension. The horizontal slices in x-direction (Fig. 5.30 bottom) show that the perched saltwater moves from

WNW to ESE directions. At the eastern corner of the model, at 70 m model distance (in x-direction), the perched saltwater is completely absent and the medium resistivity layer can be well-defined. Fig. 5.30 bottom shows variations in the thickness and resistivities of the near surface layer. Both sections (Fig. 5.30 top and bottom) show that the upper surface layer is highly inhomogeneous and its resistivity can change rapidly in a short distance. In general, the sections represent high resistivity values at the eastern corner of the model which corresponds to fine sand and silty sand. The high surface resistivity values ($> 38 \Omega\text{m}$) at around 50 m model distance, in X-direction, can be attributed to fine and medium sand sediments of the reclaimed road (Fig. 5.29).

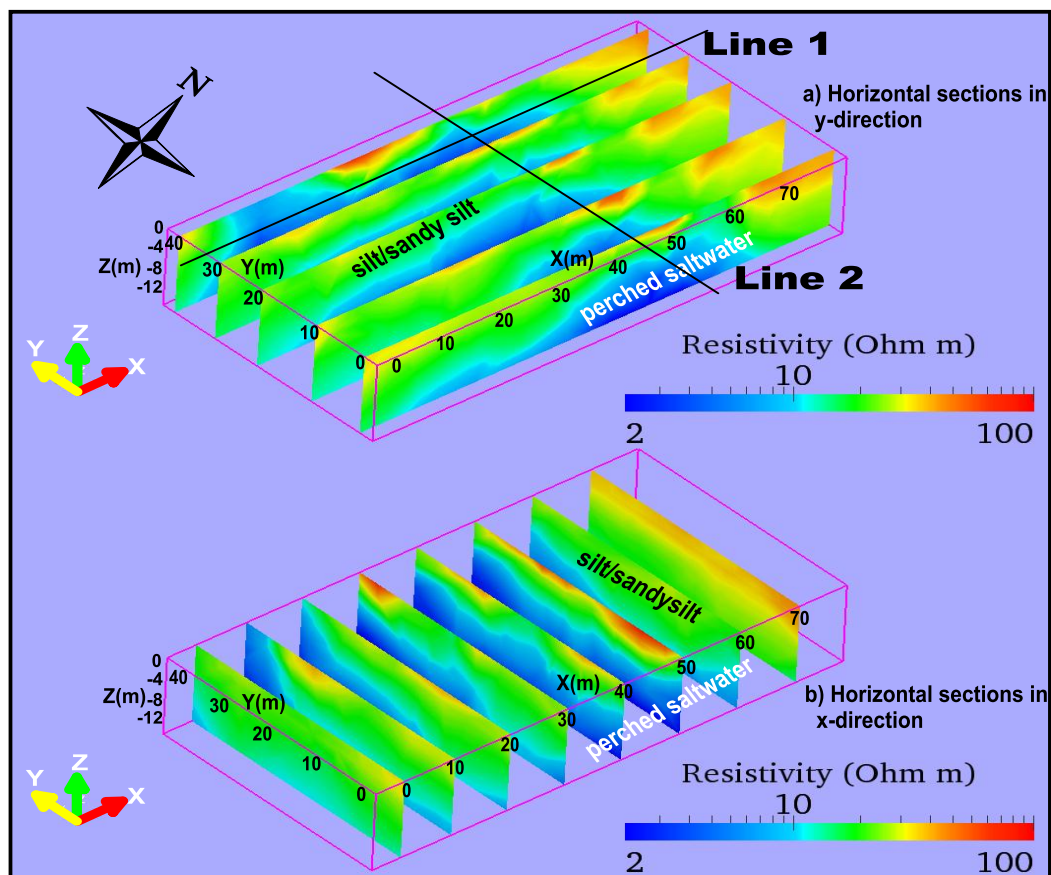


Fig. 5.30: 3D inverted model, of eight orthogonal WB profiles, in the form of horizontal sections in y-(top) and x-directions (bottom). Line 1 and Line 2 are the locations of 2D DC profiles (see Fig 5.12).

Figs. 5.31 and 5.32, respectively, show 3D inversion results of PP and DD data sets. As it is observed, all inverted models are quite similar to the 3D WB model (Fig. 5.30). They show the extension of the perched saltwater and the upper near surface resistivity layer. Similar to the WB model, it is seen that there is heterogeneity within the upper surface layer. Between ~ 10 m and ~ 35 m of 3D PP model distances (in y-direction), high resistivity values ($> 30 \Omega\text{m}$) of the surface layer can be observed. Based on our field observation, the resistivity values of this layer are not reliable, which is due to the poor resolution of PP configuration at a depth less than 1 m with using 5 m electrode spacing.

The comparison of the 3D DD sections with the PP and WB models shows that the DD model has the best horizontal resolution. It shows that the top upper resistivity layer has a variation in resistivity values which ranges from $\sim 20 \Omega\text{m}$, which corresponds to silt to sandy silt, to $\sim 30 \Omega\text{m}$ corresponding to fine to medium sand. The DD model also displays a clear picture for the perched saltwater and the model represents a good matching between the 2D DC profiles and the HEM results. On the contrary, a poor horizontal resolution can be observed at the eastern corner of the PP model where high resistivity values can be noticed. Obviously, DD produces the best image followed by WB and then PP. Finally, the three models support each other and they show a good correspondence with the nearest borehole data (WIT01) and other geophysical results.

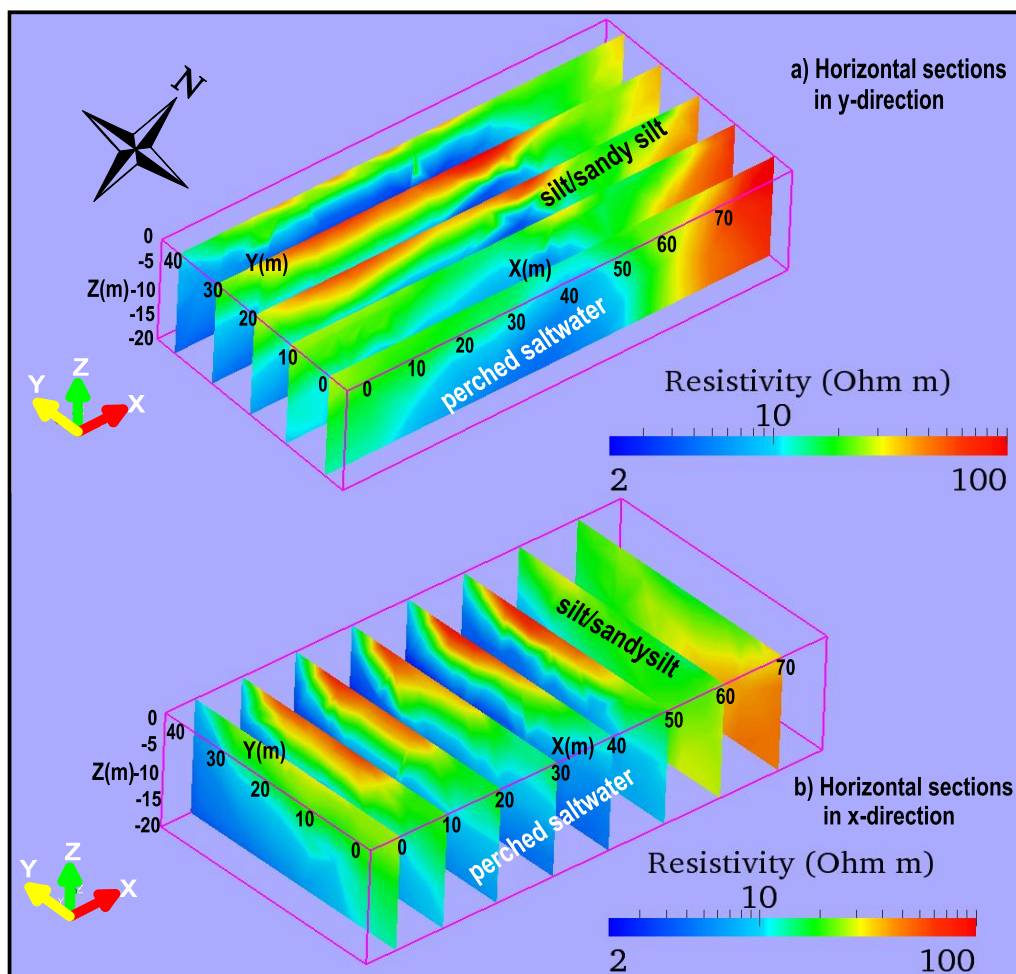


Fig. 5.31: 3D inverted model of PP data in the form of horizontal sections in y-(top) and x-directions (bottom).

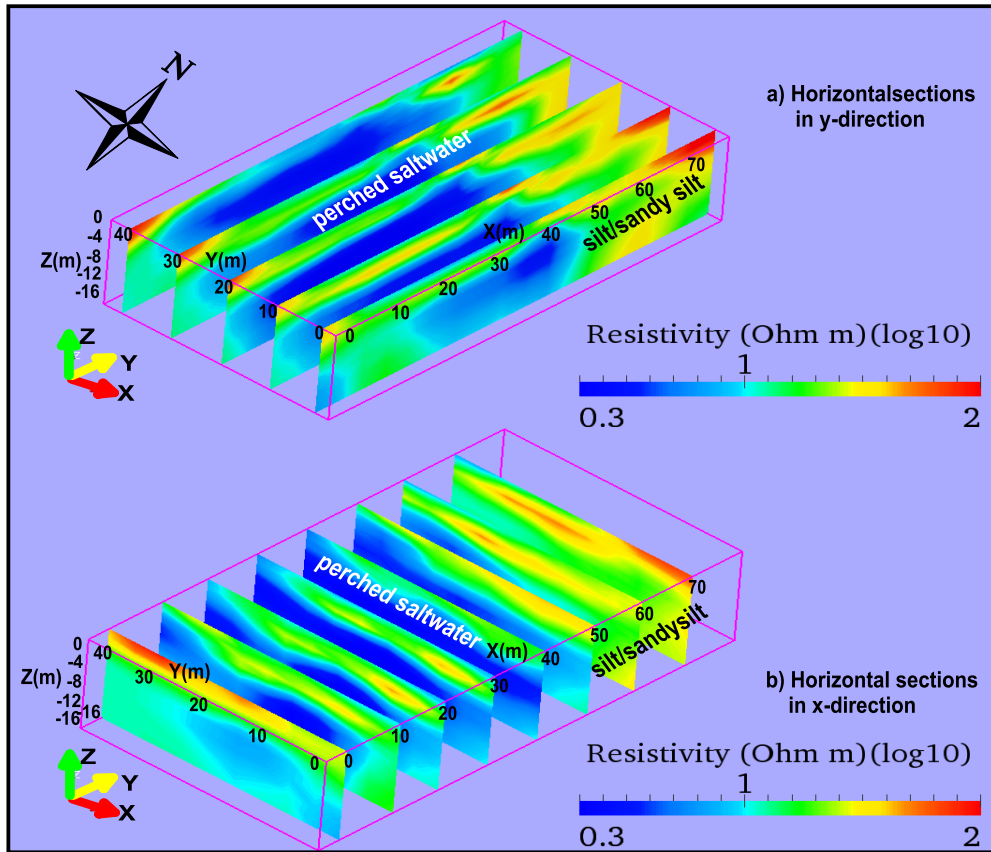


Fig. 5.32: 3D inverted model of DD data in the form of horizontal sections in y-(top) and x-directions (bottom).

5.5 SÜDERSCHIEDUNG DATA INTERPRETATION

The Süderscheidung site located at Lüdingworth area is named “C”. The geophysical measurements (DC and FDEM soundings and 2D DC and SIP profiling) and the borehole locations are shown in Fig. 5.33.

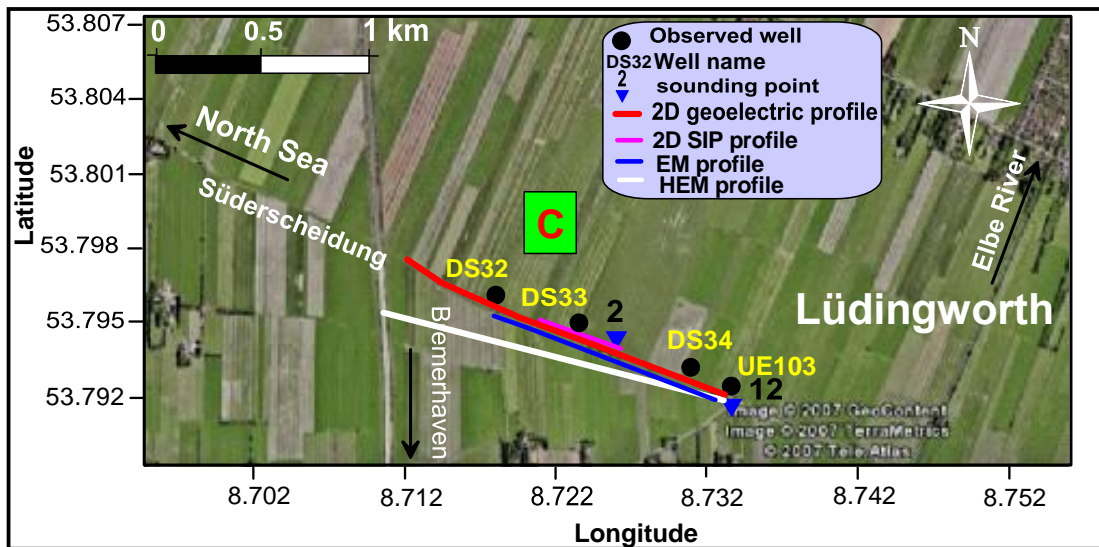


Fig. 5.33: Location map of the Süderscheidung site (named C) showing the geophysical measurements (inset map © Google Earth).

Fig. 5.34 shows the subsurface tidal sediments at this site, derived from borehole information. The major difference between these boreholes is the thickness of the clay layer. The intercalated peat horizons are an evidence of different regression phases along this coastal area (Streif, 1982). Geologically, the shallow tidal aquifer, Holocene and upper Pleistocene (Weichselian sand and Eemian clay) deposits, consists mainly of silt, sandy silt, clay and fine sand. Younger tidal channels eroded the Holocene sediments and cut down into the basal peat. Here, we aim to characterize and image the main shallow sedimentary features and the perched saltwater layer within the tidal flat deposits. Also, the saltwater intrusion and freshwater Pleistocene aquifer will be addressed.

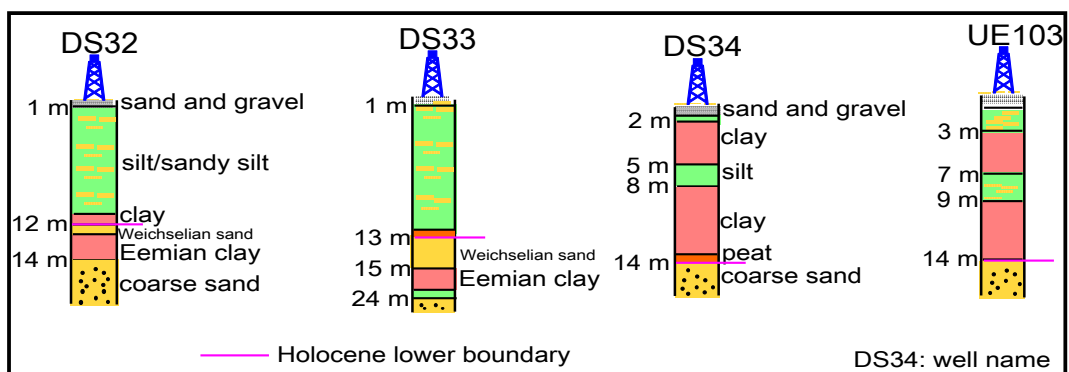


Fig. 5.34: Lithology at the boreholes DS32, DS33, DS34 and UE103, Süderscheidung site.

5.5.1 1D INTERPRETATION

In addition to the measured DC resistivity soundings (see subsection 5.1.2), FDEM soundings were measured at this location. Both DC and FDEM soundings will be discussed in detail in this subsection. The processing and inversion steps of DC and FDEM soundings were discussed in the former chapter (see subsection 4.4.1).

Models for 1D resistivity soundings show curves exhibiting different geoelectrical layers (Fig. 5.35). The upper surface layer is characterized by high resistivity values ($> 100 \Omega\text{m}$) with 0.8 m maximum thickness, corresponding to recent unconsolidated deposits (sand and gravel). It overlays a medium resistivity layer, which has thickness and resistivity values ranging from 10 m to 11 m and $8 \Omega\text{m}$ to $13 \Omega\text{m}$, respectively, corresponding to Holocene silt, clay and sandy silt. This layer overlays a thin high conductivity layer at sounding no. 1 corresponding to saltwater saturated sand (borehole DS33); but it overlays a high resistivity layer ($40 \Omega\text{m}$) at sounding no. 2, which corresponds to coarse sand (borehole UE103). At sounding no. 2, the high conductivity layer ($2 \Omega\text{m}$) rests on a medium resistivity layer ($17 \Omega\text{m}$), which reflects the presence of a perched saltwater over an impermeable layer of Eemian clay (aquiclude) (DS33). These last two layers of medium and low resistivity values are absent at sounding no. 12. At sounding no. 2, the high resistivity layer, which was also observed at borehole UE103, is deeper (~ 23 m depth) than at sounding no. 12 with a higher resistivity value of 72

Ωm . It overlies a low resistivity layer ($3 \Omega\text{m}$) at about 70 m depth reflecting saltwater intrusion (borehole UE103). Geologically, the upper boundary of the high resistivity coarse sandy layer ($40 \Omega\text{m}$ to $72 \Omega\text{m}$) is considered a base to the tidal flat deposits.

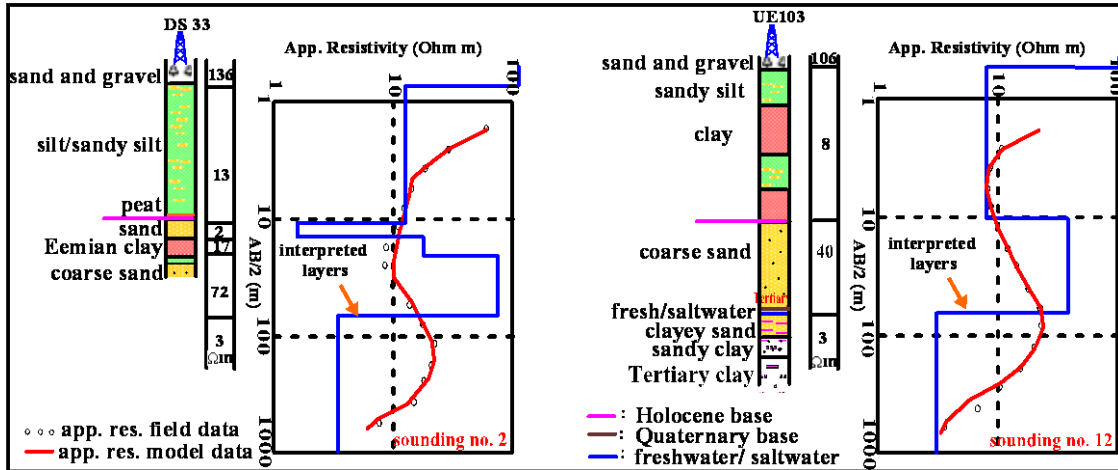


Fig. 5.35: Correlation between the interpreted resistivity layers and observed borehole data at soundings no. 2 (left) and 12 (right).

Here the FDEM method was applied to augment 1D DC results by constructing a 2D cross-section from stitched 1D FDEM soundings. According to the inversion results along the test profile (see subsection 4.4.1), the FDEM data have been sampled using 50 m and 10 m coil separation and station interval, respectively. The inphase and quadrature raw data (Fig. 5.36) show only significant lateral variations for the five highest frequencies. At lower frequencies (110 Hz, 220 Hz and 440 Hz) a little or no perceptible inphase or quadrature response can be observed. In general, at higher frequencies (880 Hz, 1760 Hz and 3520 Hz) a broad positive inphase anomaly and a negative quadrature response with positive shoulders can be noticed.

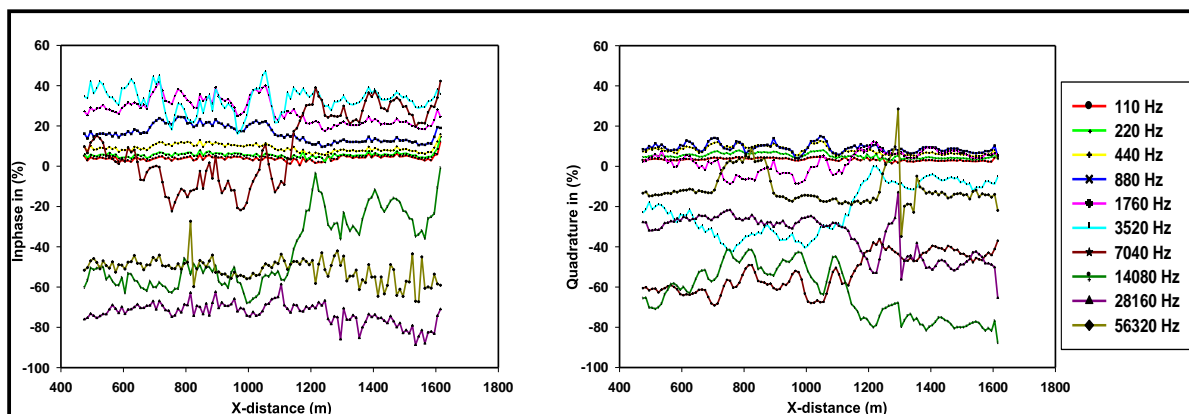


Fig. 5.36: FDEM raw data: Inphase (left) and quadrature (right) components for different frequencies.

A good starting model for the inversion process was derived from the nearest four EM soundings in the available boreholes. The inversion was carried out using Ridge regression in a multiple iteration mode (see subsection 4.4.1). Beginning from these reference soundings and using a kind of recursive starting modeling (which means the inversion result of the previous sounding is used as starting model for the present one), a stitched resistivity section could be correctly constructed. An example of 1D inversion results of the FDEM soundings is shown in Fig. 5.37. Fig. 5.37 (left) shows the raw data (inphase and quadrature components) of EM sounding no. 34. The starting model was derived from borehole DS33 and DC sounding no. 2 (Fig. 5.37, right). The comparison between the 1D inversion results of both DC and FDEM surveys is shown in Fig. 5.37 (middle). The calculated model, considering a five-layer starting model, shows an acceptable fit with the raw data (Fig. 5.37, left). At low frequencies, the fit between the measured quadrature data and the computed model is better than for the inphase component. This can be attributed to the linear relation between the quadrature component and the low to moderate conductive layer (*McNeill, 1980*) and/or presence of noisy inphase field data. On the other hand, at higher frequencies, the computed models of quadrature and inphase components show a bad fit with the measured data (Fig. 5.37, left).

The misfit between measured data and the computed model at the highest frequencies can be interpreted as a result of coupling effect. Regarding the DC inversion results at sounding no. 2, a thin high conductivity layer can be observed between two medium resistivity layers (Fig. 5.37, middle). This corresponds to the perched saltwater, which is embedded between the peat and Eemian clay (Fig. 5.37, right). The 1D EM inversion results show two medium resistivity layers (Fig. 5.37, middle): (a) The upper medium resistivity layer ($11 \Omega\text{m}$) which is covered by a high resistivity layer ($> 100 \Omega\text{m}$) corresponding to near surface sand and gravel sediments; (b) the lower medium resistivity layer ($9 \Omega\text{m}$) corresponding to tidal deposits (fine sand, Eemian clay and silt) which overlays a high resistivity layer, corresponding to coarse sand. In general, the inverted data show good results, although not in full, with the observed borehole and 1D DC sounding results (Fig. 5.37, middle).

The high conductivity layer, corresponding to the perched saltwater, appears shallower in the EM layered-earth model than in the DC inversion results (Fig. 5.37, middle). This probably can be attributed to the higher sensitivity of the EM method to the conductive layer than for the DC soundings. The EM technique cannot distinguish between saltwater saturated Weichselian sand and Eemian clay, they appear as one geoelectric layer. This is because its peak response comes from shallower sediments and/or both layers have high conductivity values with insignificant thickness relative to depth. Because the EM effective exploration depth is approximately 0.5 to 1.5 times the intercoil spacing for the vertical dipole mode (*McNeill, 1980*), the DC sounding (Fig. 5.37, middle) resolves one layer more ($3 \Omega\text{m}$) than the EM inversion.

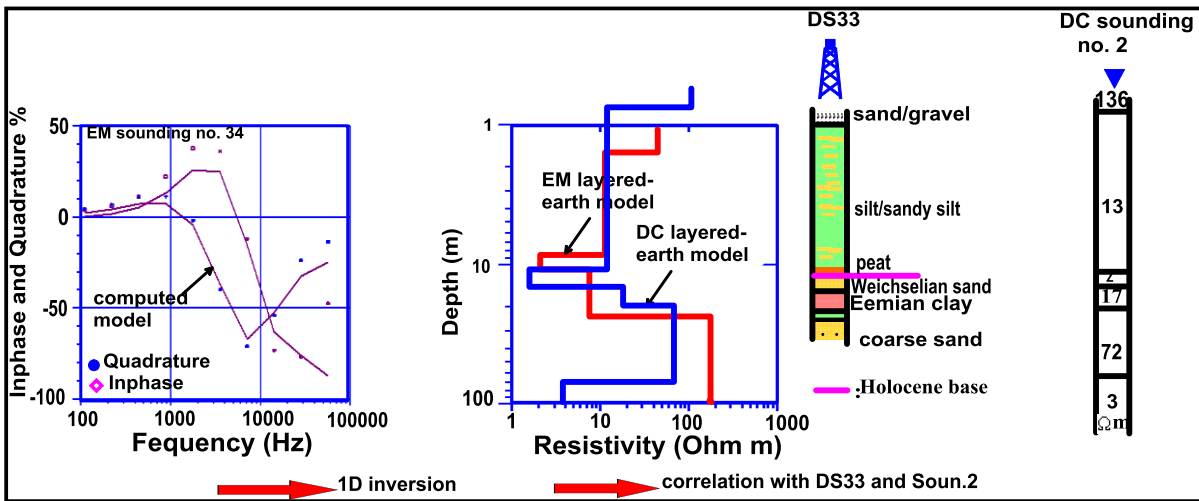


Fig. 5.37: An example of FDEM sounding data (inphase and quadrature) for different frequencies (left) and the 1D inverse model (middle) results in correlation with borehole no. DS33 and DC sounding no.2 (right).

The results obtained from the inversion of 115 EM soundings, which were measured along a profile extending from west to east direction (Figs. 5.33), are used to construct a geoelectric cross-section (Fig. 5.38) by stitching the 1D inversion results. Most of the data misfits fluctuate around 8 RMS%, but generally don't exceed 16 RMS%, for all soundings (Fig. 5.39). The geoelectric cross-section consists of five layers with 40 m maximum depth. The first layer, which corresponds to surface sand and gravel sediments, has a resistivity value and thickness of 60 Ωm and 1.5 m, respectively. The second layer, which corresponds to Holocene tidal deposits of silt, sandy silt and clay, shows medium resistivity values ranging from 10 Ωm to 35 Ωm and thickness within the range of 3 m to 7 m. The third layer has low resistivity values ($< 3 \Omega\text{m}$) corresponding to a perched saltwater layer and its thickness ranges from 3 m to less than 1 m within the Holocene tidal deposits. The fourth layer has moderate resistivity values (8 Ωm to 20 Ωm) and its thickness ranges from 8 m to 18 m. This layer is associated with clay containing intercalations of sand and silt. The fifth layer shows a high resistivity value ($> 100 \Omega\text{m}$) representing a coarse sandy layer. The depth of this layer varies from 14 m to 26 m.

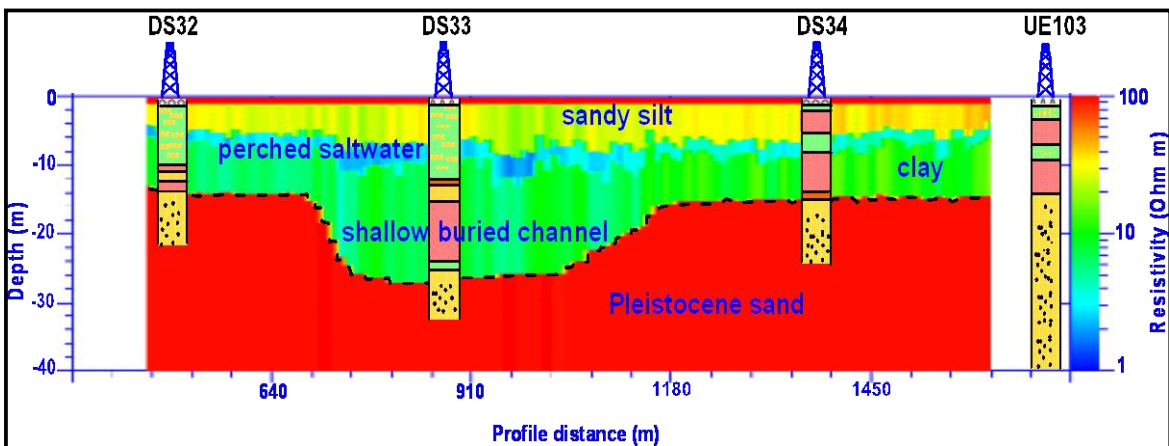


Fig. 5.38: Stitched resistivity sections from 1D FDEM inversion with boreholes for comparison.

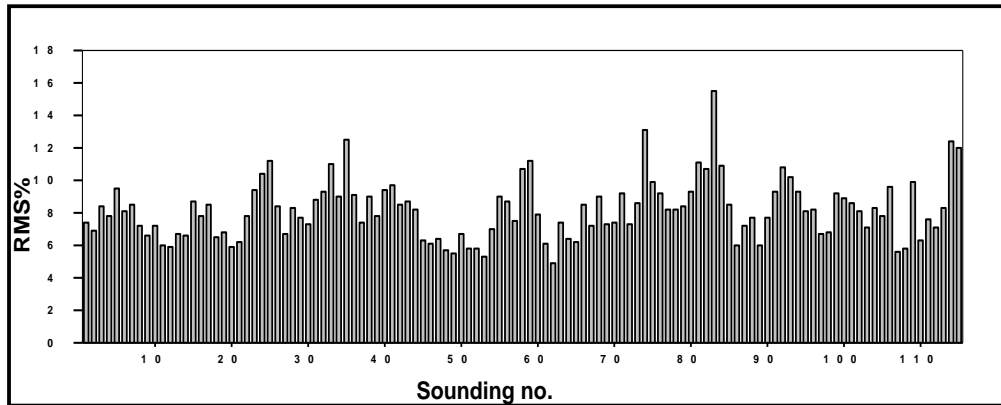


Fig. 5.39: The RMS misfit values of all FDEM soundings at Süderscheidung site.

The overall picture shows good inversion results with the available borehole data. From profile meter 690 to 1160, the increasing thickness of the fourth layer produces a channel-like feature which might be due to cutting down into the upper Pleistocene sediments, the fifth layer, and fillings of tidal fine sediments which occurred during the transgression process (Streif, 1982).

5.5.2 2D DC RESISTIVITY IMAGING

Although the 1D resistivity soundings gave useful information about the geological situation and the subsurface aquifer conditions, those results can only be applied to the immediate vicinity of soundings. Firstly, the 2D DC profiling using WA and WB were carried out to image the saltwater occurrences and to image the Pleistocene freshwater aquifer. Secondly, the 2D data were used to characterize the heterogeneity within the tidal deposits and to confirm the shallow channel-like feature which was observed in the FDEM cross-section (Fig. 5.38). The location of the 2D DC profile is shown in Fig. 5.33. Fig. 5.40 shows the inversion results of the WN, WB and combined WN and WB data sets. The high RMS values can be attributed to dense measurements for long electrode separations. They produce a difficulty to control the data quality, which decreases the fitting between measured and calculated data.

As it is observed, all inverted models show three main geoelectrical layers of medium, high and low resistivity values. The upper part of the WN model is characterized by a medium resistivity layer, which corresponds to Holocene tidal deposits of silt and clay. A smearing to the lower boundary of this layer can be observed along the whole profile with increasing its thickness, up to 40 m, around borehole DS33 (Fig. 5.40 top). The second geoelectrical layer is characterized by relatively high resistivity values corresponding to the Pleistocene freshwater aquifer. A low resistivity layer ($\sim 3 \Omega\text{m}$) can be observed at ~ 80 m, which can be interpreted as saltwater intrusion. The WN model gives poor resolution for the upper boundary of the freshwater aquifer; but the contact between the saltwater intrusion and the freshwater aquifer can be well identified.

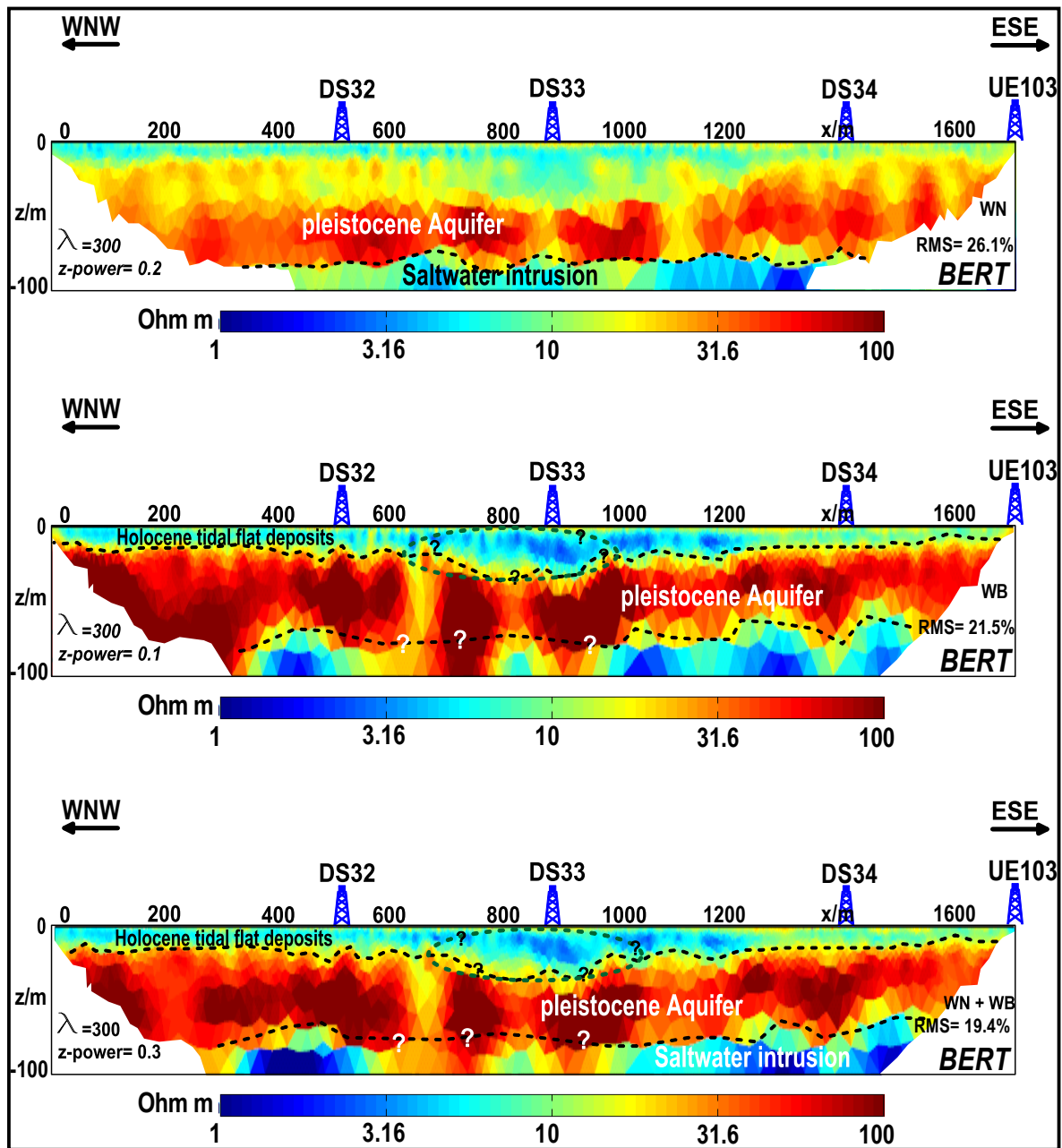


Fig. 5.40: Inversion results: (top and middle) resistivity models obtained by WN and WB data sets, respectively. (bottom) Combined inverted model obtained by WN and WB data sets; λ and z-power are the used regularization parameters.

The WB inverted model (Fig. 5.40 middle) gives good resolution for the Holocene tidal flat deposits and the freshwater Pleistocene aquifer. The upper boundary of the Pleistocene aquifer can be well determined, it ranges from about 10 m to 35 m depth. A low resistivity value ($< 3 \Omega\text{m}$) can be observed within the tidal deposits which can be interpreted as the perched saltwater. It is clear that the saltwater intrusion can not be observed at the central part of the WB model (between ~ 600 m and ~ 1000 m profile distances), where the thickness of tidal deposits increases and the perched saltwater is

present. In general, the WB model shows a smearing to the lower boundary of the freshwater aquifer. The average depth of the saltwater intrusion ranges from 65 m to 75 m.

In Fig. 5.40 bottom, the model from the joint inversion of both WN and WB data sets is presented. As it is seen, this model is quite similar to the WB model. In spite of this similarity, the combined inversion model gives less smearing between the saltwater intrusion and the Pleistocene aquifer. The saltwater depth is about 70 m. Finally, the study of both WN and WB models is redundant and they support each other for a good mapping to coastal areas. In addition, it is seen that the joint inversion model produces satisfactory results for shallow investigations.

Fig. 5.41 shows the inversion results of HEM data at this site (Fig. 5.33). The depth of the low resistivity layer corresponding to saltwater intrusion ranges from about 60 m to 80 m. Because of presence of a shallow low resistivity layer ($3 \Omega\text{m}$) with increasing thickness of tidal deposits between about 300 m and 700 m distance of the HEM profile, the saltwater intrusion can not be observed. A relatively low resistivity layer can be observed at about 60 m depth at the first 200 m of the HEM profile which can be interpreted as Lauenburg clay. It is clear that the high resistivity layer, which corresponds to the Pleistocene aquifer, is covered by a thick medium ($\sim 10 \Omega\text{m}$) to relatively low resistivity layer ($\sim 7 \Omega\text{m}$) corresponding to tidal clay and silt deposits. It is seen also that the resistivity of tidal deposits at the western part of the profile is less than at the eastern part. In comparison with the available borehole data, the DC resistivity imaging characterizes the heterogeneity and the thickness variations within the tidal deposits more accurately than the HEM results.

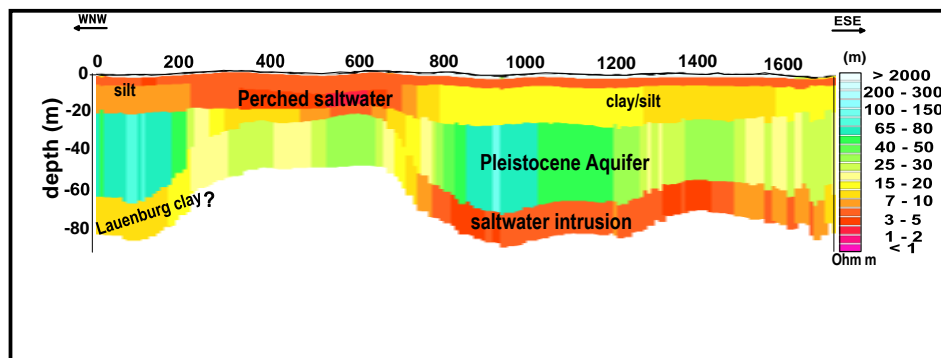


Fig. 5.41: HEM resistivity section (Siemon et al., 2004) at Süderscheidung site (see Fig. 5.33). Note the reverse colour coding for resistivity data.

For a more detailed study of the heterogeneity within tidal flat deposits, a cutting off to geometric factors (G) higher than 1980 m was carried out for the combined WN and WB data sets using DC2DInvRes program. Fig. 5.42 shows the raw data of the apparent resistivity, together with the calculated data and the misfit between them. The inspection of the pseudo-section (Fig. 5.42, top) indicates two layers of medium and high resistivity values. A high conductivity zone can be observed

within the upper layer. A good misfit percentage can be observed (Fig. 5.42, bottom) between the measured and the calculated apparent resistivity data.

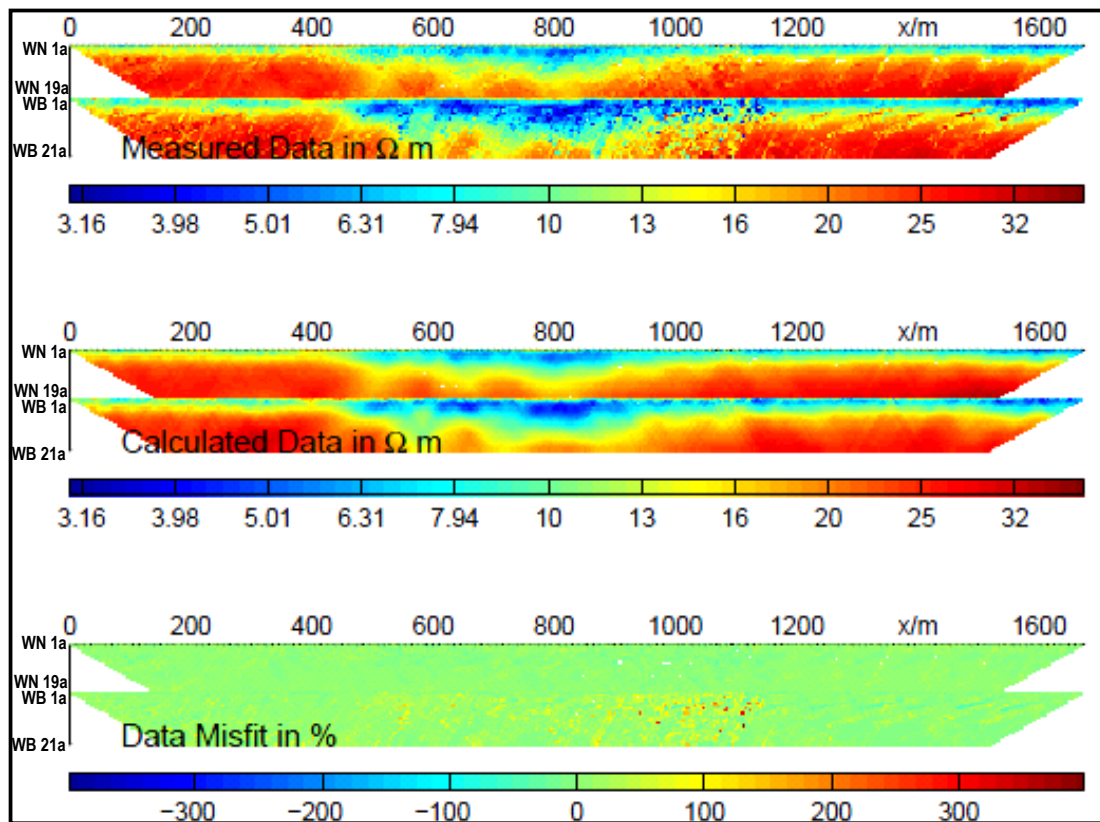


Fig. 5.42: Pseudo-sections of the measured apparent resistivity (top panel) of combined WN and WB data sets, calculated resistivity (middle panel) and relative difference between measured and apparent resistivities (bottom panel) of the 2D DC profile (see Fig. 5.33).

Fig. 5.43 shows the inversion results of apparent resistivity data (Fig. 5.42) using the DC2DInvRes program of first order smoothness constraints with fixed regularization parameter, $\lambda = 148$. To enhance the vertical resolution of the inversion process, the free parameter of w_z was decreased down to 0.3λ . The subsurface resistivity distributions can be differentiated into two main stratigraphic units. The thickness of the upper one ranges from 14 m to 30 m with 8 Ωm average resistivity. In comparison with borehole information, it can be interpreted as tidal flat deposits of silt, sandy silt and clay. At the central part of the profile (between ~ 780 m and ~ 980 m distance), an increase of the tidal deposits thickness (reach up to ~ 30 m) can be observed. This produces a channel-like feature extending from ~ 630 m to ~ 1160 m distance. This feature can be interpreted as a sheltered area of tidal flat deposits, from tidal erosion, in the brackish water environment of ancient coastal lagoons (Streif, 1982 and 2004). Within the tidal deposits, a shallow low resistivity layer (3 Ωm) at ~ 6 m depth can be noticed between 0 m and ~ 1220 m distance. It can be well observed between 800 m and 1220 m profile distance, where it becomes thicker than at the western part of the profile (between 0 and 800 m). The resistivity of the second unit ranges from 40 Ωm to 100 Ωm corresponding to the coarse sand

sediments in comparison with borehole data. The depth of this unit is ~14 m and becomes deeper (~30 m) at the central part of the 2D profile, below the channel-like feature (Fig. 5.43). The upper surface of this unit is characterized by undulations which are proportional to the changes in the perched saltwater and clay thicknesses.

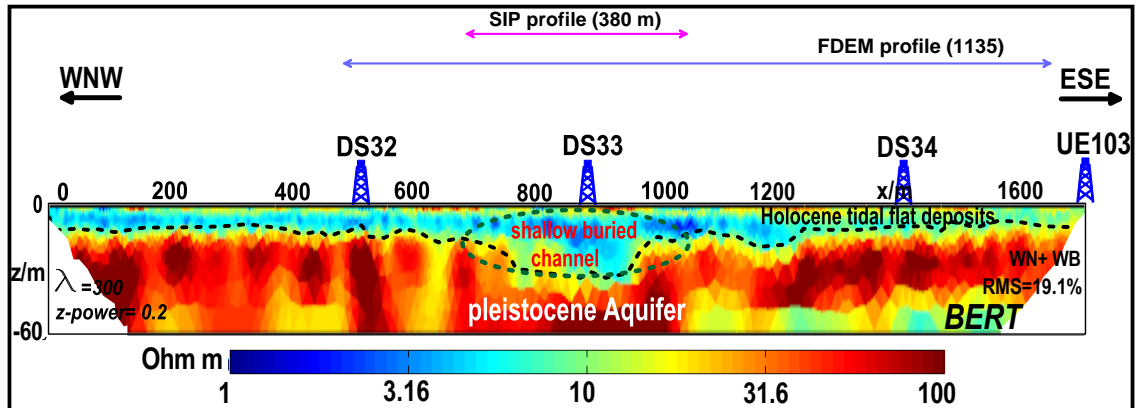


Fig. 5.43: Shallow electrical imaging from 2D inversion of combined WN and WB data sets showing the shallow channel feature within tidal deposits with the locations of drilled boreholes, FDEM profile and SIP profile, λ and w_z are the regularization parameters using the DC2DInvRes program.

Inspection of the FDEM cross-section (5.38) and the DC 2D image (Fig. 5.43) shows similar features of the perched saltwater layer and shallow channel. There are few differences between the two inversion models:

- In the 2D DC profiles (Fig. 5.40), the tidal flat deposits are represented by a lower resistivity value (~ 8 Ω m) than in the FDEM cross-section (~ 14 Ω m).
- The 2D profiles show an undulating upper surface of the Pleistocene sandy aquifer, which produces difficulties in detecting the accurate depth and width of the shallow channel feature.
- The 2D profile shows variations in the saltwater intrusion depth with a smearing to the lower boundary of the Pleistocene aquifer (Fig. 5.40).

These differences are probably attributed to the limitations of the 2D imaging in presence of a shallow high conductivity layer. Similar limitations were observed by *Kilner et al. (2005)* in detecting thin sand and gravel layers underlying electrically conductive clay in Eastern England. In addition, in Fig. 5.40 the saltwater intrusion can not be resolved at the central part of the WB and combined WN and WB data sets. Therefore, a 2D synthetic modeling was carried out to verify the appropriateness of the 2D interpretation. Throughout, the modeling emulated 2D profilings with the WN, WB and combined WN and WB data sets.

5.5.2.1 SYNTHETIC MODELING

In synthetic modeling, the input resistivity model was deduced from our geological background, available boreholes and the results of geophysical methods at this site (Fig. 5.44a). The synthetic data and inversion process were carried out using the DC2DInvRes modeling software. The

apparent resistivities that would arise from the synthetic model response of WN and WB configurations using electrode spacings of 5 m were calculated. The effect of the noise was investigated by applying Gaussian noise of 3% plus 100 nV at 300 mA to the modeled apparent resistivity data prior to the inversion process, in order to simulate measurement errors that occur in the real data (Fig. 5.44b).

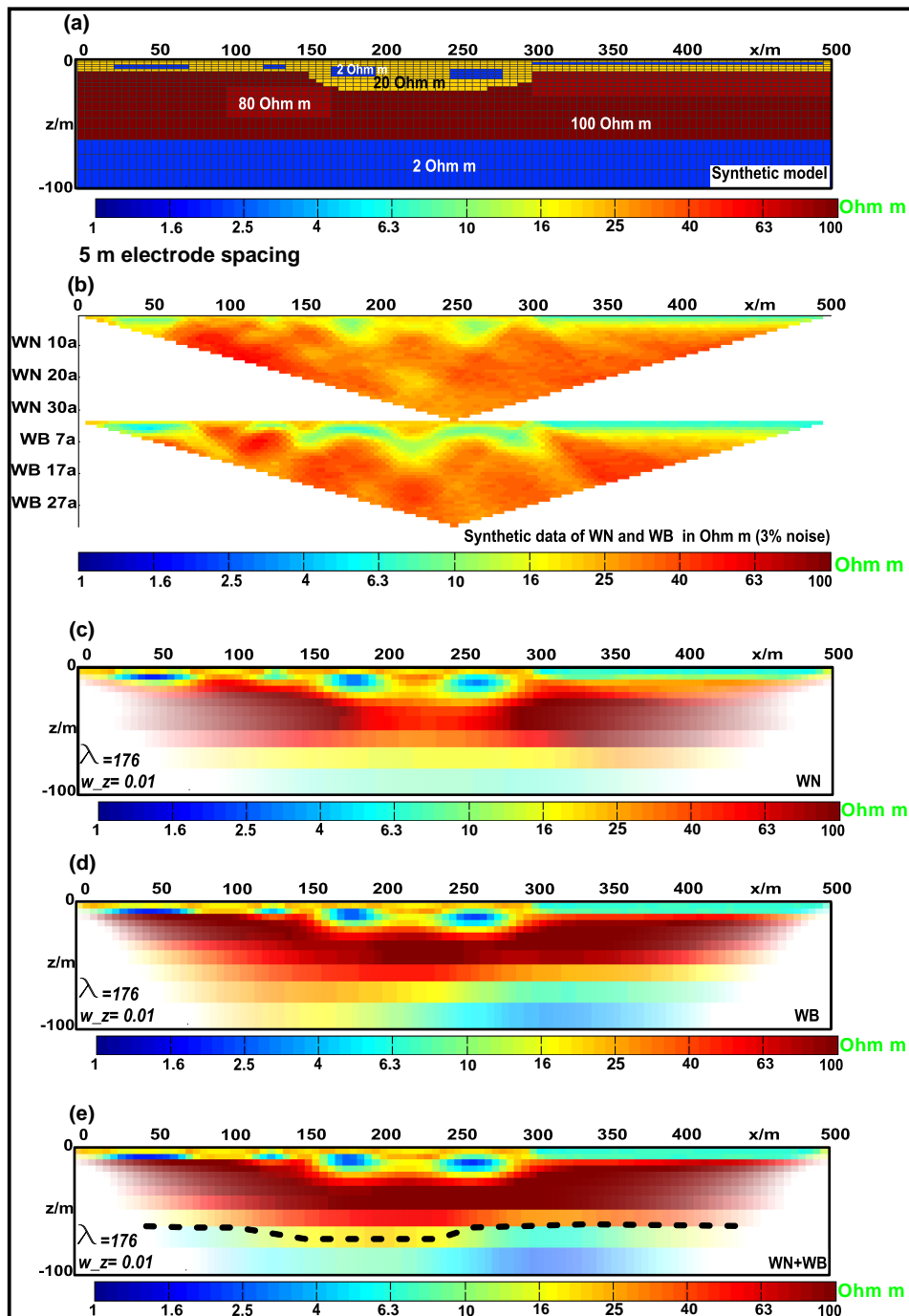


Fig. 5.44: (a) The synthetic model; (b) combined apparent resistivity data of WN and WB configurations and inverted model resistivity profiles obtained by (c) WN, (d) WB and (e) combined WN and WB data sets.

The synthetic model (Fig. 5.44a) consists of a medium resistivity layer of 20 Ωm (silt). The thickness of this layer ranges from 10 m to 24 m. A low resistivity layer of 2 Ωm has been embedded within this layer at different depths, at about 1 to 5 m depth, and with different thicknesses corresponding to the perched saltwater. Its thickness ranges from 1.5 m to 7 m (at the central part of the model). A channel-like feature can be observed at the central part of the model (24 m is its maximum depth). The medium resistivity layer rests on a high resistivity layer (80 Ωm to 100 Ωm), which corresponds to Pleistocene coarse sand aquifer. It rests on a low resistivity layer (2 Ωm) corresponding to saltwater intrusion at 62 m depth.

Fig. 5.44 (c and d) shows the inversion results of individual WN and WB apparent resistivity data. In addition, Fig. 5.44e shows the inversion results of combined WN and WB data sets (Fig. 5.44, b). The inversion process is based on the Gauss-Newton smoothness constrained least-squared method using the DC2DInvRes program. The regularization parameters were chosen to get the best fitting between the input and the inverted models. To resolve the heterogeneity within the input model, we used low values of regularization parameters. λ and w_z were 176 and $0.01 \cdot \lambda$, respectively.

The perched saltwater can be resolved at the central and western parts of the inverted models. In contrast, the thin conductive layer (1 m) is overlooked and cannot be resolved within the silty layer (20 Ωm) at the eastern part of the inverted models. Therefore, the silty layer would be interpreted as having a lower resistivity value ($\sim 7 \Omega\text{m}$) than in reality. The WN model (Fig. 5.44c) represents a smearing to the lower boundary of the perched saltwater layer by amplifying the vertical and lateral effects. This smearing effect is proportional to the perched saltwater thickness. Moreover, in the WN model the resistivity of the Pleistocene aquifer is lower than in reality in presence of the perched saltwater and the silty layer thickness is increased. Consequently, the Pleistocene aquifer will be interpreted to be deeper than in reality.

The inspection of both the WB and the combined WN and WB models (Fig. 5.44 d and e) shows that the boundary between the silt and the Pleistocene aquifer can be better defined than in the WN model. The WB and the combined WN and WB models represent the shallow channel feature thickness thicker (~ 29 m) than in reality, especially in presence of the perched saltwater. This smearing introduces limited undulations in the upper boundary of the Pleistocene aquifer at the central part. Regarding to this smearing, it can be noted that a sharp contact between silt and coarse sand layers is reduced with increasing the perched saltwater thickness. Both the WB and the combined WN and WB data sets assign the true resistivity for the Pleistocene aquifer with a high resolution.

The saltwater intrusion can not be well observed from the WN model. The WB model shows a smearing to the upper boundary of the saltwater intrusion especially at the central part of the profile, where the shallow channel and the perched saltwater are present. It can be deduced that a presence of a shallow conductive layer, like a perched saltwater formation, will decrease the resolution of the WB model with increasing depth. The saltwater intrusion imaging will be reinforced by combining WN

and WB data sets. The joint inversion improves the saltwater intrusion imaging with decreasing the smearing to its upper boundary in presence of a channel feature.

These limitations lead to a misinterpretation of a resistivity inverted model at this site. In this case, the shallow channel lower boundary will be interpreted as being deeper than in reality; in addition to misinterpretation of low resistivity values. Finally, the synthetic model provides an interpretation and the reasons for the differences between the inversion results of the FDEM cross-section and the 2D resistivity (Figs. 5.38 and 5.43), where there are differences in detecting the shallow channel lower boundary (~ 4 m), perched saltwater and tidal sediments resistivity values. In addition, it explains the reasons for variations in detection the saltwater intrusion depth from different configurations (Fig. 5.40) and the HEM section (5.41).

5.5.2.2 2D SIP INVERSION RESULTS

For a more detailed study of the heterogeneity (the perched saltwater, silt and clay) within the shallow channel-like feature, a long SIP profile was measured (see section 4.3). The SIP profile location in relation to the FDEM and 2D DC profiles is shown in Fig. 5.43.

The SIP inversion results and coverage sections, from 0.625 Hz up to 20 Hz, are shown in Fig. 5.45¹³. The conductivity magnitude $|\sigma|$ imaged up to 20 Hz exhibits a predominantly layered structure, with lateral variations within these layers (Fig. 4.49, left). Below the medium resistivity soil (~0.06 S/m), a high conductivity layer (> 0.3 S/m) can be recognized in all conductivity magnitude sections, which correspond to clay and silt. The maximum thickness and conductivity values of this layer can be observed at the central part of the 2D profile, especially around 825 m profile distance. This layer becomes shallower and thinner at the eastern (~1025 m) and western boundary (~725 m) of the profile. It can be seen that this layer overlays a low conductive layer (< 0.03 S/m) corresponding to Pleistocene sand.

The phase φ images of the complex electrical conductivity are shown in Fig. 5.45 (middle). They don't exhibit a clear layering in comparison with the conductivity magnitude sections. In general, the phase values increase with depth at all frequencies. It can be observed that the inverted sections of frequencies 1.25 Hz and 2.5 Hz show, in general, the same features. The few differences between these two images can be attributed to the difference in data coverage (Fig. 5.45, right). At about 20 m depth and around 870 m profile distance, the irregularity and/or discontinuity in the upper surface of the deep high phase layer can be attributed to the low data coverage, location of overlapping of 2D profiles (Fig. 4.4). Based on the coverage sections, the 2D phase section at 1.25 Hz and 2.5 Hz are more reliable than 0.625 Hz, because they have higher data coverage than the phase section of 0.625 Hz. Although good data coverage can be observed for other sections (> 2.5 Hz), the phase images can not be compared with each other and the phase values are rather poorly resolved. Above 10 Hz,

¹³ Note that the SIP inversion results ($|\sigma|$ and φ) for higher frequencies are shown in Appendix E.

the EM coupling can be well noticed where the phase sections are dominated by very high phase values (> 10 mrad) (see subsection 4.4.2). Therefore, 1.25 Hz and 2.5 Hz were selected to study the heterogeneity within the tidal deposits and to allow comparison with the DS33 borehole data.

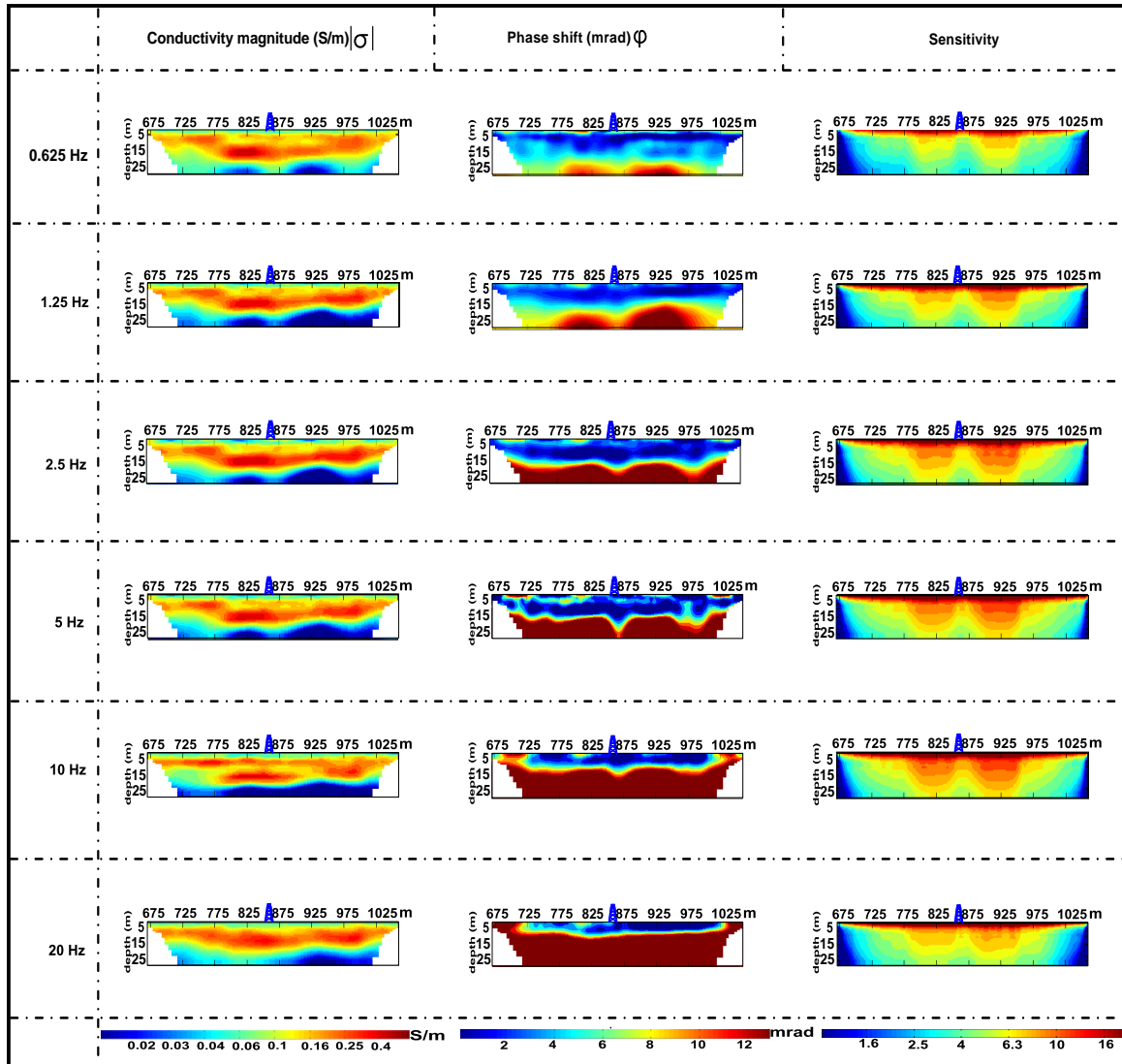


Fig. 5.45: (left) The complex conductivity magnitude $|\sigma|$, (middle) conductivity phase shift φ and (right) coverage sections for 6 selected frequencies (0.625 Hz, 1.25 Hz, 2.5 Hz, 5 Hz, 10 Hz and 20 Hz).

The inversion results of 1.25 Hz and 2.5 Hz were enlarged and presented in the form of conductivity magnitude $|\sigma|$, the conductivity real part σ' , the phase φ and the conductivity imaginary part σ'' (Figs 5.46 and 5.47). Both phase and magnitude parameters are independent. On the other hand, both real and imaginary parameters are equal to the multiplication of the independent parameters $|\sigma|$ and φ . The images look realistic and coincide well with the available borehole data. In general, the $|\sigma|$ and σ' images are directly proportional to the electrolytic conduction in connected pore spaces by ionic migration. Therefore, the conductivity magnitude images (Figs 5.46a and 5.47a) and real conductivity images (Figs 5.46b and 5.47b) show the same features of a highly conductive layer

corresponding to the perched saltwater and Eemian clay. The discrimination between the brackish to saline water and clay can not be achieved from the $|\sigma|$ and σ' images. The depth of the high conductivity layer ranges from ~5 m to ~8 m and its thickness ranges from 10 to 15 m. It corresponds to the perched saltwater and sandy silt to silty lay, as seen in FDEM cross-section (Fig. 5.38) and 2D DC image (Fig. 5.43). This layer is covered by a moderate conductivity layer, which corresponds to sandy silt, and it overlies a low conductivity layer that corresponds to sand and/or silty sand. There is a transition zone between the high and low conductivity layers, which could correspond to silt.

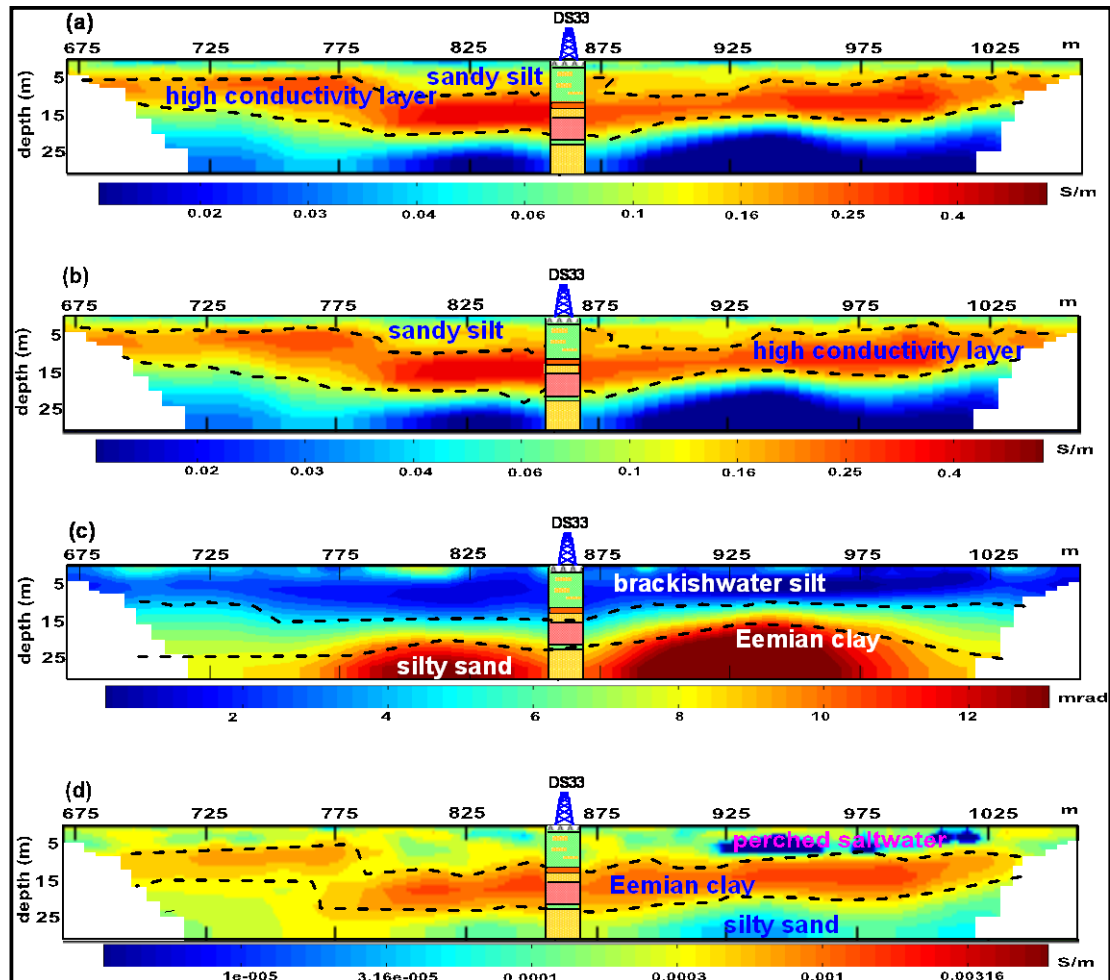


Fig. 5.46: Conductivity magnitude (a), real part of conductivity (b), phase shift (c) and imaginary part of conductivity (d) in the 2D image plane as determined by complex resistivity inversion at 1.25 Hz.

The phase images (Figs. 5.46c and 5.47c) show additional geological information within the coastal tidal deposits. Both phase images, at 1.25 Hz and 2.5 Hz, show an upper layer of low phase values corresponding to brackishwater and/or saltwater sandy silt with 15 m maximum thickness at the borehole location. It overlies a moderately phase layer, which corresponds to the upper boundary of the Eemian clay layer. This layer can be observed at ~10 m depth at the eastern and western part of the profile. At ~20 m depth, a third high phase layer (> 10 mrad) can be observed which corresponds to fine sand. A good agreement can be observed between the borehole data and the phase inversion

results. The main differences between the phase images at 1.25 Hz (Fig. 5.46c) and 2.5 Hz (Fig. 5.47c) are: (a) the upper low phase layer in 2.5 Hz image is more thicker than 1.25 Hz model and (b) the contact between the Eemian clay and the lower silty sand layer is better defined from 2.5 Hz model than 1.25 model. A possible explanation of the low phase layer is that the fossil groundwater could not be replaced by freshwater due to the thick clay layer below (Hördt *et al.*, 2009). It may correspond to brackishwater clayey silt and/or silt layer. The 2.5 Hz model represents more reliable features than 1.25 Hz model for two reasons: Firstly, the phase image at 2.5 Hz represents higher sensitivity values (Fig. 5.45) than 1.25 Hz image and consequently it is more reliable (Günther, 2004). Secondly, a better fitting between the inversion results and the borehole information, DS33, can be observed in 2.5 Hz model than 1.25 Hz.

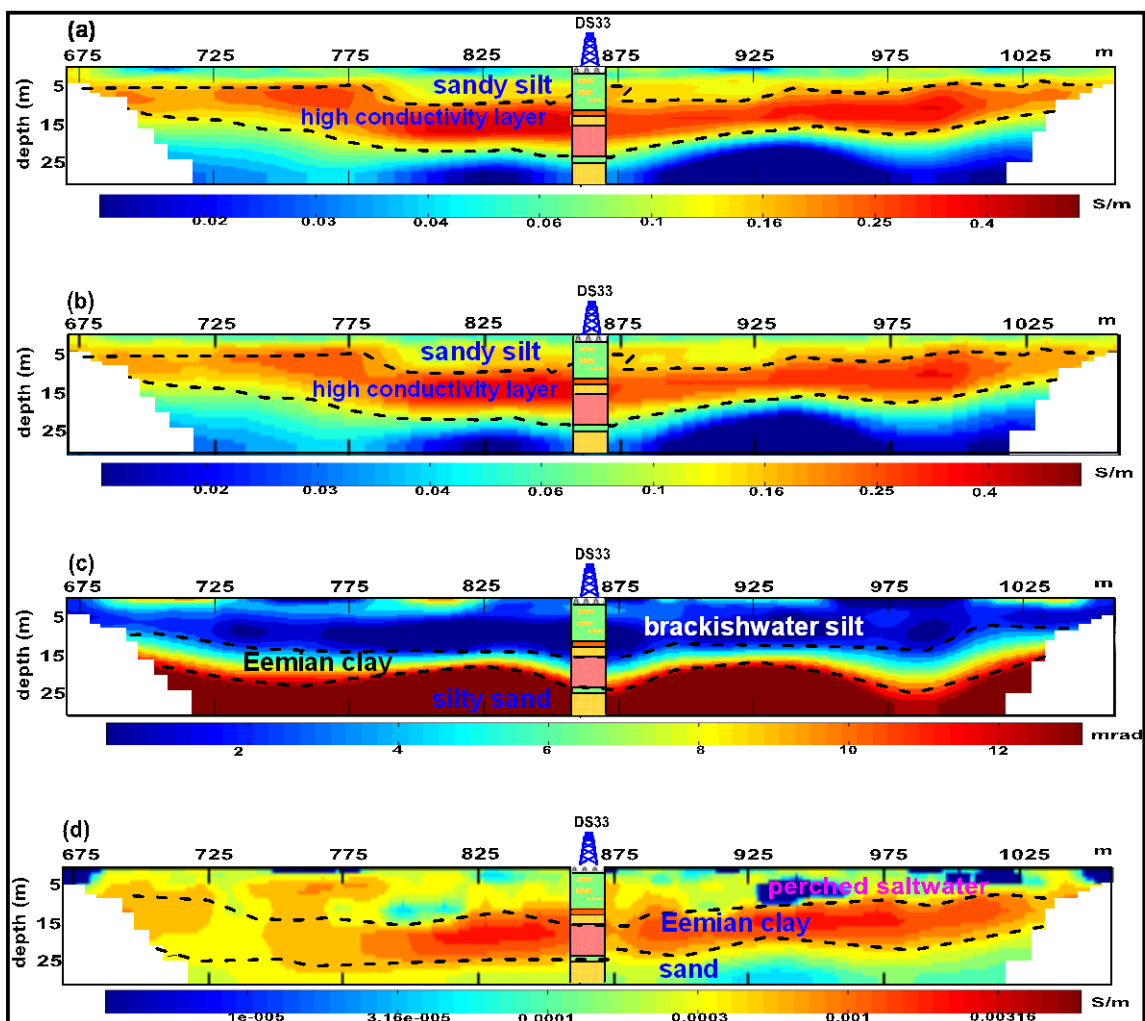


Fig. 5.47: Conductivity magnitude (a), real part of conductivity (b), phase shift (c) and imaginary part of conductivity (d) in the 2D image plane as determined by complex resistivity inversion at 2.5 Hz.

The discrimination between clay, the brackishwater silt and the perched saltwater can be even better imaged and characterized by the imaginary part (Figs. 5.46d and 5.47d), which is a combination of the magnitude and phase data, but it is dominated by the conductivity magnitude

values. The images of imaginary part show a highly conductive layer, which becomes shallower and thinner to the eastern and western parts of the profile. It corresponds to the Eemian clay layer overlying a medium to low conductivity layer which corresponds to fine sand and/or silty sand. The variations in the clay thickness and depth could reflect the base of the channel-like feature which was observed in FDEM cross-section (Fig. 5.38) and 2D DC profile (Fig. 5.43). A shallow low conductivity parts can be observed between ~925 m and ~1025 m profile distances (Figs. 5.46d and 5.47d) corresponding to the perched saltwater (zero phase angle). The imaginary conductivity image introduces new information about the heterogeneity within the tidal deposits above the Eemian clay layer. Consequently, the low phase layer can be divided into perched saltwater and brackishwater sandy silt layers.

5.6 DISCUSSION

The results of geophysical measurements indicate that the subsurface resistivity distributions in the whole area are highly inhomogeneous. In both DC and FDEM methods, the 1D inversion process was done for each sounding separately. We could modify the inversion results regarding the starting model derived from the borehole data; in addition we were able to compare the soundings inversion results with each other. In conclusion the 1D inversion was robust and reliable.

The results of the 1D DC survey show a general picture of the geological and hydrogeological situations in the investigated area. The geoelectrical cross-sections indicate that the saltwater intrusion appears as a wedge-like form from east to west direction, i.e., it is shallower (~ 25 m) and thicker at the eastern part than at the western part. The maximum thickness of Pleistocene sediments, the main freshwater aquifer, can be observed at the western part to be greater than 100 m.

The integration of DC and FDEM methods can be considered as useful geophysical mapping strategy for characterizing the coastal areas. Adopting a 1D structure and extensive boreholes data, the 1D FDEM inversion results appear to be robust and reliable; the method turns out to be applicable and suitable in coastal survey areas. In presence of anthropogenic features (metal pipes etc.) with expected high noise levels, an acceptable fit between EM raw data and a calculated model can be expected only for low frequency data (< 2000 Hz) and, consequently, an acceptable imaging to deep saltwater with a high RMS error will be achieved. In a noisy area, DC resistivity soundings are necessary to derive the FDEM starting model and to predict the resistivity values of the shallow layers, i.e., high frequency data. The optimum coil spacing and station intervals for deep saltwater imaging (~ 60 m) are 100 m and 10 m, respectively. On the other hand, 50 m and 10 m coil spacings and station intervals, respectively, are the best FDEM field parameters to characterize the heterogeneity within tidal deposits coastal areas. Therefore, in this case study, the FDEM can be considered as an alternative to DC Schlumberger soundings to combine large information about the coastal area in a shorter time with a high lateral resolution as a result of a short station distance.

The magnitude of the sensitivity values represents the reliability of the corresponding model resistivity derived from inversion. Both sensitivity analysis and synthetic modeling are necessary to judge the model reliability. Synthetic modeling indicates that for a highly conductive layer imaging, WN and WB make a worse by amplifying lateral and vertical effects (smearing) and, consequently, its thickness or depth will be greater than in reality. Under certain circumstances, e.g., a presence shallow channel or perched saltwater, both WB and SC represent low spatial vertical resolution. These limitations are related to electrical current behavior at resistivity boundaries, where the current prefers to travel and diverge through low resistivity layers rather than highly resistive layers (*Telford et al., 1990*). This leads to a decrease of the potential gradient at the lower boundary of the low resistivity layer and produces a smearing to its lower boundary. Consequently, a sharp contact cannot be observed and a poor vertical resolution will be achieved with increasing depth.

There is no single optimum configuration which can give valid and useful results. Under no or limited prior information, the joint inversion of different configurations could improve the reliability of the resulting model, with high lateral and vertical resolution and a better depth penetration than individual configurations. A joint inversion of WB and SC data sets was proved to be useful for studying the saltwater and heterogeneities of coastal deposits. For 2D deep saltwater resistivity imaging, it is not advisable to apply individual SC configuration. Extra processing is needed for 2D SC data during inversion process to reach the best regularization parameters, which give an optimized model.

The inspection of both WN and WB 2D inverted models shows that these configurations are effective for delineating both shallow sedimentary structures and deep saltwater intrusions. In case of increasing the thickness of tidal deposits in the form of channel feature, WB shows a limitation in imaging the saltwater intrusion. WB appears as an effective configuration to image the shallow sedimentary structures within the tidal deposits in coastal areas, but a smearing to the boundaries of these structures can be observed. On the contrary, the WN inverted model shows the insignificance of 2D resistivity imaging for mapping the shallow channel within tidal coastal aquifers. The joint inversion of WN and WB data set shows higher horizontal coverage and better vertical resolution than individual configurations for imaging the shallow sedimentary structures within the tidal deposits.

2D and 3D inversion results show variations in thickness and resistivity values of tidal flat deposits, e.g., shallow channel feature. The maximum tidal flat thickness (~ 24 m) can be observed at the southern part of the investigated area. The central and southern parts are most affected by perched saltwater where these sites are characterized by fine tidal flat deposits. The interpreted perched saltwater is observed in HEM map (Fig. 4.1) as a shallow high conductive zone.

The inspection of 3D DC measured data of WB, DD and PP configurations show that: (1) WB in the form of 2D orthogonal profiles provides a quick and cost effective tool for perched saltwater imaging. It amplifies the lateral effects of conductive layers and consequently they appear thicker and wider than in reality. (2) 3D DD is the best horizontal resolution configuration and the reciprocity

measurements are required to evaluate the data accuracy; note that DD configuration has the lowest signal-to-noise ratio. (3) For 3D PP it is easy to automate the data acquisition and check the data quality in the field. 3D PP survey provides good results for saltwater imaging with poor horizontal resolution. Similar to WB, it is not advisable to use individual PP in 3D horizontal heterogeneity imaging. Finally, the inspection of 3D WB, DD and PP results is effective to evaluate the horizontal and vertical structures, because each configuration will provide an advantage to certain extent.

SIP measurements indicate that looking at the magnitude, phase and imaginary part can be constructive. The imaginary part reflects more information about the clay layer extension within the tidal deposits. In the study area (Süderscheidung site), it becomes shallow and thin away from the central part of the shallow channel. The conductivity phase presents an accurate detection to the brackish/perched saltwater, e.g., patched forms, more than DC and FDEM methods. Field inversion of SIP data provides more detailed information about the heterogeneity within the shallow channel feature. The clay, silt, brackishwater and coarse sand can be well recognized, which can be used to predict the paleo-environment in coastal areas. Our results encourage the wider adaption of SIP to characterize the heterogeneity within tidal deposits in coastal areas. Smoothness constraint inversion using FD scheme improves the interpretability of resistivity/IP data. In the field, a frequency range of 0.625 Hz to 10 Hz appears to be optimum considering survey time and cost.

In general, the clay content is an important factor in the formation of the IP response. *Vanhala (1997)* studied the relation between the phase behavior with different grain sizes for a variety of soil samples. A decrease in phase shift for smaller grain size (clays and clayey silts) was observed (*Vanhala and Soininen, 1995; Vanhala, 1997*) which can be attributed to the increasing dominance of the ohmic interface conduction inherent to clay minerals (*Schön, 1996*). On the other hand, the highest polarizability was observed for sandy silt and fine sands. On the contrary, in our SIP interpretation the Eemian clay shows high phase values. In addition, the coarse sandy layer at ~ 21 m depth, based on the borehole information, shows higher phase values than Eemian clay. These results encouraged us to drill a borehole adjacent to DS33 borehole to get representative samples from Eemian clay and the lower sandy layer. Fig. 5.48 shows core samples from 9 m to 23.5 m depths, the detailed soil samples description is shown in Appendix F. It is clear that the Eemian clay is not pure (thick) clay but it is rich in fossils (diatoms), silt, which could produce pore spaces within the clay and increase the magnitude of membrane polarization. In addition, fine sand (e.g., 22.5 m depth) can be observed below the Eemian clay layer. Note that the diatomaceous layer has high inner surface area (*Losic et al., 2010*) which increases the cation exchange capacity (CEC) and, consequently, the phase response. Accordingly, the ion selective paths dominate over the ohmic conduction, which will increase the phase response in the inverted sections.



Fig. 5.48: Representative core samples from Eemian clay layer adjacent to the DS33 borehole location.

5.7 HYDRAUCIC CHARACTERISTICS OF TIDAL DEPOSITS

Based on the field observations from boreholes in the considered area, the Holocene aquifer represents the upper aquifer in the study area. Four known k_f values for this aquifer, derived from pumping test and grain size analysis, of four observed wells (DS29, BEA01, BIN01 and BUC01) are available. Here, we will discuss the hydrogeological characteristics of the shallow tidal aquifer to obtain qualitative and quantitative information about the k_f and K values. The resistivity measurements of DC and SIP will be used to study the aquifer properties.

5.7.1 QUALITATIVE INTERPRETATION

The multilayer Holocene interpretations of DC sounding points from the observed wells can be theoretically reduced to a single aquifer resistivity value. Since reduction needs to consider only the longitudinal direction, the single aquifer resistivity value ρ_L from the field data can be used as a representative value of the entire aquifer section (Kosinski and Kelly, 1981).

Fig. 5.49 (a) shows the location map of the considered area with two representative boreholes. The boreholes indicate that silt/silty sand and clay/silty clay sediments are dominated at the northern and southern parts, respectively. The DC secondary geoelectrical parameters (see subsection 3.1.3) were calculated for the Holocene tidal aquifer ($> 5 \Omega\text{m}$), which floats on the top of the perched saltwater ($< 3 \Omega\text{m}$). The aquifer thickness ranges from 6.5 m to 17.5 m (Fig. 5.49b). The minimum thickness can be observed at the central and southwestern parts, where the perched saltwater is present (see Figs. 5.3 and 5.4). The secondary geoelectrical parameters are represented in the form of five contour maps (Fig. 5.49, c to g).

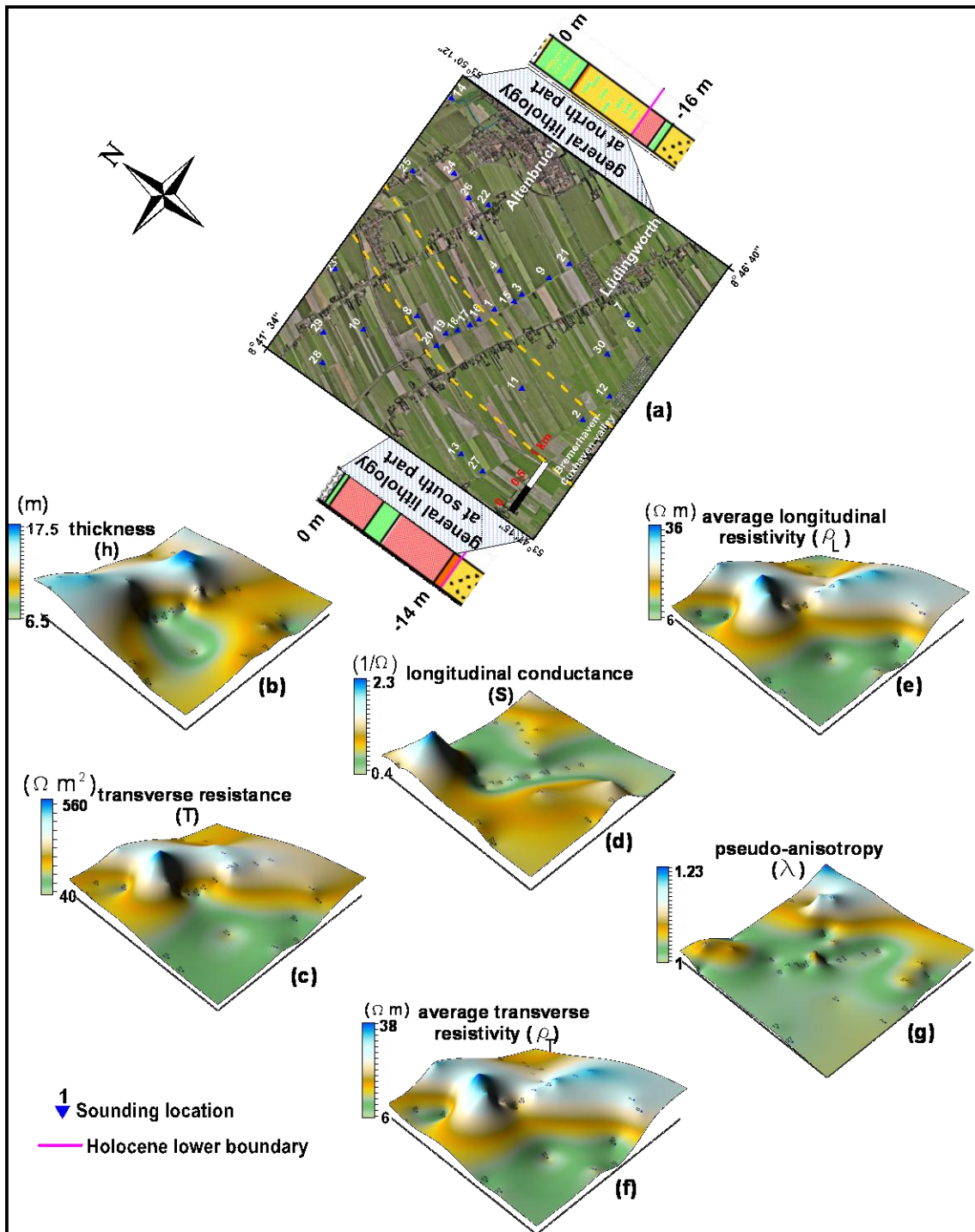


Fig. 5.49: (a) Location map showing the Holocene general geology (inset map © Google Earth), (b) thickness map and (c to g) secondary geoelectrical parameters of Holocene tidal deposits to the top of the perched saltwater ($< 3 \Omega m$), (c) transverse resistance T , (d) longitudinal conductance S , (e) average longitudinal resistivity ρ_L , (f) average transverse resistivity ρ_T and (g) pseudo-anisotropy λ .

The transverse resistance T contour map (Fig. 5.49 c) shows minimum values at the southwestern part (soundings 2, 11, 12, 13, 27 and 30). An increase of “T” values can be observed at the eastern and northern parts. Fig. 5.49 (d) shows an increase of longitudinal conductance S at the western and southwestern parts. A minimum “S” value can be noted at the central and southeastern parts. According to *Kosinski and Kelly (1981)* and *Niwas and Singhal (1981 and 1985)*, there is a direct relation between transmissivity and “T” (see subsection 3.6.2). According to *Oteri (1981)*, the marked increase of “S” may correspond to an average increase of the clay content. These qualitative interpretations can be confirmed by the observed borehole information and DC inversion results, which show a dominance of fine sediments at the southern parts. Based on these interpretations, the increase of “S” at the western and southwestern parts may provide a protection, in the form of aquiclude, of the Holocene and Pleistocene freshwater aquifers. On the other hand, the increase of “T” at the central and western part reflects that the surface pollution, e.g., saltwater, can path downward and to contaminate the shallow aquifer, which can be noted in the presence of the perched saltwater.

A similarity, in general, of both average longitudinal and transverse resistivity (ρ_L and ρ_T , respectively) contour maps (Fig. 5.49, e and f) can be noted. In addition, it can be observed that the data range of ρ_L is slightly less than ρ_T , which indicates that the current flow along the bedding planes is less than that normal to the bedding planes (*Flathe, 1955*). According to the analogy between the current flow and water flow (see Appendix A), Fig. 5.49 (e and f) indicate that the hydraulic conductivity in horizontal direction is slightly greater to that perpendicular to the bedding plane. Furthermore, according to *Keller (1982)* ρ_L is dominated by more conductive layers, whereas ρ_T increase rapidly even if a small fraction of resistive layers are present.

The determination of electrical anisotropy λ is desirable as it may indicate the presence of otherwise unresolved thin layers (*Christensen, 2000*). In general, the “ λ ” can be attributed to the heterogeneity within layers (see subsection 3.1.3). Fig. 5.49 (g) shows that the “ λ ” ranges from 1 to 1.28 (dimensionless). The high values of “ λ ” can be observed at the northeastern part and northwestern parts. According to *Flathe (1955)*, high “ λ ” can be attributed to alternating layers of clay and fine sand. The “ λ ” can also be interpreted as a result of intercalation of different grain sizes in the same layer (*Frohlich, 1974*). In addition, *Singh and Singh (1970)* pointed out that lower values of “ λ ” correspond to high aquifer potential zones. Based on these discussions and the field observations, in general, a high groundwater potentiality can be expected at the northeastern and northwestern parts of the area.

5.7.2 QUANTITATIVE INTERPRETATION

In Cuxhaven area, Eq. (4.2) was applied and correlated with the observed k_f values. In addition, it was compared with the results of other published empirical equations (see subsection 3.6.2). Finally, the measured 2D SIP data were used to calculate the hydraulic conductivity at the southern part of Cuxhaven area using various published approaches (see subsection 3.6.3).

Holocene tidal deposits aquifer, Cuxhaven area

Similar to the previous discussions in chapter 4 (see section 4.5), in Cuxhaven area an exercise has also been made using Eq. (4.2) for four DC sounding data (nos. 6, 7, 14 and 20), which are close to the four known k_f values. Then, the estimated k_f values were correlated with those derived from Niwas and Singhal (1981) empirical relation and the observed k_f values. The results (Table 5.1) have shown a very close semblance with the observed k_f values and those derived from Eq. (3.57). Note that these estimated k_f values for saturated Holocene tidal deposits (of $> 5 \Omega\text{m}$), which are above the perched saltwater ($< 3 \Omega\text{m}$) and, consequently, its thickness is small.

Sounding no.	Well name	Aquifer thickness (h) m	Aquifer resistivity (ρ) Ωm	k_f -values (pumping test/ grain size) m/day	$k_f = ((k_f \sigma) T) / h$ m/day	$k_f = A \rho^B$ m/day
7	BEA01	7.92	32.3	1.1 (pumping test)	1	1.04
20	BUC01	9.05	35.6	1.3 (grain size)	0.7	1.2
6	SUM01	3.17	32.3	0.85 (grain size)	0.9	1.04
14	BIN01	4.56	29.2	0.86 (grain size)	0.86	0.87
where $k_f \sigma = 0.029$ (Niwas and Singhal, 1981), $A = 0.002$ and $B = 1.8$					$\delta = 1.1$	$\delta = 1$

Table 5.1: Aquifer parameters of DC soundings and estimated k_f using Eqs. (3.57) and (5.2) in correlation with observed values from pumping test and grain size analysis.

The 2D SIP inversion results at 2.5 Hz (Fig. 5.47) were used to derive the k_f values at site C (Fig. 5.33) using Börner *et al.* (1996) and Slater and Lesmes (2002a) models (see subsection 3.6.3). Because these models assume saturated conditions, the results are valid only below the groundwater table, as indicated in the Fig. 5.50. From the field observation, the water conductivity was measured at about 3 m depth and it was 0.7 S/m. This value was used to calculate the formation factor using Eq. (3.63). We used standard values of $a = 0.00475$, $c = 3.1$ and $l = 0.1$ for Börner model. These parameters were recommended by Weller and Börner (1996) and Hördt *et al.* (2009), especially when there are no known k_f values from pumping tests or grain size analysis. Slater and Lesmes (2002a) model shows a small range of adjustable parameters. Consequently, the values of $m = 2.2 \cdot 10^{-4}$ and $n = 0.9$ were suggested in our study, which give the hydraulic characteristics of both clay/silt and sand unconsolidated sediments. The k_f values obtained from Slater and Lesmes (2002a) model are greater than the estimated from Börner *et al.* (1996) model. Compared with the lithology of DS33, the images look reasonable: the decrease of k_f values ($\sim 5 \cdot 10^{-7}$ m/s) between ~ 12 m and ~ 22 m can correspond to the known Eemian clay. The increase of k_f values ($\sim 5 \cdot 10^{-5}$ m/s) at ~ 23 m are likely to be caused by the sand aquifer. A medium k_f values ($\sim 10^{-6}$ m/s) between 3 m and 12 m can be attributed to sandy silt sediments. The increase of k_f values at ~ 7 m depth and between 925-960 profile meter, which represent very low imaginary parts of conductivities (Fig. 5.47d), can be attributed to the brackishwater to saltwater sandy silt aquifer. Consequently, both images assigned incorrect k_f values for this part of the profile, which can be attributed to a dominance of ohmic conduction over the interface conductivity.

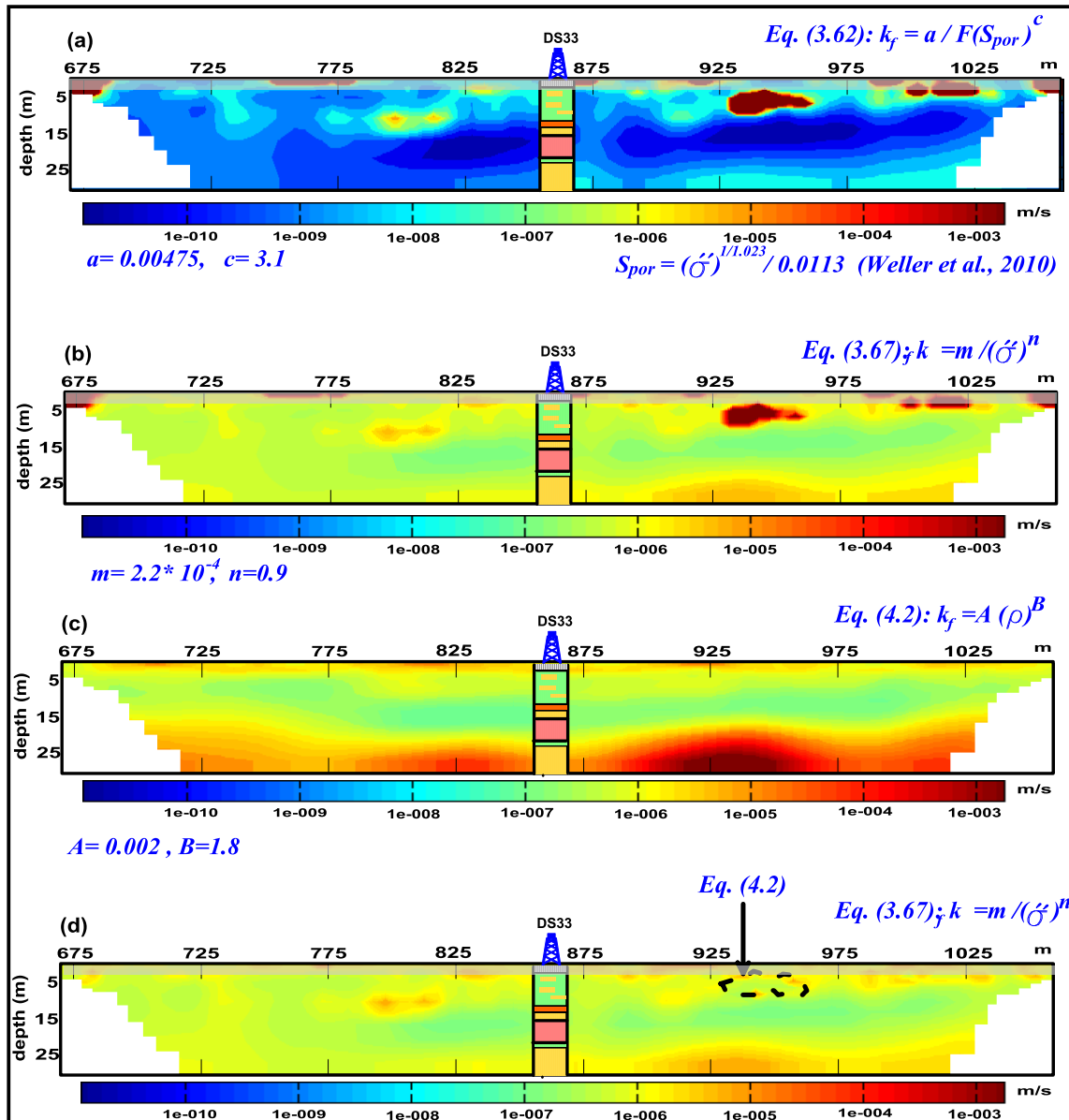


Fig.5.50: Hydraulic conductivity sections estimated from conductivity model shown in Fig. 5.47 using (a) Børner model (Eq. 3.62) with parameters $a = 0.00475$, $C = 3.1$ and $l = 0.1$, (b) Slater and Lesmes model (Eq. 3.67) with parameters $m = 1.7 * 10^{-4}$ and $n = 1.3$ and (c) the power law relation (Eq. 4.2) using parameters $A = 0.002$ and $B = 1.8$. The shaded area denotes the unsaturated zone where the equations are invalid. (d) The hydraulic conductivity image using the Slater and Lesmes model with replacing the ambiguous shallow high hydraulic conductivity part, which is surrounded by the dashed line, using Eq. (4.2). The average lithology has been inserted with proper scaling for comparison.

The deduced power law relation (Eq. 4.2) was also applied along this profile. Fig. 5.50 (c) shows the image of estimated hydraulic conductivity values using $A = 0.002$ and $B = 1.8$ (see Table 5.1). In general, this image is slightly similar to Slater and Lesmes model (Fig. 5.47b). Because Eq. (4.2) depends mainly on least-squares fit between the real part of conductivity and measured k_f -values, the assigned incorrect k_f values, discussed above for Børner and Slater and Lesmes models,

are absent. Compared with the lithology of DS33, this image looks more reasonable than *Slater* and *Lesmes* model image. It represents three hydraulic conductivity zones: medium (upper part) corresponds to sandy silt, low (middle part) corresponds to Eemian clay and high (lower part) corresponds to sandy aquifer. According to *Brassington (1988)* and *Panteleit et al. (2006)* of indicative k_f values of some rock types (see section 2.3) and in correlation with the borehole, DS33, Eq. (4.2) provides a degree of accuracy along this profile. The calculated k_f values can correspond to sandy silt ($\sim 10^{-6}$ m/s), clay ($\sim 10^{-7}$ m/s) and fine to medium sand ($\sim 10^{-5}$ - 10^{-3} m/s). Regarding to the core samples (Fig. 5.48), the Eemian clay is rich in fossils and intercalated with fine sand and consequently the k_f values might not be very low.

According to the above results and the similarity between the last two images (Fig. 5.50b and c), Eq. (4.2) was applied with *Slater* and *Lesmes* model to calculate the k_f values. Eq. (4.2) was applied at the part of the profile where the ohmic conduction is dominated, i.e., the imaginary part of conductivity is very low (at ~ 7 m depth and between 925-960 profile meter). Fig. 5.50 (d) represents where Eq. (4.2) was applied within the image using *Slater* and *Lesmes* model.

5.7.3 DISCUSSION

In the present case, a study of the DC secondary geoelectrical parameters has been found to be useful in specifying potential groundwater zones. Qualitatively, they can be applied to know a general overview about hydraulic characteristics of aquifers before going to detailed studies. Quantitatively, in general, the use of DC resistivity method may be feasible when a lot of prior information is available, which improves the interpretation results and, consequently, the k_f estimation. A power law relationship between the aquifer resistivity ρ and k_f using the DC soundings was assessed. This relation provided a good correlation with the observed k_f , which were derived from pumping test and grain size analysis of various geological conditions. The negative relation may be expected for consolidated aquifer where the flow of current and water will depend on the connectivity of fractures within the aquifer. On the other hand, the positive relation may be expected for unconsolidated aquifer where the current flow will be electrolytically by the water ions.

The inspection of the hydraulic conductivity images shows that the average k_f values using *Börner* model are smaller than *Slater* and *Lesmes* model. The calculated k_f values after *Börner* model are almost two orders lower of magnitude than *Slater* and *Lesmes* model, even though we used the parameters m and n , within the suggested by the authors, which produce the minimum k_f values. The using of *Börner* model can not discriminate the variation of k_f values between the sand aquifer and the Eemian clay. This discrepancy between both models can be attributed to the nature of samples used to derive each model. The *Slater* and *Lesmes* samples consist of 4 sands, 5 tills, 5 alluvial silt/sands, and 17 artificial mixtures of till, sand and clay. On the other hand, *Börner et al. (1996)* do not describe their samples but in general their data set includes more coarse-grained materials than *Slater* and *Lesmes* samples. In addition, the range of the adjustable parameters of *Slater* and *Lesmes* model are

much smaller than parameters range of *Börner* model. It is clear that both *Börner* and *Slater* and *Lesmes* models depend on the values of imaginary conductivity part, which depends on the salinity and the type of the pore fluid (*Hördt et al., 2009*). Consequently, the accurate determination of imaginary conductivity part is an important factor affecting hydraulic conductivity estimation in the field.

With our borehole data, we have mainly fine-grained sediments, i.e., we have relatively low hydraulic conductivities and large imaginary conductivities. The inspection of the DS33 core samples indicates that our borehole data seem to be in favor of *Slater* and *Lesmes* model. The poor k_f calculation for the deep sandy aquifer can be attributed to the low data coverage at the lower part of the 2D profile (Fig. 5.45, right) and/or the increasing of imaginary electrical conductivities of Eemian clay, especially at the central part of the profile, which probably causes a smearing to the upper boundary of sandy aquifer. Because the coastal area shows variations in salinity and pore fluid in a short distance, the possibility to calibrate these models to derive the values of adjustable parameters is difficult. Accordingly, the inaccurate estimation of k_f might be expected from field data. Finally, lab SIP measurements might lead to a refinement of the k_f estimation, in condition of presence an observed k_f data using pumping test or grain size.

The power law relation (Eq. 5.2) was calibrated with observed k_f values from grain size and pumping tests and a degree of accuracy was accomplished. The real conductivities from 2D SIP profile provide reasonable k_f results, which are in agreement with the average lithology. Below ~ 23 m depth, the k_f values strongly increase. This might be in coincidence with the medium sand. Fig. 5.54 (c) shows variations of k_f values between Eemian clay and Pleistocene sandy layers. This is not perfectly resolved by using *Börner* and *Slater* and *Lesmes* models, which exhibit little variations of k_f values. Although the imaginary conductivities provide more valuable information about the variations in pore sizes and the heterogeneities than real conductivities, the real conductivities are less sensitive to the variations of salinity. Therefore, when both conditions of heterogeneity in the grain size and salinity variations are present, the use of both real and imaginary conductivities to calculate k_f might be valuable. By correlation between both results, the integration can be achieved.

6 SUMMARY AND CONCLUSIONS

Coastal areas are transitional areas between the land and sea and often characterized by high population pressure due to rapid urbanization processes. Accordingly, there is increasing awareness of the importance of such areas. Close to the estuary of the Elbe River (northern part of Germany), the Cuxhaven coastal area is strongly affected by saltwater contaminations. A HEM survey represented a shallow conductive zone at the central part of this coastal area; in addition to deep saltwater intrusion. Schematically, *Streif (2004)* expected a presence of shallow channel-like features within the tidal deposits in this coastal area. Hydrogeologically, the Holocene tidal sediments are characterized by a low permeable property and consequently there is no recharge to these sediments (*Panteleit et al., 2001a*). They show medium to poor hydraulic conductivity values (*Panteleit, 2006*). Accordingly, more detailed multidimensional environmental and hydrogeophysical studies have been required to outline the hydrogeological conditions in the Cuxhaven coastal area. The thesis motivated to:

- ✚ Evaluate the geoelectrical methods (DC, FDEM and SIP) in imaging and characterizing the younger glaciation freshwater quaternary aquifer and saltwater intrusion.
- ✚ Identify the HEM shallow conductive zone, which was observed over the Cuxhaven coastal area.
- ✚ Evaluate the geoelectrical methods in imaging and characterizing the shallow channel-like features within the tidal deposits.
- ✚ Study the hydraulic characteristics of Holocene tidal deposits using the geoelectrical methods (DC and SIP). In addition, to attempt to assess an empirical equation to derive the hydraulic conductivity k_f and transmissivity K .

Geologically, the study area is located near to the estuary of the Elbe River (northern part of Germany). The Quaternary period is characterized by many marine regressions (cool climate) and transgression (warm climate) phases. Three regional glaciations affected north-western Europe to

different extents during the Elsterian (Anglian), Saalian (Wolstonian) and Weichselian (Devensian) glacial stages (Streif, 2004). The deposition of the Eemian clay can be attributed to a coastal transgression as the deposits of marine origin (Sindowski, 1969). At the end of Weichselian cold stage the sea level dropped to 110-130 m below the present level and Holocene transgression inundated the landscape, and presently tidal flats, extended marshes and raised bogs are developed (Streif, 2004). The seaward part of Holocene accumulation wedge mainly consists of pure fine- to medium-grained sand deposited on high-energy environments like the foreshore area. Further inland, it consists of fine sand, silt and clay layers deposited in sheltered or open tidal-flats as well as in the brackish-water environment of coastal lagoons and estuaries alternating with peat layers which were formed in coastal bogs (Streif, 2004).

A total of 30 DC resistivity soundings using Schlumberger configuration were conducted in the study area with 500 m maximum half electrode spacing (AB/2). They were measured to define the geoelectric boundaries of the subsurface layers and acquire general information about the geological situation before carrying out the 2D resistivity profiling. They were distributed to cover the whole area and some of these soundings were conducted close to some boreholes to derive the DC resistivity spectrum. In addition, some of these soundings were concentrated over the observed HEM shallow inductive zone. The measured 1D resistivity data was processed and inverted using IPI2win program (Bobachev, 2002), which based on linear filtering as 1D forward modeling. To overcome the 1D equivalence problems, the starting model was derived from borehole data. The resistivity spectrum was deduced from the 1D DC resistivity calibrations with the borehole data.

The 1D DC inverted data was illustrated in the form of geoelectrical cross-sections and horizontal slices (3D visualizations). It can be concluded that the subsurface resistivity distributions in the whole area are highly inhomogeneous. The results showed that the middle Quaternary sediments are the main freshwater aquifer in this area. The resistivity of the Quaternary aquifer is greater than 38 Ωm . The Pleistocene aquifer is covered by Holocene tidal deposits of mainly silt and silty sand. The maximum thickness of tidal deposits is ~18 m. In addition, two saltwater zones were also observed; a shallow perched saltwater above Eemian clay and a saltwater intrusion at lower boundary of Pleistocene aquifer which consists mainly of coarse sand. The perched saltwater can be noticed at the central and southern parts of the study area. The saltwater intrusion becomes shallower at the northern and eastern parts (~40 m maximum depth) than at the western and southern parts (> 100 m).

Consequently, the study area was divided in to three sites for multidimensional resistivity imaging. The DC resistivity configurations for 2D and 3D imaging were selected according to the advantages and the results of previous published applications of each configuration. In addition, the electrode spacings were selected according to the 1D DC resistivity results and HEM inversion results. For example, because the saltwater intrusion is shallower at the northern part than at the central and southern parts, 2m and 5 m electrode spacings were applied, respectively. The 2D/3D apparent resistivity data was processes and inverted using the DC2DInvRes/DC3DInvRes (Günther, 2004) and

BERT (Günther et al., 2006 and Rücker et al., 2006) programs. They are based on numerical modeling techniques using finite-difference, FD, and finite-element, FE, methods, respectively. The role of the inversion program is to minimize the difference between the calculated and measured resistivities by updating the calculated values through an iterative manner. The process is carried out using quasi-Newton smoothness constrained least-squares (L2) algorithms.

At the northern part, the Altenbruch site, a 2D profile was measured using two types of configurations, WN and WB. The 2D profile was 380 m long. The maximum electrode spacing, a , was 66 m and 48 m, respectively, for WN and WB, i.e., the maximum data level (n) was 33 and 24, respectively. A synthetic modeling was also done to confirm the 2D inversion results and to assess the joint inversion of WA and WB data sets. The input synthetic model simulated the geological and hydrogeological situations at this site. A series of 9 lines using 288 electrodes with 2 m electrode spacings (32 * 9 grid) was used for 3D DC data acquisition. Because of simplicity in field implementation, a 3D survey design using a sparse set of lines was applied. The joint inversion of WB and DD data sets was assessed. Finally, the inverted data was correlated with HEM inversion results.

Based on the electrical resistivity tomography (ERT) at Altenbruch, the following observations can be concluded:

- The combination of WN with WB data sets allows a good resolution for mapping the very low resistivity layer. The average saltwater intrusion depth is about 20 m. The individual configurations show limitations in detection the saltwater depth and the heterogeneity within the tidal deposits.
- The synthetic modeling shows that the heterogeneity within the tidal deposits can be a slightly better resolved by combined WN and WB data sets than individual configurations. The undulation in the upper surface of saltwater layer in the combined WA and WB inverse model is less than for the individual configurations. Finally, it has proved to be useful to combine WA and WB data sets for delineating the freshwater-saltwater boundary.
- The 3D joint inversion of WB and DD data sets shows a good vertical and horizontal resolution and a good correlation with the borehole data. Individual WB and DD show limitations in horizontal resolution and penetration depth, respectively. The maximum freshwater aquifer thickness is 10 m and corresponds to silt and fine sand of upper Quaternary deposits.

At the central part (Lüdingworth, Norderscheidung), DC and FDEM measurements were carried out. First, away from EM noise sources (e.g., current cables and metals) FDEM soundings (36) were acquired. They were measured along one profile using vertical dipole configuration with a broad frequency range (10 frequencies, from 110 Hz to 56320 Hz). The profile length was 360 m. The FDEM profile was close to a DC sounding and a borehole in the considered area. The coil and sounding spacings were 100 m and 10 m, respectively. The choice of field survey parameters were based on published data in Canada, measured over geological conditions similar to our area. The measured data in the form of inphase and quadrature components were processed and inverted using the IX1Dv3 (2006) program. The data are already expressed in percent of the primary field and this unit is

used also for the RMS error. The forward modeling based on 1D linear filter similar to the IPI2win program. To select the model that represents the best conditions of the subsurface, the starting model was derived from borehole data and DC sounding results. The inversion is carried out using single or multiple iterations (*INTERPEX, 2006*).

A couple of 2D DC perpendicular profiles and a 3D grid were measured at Norderscheidung site. Because the WN configuration showed limitations in bad coverage and smearing of freshwater-saltwater boundary at the northern part, WB and SC configurations were assessed at this site. Before applying these configurations, the geological information of borehole WIT01 and the inversion results of FDEM soundings were simulated by preparing a synthetic model using 5 m electrode spacing. The forward calculation of the input model for both WB and SC configurations was calculated using the FD method. The inversion process was carried out using nonlinear smoothness constrains least-squares optimization technique. Accordingly, WB and SC configurations were assessed under the geological and hydrogeological situation at this site.

Consequently, the 2D DC profiles were measured using WB and SC configurations at 5 m electrode spacing. The first 2D DC profile runs parallel to the FDEM profile. It was 715 m long using 144 electrodes. For the WB configuration, the maximum electrode spacing was 235 m ($n=47$). For the SC configuration, we started with the “ a ” spacing (which is the distance between the P1-P2 potential dipole) equals to 5 m and we repeated the measurements with “ n ” values of 1, 2, 3, 4, 5, 6, 7 and 8. Then, the “ a ” spacing was increased to 10 m, and measurements with “ n ” equals to 1, 2, 3, 4, 5, 6, 7 and 8 were carried out. This process was repeated until “ a ” equals 40 m. The second 2D profile was 1615 m long. The roll along method was used to acquire the 2D data using 144 electrodes. The same WB and SC parameters (“ a ” and “ n ”) of the first profile were used for this long profile, but the maximum “ a ” distance was 45 m for the SC configuration. The 2D DC data were processed using the DC2DInvRes and inverted using the BERT program. The inverted model reliability of both WB and SC configurations were checked using different values of regularization parameters. In addition, the model sensitivity was checked to study the model reliability. The 2D profiles were correlated with the available boreholes and HEM sections at this site.

The 3D DC survey was carried out using 128 electrodes and 5 m electrode spacing. The electrodes were arranged in a grid of 16 * 8 electrodes. Eight orthogonal 2D parallel profiles using WB configuration were measured in one direction (y) to acquire the 3D data. The maximum current electrode spacing was 25 m. On the other hand, a complete data set survey technique was used to acquire the 3D data acquisition using PP and DD configurations. For PP and DD configurations, the maximum current electrode spacing was 75 m and 15 m, respectively. It was noted that the 3D DD DC survey was more sensitive to noise which was clearly observed from reciprocity measurements than the PP configuration. In addition, a lot of time was consumed for the DD survey. The forward calculations of both WB and PP data sets were done using the FE method. The BERT program was

used to invert these data. Because of the huge number of 3D DD data points, the FD method and the DC2DInvRes program were used for forward calculations and the inversion process, respectively.

According to the inversion results at Norderscheidung site, it can be concluded that:

- Under no or limited prior information, the combined inversion of WB and SC data sets can produce a sensible fusion for saltwater imaging and complicated subsurface structure when the configurations cannot separately produce a reliable resistivity model. On the contrary, there is no guarantee that the combined inversion of WB and SC data set will produce a superior subsurface image to ones produced by individual inversions in another area.
- For a highly conductive layer imaging, WB presents a worse by amplifying lateral and vertical effects (smearing) and, consequently, its thickness or depth will be greater than in reality.
- For deep saltwater imaging, it is not advisable to apply individual SC configuration, as it shows difficulties to reach optimum regularization parameters.
- In presence of anthropogenic features (metal pipes etc.) with expected high noise levels, an acceptable fit between EM raw data and calculated model can be expected only for low frequency data (< 2000 Hz). With a high RMS error, an acceptable imaging of deep saltwater will be achieved only.
- In a noisy area, DC soundings cannot be considered as an alternative to FDEM soundings. DC soundings are necessary to derive a FDEM starting model and to predict resistivity values of the shallow layers, i.e. for high frequency data.
- Based on our inversion results, the isolated HEM shallow high conductive layer can be interpreted as perched saltwater. Its extension and thickness were well imaged using DC and HEM results.
- The 3D models of WB, PP and DD configurations support each other and they show a good correspondence with the nearest borehole data and other geophysical results. The 3D imaging using 2D orthogonal 2D profiles provides a quick and cost effective tool for perched saltwater imaging. It is easier to automate the data acquisition of 3D PP configuration and check the data quality in the field than to apply DD configuration, which is characterized by the lowest signal-to-noise ratios.
- FDEM and DC resistivity imaging characterize the heterogeneity within Pleistocene deposits and saltwater intrusion more accurately than HEM results.

At the southern part, the Süderscheidung site, FDEM, DC and SIP methods were applied for imaging the saltwater-freshwater boundary and shallow sedimentary structures. Before 2D imaging, 1D soundings using FDEM methods were conducted. Prior to the FDEM field measurements, a short FDEM profile was tested in order to obtain the optimal coil separations and station intervals which can be applied in the study area; and to examine the stray coupling effect between the transmitter Tx and receiver Rx. The FDEM measurements were carried out to evaluate this method, by constructing a 2D cross-section, in characterizing the perched saltwater and shallow channel within the tidal flat deposits. A total of 115 FDEM soundings, along a 1135 m profile, were collected. The FDEM survey was operated in vertical-dipole mode (horizontal, coplanar coils) with a broad frequency range (10 frequencies, from 110 Hz to 56320 Hz).

Based on the borehole information, field observations and 1D inversion results, the saltwater intrusion at Süderscheidung site is deeper than at northern and central parts of the study area. Because the SC configuration shows limitations in imaging the saltwater intrusion at the central part, it was not recommended at this site. Accordingly, WN and WB configurations were applied. Especially WB shows good results at the northern and central part. The 2D measurements were carried out at the location of the FDEM profile to construct a 2D image and to study its limitations. The 2D profile was measured using a system of 192 electrodes with an electrode spacing of 5 m. The profile length was 1675 m. The roll along-method was applied to acquire the 2D data. The maximum current electrode spacing was 705 m and 235 m for WN and WB, respectively. Similar to the Norderscheidung site, the data was processed using the DC2DInvRes and the inverted using BERT programs. To identify the appropriateness of 2D interpretation, a synthetic modeling was carried out. The input resistivity model was deduced from our geological background, available boreholes and the results of geophysical methods at this site. The synthetic data and inversion process were carried out using the DC2DInvRes modeling software.

Furthermore, to obtain detailed information and characterization of the tidal flat deposits and based on FDEM and DC inversion results, a long spectral induced polarization (SIP) profile was carried out using the dipole-dipole configuration with 5 m electrode spacing. 36 remote units were used in SIP data acquisition using a wide frequency range from 0.625 Hz to 1000 Hz (10 frequencies). The SIP 2D profile was 380 m long and it was located at the FDEM profile. The data of the 2D SIP profile was conducted as combined data set from the three measured overlapped profiles (P1, P2 and P3); each profile was 180 m long with an overlap of 80 m. the measured data, resistivity magnitude and phase, was processed and inverted using DC2DInvRes program.

The main implications of the results at the southern part are:

- The resistivity measurements (DC, FDEM and SIP) identify a zone of perched saltwater as well as a high heterogeneity within the near-surface Quaternary tidal flat deposits, which form a shallow channel-like feature.
- The FDEM method can be considered as a fast alternative sounding method to image tidal sediments and the perched saltwater in a shorter time with higher accuracy than DC soundings.
- Adopting a 1D structure and using extensive borehole data in the study area, the 1D FDEM inversion results appear to be robust and reliable; the method turns out to be applicable and suitable in this coastal area. 50 m and 10 m coil spacing and station intervals, respectively, are the best FDEM field parameters to characterize the heterogeneity within tidal deposits here.
- In absence of boreholes or wells, 2D DC and SIP methods are more stable and can be applied better than FDEM soundings to avoid the misinterpretation from equivalence or ambiguity effects.
- The combined configurations of WN with WB data improve the ratibility of the resulting models and allow a good resolution for mapping the near-surface geology and saltwater-freshwater boundary.

- The thickness of tidal flat deposits and the shallow channel may be underestimated by the 2D resistivity technique in presence of conductive layers (perched saltwater and clay), which can mask an underlying resistive (sand) layer.
- In presence of high conductive layers, the synthetic modeling is necessary to interpret and study 2D images, especially in characterizing tidal deposits in coastal areas. Certain limitations in detecting the perched saltwater and shallow channel depth and width can be observed in the synthetic model, which has to be taken into consideration when interpreting the 2D field data.
- The phase and imaginary conductivity images (SIP measurements) reflect different subsurface characteristics and thus looking at both of them is instructive.
- Smooth model inversion improves the interpretability of resistivity/IP data. In the field, a frequency range of 0.1 to 10 Hz appears to be optimum considering survey time (and cost).
- The IP conductivity phase presents an accurate detection of the perched saltwater, e.g., in patched forms, better than DC and FDEM methods.
- DC resistivity imaging characterizes the heterogeneity and the thickness variations within the tidal deposits more accurately than HEM results.

The DC geoelectrical parameters (Dar-Zarrouk) are calculated from 1D DC soundings. They were interpreted qualitatively in the terms of hydraulic conductivity, transmissivity, clay content, grain size distribution and potentiality of the aquifer. Then, an empirical relationship between the aquifer resistivity ρ and K and/or k_f using DC soundings was derived. This equation depends on the power law relation between the measured k_f values and aquifer resistivities. Because a few measured k_f values (using pumping test and grain size analysis) are available in the Cuxhaven area, this relation was assessed and tested using various published 1D DC data. In addition, at the southern part SIP inverted data was used to derive k_f values using *Börner et al. (1996)* and *Slater and Lesmes (2002a)* models. The real conductivity values of SIP inverted data was used to calculate k_f values using the deduced power law relation.

Based on the k_f calculations using various approaches the following conclusions could be drawn:

- The resistivity sounding method offers great advantages in hydraulic parameters estimation with low cost and high density in optimized time.
- The geoelectrical parameters (Dar-Zarrouk) represent a good qualitative interpretation to the Holocene aquifer.
- Good estimations of k_f values are obtained using aquifer resistivity for unconsolidated sediments with the form of $(\rho)^A \cdot h \cdot B$. However, it would be meaningful if it is tested in areas with diverse geological environments, which may generalize it.
- The calculated k_f values after the *Börner* model are almost two orders of magnitude lower than those of the *Slater* and *Lesmes* model, which can be attributed to the nature of samples used to derive each model.

- Because the coastal area shows variations in salinity and pore fluid in a short distance, the possibility to calibrate the *Börner* and *Slater* and *Lesmes* models to derive the values of adjustable parameters could be difficult.

Outlook

+ Further Holocene structures (e.g., shallow channels) are expected at the central part of the study area. Consequently, further geophysical studies incorporating DC profiling and closely spaced FDEM soundings are recommended.

+ Our results encourage the wider adaption of SIP to characterize the heterogeneity within tidal deposits in coastal areas. Additional SIP in combination with DC profiling should be conducted on long survey lines at the central part of the study area.

+ Further work including pumping tests, hydraulic tomography and additional SIP lab measurements would help to assess the reliability of derived hydraulic properties.

+ The main focus should be on the spectral analysis of IP data. The aim should be to find relations between relaxation time and hydraulic parameters.

+ It is required to do a grain size analysis and electro-scan to the Eemian clay samples, which were collected at the southern part of the study area, to interpret the high IP phase behavior.

LIST OF FIGURES

1.1	<i>Flowchart relevance to the steps of planning the research work</i>	4
2.1	<i>Location map of the study area</i>	7
2.2	<i>Digital elevation model of the Cuxhaven-Bremerhaven region</i>	8
2.3	<i>Trends and dynamics of sea-level changes</i>	8
2.4	<i>Geological setting through the Cuxhaven area</i>	10
2.5	<i>Lithological information from observed boreholes</i>	12
2.6	<i>Generalized geological cross-section</i>	13
2.7	<i>A Schematic cross-section through the coastal Holocene</i>	13
2.8	<i>Location map of the coastal area and the hydraulic flow pattern</i>	14
3.1	<i>Typical current and idealized voltage waveforms</i>	16
3.2	<i>Principle of resistivity measurement</i>	17
3.3	<i>The current flow lines</i>	18
3.4	<i>Current flow patterns</i>	18
3.5	<i>Electrical properties of common rocks and minerals</i>	19
3.6	<i>Setup for 2D Wenner resistivity measurements</i>	23
3.7	<i>The use of the roll-along method</i>	24
3.8	<i>Arrangement of electrodes</i>	25
3.9	<i>The 3D survey techniques</i>	25
3.10	<i>Sketch of the distribution of the ionic species in the electrical double layer</i>	28
3.11	<i>Schematic of ion-conductive zones in porous rocks</i>	29
3.12	<i>Complex resistivity signal for a distinct frequency</i>	31
3.13	<i>Some common electrode configurations</i>	32
3.14	<i>2D sensitivity section for the common electrode configurations</i>	34
3.15	<i>The primary and secondary electromagnetic field</i>	39
3.16	<i>Common loop configurations</i>	41
3.17	<i>Schematic diagram of the resistivity data interpretation process</i>	42

4.1	Location map of the study area.....	56
4.2	RESECS multi-channel resistivitymeter.....	57
4.3	MaxMinI+10 EM instrument.....	60
4.4	Location map of EM and SIP measurements.....	61
4.5	SIP256C instrument for IP measurements.....	62
4.6	Correlation between the interpreted resistivity layers and the observed borehole data.....	64
4.7	An example of FDEM sounding data.....	65
4.8	Stitched FDEM resistivity sections.....	66
4.9	Inphase component for different frequencies to demonstrate the stray coupling effects.....	67
4.10	Pseudosections of the measured apparent resistivity.....	68
4.11	3D data set, derived from orthogonal 2D WB profiles.....	68
4.12	3D PP data set, derived from complete data set technique.....	69
4.13	Sample complex apparent resistivity data set.....	70
4.14	Histogram of apparent resistivity 3D DD data set.....	71
4.15	Reciprocity crossplot of normal and reverse 3D PP data set.....	71
4.16	SIP measured apparent resistivity section and histogram.....	72
4.17	Horizontal slices of the model obtained from the 3D inversion.....	74
4.18	$k_f S$ for various wells and (b) relationship between aquifer resistivity and k_f	76
4.19	$k_f \sigma$ for various wells and (b) relationship between aquifer resistivity and k_f	77
4.20	Relationship of aquifer resistivity vs. k_f with regression line.....	78
4.21	Correlation of the estimated hydraulic conductivity using the power law relation.....	79
5.1	A resistivity spectrum.....	81
5.2	Apparent resistivity and stitched resistivity sections.....	82
5.3	3D visualization resistivity model.....	85
5.4	Resistivity distribution of tidal flat deposits with different depths.....	86
5.5	Location map of Altenbruch site.....	87
5.6	Comparison of borehole lithology with the measured apparent resistivity.....	87
5.7	The 2D interpretation sections at Altenbruch.....	89
5.8	Synthetic modeling and sensitivity analysis at Altenbruch.....	91
5.9	3D inverted models of WB and DD at Altenbruch.....	92
5.10	3D joint inversion results of combined WB and DD data sets at Altenbruch.....	93
5.11	3D visualization of 2D DC profile and 3D model at Altenbruch.....	94
5.12	Map of the Norderscheidung site.....	95
5.13	FDEM raw data at Norderscheidung site.....	96
5.14	FDEM sounding data and 1D inverse model.....	96
5.15	Stitched resistivity section from 1D FDEM inversion.....	97
5.16	Representative FDEM soundings and their 1D Ridge Regression inversion results.....	98
5.17	The RMS misfit values of all FDEM soundings.....	99
5.18	A synthetic model for numerical imaging experiment at Norderscheidung.....	101
5.19	WB 2D DC pseudo-section at Norderscheidung.....	102
5.20	SC 2D DC pseudo-section at Norderscheidung.....	102
5.21	Inverse model resistivity sections obtained by WB and SC data sets at Norderscheidung.....	105

5.22	<i>HEM resistivity section at Norderscheidung</i>	105
5.23	<i>Sensitivity analysis and inversion results of combined WB and SC data sets at Norderscheidung</i>	107
5.24	<i>WB 2D DC pseudo-section at Norderscheidung</i>	108
5.25	<i>SC 2D DC pseudo-section at Norderscheidung</i>	108
5.26	<i>2D Inversion results at Norderscheidung</i>	110
5.27	<i>Fence diagram showing the relation between Norderscheidung 2D resistivity sections</i>	111
5.28	<i>HEM resistivity section at Norderscheidung</i>	111
5.29	<i>A fence diagram of 3D WB model with 2D DC resistivity profiles at Norderscheidung</i>	112
5.30	<i>3D inverted model, of eight orthogonal WB profiles at Norderscheidung</i>	113
5.31	<i>3D inverted model of PP data at Norderscheidung</i>	114
5.32	<i>3D inverted model of DD data at Norderscheidung</i>	115
5.33	<i>Location map of Süderscheidung site</i>	115
5.34	<i>Lithology at the boreholes DS32, DS33, DS34 and UE103, Süderscheidung site</i>	116
5.35	<i>Correlation between the 1D interpretation and observed borehole data at Süderscheidung site</i>	117
5.36	<i>FDEM raw data: Inphase and quadrature components for different frequencies at Süderscheidung site</i> ...	117
5.37	<i>FDEM sounding data in correlation with borehole and DC sounding data at Süderscheidung site</i>	119
5.38	<i>Stitched resistivity sections from 1D FDEM inversion at Süderscheidung site</i>	119
5.39	<i>The RMS misfit values of all FDEM soundings at Süderscheidung site</i>	120
5.40	<i>2D inversion results at Süderscheidung site</i>	121
5.41	<i>HEM resistivity section at Süderscheidung site</i>	122
5.42	<i>Combined WN and WB apparent resistivity data sets at Süderscheidung site</i>	123
5.43	<i>Shallow electrical imaging from 2D inversion of combined WN and WB data sets at Süderscheidung</i>	124
5.44	<i>The synthetic modeling of WA and WB configurations at Süderscheidung site</i>	125
5.45	<i>The complex conductivity magnitude, phase and sensitivity sections at Süderscheidung site</i>	128
5.46	<i>Magnitude, real part, phase shift and imaginary part of conductivity at 1.25 Hz at Süderscheidung site</i>	129
5.47	<i>Magnitude, real part, phase shift and imaginary part of conductivity at 2.5 Hz at Süderscheidung site</i>	130
5.48	<i>Representative core samples from Eemian clay layer at Süderscheidung site</i>	134
5.49	<i>Secondary geoelectrical parameters of Holocene tidal deposits</i>	135
5.50	<i>Hydraulic conductivity sections estimated from SIP data using various approaches</i>	138
C.1	<i>1D inversion results of DC sounding points with boreholes calibration</i>	151
D.1	<i>Sensitivity analysis and inversion results of WB data at Norderscheidung</i>	153
D.2	<i>Sensitivity analysis and inversion results of SC data at Norderscheidung</i>	154
E.1	<i>The complex conductivity magnitude, phase shift and sensitivity sections for frequencies 40 Hz, 80 Hz and 125 Hz frequencies</i>	154
F.1	<i>Soil samples description close to borehole DS33 from 9 m to 24 m depth</i>	155

LIST OF TABLES

2.1	<i>Stratigraphic record of Middle and Upper Pleistocene</i>	10
4.1	<i>Aquifer parameters of Dc soundings and estimated k_f</i>	76
4.2	<i>Correlation of measured k_f using pumping test and estimated k_f at Nigeria sandy aquifer</i>	77
4.3	<i>Aquifer parameters of sounding locations and estimated k_f at Nigeria sandy aquifer</i>	77
4.4	<i>Aquifer parameters of DC soundings and estimated k_f at India hard rock aquifer</i>	79
5.1	<i>Aquifer parameters of DC soundings and estimated k_f at Cuxhaven coastal area</i>	137

BIBLIOGRAPHY

Alley, R. B., Marotzke, J., Nordhaus, W. D., Ovrpeck, J. T., Peteet, D. M., Pielkejr., R. A., Pierrehumbert, R. T., Rhines, P. B., T. F. Stocker, Talley, L. D. and Wallace, J. M., 2003. Abrupt climate change. *Science*, 299, 2005-2010.

Allred, B., Groom, D., Ehsani, M. R. and Daniels, J. J., 2008. Resistivity methods. In: Allred, B., Ehsani, M. R. and Daniels, J. J. (eds.), *Handbook of agriculture geophysics*, Chap. 5. **Taylor & Francis Group, LLC, 85-108.**

Anderson, W.,1989. A hybrid fast Hankel transform algorithm for electromagnetic modeling. *Geophysics*, 54, 263-266.

APEX Parametric Limited, 1998. Operations manual, MAXMIN I+10 EM system. Ontario, Canada.

Archie, G. E., 1942. The electrical resistivity log as an aid in determining some reservoir characteristics. American Institute of Mineral and Metal Engineering, Technical publication, *Petroleum Technology*, 146, 8-13.

Athanasiou, E. N., Tsourlos, P. I., Papazachos, C. B. and Tsokas, G. N., 2007. Combined weighted inversion of electrical resistivity data arising from different array types. *Journal of applied Geophysics*, 62, 124-140.

Auken, E., and Christiansen, A. V., 2004. Layered and laterally constrained 2D inversion of resistivity data. *Geophysics*, 69, 752-761.

Baines, D., Smith, D. G., Froese, D. G., Bauman, P. and Nimeck, G., 2002. Electrical resistivity ground imaging (ERGI): a new tool for mapping the lithology and geometry of channel-belts and valley-fills. *Sedimentology*, 49, 441-449.

Barlow, P. M., 2003. Groundwater in freshwater-saltwater environments of the Atlantic Coast. U.S. Geological Survey Circular, 1262 p.

Bazinet, R., 2000. Less electrodes for improved resistivity profiling. The 6th Meeting of Environmental and Engineering Geophysics, Bochum, Germany, El 17.

Beard, L. P. and Morgan, F. D., 1991. Assessment of 2-D resistivity structures using 1-D inversion. *Geophysics*, 56, 874-883.

Behre, K.-E., 2004. Coastal development, sea-level change and settlement history during the later Holocene in the clay district of Lower Saxony (Niedersachsen), northern Germany. *Quaternary International*, 112, 37-53.

Bentley, L. R and Gharibi, M., 2004. Two-and three-dimensional electrical resistivity imaging at a heterogenous remediation site. *Geophysics*, 69, 674-680.

Besenecker, H., Daniels, C. H., Hofmann, W., Höhndorf, A., Knabe, W. and Kuster, H., 1981. Horizontbeständige Schwermineralanreicherungen in Pliozänen Sanden des Niedersächsischen küstenraumes. *Geologisches Jahrbuch*, D49, Hannover, 23 p.

Bing, Z., and Greenhalgh, S. A., 2001. Finite element three-dimensional direct current resistivity modeling: Accuracy and efficiency considerations. *Geophysics Journal International*, 145, 679–688.

Binley, A. and Kemna, A., 2005. DC resistivity and induced polarization methods. In: Rubin, Y. and Hubbard, S. S (eds.), *Hydrogeophysics*, Chap. 5. Water science and technology library, Springer, Netherlands, 50, 129-156.

Bobachev, A., Modin, I. N., Pervago, E. V. and Shevnin, V. A., 1999. Stream-function used for current-lines construction in 2-dimension DC modeling. The 5th Meeting EEGS-ES, Budapest, 5-9 September 1999.

Bobachev, A., 2002. IPI2Win: A Windows software for an automatic interpretation of resistivity sounding data. Ph.D. thesis, Moscow state Univ.

Bobachev, A., Modin, I. and Shevnin, V., 2003. IPI2Win V2.0: User's guide, Moscow State Univ., Geological Faculty, Dept. of Geophysics, http://geophys.geol.msu.ru/rec_lab3.htm.

Börner, F. D., Schön, J. H., 1991. A Relation between the Quadrature component of electrical conductivity and the surface area of sedimentary rocks. *Log Analyst*, 32, 613–613.

Börner, F. D., Schopper, W. and Weller, A., 1996. Evaluation of transport and storage properties in the soils and groundwater zone from induced polarization measurements. *Geophysical Prospecting*, 44, 583–601, doi:10.1111/j.1365-2478.1996.tb00167.x.

Brassington, R., 1988. Field hydrogeology. Geological Society of London Handbook Series. Open Univ. press, 175 p.

Broyden, C. G., 1965. A class of methods for solving nonlinear simultaneous equations. *Mathematics of Computation*, 19, 577-593.

Cagniard, I., 1952. La prospection geophysique des eauc Sousterraines. Colloque d'Ankara sur l'Hydrologie de la zone Arids, UNESCO, 184-190.

Cameo, E. A., 2006. Seawater intrusion in complex geological environments. Ph.D. thesis, Technical Univ. of Catalonia, UPC.

Cameron, T. D. J., Stoker, M. S. and Long, D., 1987. The history of Quaternary sedimentation in the UK sector of the North Sea Basin. *Journal of the Geological Society of London*, 144, 43-58.

Cameron, T. D. J., van Doorn, D., Laban, C. and Streif, H., 1993. Geology of the southern North Sea Basin. In: Hillen, R. and Verhagen, H. (eds.), *Coastlines of the southern North Sea*. American Society of Civil Engineers, New York, 14-26.

Carman, P. C., 1939. Permeability of saturated sands. soils and clays. *Journal of Agric. Sci.*, 29, 263-273.

Chandra, S., Ahmed, S., Ram, A. and Dewandel, B., 2008. Estimation of hard rock aquifer hydraulic conductivity from geoelectrical measurements: A theoretical development with field application. *Journal of Hydrology*, 357, 281-227, doi: 10.1016/j.jhydrol.2008.05.023.

Chang, P-Y, Chang, S-K., Liu, H-C and Wang, S. C., 2011. Using integrated 2D and 3D resistivity imaging methods for illustrating the mud-fluid conduits of the Wushanting mud Volcanoes in southwestern Taiwan. *Terr. Atmos. Ocean. Sci.*, 22(1), XXX-XXX (early release), doi:10.3319/TAO.2010.06.21.01(TT).

Christensen, N. B., 1990. Optimized fast Hankel transform filters. *Geophysical prospecting*, 38, 545-558.

Christensen, N. B., 2000. Difficulties in determining electrical anisotropy in subsurface investigations. *Geophysical Prospecting*, 48, 1-19.

Christensen, N. B. and Sørensen, K., 2001. Pulled array continuous electrical sounding with an additional inductive source. An experimental design study. *Geophysical Prospecting*, 49 (2), 241-254.

Claerbout, J. F. and Muir, F., 1973. Robust modeling with erratic data. *Geophysics*, 38, 826-844.

Clavier, C., Coates, G. and Dumanoir, R., 1984. The theoretical and experimental bases for “dual water” model for the interpretation of shaley sands. *Society of petroleum Engineering Journal*, 4, 153-168.

Coggon, J. H., 1971. Electromagnetic and electrical modeling by the finite element method. *Geophysics*, 36, 132– 155, 1971.

Coggon, J. H., 1973. A comparison of IP electrode arrays. *Geophysics*, 38, 373-761.

Constable, S. C., Parker, r. L. and Constable, C. G., 1987. Occam’s inversion: A practical algorithm for generating smooth models from EM sounding data. *Geophysics*, 52, 289-300.

Corriols, M. and Dahlin, T., 2008. Geophysical characterization of the león-Chinandega aquifer, Nicaragua. *Journal of Hydrogeology*, 16, 349-362.

Corriols, M., Nielsen, M., Dahlin, T. and Christensen, N., 2009. Aquifer investigations in the LeÓN-Chinandega plains, Nicaragua, using electromagnetic and electrical methods. *Near Surface Geophysics*, 7, 413-425.

Dahlin, T., 1993. On the automation of 2D resistivity surveying for engineering and environmental applications. Ph.D. thesis, ISRN LUTVDG/TVDG-1007-SE, ISBN 91-628-1032-4, Lund Univ., 187 p.

- Dahlin, T., Johansson, S. and Landin, O., 1994.** Resistivity surveying for planning of infrastructure. Proceedings of surveying for planning of infrastructure. Proceedings of SAGEEP 94 (Symposium on the Application of Geophysics to Engineering and Environmental Problems). Boston, March 27-31, 509-528.
- Dahlin, T., 1996.** 2D resistivity surveying for environmental and engineering applications. First Break, 14(7), 275-283.
- Dahlin, T. and Loke, M. H., 1997.** Quasi-3D resistivity imaging: mapping of 3D structures using two dimensional DC resistivity techniques. Proceedings of the 3rd Environmental and Engineering Geophysics Meeting, Aarhus, Denmark, Exp. Abst., 143-146.
- Dahlin, T. and Loke, M. H., 1998.** Resolution of 2D Wenner resistivity imaging as assessed by numerical modeling. Journal of Applied Geophysics, 38(4), 237-249.
- Dahlin, T., 2001.** The development of DC resistivity imaging techniques. Comput. Geosci., 27, 1019-1029.
- Dahlin, T. and Zhou, B., 2004.** A numerical comparison of 2D resistivity imaging with 10 electrode arrays. Geophysical Prospecting, 52, 379-398.
- Daniels, J., Vendl, M. and Ehsani, M. R., 2008.** Electromagnetic induction methods. In: Allred, B., Ehsani, M. R. and Daniels, J. J. (eds.), Handbook of agriculture geophysics, Chap. 6. Taylor & Francis Group, LLC, 109-128.
- Das, U. C., 1995.** Apparent resistivity curves in controlled source electromagnetic sounding directly reflecting true resistivities in a layered earth. Geophysics, 60, 53-60.
- Davis, P., Greenhalgh, S. and Merrick, N., 1980.** Resistivity sounding computations with any array using a single digital filter. Geophysics, 11, 45-62.
- de Lima, O. A. L. and Sharma, M. M., 1990.** A grain conductivity approach to shaly sand. Geophysics, 50, 1347-1356.
- de Lima, O. A. L., Clennell, M. B., Nery, G. G. and Niwas, S., 2005.** A volumetric approach for the resistivity response of freshwater shaly sand. Geophysics, 70 (1), 1-10.
- deGroot-Hedlin, C. and Constable, S., 1990.** Occam's inversion to generate smooth, two dimensional models from magnetotelluric data. Geophysics, 55, 1613-1624.
- Dey, A. and Morrison, H. F., 1979a.** Resistivity modeling for arbitrary shaped two-dimensional structures. Geophysical Prospecting 27, 1020-1036.
- Dey, A. and Morrison, H. F., 1979b.** Resistivity modeling for arbitrarily shaped three dimensional shaped structures. Geophysics 44, 753-780.
- Domenico, P. A. and Schwartz, F. W., 1990.** Physical and chemical Hydrology. Wiley Press, 324 p.
- Drahor, M. G., Göktürkler, M. A., Kurtulmus, T. Ö. and Tuna, N., 2007.** 3D resistivity imaging from an archaeological site in south-western Anatolia, Turkey: a case study. Near surface Geophysics, 5(3), 195-201.
- Dukhin, S. and Shilov, V. N., 1974.** Dielectric phenomena and the double layer in disperse systems and polyelectrolytes. John Wiley & Sons, New York, 192 p.

- Edwards, L. S., 1977.** A modified Pseudosection for resistivity and IP. *Geophysics*, 42, 1020-1036.
- Ekwe, A. C., Onu, N. N. and Onuoha, K. M., 2006.** Estimation of aquifer Hydraulic characteristics from electrical sounding data: the case of middle Imo River basin aquifers, south-eastern Nigeria. *Journal of spatial Hydrology*, 6(2), 121-132.
- Eleraki, M., Gasallah, M., Gemail, K. and Attwa, M., 2010.** Application of resistivity method in environmental study of the appearance of soil water in the central part of Tenth of Ramadan City, **Egypt**. *Quarterly Journal of Engineering Geology and Hydrology*, 43, 171-184.
- Ellis, R. G. and Oldenburg, D. W., 1994a.** The pole-pole 3D DC resistivity inverse problem: a conjugate-gradient approach. *Geophysics Journal International*, 119, 187-194.
- Ellis, R. G. and Oldenburg, D. W., 1994b.** Applied geophysical inversion. *Geophysical Journal International*, 116, 5-11.
- Ernstson, K. and Kirsch, R., 2006.** Geoelectrical methods. In: Kirsch, R. (ed.), *Groundwater geophysics, A tool for hydrogeology*, Chap. 3. Springer Berlin Heidelberg, Germany, 85-108.
- Everett, M. and Meju, M., 2005.** Near-surface controlled-source electromagnetic induction: background and recent advances. In: Rubin. Y. and Hubbard. S. S. (eds.), *Hydrogeophysics*, Chap. 6. Water science and technology library, Springer Netherlands, 50, 157-183.
- Fitterman, D. V. and Deszcz, P. M., 2001.** Saltwater intrusion in Everglades National Park, Florida. 1st International Conference on Saltwater and Coastal Aquifers-Monitoring, SWICA-M3, Modeling and Management, Essaouira, Morocco, April 23-25.
- Flathe, H., 1955.** Possibilities and limitations in applying geoelectrical methods to hydrogeological problems in the coastal area of northwest Germany. *Geophysical prospecting*, 3, 95-110.
- Fluche, B. and Sengpiel, K.-P., 1997.** Grundlagen und Anwendungen der Hubschrauber-Geophysik. In: Beblo, M. (ed.), *Umweltgeophysik*. Ernst and Sohn, Berlin, 363-393.
- Foged, N., 1987.** The need for Quaternary geological knowledge in geotechnical engineering. *Boreas*, 16 (4), 419-424.
- Fox, R. C., Hohmann, G. W., Killpack, T. J., and Rijo, L., 1980.** Topographic effects in resistivity and induced-polarization surveys. *Geophysics*, 45(1), 75–93.
- Friedel, S., 2000.** Über die Abbildungseigenschaften der geoelektrischen Impedanztomographie unter Berücksichtigung von endlicher Anzahl und endlicher Genauigkeit der Meßdaten. Dissertation, Univ., Leipzig, Germany. *Berichte aus der Wissenschaft*, Aachen, Germany.
- Friedel, S., Thielan, A. and Springman, S. M., 2006.** Investigation of a slope endangered by rainfall-induced landslides using 3D resistivity tomography and geotechnical testing. *Journal of Applied Geophysics*, 60, 100-114.
- Friedhoff, T., 2001.** Wasserhaushaltsuntersuchungen im tiefeinflussten Einzugsgebiet der Modem (Land Hadeln). Diplomarbeit, Univ. Bremen, Germany
- Frohlich, R. K., 1974.** Combined geoelectrical and drill-hole investigations for detecting freshwater aquifers in northwestern Missouri. *Geophysics*, 39, 340-352.

- Fulda, C., 2002.** Numerische Studie zur Salz-/Süßwasserverteilung im Rahmen der Cuxhavener Forschungsbohrung. Mitteilungen der Deutschen Geophysikalischen Gesellschaft Sonderband II, 10-26.
- Gabriel, G., Kirsch, R., Siemon, B. and Wiederhold, H., 2003.** Geophysical investigation of buried Pleistocene subglacial valleys in Northern Germany. *Journal of Applied Geophysics*, 53, 159-180.
- Gemail, Kh., Samir, A., Oelsner, Chr., Mousa, S. E. and Ibrahim, Sh., 2004.** Study of saltwater intrusion using 1D, 2D and 3D resistivity surveys in the coastal depressions at the eastern part of Matruh area, Egypt. *Near Surface Geophysics*, 2, 101-107.
- Gharibi, M. and Bentley, L. R., 2005.** Resolution of 3-D electrical resistivity images from inversion of 2-D orthogonal lines. *Journal of Environmental and Engineering Geophysics*, 10 (4), 339-349.
- Griffiths, D. H. and Turnbull, J., 1985.** A multi-electrode array for resistivity surveying. *First Break* 3 (7), 16-20.
- Griffiths, D. H., Turnbull J. and Olayinka, A. I., 1990.** Two-dimensional resistivity mapping with a computer- controlled array. *First Break*, 8, 121-129.
- Griffiths, D. H. and Barker, R. D., 1993.** Two-dimensional resistivity imaging and modeling in areas of complex geology. *Journal of Applied Geophysics*, 29, 211-226.
- Günther, T., 2004.** Inversion methods and resolution analysis for the 2D/3D reconstruction of resistivity structures from DC measurements. Ph.D. thesis, Technische Univ., Freiberg, Germany.
- Günther, T., Rücker, C. and Spitzer, K., 2006.** 3-d modeling and inversion of dc resistivity data incorporating topography-part II: Inversion. *Geophysics Journal International*. 166(2), 506-517.
- Hansen, P. C. and O'Leary, D. P., 1993.** The use of the L-curve in the regularization of discrete ill posed problems. *SIAM Journal on Scientific Computing*, 14, 1487-1503.
- Hazen, A., 1911.** Discussion: Dams on sand foundations. *Trans. Am. Soc. Of Civil Engineers*, 73, 199.
- Heigold, P. C., Gilkeson, R. H., Cartwright, K. and Reed, P. C., 1979.** Aquifer transmissivity from the surficial electrical methods. *Ground Water*, 17 (4), 338-345.
- Hinze, C., Höfle, H-C., Jordan, H., Mengeling, H., Meyer, K-D, Rohde, P. and Streif, H., 1995.** Quartärgeologische Übersichtskarte von Niedersachsen und Bremen 1:500 000, Niedersächsisches Landesamt für Bodenforschung, Hannover.
- Höfle, H-C., Merkt, J. And Müller, H., 1985.** Die Ausbreitung des eem-Meeres in nordwestdeutschland. *Eiszeitalter und Gegenwart*, 35, 49-59.
- Hohmann, G. W., 1988.** Numerical modeling for electromagnetic methods of geophysics. In: Nabighian, M. N. (ed.), *Electromagnetic methods in applied geophysics*. Society of Exploration Geophysics, V.1, 313-363.
- Hördt, A., Blaschek, R., Kemna, A. and Zisser, N., 2007.** Hydraulic conductivity estimation from induced polarisation data at the field scale—the Krauthausen case history. *Journal of Applied Geophysics*, 62, 33–46.

- Hördt, H., Druiventak, A., Blaschek, R., Binot, F., Kemna, A., Kreye, P. and Zisser, N., 2009.** Case histories of hydraulic conductivity estimation with induced polarization at the field scale. *Near Surface Geophysics*, 7, 529-545.
- Huntley, D., 1986.** Relations between permeability and electrical resistivity in granular aquifers. *Groundwater*, 24 (4), 466-474.
- Huuse, M. and Lykke-Andersen, H., 2000.** Over deepened Quaternary valleys in the eastern Danish North Sea: morphology and origin. *Quaternary Science Reviews* 19, 1233-1253.
- Inman, J. R., 1975. Resistivity inversion with ridge regression.** *Geophysics*, 40, 798-817.
- INTERPEX, 2006.** IX1Dv3 tutorial: 1D sounding inversion, <http://www.interpex.com/ix1d/ix1dv3>.
- IX1Dv3, 2006.** A software for direct current (DC) resistivity, induced polarization (IP), magnetotelluric (MT) and electromagnetic sounding inversion, <http://www.interpex.com/ix1dv3/ix1dv3.html>.
- Jackson, D. D., 1972.** Interpretation of inaccurate, insufficient and inconsistent data. *Geophys. Journal Roy. Astr. Soc.*, 28, 97-109.
- Jakson, P. D., Taylor-Smiths, D. and Stanford, P. N., 1978.** Resistivity- porosity-particles shape relationships for marine sands. *Geophysics*, 43, 1250-1268.
- Jackson, J. D., 1998.** *Classical Electrodynamics*. 3rd edn., John Wiley & Sons, 808 p.
- Janik, M. and Krummel, H., 2006.** Geoelectrical methods. In: Kirsch, R. (ed.), *Groundwater geophysics, A tool for hydrogeology*, Chap. 3. Springer Berlin Heidelberg, Germany, 109-113.
- Joon, B., Laban, C. and van der meer, J. J. M., 1990.** The Saalian glaciation in the Dutch part of the North Sea. *Geologie en Mijnbouw*, 69, 151-158.
- Jougnot, D., Ghorbani, A., Revil, A., Leroy, P. and Cosenza, P., 2010.** Spectral Induced Polarization of partially saturated clay-rocks: a mechanistic approach. *Geophysical Journal International*, 180(1), 210–224, doi:10.1111/j.1365- 246X.2009.04426.x.
- Jupp, D. L. B. and Vozoff, K., 1975.** Stable iterative methods for the inversion of geophysical data. *Geophys. Journal Roy. Astr. Soc.*, 42, 957-976.
- Khalil, M. H., 2006.** Geoelectric resistivity sounding for delineating salt water intrusion in the Abu Zenima area, west Sinai, Egypt. *Journal of Geophysics and Engineering*, 3, 243-251.
- Keller, G. V., 1982.** Electrical properties of rocks and minerals. In: Carmichael, R. S. (ed.), *Handbook of physical properties of rocks*. Boca Raton, FL: CRC Press, 217-293.
- Keller, G. V. and Frischknecht, F. C., 1966.** *Electrical methods in geophysical prospecting*. Pergamon Press, London, 517 p.
- Kemna, A., 2000.** Tomographic inversion of complex resistivity theory and application. Ph.D. thesis, Ruhr Univ., Bochum, Germany.
- Kemna, A., Räckers, E. and Dresen, L., 1999.** Field applications of complex resistivity tomography. *Proceedings of the 69th Annual International Meeting, Society Exploration Geophysicist*, Exp. Abst, 331-334.

Kessels, W., Dörhöfer, G., Fritz, J. and Fulda, C., 2000. Das Forschungsprojekt "Bremerhaven-Cuxhavener Rinne" zur Beurteilung von Grundwasservorkommen in Rinnensystemen. Arbeitshefte Wasser, 1, 189-203.

Kilner, M., West, L. and Murray, T., 2005. Characterization of glacial sediments using geophysical methods for groundwater source protection. *Journal of Applied Geophysics*, 57, 293-305.

Kirsch, R., Rumpel, H-M., Scheer, W. and Wiederhold, H., 2006. Introduction-buried valleys and the burval project. In: Kirsch, R., Rumpel, H-M., Scheer, W. and Wiederhold, H. (eds.), *Groundwater Resources in Buried Valleys*. GGA-Institute, Hannover, Germany, 3-7.

Klein, J. and Lajoie, J., 1980. Electromagnetic prospecting for minerals. *Practical Geophysics for the Exploration Geologist*, Northwest Mining Associations, Spokane, WA, 239-290.

Klitzsch, N., 2003. Ableitung von Gesteinseigenschaften aus Messung der Spektralen Induzierten Polarisation (SIP) an Sedimentgesteinen. Ph.D. thesis, TU Univ., Leipzig, Germany.

Knudsen, K. L., 1993. Late Elsterian-Holsteinian foraminiferal stratigraphy in boreholes in the Lower Elbe area, NW Germany. *Geologisches Jahrbuch, A* 138, 97-119.

Koefoed, O., 1979. *Geosounding principles, 1, resistivity sounding measurement*. Elsevier Scientific Publishing Co., Amsterdam, 276 p.

Kosinsky, W. K. and Kelly, W. E., 1981. Geoelectric soundings for predicting aquifer properties. *Groundwater*, 19, 163-171.

Kozeny, J., 1927. Über kapillare Leitung des Wassers im Boden. *Sitzungsber Akad Wiss Wien Math Naturwiss K1 Abt.*, 1(136), 271-306.

Kruschwitz, S. F., 2007. Assessment of the complex resistivity behavior of salt affected building materials. Ph.D. thesis, Technischen Univ., Berlin, Germany.

Kuster, H. and Meyer, K.-D., 1979. Glaziäre Rinnen im Mittleren und Nordöstlichen Niedersachsen. *Eiszeitalter und Gegenwart*, 29, 135-156, Hannover.

Laban, C., 2000. The Pleistocene glaciations in the Dutch sector of the North Sea-a synthesis of sedimentary and seismic data. *Academisch Proefschrift*, Enschede, 194 p.

LaBrecque, D. J., Miletto, M., Daily, W., Ramirez, A. and Owen, E., 1996. The effects of noise on Occam's inversion of resistivity tomography data. *Geophysics*, 61, 538-548.

Lange, G. and Seidel, K., 2007. Electromagnetic methods. In: Knödel, K., Lange, G and Voigt, H.-J. (eds.), *Environmental geology*, Chap. 4. Springer Berlin Heidelberg, 239-282.

Leroy, P., Revil, A., Kemna, A., Cosenza, P. and Ghorbani, A., 2008. Spectral induced polarization of water-saturated packs of glass beads. *Journal of Colloid Interface Sci.*, 321, 103-117, doi:10.1016/j.jcis.2007.12.031.

Leroy, P. and Revil, A., 2009. A mechanistic model for the spectral induced polarization of clay material, *Journal Geophysical Research*, 114, B10202, doi:10.1029/2008JB006114.

Lesmes, D. P. and Friedman, S. P., 2005. Relationships between the electrical and hydrogeological properties of rocks and soils. In: Rubin, Y. and Hubbard, S. S. (eds.), *Hydrogeophysics*, Chap. 4. Water science and technology library, Springer, Netherlands, 50, 87-128.

Levenberg, K., 1944. A method for the solution of certain non-linear problems in least-squares. *Quart. Appl. Math.*, 2, 164-168.

LGN, 1999. Digitales Geländemodell.- Landesvermessung und Geobasisinformation Niedersachsen, Hannover.

Li, Y. and Oldenburg, D. W., 1992. Approximate inversion mapping in DC resistivity problems. *Geophysical Journal International*, 109, 343-362.

Lines, L. and Treitel, S., 1984. Tutorial: A review of least-squares inversion and its application to geophysical problems. *Geophysical Prospecting*, 32, 159-186.

Linke, G., 1993. Zur Geologie und Petrographie der Forschungsbohrungen qho 1-5, der Bohrung Hamburg-Billbrook und des Vorkommens von marinem Holstein im Gebiet Neuwerk-Scharhörn. *Geologisches Jahrbuch*, A 138, 35-76.

Loke, M. H. and Barker, R. D., 1995. Least-squares deconvolution of apparent resistivity pseudo-sections. *Geophysics*, 60, 1683-1690.

Loke, M. H. and Barker, R. D., 1996a. Practical techniques for 3D resistivity surveys and data inversion. *Geophysical Prospecting*, 44, 499-523.

Loke, M. H. and Barker, R. D., 1996b. Rapid least-squares inversion of apparent resistivity pseudo-sections using quasi-Newton method. *Geophysical Prospecting*, 44, 131-152.

Loke, M. H. and Dahlin, T., 1997. A combined Gauss-Newton and quasi-Newton inversion method for the interpretation of apparent resistivity pseudosections. *Proceedings of the 3rd Environmental and Engineering Geophysics Meeting*, Aarhus, Denmark, Exp. Abst., 139-142.

Loke, M. H., 2001. Res2Dinv software user's manual, version 3.4. Geotomo Software, Penang, Malaysia.

Loke, M. H., 2004. Tutorial : 2-D and 3-D electrical imaging surveys. Penang, Malaysia, Univ., Sains Malaysia, 129 p.

Long, D., Laban, C., Streif, H., Cameron, T. D. J. and Schüttenhelm, R. T. E., 1988. The sedimentary record of climatic variation in the southern North Sea. *Philosophical Transactions of the royal Society of London*, 318B, 523-537.

Losic, D., Yu. Y., Aw, M. S., Simovic, S. S., Thierry, B. and Addai-Mensah, J., 2010. Surface functionalization of Diatoms with dopamine modified iron oxide nanoparticles: towards magnetically Guided drug microcarriers with biologically derived morphologies. *Electronic Supplementary Information (ESI) for Chemical Communication*, Royal Society of Chemistry, S1-S12.

Lowry, T., Allen, M. B. and Shive, P. N., 1989. Singularity removal: A refinement of resistivity modeling techniques. *Geophysics*, 54, 766-774.

Maillet, R., 1947. The fundamental equations of electrical prospecting. *Geophysics*, 12, 529-556.

- Marquardt, D. W., 1963.** An algorithm for least-squares estimation of non-linear parameters. *SIAM Journal*, 11, 431-441.
- Maurer, H., Börner, D. E. and Curtis, A., 2000.** Design strategies for electromagnetic geophysical surveys. *Inverse Problems*, 16, 1097-1117.
- Mazac, O., Kelly, W. E. and Landa, I., 1985.** A hydrogeophysical model for relations between electrical and hydraulic properties of aquifers. *Journal of Hydrology*. 79. 1-19.
- Mazac, O., Cislérova, M. and Vogel, T., 1988.** Application of geophysical methods in describing spatial variability of saturated hydraulic conductivity in the zone of aeration. *Journal of Hydrology*, 103, 117-126.
- Mazac, O., Cislérova, M., Kelly, W. E., Landa, I. and Venhodova, D., 1990.** Determination of hydraulic conductivities by surface geoelectrical methods. In: Ward, S. H. (ed.), *Geotechnical and environmental geophysics*. Society of Exploration Geophysicists, Tulsa, V2, 125-131.
- McNeill, J. D., 1980.** Electromagnetic terrain conductivity measurements at low induction numbers. *GEONICS Technical Note TN6*.
- Meju, M. A., 1994.** Biased estimation: a simple framework for parameter estimation and uncertainty analysis with prior data. *Geophysical Journal International* 119, 521-528.
- Milsom, J., 2003.** *Field geophysics*. 3rd edn., John Wiley & Sons Ltd, England, 247 P.
- Mundry, E. and Dennert, U., 1980.** Das Umkehrproblem in der Geophysik. *Geologisches Jahrbuch*, Reihe E19:19-39.
- Nabighian, M. N. and Asten, M., 2001.** Metalliferous mining geophysics-state of the art in the last decade of the 20th century and beginning of the new Millennium. *Geophysics*, Paper #01113r, 32 p., <http://www.geo-online.org/>.
- Niwas, S. and Singhal, D. C., 1981.** Estimation of aquifer transmissivity from Dar-Zarrouk parameters in porous media. *Journal of Hydrology*, 50, 393-399.
- Niwas, S. and Singhal, D. C., 1985.** Aquifer transmissivity of porous media from resistivity data. *Journal of Hydrology*, 82, 143-153.
- NLFB, 1999.** Geologisch Übersichtskarte von Niedersachsen und Bremen 1:500.000 (GÜK500).- Niedersächsisches Landesamt für Bodenforschung, Hannover.
- Noell, U. and Panteleit, B., 2004.** Geophysical detection and hydrochemical analysis of an isolated shallow salt water body near Cuxhaven, Lower Saxony, Germany. *Groundwater and saline intrusion- Selected papers from the 18th salt Water Intrusion Meeting (18 SWIM)*, Cartagena, 417-434.
- Nordsiek, S. and Weller, A., 2008.** A new approach to fitting induced polarization spectra. *Geophysics*, 73, 235-245.
- Oldenburg, D. W. and Li, Y., 1994.** Inversion of induced polarization data. *Geophysics*, 59, 1327-1341.

Oldenburg, D. W., 2001. Univ. of British Columbia - geophysical inversion facility inversion and modeling of applied geophysical electromagnetic data (IMAGE). Consortium: <http://www.geop.ubc.ca/gif/research/image/index.html>.

Oteri, A. U., 1981. Geoelectric investigation of saline contamination of chalk aquifer by mine drainage water at Tilmanstone, England. *Geoexploration*, 19, 179-192

Palacky, G., 1987. Resistivity characteristics of geological targets. In: Nabighian M. N. (ed.), *Electromagnetic methods in applied geophysics*. Society of Exploration Geophysicists, Tulsa, V.1, 53-129.

Palacky, G., 1991. Application of the multi-frequency horizontal loop EM method in overburden investigations. *Geophysical Prospecting*, 39 (8), 1061-1082.

Panteleit, B., Binot, F., Kessels, W., Schulz, H. D., and Kantor, W., 2001a. Geological and geochemical characteristics of a salinization-zone in a coastal aquifer. In: Seiler, K.-P. and Wohnlich, S. (eds.), *New Approaches Characterizing Groundwater Flow*. Lisse, Abington, Exton, Tokyo, A. A. Balkema, V.2, 1237-1241.

Panteleit, B., Kessels, W., Kantor, W. and Schulz, H. D., 2001b. Geochemical characteristics of salinization-zones in the Coastal Aquifer Test Field (CAT-Field) in North-Germany. 1st International Conference on Saltwater and Coastal Aquifers-Monitoring, SWICA-M3, Modeling and Management, Essaouira, Morocco, April 23-25.

Panteleit, B., 2004. Hydrochemical characterization of a coastal aquifer test field at the German North Sea coast. In: Panteleit (ed.), *Berichte aus dem Fachbereich Geowissenschaften der Univ. Bremen*, Nr. 225, 33-44.

Panteleit, B., Kessels, W. and Schulz, H. D., 2004. Geochemical processes in the salt-fresh water transition zone-exchanger reactions in a 2D-sand-tank Experiment. In: Panteleit (ed.), *Berichte aus dem Fachbereich Geowissenschaften der Univ. Bremen*, Nr. 225, 64-79.

Panteleit, B., Kessels, W. and Binot, F., 2006. Mud tracer test during soft rock drilling. *Water Resources Research*, 42, W11415, 1-13.

Panteleit, B., Hamer K., Kringel, R., Kessels, W. and Schulz, H. D., 2010. Geochemical processes in the saltwater-freshwater transition zone: comparing results of a sand tank experiment with field data. *Environmental Earth Science Journal*, doi: 10.1007/s12665-010-0499-1.

Pape, H., Riepe, L. and Schopper, J. R., 1987. Theory of self-similar network structures in sedimentary and igneous rocks and their investigation with microscopical and physical methods. *Journal of Microscopy*, 148, 121-147.

Parasnis, D. S., 1973. *Mining geophysics*. 2nd edn., Elsevier, Amsterdam, 395 p.

Parasnis, D. S., 1997. *Principles of applied geophysics*. 5th edn., Chapman and Hall, London, 429 p.

Pelton, W. H., Ward, S. H., Hallof, P. G., Sill, W. R. and Nelson, P. H., 1978. Mineral discrimination and removal of electromagnetic coupling with multifrequency IP. *Geophysics*, 43, 588-609.

- Pelton, W. H., Sill, W. R. and Smith, B. D., 1983.** Interpretation of complex resistivity and dielectric data, Part I. *Geophysical Transactions*, 29, 297-330.
- Praeg, D., 1996.** Morphology, stratigraphy and genesis of buried Mid-Pleistocene tunnel-valleys in the southern North Sea basin. Ph.D. thesis, Univ. of Edinburgh.
- Pridmore, D. F., Hohmann, G. W., Ward, S. H. and Sill, W. R., 1981.** An investigation of finite-element modeling for electrical and electromagnetic data in three dimensions. *Geophysics*, 46, 1009–1024.
- Purvance, D. and Andricevic, R., 2000.** Geoelectrical characterization of the hydraulic conductivity field and its spatial structure at variable scales. *Water Resour. Res.*, 36 (10), 2915-2924.
- Radic, T., Kretzschmar, D. and Niederleithinger, E., 1998.** Improved characterization of unconsolidated sediments under field conditions based on complex resistivity measurements. *Proceedings of the 4th Meeting of Environmental and Engineering Geophysics*, Exp. Abst.
- Radic, T., 2004.** Elimination of cable effects while multichannel SIP measurements. *Proceedings of the 10th Meeting of Environmental and Engineering Geophysics*, Exp. Abst.
- Revil, A. and Florsch, N., 2010.** Determination of permeability from spectral induced polarization in granular media. *Geophysical Journal International (GJI)*, doi: 10.1111/j.1365-246X.2010.04573.x.
- Reynolds, J., 1997.** An introduction to applied and environmental geophysics. John Wiley & Sons Ltd, New York, USA, 796 p.
- Rockware, 2009.** Rockworks 2009 user manual, Rockware Incorporated, www.rockware.com.
- Roy, A. and Apparao, A., 1971.** Depth investigation in direct current methods. *Geophysics*, 36(5), 943-959.
- Roy, K. K. and Elliot, H., 1980.** Model studies on some aspects of resistivity and membrane polarisation behavior over a layer Earth. *Geophysical Prospecting*, 28, 759–775.
- Rubin, Y. and Hubbard, S. S., 2005.** Introduction to hydrogeophysics. In: Rubin, Y. and Hubbard, S. S. (eds), *Hydrogeophysics*, Chap. 1. Water science and technology library, Springer Netherlands, 50, 3-21.
- Rücker, C., Günther, T. and Spitzer, K., 2006.** 3-d modeling and inversion of dc resistivity data incorporating topography-part I: Inversion. *Geophysics Journal International*, 166(2), 495-505.
- Sasaki, Y., 1992.** Resolution of resistivity tomography inferred from numerical simulation. *Geophysical prospecting*, 40, 453-464.
- Sasaki, Y., 1994.** 3D resistivity inversion using the finite element method. *Geophysics*, 59, 1839-1848.
- Sasaki, Y., 1989.** Two-dimensional joint inversion of magnetotelluric and dipole-dipole resistivity data. *Geophysics*, 54, 254-262.
- Scales, L. E., 1985.** Introduction to non-linear optimization. MacMillan Publishing Co.
- Scheidegger, A. E., 1974.** The physics of flow through porous media. 3rd edn., Univ. of Toronto Press, Toronto, 353 p.

- Schön, J. H., 1996.** Physical properties of rocks-fundamental and principles of petrophysics. Handbook of geophysical exploration. Seismic exploration, 18. Pergamon Press, 583 p.
- Schön, J. H., 2004.** Coefficient of friction and wear a carbon fiber epoxy matrix composite. Wear Journal, 257, 395-407.
- Schwarz, C., 1996.** Neue Befunde zur Verbreitung und Dimension Pleistozäner Rinnensysteme auf dem deutschen Nordseeschelf. Geologisches Jahrbuch A146, 233-244.
- Seidel, K. and Lange, G., 2007.** Direct current resistivity methods. In: Knödel, K., Lange, G and Voigt, H.-J. (eds.), Environmental geology, Chap. 4. Springer Berlin Heidelberg, 205-238.
- Sen, P. N., Goode, P. A. and Sibbit, A., 1988.** Electrical conduction in clay bearing sandstones at low and high salinities. Journal of Applied Physics, 63, 4832-4840.
- Sengpiel, K. P., 1983.** Resistivity depth mapping with airborne electromagnetic survey data. Geophysics, 48 (2), 181-196.
- Sengpiel, K. P., 1990.** Theoretical and practical aspects of ground-water exploration using airborne electromagnetic techniques. In: Fitterman, D. V., (ed.), Developments and Applications of Modern Airborne Electromagnetic Surveys. U.S. Geological Survey Bulletin, 1925, 216 p.
- Sengpiel, K. P. and Siemon, B., 1998.** Examples of 1-D inversion of multifrequency HEM data from 3-D resistivity distributions. Exploration Geophysics, 29 (1 and 2), 133-141.
- Serra, O., 1984.** The measurement of resistivity. In Serra, O. (ed.), Fundamentals of well-log interpretation, Chap. 3. Elsevier, New York, 51-76.
- Sharma, P. V., 1997.** Environmental and engineering geophysics. Cambridge Univ. Press, 475 p.
- Sheriff, R. E., 1991.** Encyclopedic dictionary of exploration geophysics. 3rd edn., Society of Exploration Geophysicists, Tulsa, 384 p.
- Shevnin, V. A., Delgado-Rodríguez, O., Mousatov, A. and Ryjov, A. 2006.** Estimation of hydraulic conductivity on clay content in soil determined from resistivity data. Geofísica Internacional, 45 (3), 195-207.
- Siegel, H. O., 1959.** Mathematical formulation of type curves for induced polarization. Geophysics, 24(3), 546-565.
- Siemon, B., Röttger, B. and Eberle, D., 2001a.** Airborne geophysical investigation of saltwater intrusions and coastal aquifers in NW Germany. Proceedings of the 7th Meeting Environmental and Engineering Geophysics, 228-229.
- Siemon, B., Sengpiel, K.-P., Rehli, H.-J., Röttger B. and Eberle, D., 2001b.** Identification of saltwater intrusions in coastal aquifer using the BGR Helicopter-borne Geophysical System. SWICA-M³, 2001.
- Siemon, B. and Binot, F., 2003.** Aerogeophysikalische Erkundung von Salzwasserintrusionen und Küstenaquiferen im Gebiet Bremerhaven-Cuxhaven, Verfyierung der AEM-Ergebnisse. In: Hördt, A. and Stoll, J. (eds.), Protokoll über das 19. Kolloquium, "Electromagnetische Tiefenforschung", Burg Ludwigstein, 319-328.

Siemon, B., Eberle, D. G. and Binot, F., 2004. Helicopter-borne electromagnetic investigation of coastal aquifers in North-West Germany. *Zeitschrift für Geologische Wissenschaften*, 32, 358-395.

Siemon, B., 2006. HEM data processing and interpretation at BGR. Extended abstracts book, AEM workshop, Hannover 2006: Airborne EM-Recent Activities and Future Goals: 45-49.

Silvester, P. P. and Ferrari R. L., 1990. Finite elements for electrical engineers. 2nd edn., Cambridge Univ. Press, 516 p.

Sindowski, K.-H., 1969. Geo. Karte Niedersachsen 1:25000, Erl. Blatt 2218 Cuxhaven. Niedersächsisches Amt für Bodenforschung, Hannover, 53 p.

Singh, C. L. and Singh, S. N., 1970. Some geophysical investigations for potential groundwater in part of Azamgrah area. *UP Pure Appl. Geophys.*, 82, 270-285.

Slater, L. and Lesmes, D., 2002a. Electric-hydraulic relationships observed for unconsolidated sediments. *Water resources research*, 38(10), 1213, doi:10.1029/2001WR00107.

Slater, L. and Lesmes, D., 2002b. IP interpretation in environmental investigations. *Geophysics*, 67(1), 77–88.

Slater, L. and Glaser, D. R., 2003. Controls on induced polarization in sandy unconsolidated sediments and application to aquifer characterization. *Geophysics*, 68, 1547-1588.

Slater, L., Ntarlagiannis, D. and Wishart, D., 2006. On the relation between induced polarization and surface area in metal-sand and clay-sand mixtures. *Geophysics*, 71(2), A1-A5.

Slater, L., 2007. Near surface electrical characterization of hydraulic conductivity: from petrophysical properties to aquifer geometries- A review. *Surv. Geophysics*, 28, 169-197.

Sørensen, K. I., 1996. Pulled Array Continuous Electrical Profiling. *First break*, 14, 85-90

Spitzer, K., 1995. A 3D-finite difference algorithm for DC resistivity modelling using conjugate gradient methods. *Geophysical Journal International*, 123, 903-914.

Streif, H., 1982. The occurrence and significance of peat in the Holocene deposits of the German North Sea coast. *Symposium on peat lands below sea level*, 31-41.

Streif, H., 2004. Sedimentary record of Pleistocene and Holocene marine inundations along the North Sea coast of Lower Saxony, Germany. *Quaternary International*, 112, 3-28.

Stummer, p., Maurer, H. and Green, A. G., 2004. Experimental design: Electrical resistivity data sets that provide optimum subsurface information. *Geophysics*, 69, 120-139.

Sturrock, J. T., Lesmes, D. P. and Morgan, F. D., 1998. The influence of micro-geometry on the hydraulic permeability and the induced polarization response of sandstones. *Proceedings of the Symposium on the Application of Geophysics to Engineering and Environmental Problems (SAGEEP)*, 859-867.

Sugimoto, Y., 1999. Shallow high-resolution 2-d and 3-d electrical crosshole imaging. *The Leading Edge*, 1425–1428.

Sumner, J. S., 1976. Principles of induced polarization for geophysical exploration. Elsevier, Amsterdam, the Netherland, 273 p.

- Szalai, S. and Szarka, L., 2008.** On the classification of surface geoelectric arrays. *Geophysical Prospecting*, 56, 159-175.
- Telford, W. M., Geldart, L. P. and Sheriff, R. E., 1990.** Applied geophysics. 2nd edn., Cambridge Univ. Press, Cambridge, 760 p.
- Telford, W. M., Geldart, L. P., Sheriff, R. E., and Keys, D. S., 1976.** Applied Geophysics. Cambridge Univ. Press.
- Thompson, A. H., Katz, A. J. and Krohn, C.E., 1987.** The microgeometry and transport properties of sedimentary rock. *Adv. Phys.*, 36, 624-694.
- Tikhonov, A. N. and Arsenin, V. Y., 1977.** Solution of ill-posed problems. Winston and Sons, New York, 258 p.
- Titov, K., Kemna, A., Tarasov, A. and Vereecken, H., 2004.** Induced polarization of unsaturated sands determined through time-domain measurements. *Vadose Zone Journal*, 3, 1160–1168.
- Tong, M., Li, L., Wang, W. and Jiang, Y., 2006.** Determining capillary-pressure curve, pore-size distribution and permeability from induced polarization of shaley sand. *Geophysics*, 71 (3), 22-40.
- Tournassat, C., Chapron, Y., Leroy, P., Bizi, M. and Boulahya, F., 2009.** Comparison of molecular dynamics simulations with triple layer and modified Gouy-Chapman models in 0.1MNaCl-montmorillonite system. *Journal of Colloid Interface Sci.*, 339(2), 533–541.
- Turberg, P. and Barker, R., 1996. Joint application of radiomagnetotelluric and electrical imaging surveys in the complex subsurface environments. *First Break*, 14(3), 105-112.**
- Van Overmeeren, R. A. and Ritsema, I. L., 1988. Continuous vertical electrical sounding. *First Break*, 6, 313-324.**
- Vandenbohede, A. and Lebbe, L., 2002.** Numerical modeling and hydrochemical characterization of fresh-water lens in the Belgian coastal plain. *Hydrogeology Journal online*, DOI 10.1007/s10040-002-0209-5.
- Vanhala, H. and Soininen, H., 1995.** Laboratory technique for measurement of spectral induced polarization response of soil samples. *Geophysical Prospecting*, 43, 655-676.
- Vanhala, H., 1997.** Laboratory and field results of the use of spectral induced-polarization (SIP) method for detecting organic and inorganic contaminants. Proceedings of the 3rd EEGS-ES meeting, Aarhus, DK, 37-40.
- Wagenschein, D., 2002.** Zur Unterscheidung toniger und salzwasserführender Sediment mit dem Verfahren der spektralen induzierten Polarisation (SIP). Diplomarbeit, Univ. Bremen, Germany.
- Wait, J. R., 1959.** Overvoltage research and geophysical application. International series of monographs on earth sciences, Pergomon press, Oxford, England, 4, 22–83.
- Ward, S. H. and Fraser, D. C., 1967.** Conduction of electricity in rocks. In: Hansen, D. A., Heinrichs, Jr., W. E., Holmer, R. C., MacDougall, R. E., Rogers, G. R., Sumner, J. S. and Ward, S. H. (eds.), *Mining geophysics*, Society of Exploration Geophysicists, Tulsa, Oklahoma, V. II, 197-223.

- Ward, S. H. and Hohmann, G. W., 1987.** Electromagnetic theory for geophysical applications. In: Nabighian, M. N. (ed.), *Electromagnetic methods in applied geophysics*. Society of Exploration Geophysics, V. 1, 131-311.
- Ward, S. H., 1990.** Resistivity and induced polarization methods. In: Ward, S. H. (ed.), *Geotechnical and environmental geophysics, I: Review and Tutorial*. Society of Exploration Geophysicists, Tulsa, Oklahoma, 147-189.
- Waxman, M. H. and Smits, L. J. M., 1968.** Electrical conductivities in oil bearing shaly sands. *Soc. Pet. Eng. Journal*, 8, 107–122.
- Waxman, M. H. and Thomas, E. C., 1974.** Electrical conductivities in oil-bearing shaly sands: I. The relation between hydrocarbon saturation and resistivity index. II. The temperature coefficient of electrical conductivity. *Soc. Pet. Eng. Journal*, 14: 213-225.
- Weller, A., Seichter, M. and Kampke, A., 1996.** Induced-polarization modelling using complex electrical conductivities. *Geophysics Journal International*, 127, 387–398.
- Weller, A., Slater, L., Nordsiek, S. and Ntarlagiannis, D., 2010.** On the estimation of specific surface per unit pore volume from induced polarization: A robust empirical relation fits multiple datasets. *Geophysics*, 75(4), WA105-WA112.
- Wiederhold, H., Binot, F. and Kessels, W., 2005.** Die Forschungsbohrung Cuxhaven und das Coastal Aquifer Testfield (CAT-field)-ein Testfield für angewandte geowissenschaftliche Forschung. *Angew. Geol.*, 51, 3-7.
- Wolke, R. and Schwetlick, H., 1988.** Iteratively reweighted least squares algorithms, convergence analysis, and numerical comparisons. *SIAM Journal of Scientific and Statistical Computations*, 9, 907-921.
- Worthington, P. F., 1993.** The uses and abuses of the Archie equations. 1: The formation factor-porosity relationship. *Journal of Applied Geophysics*, 30, 215-228.
- Xiang, J. N. B., Jones, D., Cheng, D. and Schlindwein, F. S., 2002.** A new method to discriminate between a valid IP response and EM coupling effects. *Geophysical Prospecting*, 50, 566-576.
- Yadav, G. S., 1995.** Relating hydraulic and geoelectric parameters of the Jayant aquifer, India. *Journal of Hydrology*, 167, 23-38.
- Zhang, J., Mackie, R. and Madden, T., 1995.** 3-D resistivity forward and inversion using conjugate gradients. *Geophysics*, 60, 1313-1325.
- Zhou, B. and Dahlin, T., 2003.** Properties and effects of measurement error on 2D resistivity imaging. *Near Surface Geophysics*, 1, 105-117.
- Zohdy, A. R., 1968.** A rapid graphical method for the interpretation of A and H-type electrical sounding. *Geophysics*, 33, 822-833.
- Zohdy, A. R., 1989.** A new method for automatic interpretation of Schlumberger and Wenner sounding curves. *Geophysics*, 54, 245-253.

Zonge, K., Wynn, J. and Urquhart, S., 2005. Resistivity, induced polarization and complex resistivity. In: Butler, D. K. (ed.), Near surface geophysics, Part 1: Concept and fundamentals. Society of Exploration Geophysicists, Tulsa, Oklahoma, 265-300.

APPENDICES

A: DARCY'S AND OHM'S LAWS

Darcy's law of water flow and Ohm's law of current flow can be written as,

$$q = -k_f \nabla h \quad (\text{A.1})$$

$$J = -\sigma \nabla V \quad (\text{A.2})$$

where q is a specific discharge in m/s, h is the water level between two points and J is the current density (A/m^2).

For a homogeneous medium the divergence of specific discharges and current density becomes zero, which can be written as

$$\nabla q = 0 \quad (\text{A.3})$$

$$\nabla J = 0 \quad (\text{A.4})$$

Now the Eqs. (A.1) and (A.2) can be written as

$$\nabla q = -\nabla k \nabla h - k \nabla^2 h = 0 \quad (\text{A.5})$$

$$\nabla J = -\nabla \sigma \nabla V - \sigma \nabla^2 V = 0 \quad (\text{A.6})$$

These are fundamental equations of, respectively, groundwater flow and electrical prospecting with direct current. If the medium is homogeneous then the above equation becomes,

$$\nabla^2 h = 0 \quad (\text{A.7})$$

$$\nabla^2 V = 0 \quad (\text{A.8})$$

These are Laplace's equations that present a clear analogy between Darcy's law of groundwater flow and Ohm's law of electrical current flow.

B: DEBYE DECOMPOSITION

Debye decomposition is an approach for computation of the relaxation time¹⁴ distribution from time-domain or frequency-domain IP data (e.g., *Pelton et al., 1978; Tong et al., 2006*). *Nordsiek and Weller (2008)* proposed a Debye decomposition procedure regarding the SIP spectra as a superposition of discrete Debye response,

$$\rho^* = \rho_0 \left(1 - \sum_{k=1}^n m_k \left(1 - \frac{1}{1+i\omega\tau_k} \right) \right) \quad (\text{B.1})$$

where, n is the number of individual Debye responses. Each Debye response is given by a specific chargeability m_k and relaxation time τ_k .

C: DC SOUNDING DATA, INVERSION AND CALIBRATION

The 1D DC data for 30 sounding points are plotted on log-log paper in the form of apparent resistivity data vs. AB/2 using IPI software (Fig. C.1). The inversion results are also presented in the form of true resistivity and thickness on the same log-log paper. The inversion results are also calibrated with the available boreholes in the study area.

¹⁴ The relaxation time is defined as a characteristic time constant of the process of decreasing the existing polarization (P), due to the occurrences of an electrical field, in absence of the electrical field at time t . This decay process can be defined as $(t) \sim e^{-t/\tau}$.

Fig. C.1: 1D inversion results of DC sounding points with boreholes calibration.

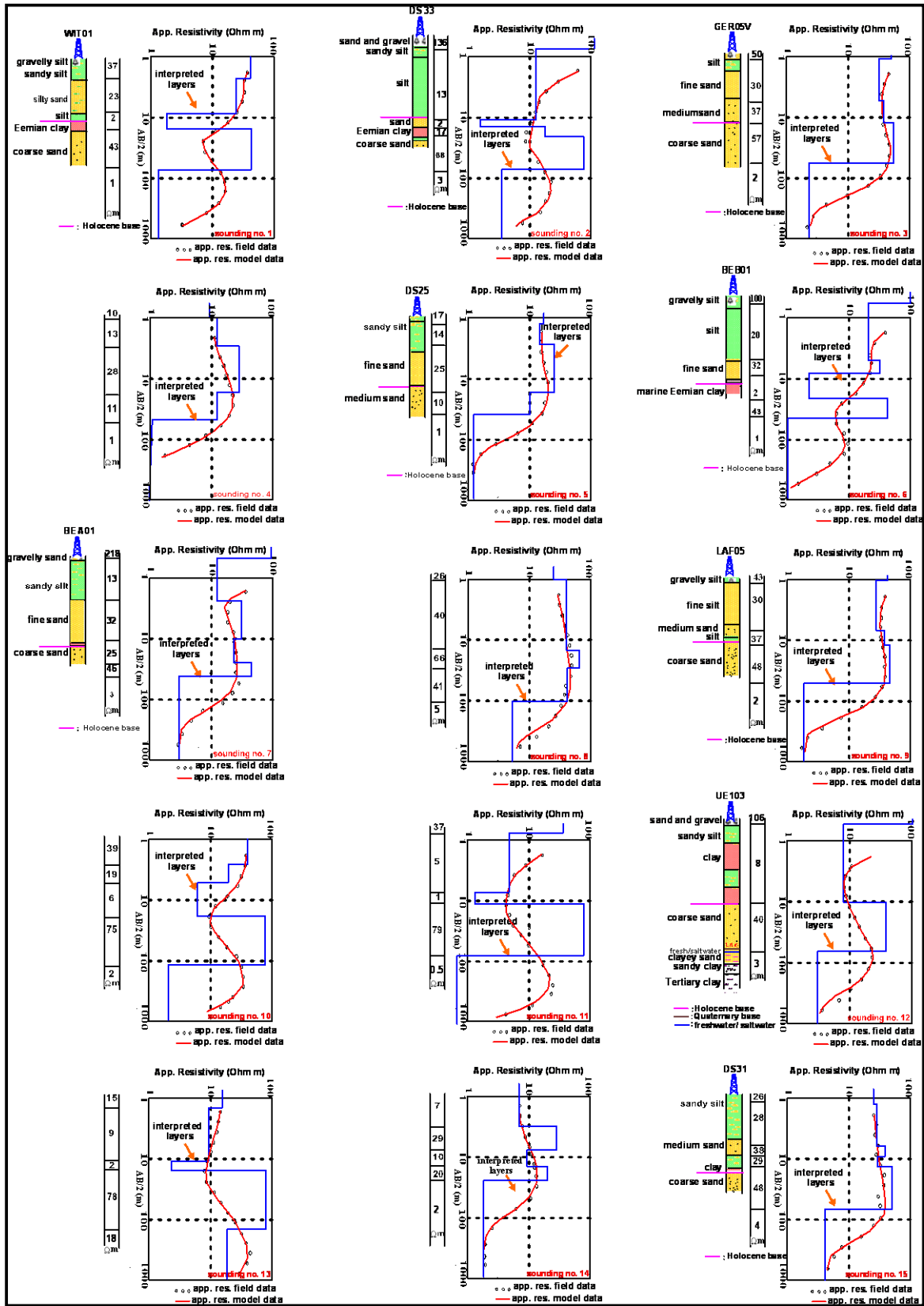
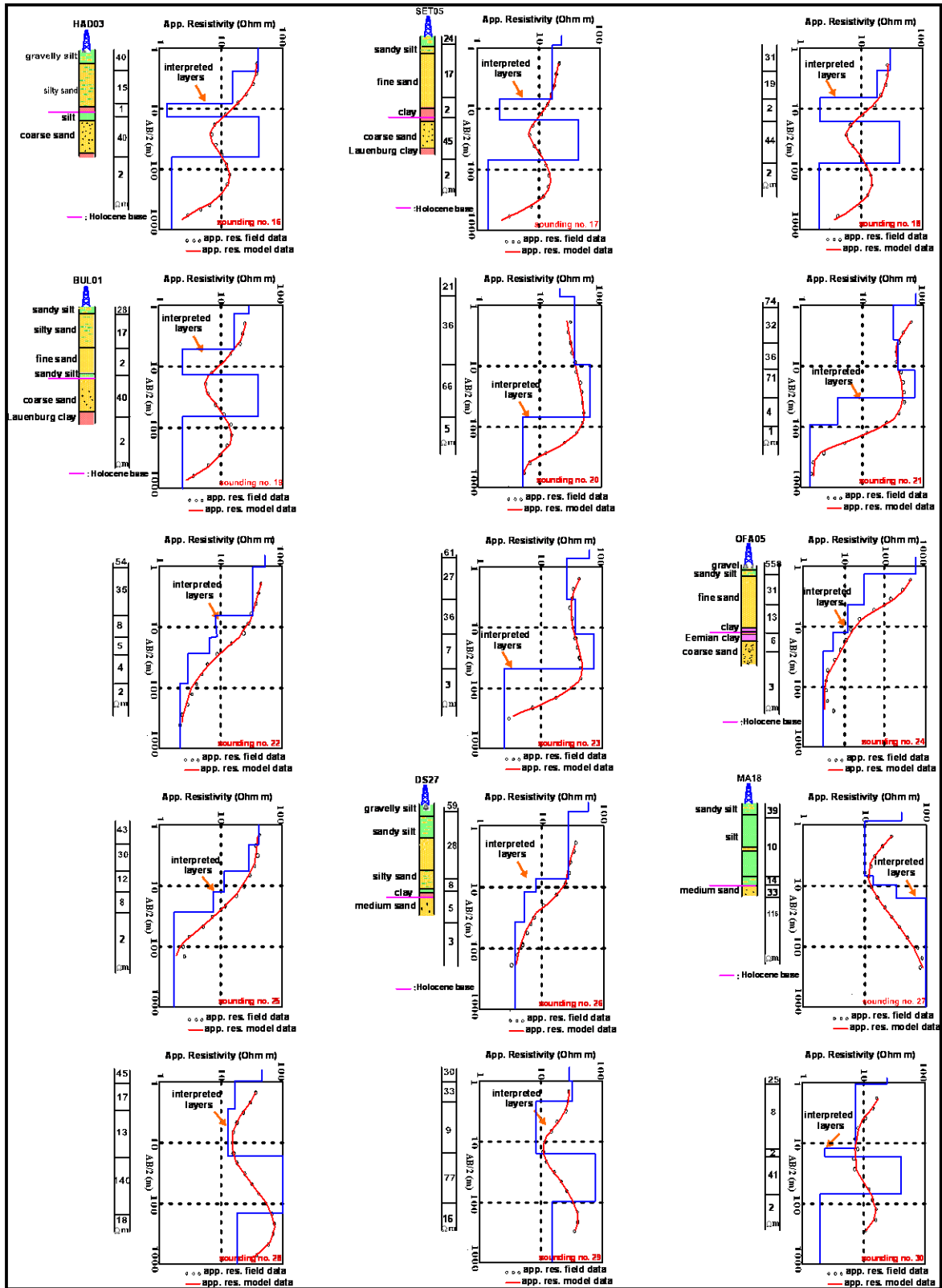


Fig. C.1 (Continued).



D: Model Reliability and Regularization Parameters

The coverage plots and the effect of regularization parameters on the reliability of the WB and SC models are shown, respectively, in Figs. D.1 and D.2 (a and b). The reliable model for WB data set can be obtained at all tested regularization parameters. It can be observed that the best data misfit percentages can be obtained by increasing both λ and z -power to certain extent. On the contrary, the information from SC models shows diversions at different regularization parameters. SC data is very sensitive to the changes of the regularization parameters. The best misfit data percentage for SC can be observed by decreasing both λ and z -power. Due to the bad data coverage of SC model, low λ and z -power values are required to get more detailed information with increasing depth.

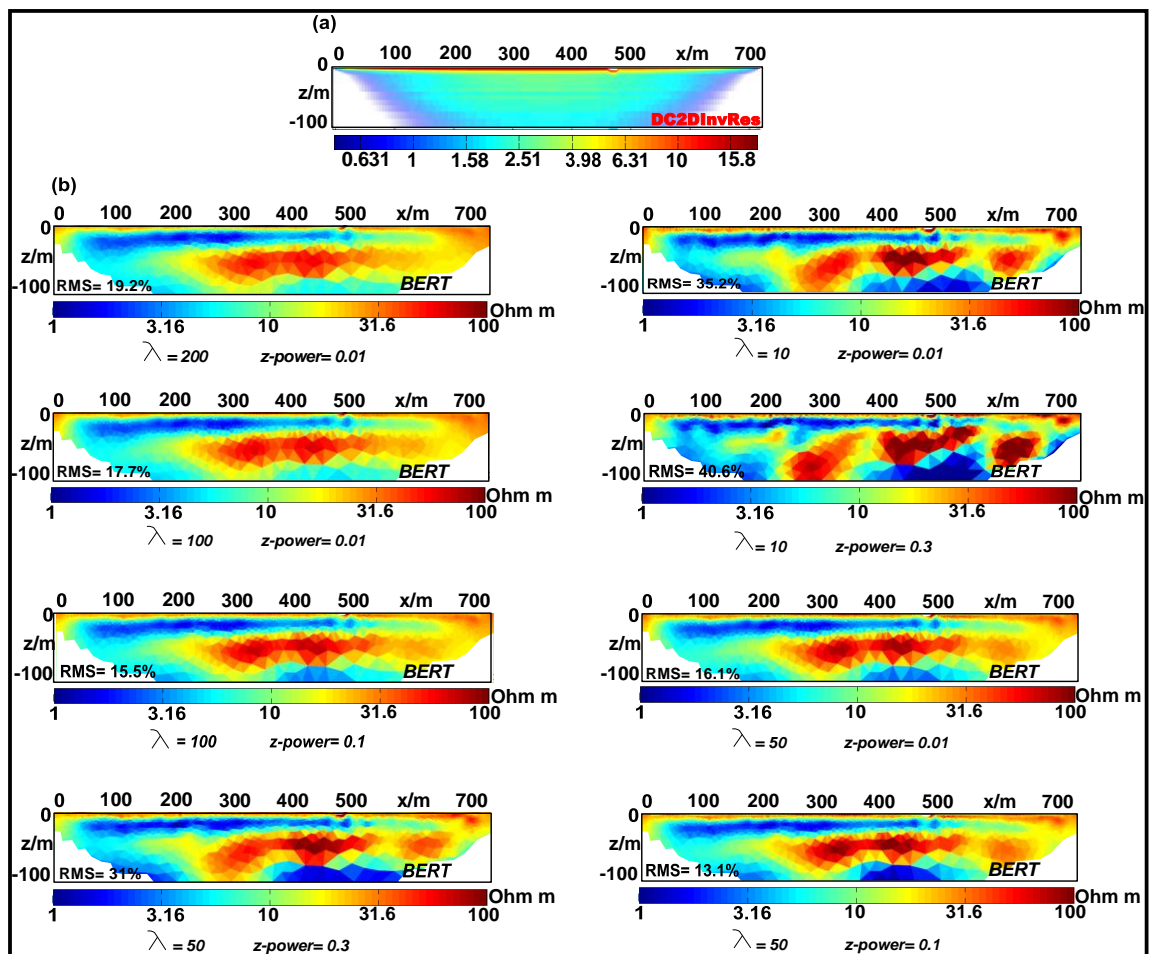


Fig. D.1: (a) Coverage plot and (b) inversion results for 8 selected regularization parameters, λ and z -power, for WB data.

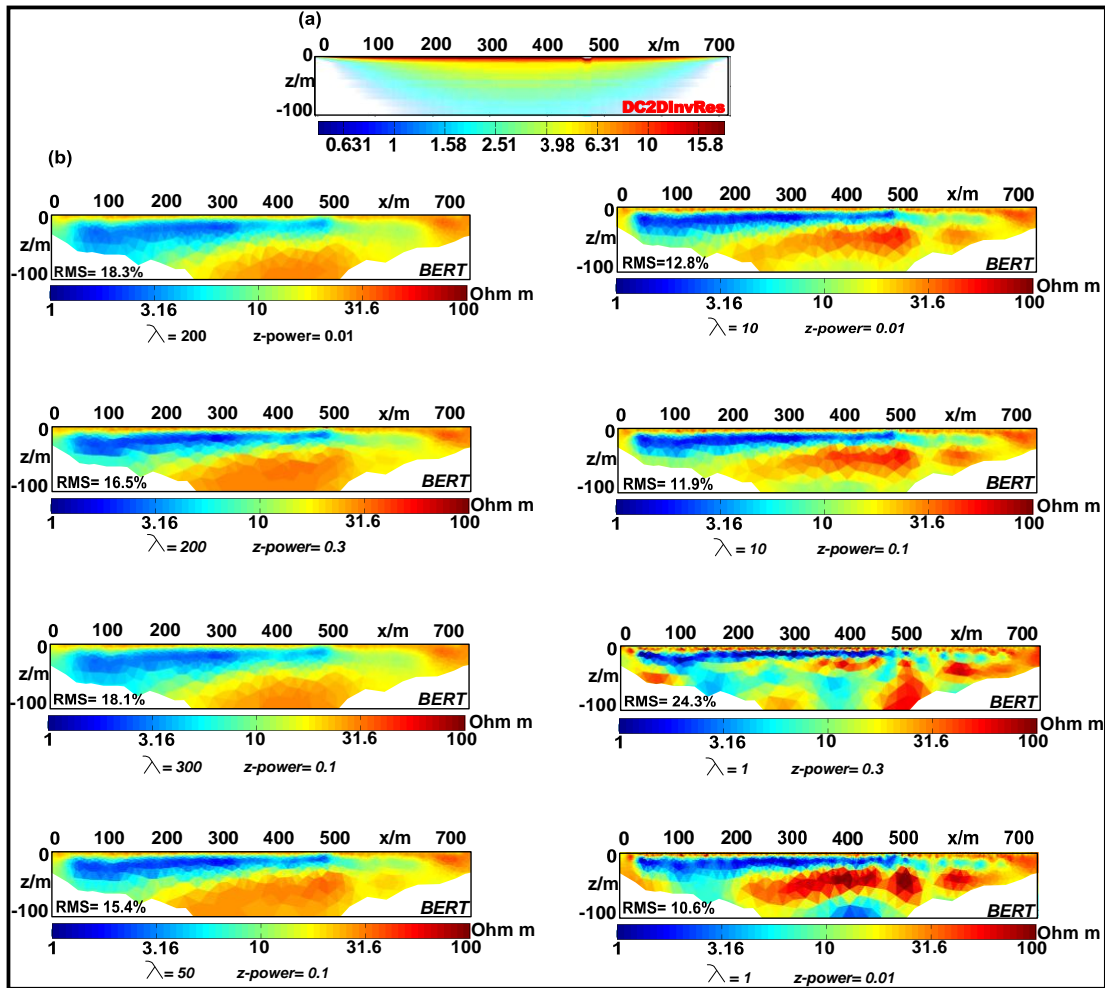


Fig. D.2: (a) Coverage plot and (b) inversion results for 8 selected regularization parameters, λ and z -power, for SC data.

E: SIP INVERSION RESULTS

Fig. D.1 shows SIP inversion results for three high frequencies of 40 Hz, 80 Hz and 125 Hz. The measured data of phase shift shows a lot of bad data points, noise, in the form of negative and zero points. In addition, a strong increase in apparent phase and decrease of conductivity magnitude values can be observed. This can be attributed to EM coupling which dominates the measured data at high frequencies (see Fig. 5.12). The data processing to this data affects the data coverage and, consequently, the reliability of inversion results, which can be indicated from sensitivity sections (Fig. E.1, right), will be restricted for the shallow part of the 2D profile (5 m maximum thickness).

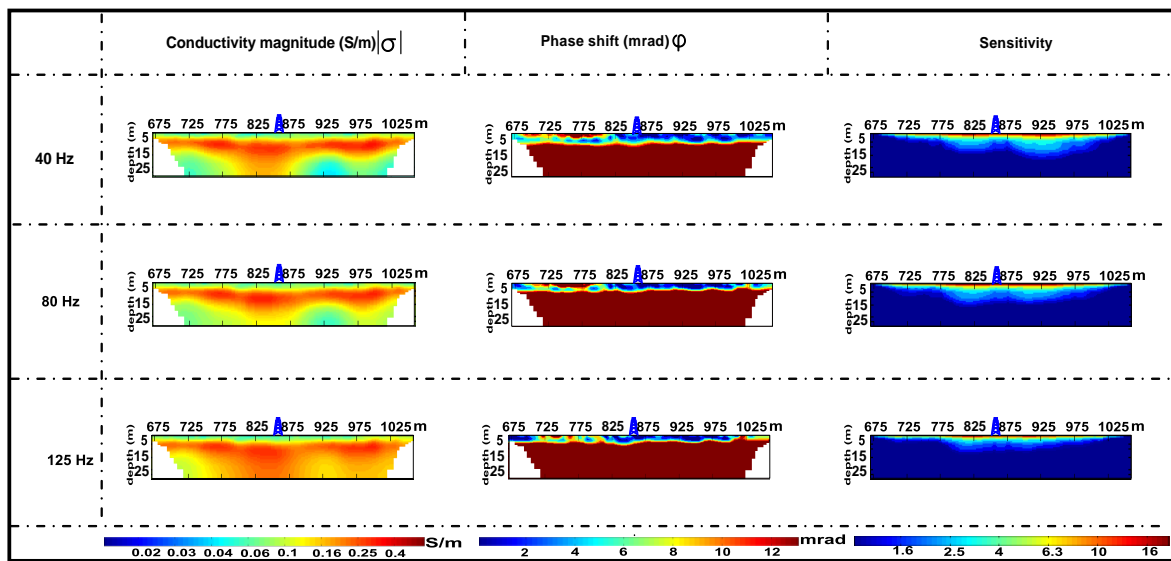


Fig. E.1: (left) The complex conductivity magnitude $|\sigma|$, (middle) conductivity phase shift ϕ and (right) sensitivity sections for frequencies 40 Hz, 80 Hz and 125 Hz frequencies.

F: SOIL SAMPLES DESCRIPTION (BOREHOLE DS33)

Close to borehole DS33, the core samples (9 m to 23.5 m depth) were well described. The detailed descriptions of tidal deposits and the lower sandy layer (middle Pleistocene) are shown in Fig. F.1. Note that the drilling and the soil samples description were carried out by Leinbiz Institute for Applied Geophysics (LIAG). The key words of this description are in the following table:

Holozän: Holocene	Ton: Clay	Kies: Gravel
Pleistozän: Pleistocene	Torf: Peat	Rechtswert: Easting
Schluff: Silt	Mudde: Mud	Hochwert: Northing
Organische: Organic	Genese: Genesis	Farbe: color

Borehole: DS33			
Depth (m)	Thickness (m)	Description	
9,00	0,40	Holozän, Ton (humos, Pflanzenreste), kalkfrei, Genese: brackisch, Farbe: grau, schwarz (fleckig), braun (fleckig)	
9,20	0,20	Holozän, Schluff (stark tonig, stark humos, viel Schilfreste), kalkhaltig, Genese: brackisch bis limnisch, Farbe: grauoliv, schwarz (fleckig) Bem: Bohrkern 9-10m	
10,00	0,80	Holozän, Schluff (stark tonig, humos, Schilfreste), kalkhaltig, Genese: brackisch bis limnisch, Farbe: grauoliv Bem: Bohrkern 9-10m	
10,45	0,45	Holozän, Schluff (feinsandig, schwach tonig), sehr schwach kalkhaltig, Farbe: grau	
10,65	0,20	Holozän, Torf (schwach feinsandig, schwach tonig), kalkfrei, Genese: Niedermoor, Farbe: dunkelbraun	
12,00	1,35	Holozän, Schluff (tonig, sehr schwach feinsandig), kalkfrei, Farbe: dunkelgrau bis grau	
Projekt:		Hydrogeophysik	
Bohrung:		SUD_DS33 / CAT_SUD_33	
Auftraggeber:		LIAG	
Bohrfirma:		LBEG	
Bearbeiter:	Binot, F.	Ansatzhöhe:	1,30 m
		Rechtswert:	3481770
Datum:	19.08.2010	Endtiefe:	24,00
		Hochwert:	5962405



Fig. F.1: Soil samples description close to borehole DS33 (Fig. 5.35) from 9 m to 24 m depth. →

Fig. F.1 (Continued).

Borehole: DS33				
Depth (m)	Thickness (m)	Description		
12,45	0,45	Holozän, Ton (stark schluffig, Mollusken), schwach kalkhaltig, Genese: Watt, Farbe: olivgrau Bem: Bohrkern 12-13m / Cardium		
12,57	0,12	Holozän, Schluff (tonig, stark humos, Holzreste), kalkfrei, Genese: limnisch bis brackisch, Farbe: olivbraun, - gebändert Bem: Bohrkern 12-13m		
12,72	0,15	Organische Basalsequenz, Torf (Holzreste), kalkfrei, Genese: Niedermoor, Farbe: dunkelbraun bis schwarz Bem: Bohrkern 12-13m		
12,88	0,16	Organische Basalsequenz, Schluff, Torf, Mudde, kalkhaltig, Genese: Niedermoor, Farbe: braunoliv, - gebändert Bem: Bohrkern 12-13m		
13,00	0,12	Organische Basalsequenz, Torf (Holzreste), kalkfrei, Genese: Niedermoor, Farbe: dunkelbraun Bem: Bohrkern 12-13m		
14,22	1,22	Weichsel-Kaltzeit, Kies (mittelsandig, schwach durchwurzelt), kalkfrei, Genese: glazifluvial, Farbe: hellgrau Bem: Bohrkern 14-15m, Gerölle: Flint, Milchquarz, wenig Feldspat		
Projekt:		Hydrogeophysik		
Bohrung:		SUD_DS33 / CAT_SUD_33		
Auftraggeber:		LIAG		
Bohrfirma:		LBEG		
Bearbeiter:	Binot, F.	Ansatzhöhe:	1,30 m	Rechtswert: 3481770
Datum:	19.08.2010	Endtiefe:	24,00	Hochwert: 5962405



Fig. F.1 (Continued).

Borehole: DS33			
Depth (m)	Thickness (m)	Description	
14,29	0,07	Weichsel-Kaltzeit, Kies (feinkiesig), kalkfrei, Genese: glazifluvial, Farbe: hellgrau Bem: Bohrkern 14-15m, wahrscheinlich erosive Basis	
14,45	0,16	Eem-Warmzeit, Ton (sehr stark schluffig, schwach humos, Holzreste, durchwurzelt), kalkfrei, Genese: Watt, Farbe: oliv Bem: Bohrkern 14-15m, sekundär entkalkt	
14,65	0,20	Eem-Warmzeit, Ton (sehr stark schluffig, Mikrofauna), kalkhaltig, Genese: Watt, Farbe: oliv, weiss (Punkte) Bem: Bohrkern 14-15m, Mikrofossilien - Foraminiferen	
15,00	0,35	Eem-Warmzeit, Ton (sehr stark schluffig, Mikrofauna, wenig Schilffeste), kalkhaltig, Genese: Watt, Farbe: oliv, weiss (Punkte) Bem: Bohrkern 14-15m, Intraklasten aus schluffigem Ton, ungerundet	
18,50	3,50	Eem-Warmzeit, Ton (sehr stark schluffig, viel Mollusken), stark kalkhaltig, Genese: Watt, Farbe: olivgrün Bem: Bohrkern 17-18m, Mollusken (dickschalig, großrippig, Cardien, Austern), Gastropoden (Turritella)	
20,20	1,70	Eem-Warmzeit, Ton (schluffig, wenig Mollusken), kalkhaltig, Genese: Watt bis brackisch, Farbe: olivgrün bis schwarzoliv bis grauoliv Bem: HCl --> H2S wird frei	
Projekt:		Hydrogeophysik	
Bohrung:		SUD_DS33 / CAT_SUD_33	
Auftraggeber:		LIAG	
Bohrfirma:		LBEG	
Bearbeiter:	Binot, F.	Ansatzhöhe:	1,30 m
		Rechtswert:	3481770
Datum:	19.08.2010	Endtiefe:	24,00
		Hochwert:	5962405



Fig. F.1 (Continued)

Borehole: DS33			
Depth (m)	Thickness (m)	Description	
21,40	1,20	Eem-Warmzeit, Mudde (schluffig, tonig), kalkhaltig, Genese: limnisch, Farbe: schwarz Bem: HCl -> H2S wird frei, nadelige Mikrofossilien	
22,17	0,77	Eem-Warmzeit, Schluff (tonig, stark organisch, sehr wenig Mollusken?), kalkhaltig, Genese: limnisch, Farbe: schwarz, oliv bis olivbraun (Oxydationsflecken) Bem: Bohrkern 21,5-22,5m - Streifen von Feinsand, hellgrau	
22,28	0,11	Eem-Warmzeit, Mudde (schluffig, tonig, organisch), kalkhaltig, Genese: limnisch, Farbe: schwarz Bem: Bohrkern 21,5-22,5m	
22,56	0,28	Eem-Warmzeit, Mudde (schwach humos), sehr stark kalkhaltig, Genese: limnisch, Farbe: hellgrau Bem: Bohrkern 21,5-22,5m	
22,71	0,15	Eem-Warmzeit, Mudde, Diatomeenmudde?, sehr stark kalkhaltig, Genese: limnisch, Farbe: weiss bis hellbeige, - gebändert Bem: Bohrkern 22,5-23,5m	
22,90	0,19	Eem-Warmzeit, Mudde (feinsandig, stark humos, stark zersetzt), schwach kalkhaltig, Genese: limnisch, Farbe: dunkelbraun Bem: Bohrkern 22,5-23,5m	
23,12	0,22	Eem-Warmzeit, Torf (feinsandig, stark zersetzt), kalkfrei, Genese: Niedermoor, Farbe: dunkelbraun Bem: Bohrkern 22,5-23,5m	
24,00	0,88	Pleistozän, Feinsand (mittelsandig, schwach kiesig, schwach durchwurzelt), kalkfrei, Genese: glazifluviatil, Farbe: hellgrau, schwarz (fleckig), - Endteufe Bem: Bohrkern 22,5-23,5m	
Projekt:		Hydrogeophysik	
Bohrung:		SUD_DS33 / CAT_SUD_33	
Auftraggeber:		LIAG	
Bohrfirma:		LBEG	
Bearbeiter:	Binot, F.	Ansatzhöhe:	1,30 m
Datum:	19.08.2010	Rechtswert:	3481770
		Endtiefe:	24,00
		Hochwert:	5962405



LIST OF SYMBOLS AND ABBREVIATIONS

ϵ	Dielectric permittivity
δ	Fluid dynamic viscosity
ϵ_0	Dielectric permittivity in free space= $8.8510 \cdot 10^{-12}$ AS/Vm
τ_k	Relaxation time
$ \rho $	Resistivity magnitude
Σ^d	Excess of surface conductivity from diffuse layer
Σ^s	Excess of surface conductivity from stern layer
A	Cross section area (m^2)
a	Dipole length
a	Cross-section area in m^2
A and B	Current electrodes
AB/2	Half current electrode spacing
AB/2	Half current electrode spacing
AC	Alternating current
B	Magnetic induction (W/m^2)
B	Equivalent conductance of (sodium) clay-exchange cations
b.s.l	Below sea level
BQ_v	Effects of surface conduction
C	Flatness filter
C*	The excess concentration produced by the polarized field
CEC	Cation exchange capacity
CPA	Constant-phase-angle model
CR	Complex resistivity
CVES	Continuous Vertical Electrical Sounding
D	Displacement current (C/m^2)
d	Measured data points

d	Grain size
d_{10}	Effective grain size (in mm), 10 % of the sample is finer
DC	Direct current
DD	Dipole-Dipole
E	East
E	Electric field intensity (V/m)
$E(\omega)$	Electrical field at angular frequency ω
EDL	Electrical double layer
EMF_c	Electromagnetic force or voltage in conductor
ERT	Electrical resistivity tomography
ESE	East- southeast
f	Frequency (Hz)
F	Electrical formation factor
$f(m)$	Response function
F_a	Apparent formation factor
FD	Finite-difference
FDEM	Frequency domain electromagnetic
FE	Frequency effect
FE	Finite-element
F_i	Intrinsic formation factor
$f_i(m)$	Model forward response
G	Geometric factor (meter)
g	Gravitational acceleration
g_i	Discrepancy vector
GM	Wenner- γ configuration
GPR	Ground penetration Radar
GPS	Global positioning system
H	Magnetic field strength
H	Magnetic field intensity (A/m)
h and H	Thickness (m) and total thickness (m), respectively
HEM	Helicopter electromagnetic
H_p	Primary magnetic field
H_s	Secondary magnetic field
HW	half-Wenner configuration
HZ	Herz
I	Current (ampere)
i	Imaginary unit = $(-1)^{0.5}$
IP	Induced polarization
J	Current density (A/m^2)
$J_0(\lambda x)$	Bessel function of zero order
J_i	Sensitivity matrix/ Jacobian matrix
$J_t(\omega)$	Total current density
K	Transmissivity

$K(\eta)/E(\eta)$	<i>Elliptic integrals of first/second order</i>
$K(\lambda)$	<i>Kernel function</i>
k	<i>The wave number</i>
k_f	<i>Hydraulic conductivity</i>
km	<i>Kilometer</i>
L	<i>self-inductance</i>
m	<i>Meter</i>
m	<i>Chargeability (V_s/V_p)</i>
M	<i>Integral chargeability</i>
m	<i>Cementation factor in Archie's law</i>
M and N	<i>Potential electrodes</i>
m_a	<i>Apparent chargeability</i>
m_j	<i>Model parameter</i>
m_k	<i>Specific chargeability</i>
MN/2	<i>Half potential electrode spacing</i>
mA	<i>millivolt</i>
MT	<i>Magnetotelluric</i>
N	<i>Number of the measured data points</i>
N	<i>North</i>
nV	<i>Nanovolt</i>
P	<i>Permeability</i>
P	<i>Polarization</i>
PACES	<i>Pulled Array Continuous Electrical sounding</i>
PD	<i>pole-dipole configuration</i>
p_i	<i>Perturbation factor</i>
PP	<i>pole-pole configuration</i>
q	<i>Specific discharge (m/s)</i>
Q_v	<i>CEC per unit pore volume (equiv litre⁻¹)</i>
R	<i>Resistance (volt/ampere)</i>
r	<i>Hydraulic radius</i>
R^2	<i>Correlation coefficient</i>
RMS	<i>Root mean square error</i>
S	<i>South</i>
S	<i>Longitudinal conductance</i>
SC	<i>Wenner-Schlumberger configuration</i>
S_{cum}/cov_j	<i>Cumulative sensitivities or coverage</i>
$S_{ij}(m)$	<i>Model mathematical sensitivity</i>
SIP	<i>Spectral induced polarization</i>
SP	<i>Self-potential</i>
S_{por}	<i>Surface area per unit pore volume ($S_{por} = r^{-1}$)</i>
S_s	<i>Specific surface area</i>
S_w	<i>Water saturation</i>
T	<i>Transverse resistance (Ohm m²)</i>

t	The time (s)
T	Tortuosity
TEM	Time domain or transient electromagnetic
$T_i(\lambda)$	Transform function
V_M and V_N	Potential at M and N electrodes, respectively
V_p	Primary voltage
V_p and V_t	Volume of pores and rocks, respectively
V_s	secondary voltage
$V_{s(t)}$	Off-time measured voltage at time t
V_{sp}	Background (self-potential) voltage
W	West
WB	Wenner- β configuration
WN	Wenner- α configuration
WNW	West-northwest
Z	Depth
α	Response parameter= $2\pi fL/R$
δ	Skin depth
ΔV	Potential difference (volt)
λ	Pseudo-anisotropy
λ_i	Damping factor
μ	Magnetic permeability
μ_0	Magnetic permeability in free space= $4\pi 10^{-7}$ Vs/Am
ρ	resistivity in Ohm m
ρ_0	Apparent resistivity at the lowest frequency
ρ_∞	Apparent resistivity at the highest frequency
ρ_a	Apparent resistivity
ρ_{ci}	Calculated apparent resistivity
ρ_d	Free charge density
ρ_{dc}	DC resistivity
ρ_{oi}	Observed apparent resistivity
ρ_s	Mineral density
ρ_T and ρ_L	Transverse and longitudinal resistivities, respectively
ρ_w	Water resistivity
$\bar{\rho}_w$	Average aquifer water resistivity
σ	Conductivity (1/ohm m=Siemens)
σ'	Real part of conductivity
σ''	Imaginary part of conductivity
σ^*	Complex part of conductivity
σ_{el}	Electrolytic conduction
σ_f	Fluid conductivity
σ_{int}	Interface conductivity
σ_{si}	relative standard deviation or error

φ	<i>Phase (mrad or deg)</i>
Φ	<i>Porosity</i>
$\Phi(m)$	<i>Model objective function</i>
ω	<i>Angular frequency ($2\pi f$)</i>
Ω_m	<i>Ohm meter</i>
$\bar{\rho}$	<i>Fluid density (1000 kg/m^3)</i>
δ	<i>Error factor</i>
r_{i-1}	<i>Model resistivity vector</i>
μ^{-1}	<i>Lagrange multiplier</i>
1D	<i>One dimensional</i>
$\ Dm\ ^2$	<i>Model roughness</i>
2D	<i>Two dimensional</i>
3D	<i>Three dimensional</i>
$n=1, n=2, \dots$	<i>2D data levels</i>